Computational Modelling of Quenching and Grinding Processes for Bearing Steels

von der Fakultät Maschinenbau
der Technischen Universität Dortmund
zur Erlangung des akademischen Grades

Doktor-Ingenieur (Dr.-Ing.)

genehmigte Dissertation

von

Tim Furlan

aus Kamen

Vorsitz:	PD Dr.-Ing. habil. Tobias Kaiser
Referent:	Prof. Dr.-Ing. habil. Andreas Menzel
Korreferenten:	Assoc. Prof. Dr.-Ing. Ralf Denzer
	Prof. Dr.-Ing. Prof. h.c. Dirk Biermann
Tag der Einreichung:	17.02.2026
Tag der mündlichen Prüfung:	24.06.2026

Bibliografische Information Der Deutschen Bibliothek
Die Deutsche Bibliothek verzeichnet diese Publikation in der Deutschen Nationalbibliografie; detaillierte bibliografische Daten sind im Internet über **http://dnb.dnb.de** abrufbar.

Bibliographic information published by Die Deutsche Bibliothek
Die Deutsche Bibliothek lists this publication in the Deutsche Nationalbibliografie; detailed bibliographic data is available in the Internet at **http://dnb.dnb.de**.

Schriftenreihe des Instituts für Mechanik

Herausgeber: Institut für Mechanik
Fakultät Maschinenbau
Technische Universität Dortmund
Leonhard-Euler-Str. 5
D-44227 Dortmund

Druck: Koffler DruckManagement GmbH

Als Manuskript gedruckt. Printed in Germany.

ISSN 2191-0022
ISBN 978-3-947323-59-3

"Joy in looking and comprehending is nature's most beautiful gift."

Albert Einstein

Acknowledgements

First and foremost, I would like to express my gratitude to Andreas Menzel for supervising this thesis, as well as for his valuable input on various parts of the research i conducted for this thesis. I would also like to thank Ralf Denzer and Dirk Biermann for acting as referees on the examination committee, and Tobias Kaiser for chairing it.

During my time at the Institute of Mechanics, I met and worked with a lot of great people. Some of them introduced me to new scientific ideas, some of them I had great conversations with on topics beyond work, and some of them became friends rather than colleagues. I would like to thank everyone i worked together with at the institute and in my projects for the great work atmosphere – there rarely was a single day where I did not like going to work. I especially appreciated working in a team where the best way to teach something was often discussed much more vividly than the best approach to a scientific problem.

Furthermore, I want to thank my friends and especially my family for their encouragement, love and support in life well beyond this thesis. Knowing I can rely on you for anything is a great privilege, which I will always be grateful for.

Dortmund, July 2026 Tim Furlan

Zusammenfassung

Die Herstellung von Wälzlagerkomponenten aus Lagerstählen wie 100Cr6 erfordert die Bearbeitung der Werkstücke in mehreren aufeinanderfolgenden Produktionsprozessen. Jeder dieser Prozesse verändert dabei den Ausgangszustand des Produkts zu Beginn des darauf folgenden Prozesses. Aus dieser Tatsache ergeben sich komplexe Zusammenhänge zwischen den Prozessparametern für die einzelnen Prozesse und den Eigenschaften des fertigen Produktes. In dieser Arbeit werden Ansätze zur numerischen Modellierung des Abschreckens und der Schleifbearbeitung in solchen Prozessketten entwickelt.

Für das Abschrecken nach der Austenitisierung wird ein vollständig thermomechanisch gekoppeltes Modell entwickelt, welches die auftretenden Phasentransformationen zu Martensit und Bainit berücksichtigt. Die athermische Umwandlung von Austenit zu Martensit wird durch eine Variante des klassischen Koistinen-Marburger Modells abgebildet, während die diffusive Umwandlung von Austenit zu Bainit mit einem JMAK-Ansatz modelliert wird. Es wird berücksichtigt, dass der entstehende Bainit einen anderen Kohlenstoffanteil als der Austenit aufweisen kann, indem die Massenbilanz für den Kohlenstoff gelöst wird. Die Parameter der Umwandlungsmodelle sind dabei im aktuellen Kohlenstoffgehalt des Austenits parametrisiert. Die Kopplung zum mechanischen und thermischen Problem entsteht aus den Transformationsdehnungen und der Freisetzung latenter Wärme während der Umwandlungen.

Beim Innenrundschälschleifen mit galvanisch gebundenen cBN Schleifscheiben ergibt sich durch die Prozesskräfte eine elastische Abdrängung zwischen Werkzeug und Werkstück, welche zu Maß- und Formfehlern führen kann. In dieser Arbeit wird eine geometrische Simulation des Schleifprozesses verwendet, wobei die Korngeometrien auf der digitalen Schleifscheibe auf Messungen realer Körner basieren. Um die elastische Abdrängung während des Schleifprozesses zu berücksichtigen, werden zwei Ersatzmodelle entwickelt: Ein Modell für den Prozesskraftbeitrag eines einzelnen Schleifkorns im Eingriff, und ein Modell für die gesamte Nachgiebigkeit zwischen Werkzeug und Werkstück. Das Kraftmodell wird anhand von Finite-Elemente-Simulationen eines idealisierten Einzelkornschnitts kalibriert, während ein statischer Ersatzversuch zur Kalibrierung des Nachgiebigkeitsmodells dient.

Für die Simulation des Einzelkorneingriffs wird außerdem ein neues, thermodynamisch konsistentes Materialmodell entwickelt. Dieses ist an das für Zerspanungssimulationen weithin genutzte Johnson-Cook Modell angelehnt, jedoch in mehreren Aspekten an das Verhalten von 100Cr6 angepasst. Um die großen Deformationen während des mesoskopischen Materialabtrags zu berücksichtigen, wird ein neues Simulations-Framework in der Finite Element Software Abaqus, basierend auf der Coupled Eulerian Lagrangian Methode, vorgestellt, und mit einem bestehenden Framework verglichen, welches auf einer periodischen Neuvernetzung basiert.

Die entwickelten Modelle verbessern die Simulationsmöglichkeiten für die Herstellung von Wälzlagerkomponenten aus 100Cr6, und tragen dadurch zu einer besseren Abstimmung der Prozessparameter verschiedener Herstellungsschritte bei.

Abstract

The manufacturing of roller bearing components from bearing steels such as 100Cr6 requires the processing of the workpieces in several successive production steps. Each of these processes modifies the initial state of the product at the beginning of the subsequent process. As a result, complex interdependencies arise between the process parameters of the individual processes and the properties of the finished product. In this work, approaches for the numerical modelling of the quenching and grinding processes in such production chains are developed.

For quenching after austenitisation, a fully thermomechanically coupled model is developed which accounts for the occurring phase transformations to martensite and bainite. The athermal transformation of austenite to martensite is modelled by a variant of the classical Koistinen–Marburger ansatz, while the diffusive transformation of austenite to bainite is modelled using a JMAK approach. It is taken into account that the resulting bainite may exhibit a different carbon content than the austenite by solving the mass balance for carbon. To this end, the parameters of the transformation models are parametrised based on the current carbon content of the austenite. The coupling to the mechanical and thermal problems arises from transformation strains and the release of latent heat during the transformations.

Due to the process forces in internal traverse grinding with electroplated cBN tools, elastic deflection occurs between the tool and the workpiece, which can lead to dimensional errors and shape deviations. In this work, a geometric simulation of the grinding process is used, where the grain geometries on the digital grinding wheel are based on measurements of real grains. To account for elastic deflection during the grinding process, two surrogate models are developed: a model for the process force contribution of a single grinding grain engaged in mesoscopic cutting, and a model for the total compliance between the tool and the workpiece. The force model is calibrated using finite element simulations of an idealised single-grain cutting process, while a static analogy test is used to calibrate the compliance model.

For the simulation of single-grain engagement, a new thermodynamically consistent material model is also developed. This model is inspired by the widely used Johnson–Cook model for cutting simulations but is adapted in several aspects to the behaviour of 100Cr6. To account for the large deformations occurring during mesoscopic material removal, a new simulation framework in the finite element software Abaqus, based on the Coupled Eulerian Lagrangian method, is presented and compared with an existing framework based on periodic remeshing.

The developed models improve the simulation capabilities for the manufacturing of roller bearing components from 100Cr6 and thereby contribute to better coordination of the process parameters across different manufacturing steps.

Publications

The following publications have been published with permission during the progress of this thesis. Since most of these were created in interdisciplinary collaboration with multiple researchers, the scientific contributions of the author of this thesis are outlined below for each publication.

Where parts of the text of this thesis have been pre-published in one of these publications, it is marked by special symbols. For example, the opening and closing markers ${}^{\text{qtd.}}_{[185]}\{$ and $\}^{\text{qtd.}}_{[185]}$ denote text pre-published in [185]. The same style is used for citations from all publications listed. The text delimited by the markers is identical word for word to the pre-published text, except for minor textual adaptations, footnotes, or variables and notation which are adapted to the conventions used in this thesis. To improve readability, the markers are not repeated when a quoted section contains a figure, table, or algorithm. However, markers do not span multiple sections. Furthermore, equations are not explicitly marked as cited from these publications, unless the surrounding text is also directly cited.

Where figures or tables are reproduced from any source, including the publications listed in this section, this fact is stated in the corresponding caption.

Peer-reviewed articles and proceedings

The following peer-reviewed articles and proceedings have been published during the progress of this thesis.

[159] N. Schmidt, T. Tsagkir Dereli, T. Furlan, R. Holtermann, D. Biermann, and A. Menzel. Towards the Prediction of Compliance Influences on Shape Deviations in Internal Traverse Grinding. In B.-A. Behrens, A. Brosius, W. Hintze, S. Ihlenfeldt, and J. P. Wulfsberg, editors, *Production at the Leading Edge of Technology*, pages 304–314. Springer Berlin Heidelberg, Berlin, Heidelberg, 2021. doi:10.1007/978-3-662-62138-7_31

[185] T. Tsagkir Dereli, N. Schmidt, T. Furlan, R. Holtermann, D. Biermann, and A. Menzel. Simulation Based Prediction of Compliance Induced Shape Deviations in Internal Traverse Grinding. *Journal of Manufacturing and Materials Processing*, 5(2):60, 2021. doi:10.3390/jmmp5020060

[53] T. Furlan, T. Tsagkir Dereli, N. Schmidt, D. Biermann, and A. Menzel. Application of the Coupled Eulerian Lagrangian method to the prediction of single-grain cutting forces in grinding. *Proceedings in Applied Mathematics and Mechanics*, 22 (1):e202200123, 2023. doi:10.1002/pamm.202200123

[172] L. Sobisch, T. Kaiser, T. Furlan, and A. Menzel. A user material approach for the solution of multi-field problems in Abaqus: Theoretical foundations, gradient-enhanced damage mechanics and thermo-mechanical coupling. *Finite Elements in Analysis and Design*, 232:104105, 2024. doi:10.1016/j.finel.2023.104105

[160] N. Schmidt, T. Furlan, J. Peters, M. Kipp, S. Kaschnitz-Biegl, A. Menzel, F. Bleicher, and D. Biermann. Meso-scale geometric modeling of cutting edges on vitrified bonded aluminum oxide grinding wheels for the multi-scale simulation of internal plunge grinding processes. *Procedia CIRP*, 133:513–518, 2025. doi:10.1016/j.procir.2025.02.088

[54] T. Furlan, M. Schewe, P. Scherm, P. Retzl, E. Kozeschnik, and A. Menzel. Modelling and finite element simulation of martensite and bainite phase transformations during quenching under consideration of carbon repartitioning. *Mechanics of Materials*, 204:105275, 2025. doi:10.1016/j.mechmat.2025.105275

The publications [159] and [185] are concerned with a framework for the simulation of internal traverse grinding, as well as with corresponding experimental investigations. Contributions of the author of this thesis mainly comprise:

- the application of a previously established finite element framework for the simulation of meso-scale cutting to develop a new surrogate model for process force contributions of individual grains during the grinding process,
- the development and comparison of the proposed compliance models for tool and workpiece holder, as well as the compliance model combining both contributions,
- the development of a Python code to evaluate the measurement data for the calibration of these compliance models,
- and, in equal collaboration with Nils Schmidt, the transfer of pixel-based grain height fields to triangulated data, as well as the development of the approximation approach to evaluate the effective rake angle based on these triangulations, enabling their application within the geometric simulation.

In addition, the conducted research for these publications was planned, discussed, and evaluated in close collaboration between all listed authors.

The research presented in [53] investigates the properties of the Coupled Eulerian Lagrangian method in the context of cutting simulations, and was mainly planned and conducted by the author of this thesis. Some precursory investigations into the method

were performed during a student project conducted by Lennart Sobisch under the co-supervision of the author.

Although the results were not directly used in the publications, it is to be mentioned that further understanding for the subject was built by the author of this thesis during the co-supervision of student theses by Pouria Araghchi ('Regelmäßige Neuvernetzung als Strategie für Finite-Elemente-Simulationen bei großen Verformungen in der Festkörpermechanik'), Lennart Sobisch ('Solution recovery and transfer in h-adaptive finite element analyses'), Jonathan Stollberg ('Remeshing of deformed bodies in large deformation FEM simulations using higher-order elements'), and Nicole Policeusz ('Auslegung, messtechnische Erfassung und FE-Simulation eines Analogieversuches zur Werkstückeinspannung beim Innenrundschälschleifen').

Co-supervising the master's thesis 'Modelling and simulation of thermo-mechanical coupling and damage in ABAQUS' by Lennart Sobisch allowed the author of this thesis to broaden his understanding of local and non-local damage models. His contributions to the publication [172], which further develops the contents of the master's thesis, are primarily focused on Abaqus-specific implementation advice for the proposed two-instance approach. The author of this thesis further improved his understanding of damage mechanics during the co-supervision of the master's thesis of Christos Charalampidis ('Investigation of a Thermodynamically Consistent Model for Large-Strain Plasticity and Ductile Damage').

For [160], the author of this thesis contributed to the shape removal algorithm, which was developed in equal collaboration with Nils Schmidt. Furthermore, the force model used is based on the model developed in [185]. The contents of [160] are not directly included in this thesis.

The publication [54] is based on a master's thesis by Philipp Scherm ('Material Modelling and Finite Element Simulation of Quenching'), which was co-supervised by the author of this thesis, and which is largely based on a project proposal co-authored by the author of this thesis. Specifically, the author of this thesis contributed the fundamental choices for the transformation models and the finite element framework. During the progress of the master's thesis, the additional aspect of variable carbon content was introduced through discussions with Philipp Retzl. For the publication of [54], the author of this thesis revisited the work to simplify the formulation of the carbon mass balance, and to introduce additional dependencies of the transformation model parameters on the carbon content based on MatCalc simulations contributed by Philipp Retzl. Both the parameter identification for the models as well as the user subroutine were reimplemented from scratch by the author of this thesis, and new examples were generated for the publication.

Non peer-reviewed articles

The following articles are related to this thesis, but have not been peer-reviewed.

[184] T. Tsagkir Dereli, D. Biermann, A. Menzel, N. Schmidt, T. Furlan, and R. Holtermann. Prozessoptimierung für das Innenrundschälschleifen. *VDI-Z*, 162(03): 25–27, 2020

[186] T. Tsagkir Dereli, T. Furlan, N. Schmidt, J. Liedel, A. Menzel, and D. Biermann. Standzeitverdopplung beim Hochgeschwindigkeits-Innenrundschälschleifen mit modifizierten galvanisch gebundenen CBN-Werkzeugen. *Diamond Business*, 2022(2), 2022

For [184], the author of this thesis contributed the sections and graphics related to the compliance models. In [186], the compliance model presented in [159] and [185] was used to support the empirical adaptation of the tool shape. Neither publication contains research directly included in this thesis.

Peer-reviewed software

Besides the articles and proceedings mentioned above, two peer-reviewed open source software packages were published, along with short articles.

[66] D. Güzel, T. Furlan, T. Kaiser, and A. Menzel. Neper-Mosaic: Seamless generation of periodic representative volume elements on unit domains. *SoftwareX*, 28:101912, 2024. doi:10.1016/j.softx.2024.101912

[55] T. Furlan, J. Stollberg, and A. Menzel. Paraqus: Exporting Finite Element Simulation Results from Abaqus to VTK. *Journal of Open Source Software*, 10(106): 5729, 2025. doi:10.21105/joss.05729

Mosaic [66] is a Python package for the transformation of representative volume elements created in the software Neper [141] to a rectilinear domain. The author of this thesis co-developed the algorithm for the transformation in the software gmsh. Mosaic was not used in the creation of this thesis.

Paraqus [55] is a Python package for the export of finite element simulations, mainly from the finite element software Abaqus, to the open vtk file format, used for example by ParaView. The package was co-developed by the author of this thesis, with a focus on the implementation of the export from Abaqus and the overall code structure. In this thesis, many visualisations for finite element results obtained in Abaqus are presented, most of which are created in ParaView based on Paraqus outputs.

Use of artificial intelligence

During the creation of this thesis, limited use of artificial intelligence (AI) based tools, mainly ChatGPT, Edison, and DeepL, was made by the author.

ChatGPT and DeepL were used for translation and language refinement. However, aside from the translation of parts of the abstract, no complete paragraphs of text in the thesis were generated by AI.

Edison and ChatGPT were used to find scientific literature related to various aspects of the thesis. These searches were always accompanied by classic keyword based web searches to avoid any bias introduced by the AI tools. All citations in this thesis are based on the author's own understanding of the sources obtained from both approaches.

ChatGPT was furthermore used for informal discussions on ideas, concepts, and modelling approaches, in a manner similar to a discussion with a colleague. It was however not used to generate original scientific results, analyses, or to draw conclusions. Any information obtained from these discussions was critically assessed and independently verified using peer-reviewed scientific literature and authoritative sources. Where methods, models, or ideas from these discussions were applied in this thesis, the appropriate scientific sources are cited.

Finally, ChatGPT was used to accelerate and improve the programming of the models presented in this thesis. While AI assistance was used for program prototyping, to correct syntax errors or to find appropriate packages for certain specific tasks, the design of the programs and choice of algorithms was performed by the author.

For all use cases listed, the author of this thesis carefully reviewed and edited all results obtained from AI based tools. Full responsibility for the content of the thesis rests with the author.

Contents

1 Introduction

This thesis is based on research conducted within the context of three different projects which were conducted in collaboration with partners from other research institutions as well as industry partners.

Specifically, the German Research Foundation (DFG) project 'Simulationsbasierte Auslegung von Hochleistungs-Innenrundschleifprozessen' (grant number 403857741) was conducted by the Institute of Mechanics (IM) and Institute of Machining Technology (ISF) of TU Dortmund University in collaboration with the industry partners Schaeffler Technologies AG & Co. KG and August Rüggeberg GmbH & Co. KG. One of the primary project goals was to adapt a simulation framework for internal traverse grinding, which was developed in a previous project, to predict the influence of various parameters of the grinding process on shape deviations of the finished product.

In the Cornet project 'P2P – Produce to Performance' (grant number 01IF00325C), organised by the research associations Forschungsgemeinschaft Werkzeuge und Werkstoffe e.V. (FGW) and EcoPlus, IM and ISF collaborated with research partners at the Institute of Materials Science and Technology (WWWT) and the Institute of Production Engineering and Photonic Technologies (IFT) of TU Wien, as well as the Institut für Werkzeugforschung und Werkstoffe (IFW) of the FGW. Furthermore, the project was supported by a user committee consisting of representatives of multiple companies. In this project, interdependencies between different processes of the production chain for bearing components were investigated, with a focus on the hardening and grinding processes. One of the main contributions of the IM to this project was the numerical modelling of phase transformations during the hardening of steel components.

Finally, the DFG project 'Entwicklung eines numerischen Spanbildungsmodells zur Vorhersage des reibungsabhängigen Spanbruchverhaltens' (grant number 539920410), which is ongoing at the time this thesis is written, aims to model chip formation and breakage during orthogonal cutting, using methods closely related to the simulation of meso-scale cutting in the DFG project 'Simulationsbasierte Auslegung von Hochleistungs-Innenrundschleifprozessen'.

1.1 Motivation

Ball and roller bearings are widely used in various industries and applications, for example wheel hubs and transmissions in the automotive sector, wind turbines in the production of renewable energy, or electric motors and robot joints in industrial automation. The interested reader is referred to Zaretsky [202] for a review of the developments since the first patent for such a bearing was applied for in 1734.

While today there is a wide variety of bearing types to choose from, most ball and roller bearings are constructed from three main components: Inner and outer rings are attached to the parts connected by the bearing, and balls or rollers between both rings allow for efficient relative motion. Many variants incorporate additional cages to ensure correct positioning of the balls or rollers.

Historically, bearings were manufactured almost exclusively from steel similar to the specification AISI 52100, and even in 2012 it was cited as the most used bearing steel [202]. In this thesis, the (nearly identical) specification 100Cr6 is used interchangeably with AISI 52100. A discussion of other steel grades used for bearing manufacturing, as well as the processing of these steels, was given by Bhadeshia [21].

The process chain for bearing components made of 100Cr6 steel is divided by Klein et al. [94] into primary shaping, forging, machining, heating, and quenching. In this thesis, a finishing step is additionally considered, in which the functional surfaces of the workpiece are ground to achieve the desired tolerances, and the methods proposed in this thesis will mainly focus on the last two stages. A graphical representation of such a process chain is shown in fig. 1.1.

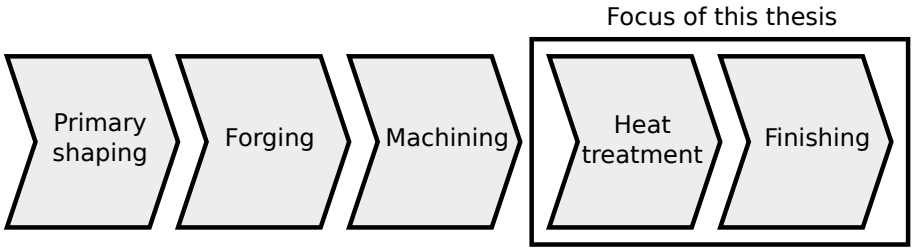

Figure 1.1: Exemplary process chain for the manufacturing of 100Cr6 bearing components.

Generally, the workpiece geometry results from the steps ending with the machining of the workpieces. The subsequent heat treatment, which consists of austenitisation, quenching to induce a martensitic hardening, and tempering, ensures adequate hardness and toughness of the raceways. Phase transformations during the heat treatment incur non-uniform residual stresses and corresponding deformations of the workpieces. Due to the strict tolerances required especially for the raceway dimensions, a finishing step – for example by grinding – is usually required to achieve the final workpiece geometry, as well as surface qualities. As indicated in fig. 1.1, this thesis focuses on the heat treatment and finishing stages of the manufacturing process.

The properties and performance of the final product are determined by complex interactions along the process chain. For example, a change in alloy composition could change the kinetics of phase transformations, changes in machining process parameters could change the thermal loading and therefore lead to surface degradation [144], or cold working before the heat treatment could change transformation temperatures, and therefore final hardness [20].

Due to the continuously increasing demands for product performance and manufacturing efficiency, a holistic consideration of process chains is becoming increasingly important. Furthermore, secondary steel usage continually increases due to cost benefits and to the movement towards a circular economy [142]. Understanding the impact of small changes in alloy composition on the final product performance is therefore paramount for future manufacturing.

1.2 Heat treatment

The state of the art for the heat treatment of 100Cr6 bearing components was summarised by Bhadeshia [21]. This section briefly reviews the aspects of this study which are most important for this thesis.

Bearing steel is usually supplied to manufacturers in a hot-rolled state with a mostly pearlitic microstructure, which includes some cementite. It is desirable to avoid cementite networks in the microstructure, which can be achieved by adequate cooling after hot deformation or by spheroidisation of the cementite through annealing.

Austenitisation is typically performed at temperatures between 840 °C and 900 °C for a duration of approximately 20 min, followed by quenching in salt or oil. At these temperatures some cementite remains in the microstructure, which can improve wear resistance. Higher austenitisation temperatures up to 1100 °C can be used to fully dissolve carbides in the microstructure. However, this usually comes at the price of larger grain sizes and therefore reduced strength.

After the quenching, the predominantly martensitic microstructure typically contains some retained austenite as well as the cementite particles mentioned above. Subsequent tempering, typically below 200 °C, can dissolve some of the retained austenite, and generally induces precipitation of carbides. Transformations of retained austenite during the subsequent processing steps or during the service life of the bearings can induce shape deviations and therefore deteriorate product performance.

While the reader is referred to [21] for a detailed review, it is mentioned here that relatively small changes in the alloy composition or the heat treatment can significantly alter the transformation kinetics and therefore the product properties. For example, it is possible to induce a transformation of the microstructure to bainite, minimising retained austenite as well as avoiding hydrogen embrittlement.

Transformation kinetics can be further influenced by changes in the alloy composition during the transformations, for example the repartitioning of carbon or chromium.

Especially for larger components, the heating and cooling of workpieces do not happen homogeneously. For this reason, larger bearing components are sometimes case hardened instead of through hardened. In such cases, the microstructure is also non-homogeneous, making accurate predictions of the overall product properties difficult.

1.3 Finishing

The finishing takes place after the heat treatment of the bearing components, and typically consists of material removal by hard turning or grinding to achieve the final workpiece dimensions, followed by a fine finishing process such as honing to produce the desired surface qualities [69]. This thesis focuses on material removal through grinding, which is a machining process with geometrically undefined cutting edges [41]. Although grinding was traditionally considered a finishing process, modern high-performance processes can be economically viable for larger material removal rates as well [97].

The requirements for high productivity and high surface qualities are generally difficult to fulfil simultaneously, as higher material removal rates increase mechanical and thermal loads [69, 97]. In internal plunge grinding (IPG), the full length of the workpiece bore is engaged with the grinding wheel at the same time. Material removal is achieved through a radial feed of the grinding tool, while the workpiece is rotated to evenly remove the material over the bore circumference. Due to the large contact area, comparatively high normal forces occur in IPG, therefore requiring rigid spindle systems, which is not usually true for high-speed spindles [57, 163, 179]. $^{\text{qtd.}}_{[185]}\{$In combination with slim tool holders, usually used in internal grinding operations so that the grinding tools can enter the bore, elastic deformations of tool and workpiece spindle are caused [120].$\}^{\text{qtd.}}_{[185]}$ This results in elastic deflection of tool and workpiece, and therefore in dimensional inaccuracies and shape deviations [23, 57, 163].

In contrast to internal plunge grinding, during internal traverse grinding (ITG) the grinding wheel is in contact only with a small axial section of the workpiece at any time, and is axially fed along the bore. In ITG, the grinding wheel exhibits two separate zones: The material removal is mainly achieved by a tapered roughing zone, while a cylindrical finishing zone improves surface quality [128, 163]. Process kinematics of IPG and ITG are schematically compared in fig. 1.2.

$^{\text{qtd.}}_{[185]}\{$Various studies [23, 121, 128] showed that internal traverse grinding has a high potential to achieve high material removal rates in combination with good surface quality in bore machining. Traverse grinding also offers high potential for external cylindrical and surface grinding operations [40, 146]. High performance internal traverse grinding with electroplated cBN grinding tools is an established manufacturing process for the efficient internal machining of chuck components, such as gears or bearing rings.$\}^{\text{qtd.}}_{[185]}$

Due to the process kinematics, normal forces and the corresponding deflections between tool and workpiece vary along the bore axis. Significant shape deviations must be expected especially at the tool entry and exit zones [75].

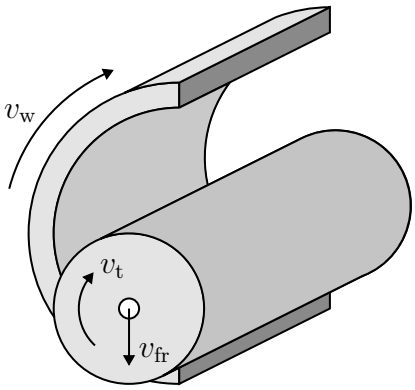

(a) Kinematics in internal plunge grinding, including the radial feed rate v_fr.

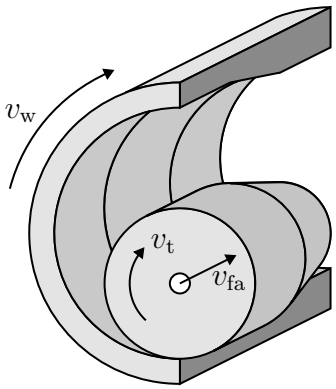

(b) Kinematics in internal traverse grinding, including the axial feed rate v_fa.

Figure 1.2: Process kinematics of internal plunge grinding and internal traverse grinding. Both sketches show the circumferential workpiece velocity v_w and tool velocity v_t. Dimensions are not to scale to improve visual clarity.

1.4 Modelling of process chains

In the context of industrial production processes, the state of a product (referring to the workpiece in the present example) is defined by Wuest et al. [200] as follows:

> The product state describes a product at a certain time during the production process or after through a combination of state characteristics. State characteristics are definable and ascertainable measures, which can be described in a quantitative or qualitative way, e.g. weight or chemical composition of the material. The product state changes due to external influence, for example machining or corrosion from t=0 to t=1 when at least one descriptive state characteristic changes.

In theory, the state of a product should completely determine its response to any additional processing, as well as the properties of the finished product – including state changes, for example due to loading, during the product life cycle. However, since it is impossible to characterise or store all relevant state characteristics, Wuest et al. [200] propose to identify especially relevant characteristics for a model of the product state.

For models of complex process chains, the identification of relevant state characteristics is challenging: A state model for such a process chain should include all relevant characteristics necessary to model the impact of each individual process on the product. However, due to the complexity of the physical processes during the processing, models proposed for individual processing steps are usually based on a limited number of variables, while implicitly assuming a given set of characteristics which are held constant. For example, flow stress models for specific materials are often calibrated for different strain rates or temperatures, while the initial microstructure due to the previous processing is not varied or even characterised. If a change in the previous processing changes the workpiece microstructure – and therefore the state of the product – before plastic deformation occurs in the process chain, such a model might be invalidated.

In recent years, research interest has increasingly focused on models which not only replicate the state of a product, but which feed back information to improve the product properties or service life. This paradigm shift is strongly intertwined with the expression 'digital twin' (DT), which, however, is not uniquely defined in the literature. According to Tomczyk and van der Valk [183], the concept was first introduced in 2003 by Grieves, and later formalised in [61], where the digital twin is defined by three main features: A physical product in real space, a virtual product in virtual space, and bidirectional data transfer. One of the main goals is described as changing 'digital factory simulation, which attempts to predict how the product is to be manufactured, into a digital factory replication, which shows how the product is actually being manufactured' [61].

For models which feed back data to the physical product, for example to adapt the parameters of subsequent manufacturing processes according to the product state, the evaluation time is an important aspect. A digital twin is considered to enable factory simulation 'in real time or near real-time' in [61]. Models which predict certain characteristics of a product based on limited input variables in a computationally efficient way are commonly referred to as surrogate models or meta models. They can be calibrated based on experimental data or simulations, but generally neglect physical relations in favour of a black-box approach. The use of surrogate models can enable inverse optimisation of product characteristics where the application of classic simulations would be impossible due to the numerical effort [106, 145]. While the term surrogate model is often used with respect to methods such as artificial neural networks or Gaussian process regression, in this thesis the calibration of selected ansatz functions – which are also efficient to evaluate – will be included in the definition.

1.5 Research objectives

To the best of the knowledge of the author of this thesis, no complete digital twin has been achieved for a process chain similar to the one presented in fig. 1.1. While the state of the art with respect to surrogate models advances at a high pace, the calibration of these models, as well as the selection of adequate state characteristics, remains an open challenge, especially when taking into account the interactions between process steps.

As manufacturers adopt more specialised production processes, such as modified heat treatments or high-performance internal traverse grinding, the need for accurate simulations increases. Traditional expert knowledge is often hard to transfer to these processes, while the economic requirements lead to a demand to choose parameters in the most efficient way possible. At the same time, trial-and-error approaches are costly and time-consuming.

A complete digital twin of the process chain is beyond the scope of this thesis, as the work is deliberately focused on selected challenges: The simulation of the heat treatment and grinding stages of the process chain. Based on such simulations, in silico experiments can give valuable insight into the interaction of state characteristics at different process steps.

2 Fundamentals of computational continuum mechanics

The models and simulations presented in this thesis are largely based on concepts of continuum mechanics. This chapter therefore gives an overview of the most important concepts for this thesis. Furthermore, two homogeneous deformation state problems of continuum mechanics are discussed, which will be used as reference examples for models proposed in the thesis. Finally, a very short overview of the finite element method is given, which was applied for various simulations presented in this thesis.

2.1 Continuum mechanics

The models derived in this thesis are formulated in the framework of continuum mechanics. This section outlines selected elements of the underlying theoretical framework. While it should provide sufficient detail to understand the derivations in the following chapters, a comprehensive discussion of this very broad topic is out of scope for this thesis, and the interested reader is referred to textbooks such as Liu [114].

In section 2.1.1, the foundations of finite strain continuum kinematics are briefly reviewed with a focus on plasticity. Thereafter, some general balance equations are discussed in section 2.1.2. By taking some assumptions and simplifications into account, the balance equations are adapted for the application to phase transformations and meso-scale cutting. The derivation of constitutive equations from a chosen free energy function is presented in section 2.1.3, and requirements for thermodynamical consistency of these equations are discussed. Finally, the application to the infinitesimal strain setting is reviewed in section 2.1.6.

2.1.1 Finite strain kinematics

In line with classical continuum mechanics, as presented in e.g. de Souza Neto et al. [36], a body $\mathcal{B}$ is considered, which occupies a region Ω_0 in space in a chosen reference configuration. For each material point (or particle), the position in the reference configuration is given by the vector $\boldsymbol{X}$. At any time t, the deformation of the body is

given by the mapping $\boldsymbol{x} = \boldsymbol{\varphi}(\boldsymbol{X})$, where $\boldsymbol{x}$ denotes the position of the particle in the current configuration, in which the body occupies the region Ω_t. Reference and current configuration are visualised in fig. 2.1. The loading of the body in both configurations introduced in the same figure will be taken into account in section 2.1.2.

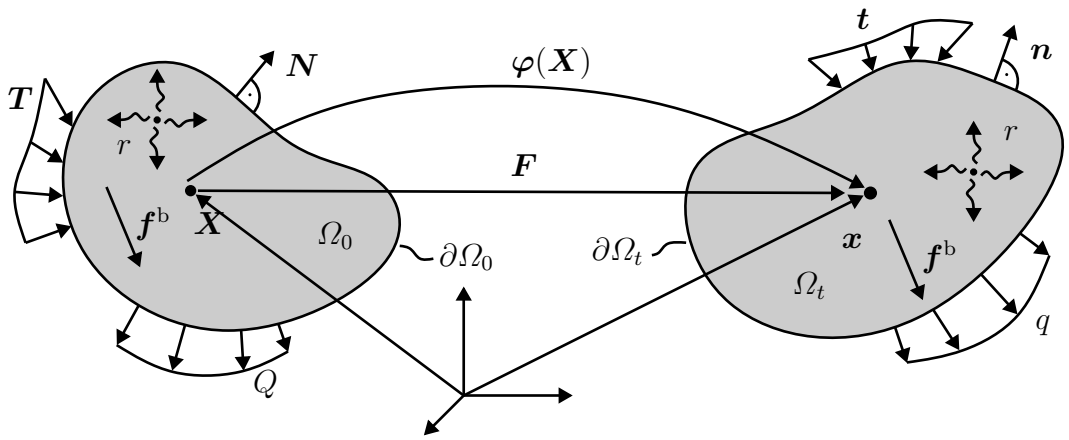

Figure 2.1: Reference and current configuration of a body $\mathcal{B}$. Surface normals are denoted as $\boldsymbol{N}$ and $\boldsymbol{n}$, surface tractions as $\boldsymbol{T}$ and $\boldsymbol{t}$, and scalar surface heat fluxes as Q and q. The body forces $\boldsymbol{f}^{\mathrm{b}}$ are mass-specific, as is the heat source r.

Based on the deformation gradient

$$\boldsymbol{F} = \frac{\partial \boldsymbol{x}}{\partial \boldsymbol{X}} \ , \tag{2.1}$$

line elements $\mathrm{d}\boldsymbol{X}$, surface elements $\mathrm{d}\boldsymbol{A}$, and volume elements $\mathrm{d}V$ in the reference configuration transform to the current configuration according to

$$\mathrm{d}\boldsymbol{x} = \boldsymbol{F} \cdot \mathrm{d}\boldsymbol{X} \ , \tag{2.2}$$

$$\mathrm{d}\boldsymbol{a} = J\, \boldsymbol{F}^{-\mathrm{t}} \cdot \mathrm{d}\boldsymbol{A} \ , \tag{2.3}$$

$$\mathrm{d}v = J\, \mathrm{d}V \ , \tag{2.4}$$

where

$$J = \det\left(\boldsymbol{F}\right) \tag{2.5}$$

denotes the determinant of the deformation gradient.

In the following, derivatives of a quantity $\bullet$ with respect to the current coordinates are denoted as e.g. $\mathrm{grad}\,(\bullet)$ and $\mathrm{div}\,(\bullet)$, while $\mathrm{Grad}\,(\bullet)$ and $\mathrm{Div}\,(\bullet)$ refer to the reference coordinates.

The polar decomposition

$$\boldsymbol{F} = \boldsymbol{V} \cdot \boldsymbol{R} = \boldsymbol{R} \cdot \boldsymbol{U} \tag{2.6}$$

separates the deformation gradient into an orthogonal rotation tensor $\boldsymbol{R}$ and the left or right stretch tensors $\boldsymbol{V}$ or $\boldsymbol{U}$. Based on $\boldsymbol{V}$ and $\boldsymbol{U}$, the left and right Cauchy-Green stretch tensors are defined as

$$\boldsymbol{b} = \boldsymbol{V}^2 = \boldsymbol{F} \cdot \boldsymbol{F}^{\mathrm{t}} \tag{2.7}$$

$$\boldsymbol{C} = \boldsymbol{U}^2 = \boldsymbol{F}^{\mathrm{t}} \cdot \boldsymbol{F} \ . \tag{2.8}$$

The spatial velocity gradient can be expressed as

$$\boldsymbol{l} = \frac{\partial \dot{\boldsymbol{x}}}{\partial \boldsymbol{x}} = \dot{\boldsymbol{F}} \cdot \boldsymbol{F}^{-1} \ , \tag{2.9}$$

and can be additively decomposed as

$$\boldsymbol{l} = \boldsymbol{d} + \boldsymbol{w} \tag{2.10}$$

into the rate of deformation tensor

$$\boldsymbol{d} = \boldsymbol{l}^{\mathrm{sym}} = \frac{1}{2}\left[\boldsymbol{l} + \boldsymbol{l}^{\mathrm{t}}\right] \tag{2.11}$$

and the spin tensor

$$\boldsymbol{w} = \boldsymbol{l}^{\mathrm{skw}} = \frac{1}{2}\left[\boldsymbol{l} - \boldsymbol{l}^{\mathrm{t}}\right] \ , \tag{2.12}$$

where only the rate of deformation tensor contributes to a stretching of the material.

The spectral decomposition of the left stretch tensor is given by

$$\boldsymbol{V} = \sum_{i=1}^{s} \lambda_i^{(\boldsymbol{V})} \, \boldsymbol{p}_i^{(\boldsymbol{V})} \ , \tag{2.13}$$

where $\lambda_i^{(\boldsymbol{V})}$ is the i^{th} of s eigenvalues of $\boldsymbol{V}$, and $\boldsymbol{p}_i^{(\boldsymbol{V})}$ is the corresponding eigenprojection. The (current configuration) Seth-Hill strain family is then defined by

$$\boldsymbol{e}^{(a)} = \begin{cases} \sum_{i=1}^{s} \dfrac{1}{2\,a}\left[\left[\lambda_i^{(\boldsymbol{V})}\right]^{2\,a} - 1\right] \boldsymbol{p}_i^{(\boldsymbol{V})} & \text{for } a \neq 0 \\ \sum_{i=1}^{s} \ln\left(\lambda_i^{(\boldsymbol{V})}\right) \boldsymbol{p}_i^{(\boldsymbol{V})} & \text{for } a = 0 \end{cases} \tag{2.14}$$

with $a \in \mathbb{N}$. In the following, the logarithmic strain tensor $\boldsymbol{\varepsilon} = \boldsymbol{e}^{(0)}$ will be considered, which is also referred to as the Hencky strain tensor in the literature (see e.g. [36]).

It will be useful in the following to consider the volumetric-deviatoric decomposition of the logarithmic strain tensor

$$\begin{aligned} \boldsymbol{\varepsilon} &= \boldsymbol{\varepsilon}^{(\mathrm{vol})} + \boldsymbol{\varepsilon}^{(\mathrm{dev})} \ , \\ \boldsymbol{\varepsilon}^{(\mathrm{vol})} &= \varepsilon_{\mathrm{m}} \, \boldsymbol{I} \ , \quad \varepsilon_{\mathrm{m}} = \frac{1}{3} \, \mathrm{tr}\left(\boldsymbol{\varepsilon}\right) \ , \\ \boldsymbol{\varepsilon}^{(\mathrm{dev})} &= \boldsymbol{\varepsilon} - \varepsilon_{\mathrm{m}} \, \boldsymbol{I} \ , \end{aligned} \tag{2.15}$$

where $\boldsymbol{I}$ denotes the second order identity tensor and

$$\mathrm{tr}\left(\boldsymbol{\varepsilon}^{(\mathrm{dev})}\right) = 0 \tag{2.16}$$

holds. From the definition of the logarithmic strain tensor, the left stretch tensor can then be written as

$$\boldsymbol{V} = \exp\left(\boldsymbol{\varepsilon}^{(\mathrm{vol})} + \boldsymbol{\varepsilon}^{(\mathrm{dev})}\right) = \exp\left(\boldsymbol{\varepsilon}^{(\mathrm{vol})}\right) \cdot \exp\left(\boldsymbol{\varepsilon}^{(\mathrm{dev})}\right) \ , \tag{2.17}$$

so that the volume change is given by

$$J = \det\left(\boldsymbol{V}\right) = \exp\left(\mathrm{tr}\left(\boldsymbol{\varepsilon}^{(\mathrm{vol})}\right) + \underbrace{\mathrm{tr}\left(\boldsymbol{\varepsilon}^{(\mathrm{dev})}\right)}_{=0}\right) = \exp\left(\mathrm{tr}\left(\boldsymbol{\varepsilon}^{(\mathrm{vol})}\right)\right) \ . \tag{2.18}$$

The deviatoric part of the logarithmic strain tensor is therefore indeed isochoric, and will be referred to as $\boldsymbol{\varepsilon}^{(\mathrm{iso})}$ in the following.

For the modelling of plasticity, it is common to introduce a stress-free, intermediate configuration. This naturally introduces the multiplicative split of the deformation gradient

$$\boldsymbol{F} = \boldsymbol{F}_{\mathrm{e}} \cdot \boldsymbol{F}_{\mathrm{p}} \tag{2.19}$$

into the elastic part $\boldsymbol{F}_{\mathrm{e}}$ and the plastic part $\boldsymbol{F}_{\mathrm{p}}$. The individual parts can be split into rotation and stretching according to the polar decomposition e.g. as

$$\boldsymbol{F}_{\mathrm{e}} = \boldsymbol{V}_{\mathrm{e}} \cdot \boldsymbol{R}_{\mathrm{e}} \ , \tag{2.20}$$

$$\boldsymbol{F}_{\mathrm{p}} = \boldsymbol{V}_{\mathrm{p}} \cdot \boldsymbol{R}_{\mathrm{p}} \ , \tag{2.21}$$

while the velocity gradient decomposes additively as

$$\boldsymbol{l} = \boldsymbol{l}_{\mathrm{e}} + \boldsymbol{l}_{\mathrm{p}} \ , \tag{2.22}$$

where

$$\boldsymbol{l}_{\mathrm{e}} = \dot{\boldsymbol{F}}_{\mathrm{e}} \cdot \boldsymbol{F}_{\mathrm{e}}{}^{-1} \tag{2.23}$$

denotes the elastic velocity gradient, and the plastic velocity gradient in the intermediate configuration

$$\bar{\boldsymbol{L}}_{\mathrm{p}} = \dot{\boldsymbol{F}}_{\mathrm{p}} \cdot \boldsymbol{F}_{\mathrm{p}}{}^{-1} \tag{2.24}$$

is pushed to the current configuration by

$$\boldsymbol{l}_{\mathrm{p}} = \boldsymbol{F}_{\mathrm{e}} \cdot \bar{\boldsymbol{L}}_{\mathrm{p}} \cdot \boldsymbol{F}_{\mathrm{e}}{}^{-1} = \boldsymbol{F}_{\mathrm{e}} \cdot \dot{\boldsymbol{F}}_{\mathrm{p}} \cdot \boldsymbol{F}_{\mathrm{p}}{}^{-1} \cdot \boldsymbol{F}_{\mathrm{e}}{}^{-1} \ . \tag{2.25}$$

The rate of deformation tensors are derived from the elastic and plastic velocity gradients as

$$\boldsymbol{d}_\mathrm{e} = \frac{1}{2}\left[\boldsymbol{l}_\mathrm{e} + \boldsymbol{l}_\mathrm{e}^{\mathrm{t}}\right] \ , \tag{2.26}$$

$$\bar{\boldsymbol{D}}_\mathrm{p} = \frac{1}{2}\left[\bar{\boldsymbol{L}}_\mathrm{p} + \bar{\boldsymbol{L}}_\mathrm{p}^{\mathrm{t}}\right] \ , \tag{2.27}$$

$$\boldsymbol{d}_\mathrm{p} = \frac{1}{2}\left[\boldsymbol{l}_\mathrm{p} + \boldsymbol{l}_\mathrm{p}^{\mathrm{t}}\right] \ , \tag{2.28}$$

where the additive decomposition

$$\boldsymbol{d} = \boldsymbol{d}_\mathrm{e} + \boldsymbol{d}_\mathrm{p} \tag{2.29}$$

holds. Similarly, the elastic and plastic spin tensors are given by

$$\boldsymbol{w}_\mathrm{e} = \frac{1}{2}\left[\boldsymbol{l}_\mathrm{e} - \boldsymbol{l}_\mathrm{e}^{\mathrm{t}}\right] \ , \tag{2.30}$$

$$\bar{\boldsymbol{W}}_\mathrm{p} = \frac{1}{2}\left[\bar{\boldsymbol{L}}_\mathrm{p} - \bar{\boldsymbol{L}}_\mathrm{p}^{\mathrm{t}}\right] \ , \tag{2.31}$$

$$\boldsymbol{w}_\mathrm{p} = \frac{1}{2}\left[\boldsymbol{l}_\mathrm{p} - \boldsymbol{l}_\mathrm{p}^{\mathrm{t}}\right] \ . \tag{2.32}$$

Assuming that the elastic strain is small, the left stretch tensor can be expressed as

$$\boldsymbol{V}_\mathrm{e} = \boldsymbol{I} + \alpha\,\boldsymbol{A} \ , \tag{2.33}$$

where $\alpha \ll 1$ is a scalar much smaller than 1, and $\boldsymbol{A}$ is a symmetric matrix with a norm $\|\boldsymbol{A}\| \leq 1$. A series expansion of the inverse then yields

$$\boldsymbol{V}_\mathrm{e}^{-1} = \boldsymbol{I} - \alpha\,\boldsymbol{A} + \alpha^2\,\boldsymbol{A}^2 - \alpha^3\,\boldsymbol{A}^3 + \dots \ . \tag{2.34}$$

Inserting eq. (2.34) into eq. (2.28), and neglecting all terms of order α^2 and higher, yields

$$\boldsymbol{d}_\mathrm{p} \approx \boldsymbol{R}_\mathrm{e} \cdot \bar{\boldsymbol{D}}_\mathrm{p} \cdot \boldsymbol{R}_\mathrm{e}^{\mathrm{t}} + \alpha\left[\boldsymbol{A} \cdot \boldsymbol{R}_\mathrm{e} \cdot \bar{\boldsymbol{W}}_\mathrm{p} \cdot \boldsymbol{R}_\mathrm{e}^{\mathrm{t}} - \boldsymbol{R}_\mathrm{e} \cdot \bar{\boldsymbol{W}}_\mathrm{p} \cdot \boldsymbol{R}_\mathrm{e}^{\mathrm{t}} \cdot \boldsymbol{A}\right] \ , \tag{2.35}$$

or, assuming the plastic spin $\bar{\boldsymbol{W}}_\mathrm{p}$ vanishes,

$$\boldsymbol{d}_\mathrm{p} \approx \tilde{\boldsymbol{d}}_\mathrm{p} = \boldsymbol{R}_\mathrm{e} \cdot \bar{\boldsymbol{D}}_\mathrm{p} \cdot \boldsymbol{R}_\mathrm{e}^{\mathrm{t}} \ . \tag{2.36}$$

2.1.2 Balance equations

In the following section, the fundamental balance equations for the model in the current configuration are presented. The derivation of these equations is presented comprehensively in textbooks such as [114], especially with regard to the required time derivatives of integrals on a region which changes with time.

Conservation of mass

For the applications under consideration, the balance of mass is simplified to the (assumption of) conservation of mass, i.e.

$$\frac{\mathrm{d}}{\mathrm{d}t}\int_{\Omega_t}\rho_t\,\mathrm{d}v = 0\ , \tag{2.37}$$

which is expressed in a local manner as

$$\dot{\rho}_t + \rho_t\ \mathrm{div}\,(\dot{\boldsymbol{x}}) = 0\ . \tag{2.38}$$

Balance of linear momentum

The balance of linear momentum is given in integral form as

$$\frac{\mathrm{d}}{\mathrm{d}t}\int_{\Omega_t}\rho_t\,\dot{\boldsymbol{x}}\,\mathrm{d}v = \int_{\Omega_t}\rho_t\,\boldsymbol{f}^{\mathrm{b}}\,\mathrm{d}v + \int_{\partial\Omega_t}\boldsymbol{\sigma}\cdot\boldsymbol{n}\,\mathrm{d}a\ , \tag{2.39}$$

which is equivalent to the local form

$$\mathrm{div}\,(\boldsymbol{\sigma}) - \rho_t\left[\ddot{\boldsymbol{x}} - \boldsymbol{f}^{\mathrm{b}}\right] = \boldsymbol{0}\ , \tag{2.40}$$

where the Cauchy stress tensor is denoted as $\boldsymbol{\sigma}$, and mass-specific body forces in the current configuration are denoted as $\boldsymbol{f}^{\mathrm{b}}$. This expression is only valid under the above assumption of mass conservation.

Balance of angular momentum

Assuming that angular momentum only arises from body forces and surface tractions, the balance of angular momentum is equivalent to the symmetry of the Cauchy stress tensor, i.e.

$$\boldsymbol{\sigma} = \boldsymbol{\sigma}^{\mathrm{t}}\ . \tag{2.41}$$

Balance of energy

The balance of energy is formulated in terms of the kinetic energy

$$\mathcal{K} = \frac{1}{2}\int_{\Omega_t}\rho_t\,\dot{\boldsymbol{x}}\cdot\dot{\boldsymbol{x}}\,\mathrm{d}v \tag{2.42}$$

and the internal energy

$$\mathcal{E} = \int_{\Omega_t}\rho_t\,e\,\mathrm{d}v\ , \tag{2.43}$$

where it is assumed that the internal energy density e exists. The power due to body forces and boundary tractions is given by

$$\mathcal{P} = \int_{\partial\Omega_t} \dot{\boldsymbol{x}} \cdot \boldsymbol{\sigma} \cdot \boldsymbol{n} \, \mathrm{d}a + \int_{\Omega_t} \rho_t \, \dot{\boldsymbol{x}} \cdot \boldsymbol{f}^{\mathrm{b}} \, \mathrm{d}v \ , \tag{2.44}$$

while the heat supply due to mass-specific heat source r and an outward heat flux $\boldsymbol{q}$ over the boundary in current configuration is given by

$$\mathcal{Q} = \int_{\Omega_t} \rho_t \, r \, \mathrm{d}v - \int_{\partial\Omega_t} \boldsymbol{q} \cdot \boldsymbol{n} \, \mathrm{d}a \ . \tag{2.45}$$

The balance of energy is then given by

$$\dot{\mathcal{K}} + \dot{\mathcal{E}} = \mathcal{P} + \mathcal{Q} \ , \tag{2.46}$$

or, after some manipulations, in local form by

$$\rho_t \, \dot{e} - \boldsymbol{\sigma} : \mathrm{grad}\,(\dot{\boldsymbol{x}}) + \mathrm{div}\,(\boldsymbol{q}) - \rho_t \, r = 0 \ . \tag{2.47}$$

This form of the balance equation is, similar to the balance of linear momentum, only valid under the assumption that the previously presented balance laws hold.

2.1.3 Entropy inequality

The entropy inequality is usually regarded as an additional condition – besides the balance equations – for a physically sound model. As for the balance equations presented in section 2.1.2, this section only briefly summarises the application of the entropy inequality under the given assumptions. A detailed derivation can be found e.g. in Liu [114].

Assuming a specific entropy density s in the current configuration, the entropy in a body is given by

$$\mathcal{S} = \int_{\Omega_t} \rho_t \, s \, \mathrm{d}v \ . \tag{2.48}$$

It is further assumed that the supply of entropy to the system is given by

$$\mathcal{R}_s = \int_{\Omega_t} \rho_t \, r_s \, \mathrm{d}v - \int_{\partial\Omega_t} \boldsymbol{q}_s \cdot \boldsymbol{n} \, \mathrm{d}a \ , \tag{2.49}$$

where r_s and $\boldsymbol{q}_s$ denote a mass-specific entropy source and the (outward) entropy flux over the boundary. The second law of thermodynamics can then be stated in terms of the entropy production $\bar{S}$ as

$$\bar{S} = \dot{\mathcal{S}} - \mathcal{R}_s \geq 0 \ . \tag{2.50}$$

The local form in terms of the specific entropy production $\bar{s}$ reads

$$\bar{s} = \dot{s} + \frac{1}{\rho_t} \operatorname{div}(\boldsymbol{q}_s) - r_s \geq 0 \ . \tag{2.51}$$

In solid mechanics, the relations

$$\boldsymbol{q}_s = \frac{1}{T} \boldsymbol{q} \tag{2.52}$$

$$r_s = \frac{1}{T} r \tag{2.53}$$

are commonly assumed[1], leading to the local form of the Clausius-Duhem inequality

$$\bar{s} = \dot{s} + \frac{1}{\rho_t} \operatorname{div}\left(\frac{1}{T} \boldsymbol{q}\right) - \frac{r}{T} \geq 0 \ , \tag{2.54}$$

where T denotes the absolute temperature. It is convenient to reformulate the entropy inequality in terms of the (Helmholtz) free energy ψ through the Legendre transformation

$$\psi(\boldsymbol{\varepsilon}, T, \boldsymbol{\xi}) = \inf_s \left(e(\boldsymbol{\varepsilon}, s, \boldsymbol{\xi}) - T\, s\right) \tag{2.55}$$

$$= e(\boldsymbol{\varepsilon}, s(\boldsymbol{\varepsilon}, T, \boldsymbol{\xi}), \boldsymbol{\xi}) - T\, s(\boldsymbol{\varepsilon}, T, \boldsymbol{\xi}) \ , \tag{2.56}$$

where $\boldsymbol{\xi}$ represents a set of internal variables. This expression for the transformation furthermore requires s to be monotonic in T and assumes that the entropy density $s(\boldsymbol{\varepsilon}, T, \boldsymbol{\xi})$ exists.

The entropy inequality then reads

$$\rho_t \dot{\psi} + \rho_t\, s \dot{T} - \boldsymbol{\sigma} : \boldsymbol{l} + \frac{1}{T} \boldsymbol{q} \cdot \operatorname{grad}(T) \leq 0 \ , \tag{2.57}$$

where the identity

$$\left[\boldsymbol{\sigma} \cdot \boldsymbol{F}^{-\mathrm{t}}\right] : \dot{\boldsymbol{F}} = \boldsymbol{\sigma} : \boldsymbol{l} \tag{2.58}$$

was exploited. Dissipation per unit current volume is given by

$$\mathcal{D}_t = \rho_t\, T\, \bar{s} = \mathcal{D}_{t,\mathrm{mech}} + \mathcal{D}_{t,\mathrm{th}} \tag{2.59}$$

with the mechanical and thermal contributions

$$\mathcal{D}_{t,\mathrm{mech}} = \boldsymbol{\sigma} : \boldsymbol{l} - \rho_t \dot{\psi} - \rho_t\, s \dot{T} \ , \tag{2.60}$$

$$\mathcal{D}_{t,\mathrm{th}} = -\frac{1}{T} \boldsymbol{q} \cdot \operatorname{grad}(T) \ . \tag{2.61}$$

[1] It should be noted that although the assumptions (2.52) and (2.53) are commonly used, they are described as 'inconsistent with the results from the kinetic theory of gases' in Liu [114], and should be regarded as part of the modelling assumptions rather than physical relations.

The Clausius-Duhem inequality

$$\mathcal{D}_t \geq 0 \tag{2.62}$$

is often separated into the Clausius-Planck inequality

$$\mathcal{D}_{t,\mathrm{mech}} \geq 0 \tag{2.63}$$

and the Fourier inequality

$$\mathcal{D}_{t,\mathrm{th}} \geq 0 \ , \tag{2.64}$$

although fulfilment of eqs. (2.63) and (2.64) is a stronger requirement than fulfilment of eq. (2.62).

Substituting

$$\dot{\psi} = \dot{e} - \dot{s}\,T - s\,\dot{T} = \frac{1}{\rho_t}\,\boldsymbol{\sigma} : \boldsymbol{l} + r - \frac{1}{\rho_t}\,\mathrm{div}\,(\boldsymbol{q}) - \dot{s}\,T - s\,\dot{T} \tag{2.65}$$

into the definition (2.60) yields the first law restated as

$$\dot{s}\,T = \frac{1}{\rho_t}\,\mathcal{D}_{t,\mathrm{mech}} + r - \frac{1}{\rho_t}\,\mathrm{div}\,(\boldsymbol{q}) \ , \tag{2.66}$$

which is a useful representation to investigate the temperature evolution.

By definition of the Kirchhoff stress tensor $\boldsymbol{\tau}$, and using its symmetry, the relation

$$\frac{1}{\rho_t}\,\boldsymbol{\sigma} : \boldsymbol{l} = \frac{1}{\rho_0}\,\boldsymbol{\tau} : \boldsymbol{d} \ . \tag{2.67}$$

holds, where $\rho_0 = J\,\rho_t$ due to conservation of mass. Therefore, eq. (2.57) can be restated as

$$\rho_0\,\dot{\psi} + \rho_0\,s\,\dot{T} - \boldsymbol{\tau} : \boldsymbol{d} + \frac{J}{T}\,\boldsymbol{q} \cdot \mathrm{grad}\,(T) \leq 0 \ . \tag{2.68}$$

Accordingly, the dissipation per unit reference volume

$$\mathcal{D}_0 = \rho_0\,T\,\bar{s} = \mathcal{D}_{0,\mathrm{mech}} + \mathcal{D}_{0,\mathrm{th}} \tag{2.69}$$

has the mechanical and thermal contributions

$$\mathcal{D}_{0,\mathrm{mech}} = \boldsymbol{\tau} : \boldsymbol{d} - \rho_0\,\dot{\psi} - \rho_0\,s\,\dot{T} \ , \tag{2.70}$$

$$\mathcal{D}_{0,\mathrm{th}} = -\frac{J}{T}\,\boldsymbol{q} \cdot \mathrm{grad}\,(T) \ , \tag{2.71}$$

and the Clausius-Duhem, Clausius-Planck, and Fourier inequalities are restated as

$$\mathcal{D}_0 \geq 0 \ , \tag{2.72}$$

$$\mathcal{D}_{0,\mathrm{mech}} \geq 0 \ , \tag{2.73}$$

$$\mathcal{D}_{0,\mathrm{th}} \geq 0 \ . \tag{2.74}$$

The corresponding form of eq. (2.66) reads

$$\dot{s}\,T = \frac{1}{\rho_0}\,\mathcal{D}_{0,\mathrm{mech}} + r - \frac{J}{\rho_0}\,\mathrm{div}\,(\boldsymbol{q}) \ . \tag{2.75}$$

2.1.4 Plasticity framework

In the following, the approach discussed by de Souza Neto et al. [36] for isotropic elasto-plasticity is adopted. Therein, the elastic logarithmic strain

$$\boldsymbol{\varepsilon}_{\mathrm{e}} = \ln\left(\boldsymbol{V}_{\mathrm{e}}\right) \tag{2.76}$$

is introduced. The following section builds on the derivatives given by de Souza Neto et al. [36] for this case, but additionally includes the dependency on temperature. It was shown by de Souza Neto et al. [36] that the rate of a free energy density of the form $\psi\left(\boldsymbol{\varepsilon}_{\mathrm{e}}, \tilde{\boldsymbol{\xi}}\right)$ can be expressed as

$$\dot{\psi} = \frac{\partial \psi}{\partial \boldsymbol{\varepsilon}_{\mathrm{e}}} : \left[\boldsymbol{d} - \tilde{\boldsymbol{d}}_{\mathrm{p}}\right] + \frac{\partial \psi}{\partial \tilde{\boldsymbol{\xi}}} \circ \dot{\tilde{\boldsymbol{\xi}}} \,, \tag{2.77}$$

where the reduced set of internal variables $\tilde{\boldsymbol{\xi}}$ does not include the plastic strains. The dissipation inequality (2.70) then reduces to

$$\mathcal{D}_{0,\mathrm{mech}} = \left[\boldsymbol{\tau} - \rho_0 \frac{\partial \psi}{\partial \boldsymbol{\varepsilon}_{\mathrm{e}}}\right] : \boldsymbol{d} - \rho_0 \left[s + \frac{\partial \psi}{\partial T}\right] \dot{T} + \rho_0 \frac{\partial \psi}{\partial \boldsymbol{\varepsilon}_{\mathrm{e}}} : \tilde{\boldsymbol{d}}_{\mathrm{p}} - \rho_0 \frac{\partial \psi}{\partial \tilde{\boldsymbol{\xi}}} \circ \dot{\tilde{\boldsymbol{\xi}}} \,. \tag{2.78}$$

Following the classic Coleman-Noll procedure leads to the constitutive relations

$$\boldsymbol{\tau} = \rho_0 \frac{\partial \psi}{\partial \boldsymbol{\varepsilon}_{\mathrm{e}}} \tag{2.79}$$

and

$$s = -\frac{\partial \psi}{\partial T} \,. \tag{2.80}$$

Furthermore, the driving forces conjugate to the internal variables are introduced as

$$\boldsymbol{g}_{\tilde{\xi}} = -\rho_0 \frac{\partial \psi}{\partial \tilde{\boldsymbol{\xi}}} \,. \tag{2.81}$$

The reduced mechanical dissipation per unit reference volume is then given by

$$\mathcal{D}^{\mathrm{red}}_{0,\mathrm{mech}} = \boldsymbol{\tau} : \tilde{\boldsymbol{d}}_{\mathrm{p}} + \boldsymbol{g}_{\tilde{\xi}} \circ \dot{\tilde{\boldsymbol{\xi}}} \,. \tag{2.82}$$

In the following, the isotropic Fourier's law

$$\boldsymbol{q} = -k_t \, \mathrm{grad}\left(T\right) \tag{2.83}$$

will be used, which by definition fulfils the Fourier inequality (2.64) for thermal conductivities $k_t > 0$. It will therefore be sufficient to show that the reduced Clausius-Planck inequality

$$\mathcal{D}^{\mathrm{red}}_{0,\mathrm{mech}} \geq 0 \tag{2.84}$$

is fulfilled to prove that a material model is consistent with the second law of thermodynamics. Based on the presented thermodynamical framework, a material model is defined by specifying the free energy density $\psi(\boldsymbol{\varepsilon}_\mathrm{e}, T, \tilde{\boldsymbol{\xi}})$ and evolution equations $\dot{\boldsymbol{\xi}}(\boldsymbol{\varepsilon}_\mathrm{e}, T, \tilde{\boldsymbol{\xi}})$.

Alternatively, by introducing the plastic logarithmic strain as

$$\boldsymbol{\varepsilon}_\mathrm{p} = \boldsymbol{\varepsilon} - \boldsymbol{\varepsilon}_\mathrm{e} \tag{2.85}$$

the free energy density and evolution equations can be specified as $\psi(\boldsymbol{\varepsilon}, T, \boldsymbol{\varepsilon}_\mathrm{p}, \tilde{\boldsymbol{\xi}})$ and $\dot{\boldsymbol{\xi}}(\boldsymbol{\varepsilon}, T, \boldsymbol{\varepsilon}_\mathrm{p}, \tilde{\boldsymbol{\xi}})$. The additive nature of the split is not mathematically motivated at this point, but rather chosen based on convenience, as the model formulation in the following sections can be derived based solely on the elastic strain.

2.1.5 Equivalent stress and strain

Similar to the von Mises equivalent stress for the Cauchy stress, the equivalent Kirchhoff stress is defined as

$$\tau^\mathrm{eq} = \sqrt{\frac{3}{2}} \left\| \boldsymbol{\tau}^\mathrm{iso} \right\| \ , \tag{2.86}$$

where $\left\| \boldsymbol{\tau}^\mathrm{iso} \right\|$ denotes the Frobenius norm of the isochoric part of the Kirchhoff stress tensor.

The equivalent plastic strain rate is introduced as

$$\dot{\varepsilon}_\mathrm{p}^\mathrm{eq} = \sqrt{\frac{2}{3}} \left\| \tilde{\boldsymbol{d}}_\mathrm{p} \right\| = \sqrt{\frac{2}{3}} \left\| \bar{\boldsymbol{D}}_\mathrm{p} \right\| \ . \tag{2.87}$$

If the Kirchhoff stress tensor and the plastic rate of deformation tensor $\boldsymbol{d}_\mathrm{p}$ are coaxial, and $\boldsymbol{d}_\mathrm{p}$ is deviatoric, the equivalent Kirchhoff stress and equivalent plastic strain rate are conjugated in terms of the plastic work, i.e.

$$\tau^\mathrm{eq} \, \dot{\varepsilon}_\mathrm{p}^\mathrm{eq} = \boldsymbol{\tau} : \tilde{\boldsymbol{d}}_\mathrm{p} \ . \tag{2.88}$$

The (accumulated) equivalent plastic strain is obtained from the integral

$$\varepsilon_\mathrm{p}^\mathrm{eq} = \int \dot{\varepsilon}_\mathrm{p}^\mathrm{eq} \, \mathrm{d}t \ . \tag{2.89}$$

2.1.6 Infinitesimal strain setting

When the deformations under consideration are comparatively small, the kinematics of continuum mechanics can be approximated by linearisation. In this section, some basic equations for this case are presented.

In the small-strain setting, no explicit distinction is made between the different configurations described in section 2.1.1. In the following, the notation for the current

configuration will be adapted for the small strain setting. In particular, the position of any particle will be denoted as $\boldsymbol{x}$, and the mass density ρ is not attached to a specific configuration. The infinitesimal strain tensor, also often referred to as the engineering strain, is defined as

$$\boldsymbol{\epsilon} = \frac{1}{2}\left[\operatorname{grad}\boldsymbol{u} + [\operatorname{grad}\boldsymbol{u}]^{\mathrm{t}}\right] \ , \tag{2.90}$$

based on the displacement field $\boldsymbol{u}(\boldsymbol{x})$. In this setting, the free energy density is expressed as a function $\psi(\boldsymbol{\epsilon}, T, \boldsymbol{\xi})$ of infinitesimal strain, temperature T, and internal variables $\boldsymbol{\xi}$.

Assuming that conservation of mass is still valid, the balance of linear momentum as well as the balance of angular momentum still hold in the forms presented in eqs. (2.40) and (2.41). The first law of thermodynamics (cf. eq. (2.47)) yields

$$\rho\,\dot{e} - \boldsymbol{\sigma} : \dot{\boldsymbol{\epsilon}} + \operatorname{div}(\boldsymbol{q}) - \rho\, r = 0 \ . \tag{2.91}$$

Based on the mechanical dissipation per unit volume

$$\mathcal{D}_{\mathrm{mech}} = \left[\boldsymbol{\sigma} - \rho\,\frac{\partial\psi}{\partial\boldsymbol{\epsilon}}\right] : \dot{\boldsymbol{\epsilon}} - \rho\,\left[s + \frac{\partial\psi}{\partial T}\right]\dot{T} - \rho\,\frac{\partial\psi}{\partial\boldsymbol{\xi}} \circ \dot{\boldsymbol{\xi}} \ , \tag{2.92}$$

the Coleman-Noll procedure yields the constitutive equations

$$\boldsymbol{\sigma} = \rho\,\frac{\partial\psi}{\partial\boldsymbol{\epsilon}} \tag{2.93}$$

and

$$s = -\frac{\partial\psi}{\partial T} \ . \tag{2.94}$$

2.2 Examples of homogeneous states of deformation

Two homogeneous example problems are introduced in this section, which will be referred to at different points throughout the thesis. A cube with edge length L is subjected to appropriate boundary conditions for uniaxial stress or simple shear. The deformation is assumed to be governed by isotropic elasticity and plasticity, and both boundary value problems are shown in fig. 2.2. Where tensor quantities are represented by their coefficient matrices in this section, the coefficients refer to the pictured x, y, z coordinate system.

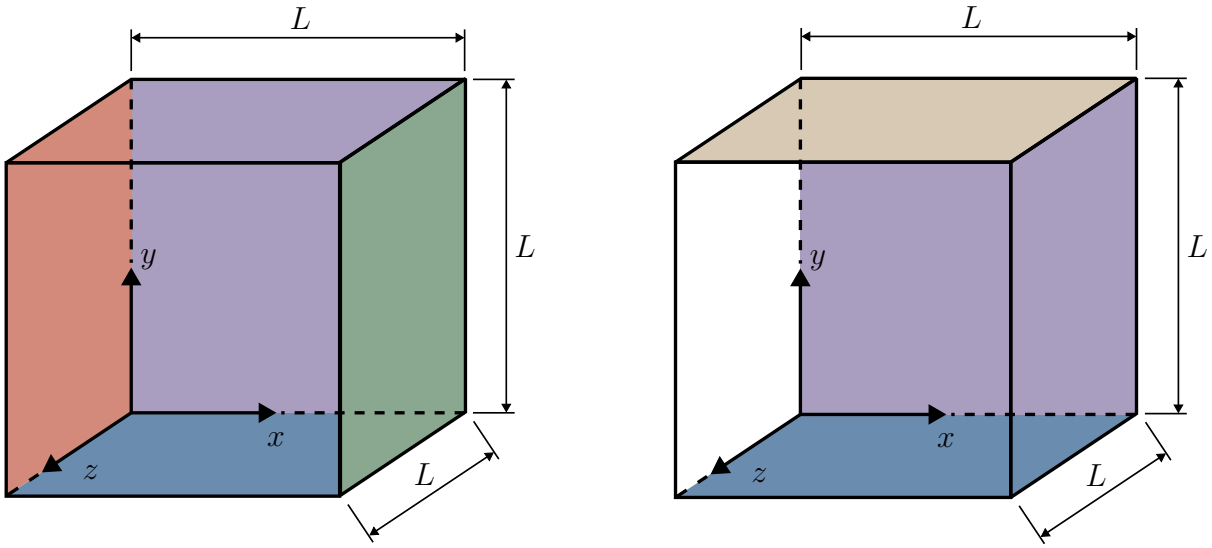

(a) Boundaries with prescribed conditions for uniaxial stress.

(b) Boundaries with prescribed conditions for simple shear.

Figure 2.2: Boundary value problems for homogeneous deformation of a cube with edge length L under uniaxial tension and simple shear. Colouring of the faces refers to the boundary conditions applied, which are specified in eq. (2.95) for uniaxial tension, and in eq. (2.96) for simple shear.

The boundary conditions for the displacements $\boldsymbol{u}$ and velocities $\boldsymbol{v}$ in the uniaxial tension setting, depicted in fig. 2.2 a), are given by

$$\begin{aligned} &u_x(x=0,y,z)=0\ , \\ &u_y(x,y=0,z)=0\ , \\ &u_z(x,y,z=0)=0\ , \\ &v_x(x=L,y,z)=\bar{v}_x\,(t)\ \ , \end{aligned} \tag{2.95}$$

while the boundary conditions for the simple shear setting shown in fig. 2.2 b) are given by

$$\begin{aligned} &u_x(x, y = 0, z) = 0 \ , && u_y(x, y = 0, z) = 0 \ , \\ &u_z(x, y, z = 0) = 0 \ , && \\ &v_x(x, y = L, z) = \bar{v}_x(t) \ , && u_y(x, y = L, z) = 0 \ . \end{aligned} \tag{2.96}$$

Since the simple shear deformation is purely deviatoric, no additional constraint is required for the displacement in z direction. It is however implied that $u_z = 0$ holds at all points for the simple shear example.

The prescribed x-component $\bar{v}_x(t)$ of the velocity vector $\boldsymbol{v}$ is given by the function

$$\bar{v}_x(t) = \begin{cases} v_0 & \text{for } t \leq \bar{t} \\ 0 & \text{for } t > \bar{t} \end{cases} \ , \tag{2.97}$$

based on the constant reference velocity v_0, and the duration $\bar{t}$ of the loading step. For all finite element calculations taking inertia into account, eq. (2.97) is regularised by a smooth step function. An edge length of $L = 10\,\mathrm{mm}$, a reference velocity of $v_0 = 1\,\mathrm{m\,s^{-1}}$, and a loading step duration of $\bar{t} = 10\,\mathrm{ms}$ are used where no other values are specified.

It will be useful in the following to express the logarithmic strain tensor and its norm as a function of time or displacement at the boundary. To this end, a dimensionless deformation measure is defined by

$$\gamma = \frac{\int \bar{v}_x(t)\,\mathrm{d}t}{L} \ . \tag{2.98}$$

In the following, approximations for the equivalent plastic strain rate and equivalent plastic strain are derived for both problems. To this end, it is assumed that the elastic contribution to the deformation gradient is small, and that therefore the approximations

$$\boldsymbol{F}_\mathrm{e} \approx \boldsymbol{I} \tag{2.99}$$

$$\boldsymbol{F}_\mathrm{p} \approx \boldsymbol{F} \tag{2.100}$$

hold.

Uniaxial tension Under the assumptions specified above, the deformation is isochoric and the deformation gradient therefore given by

$$\boldsymbol{F} = \begin{bmatrix} 1+\gamma & 0 & 0 \\ 0 & 1/\sqrt{1+\gamma} & 0 \\ 0 & 0 & 1/\sqrt{1+\gamma} \end{bmatrix} \ .$$

With

$$\boldsymbol{F}^{-1} = \begin{bmatrix} [1+\gamma]^{-1} & 0 & 0 \\ 0 & \sqrt{1+\gamma} & 0 \\ 0 & 0 & \sqrt{1+\gamma} \end{bmatrix} \tag{2.101}$$

and

$$\dot{\boldsymbol{F}} = \dot{\gamma} \begin{bmatrix} 1 & 0 & 0 \\ 0 & -\frac{1}{2}\left[1+\gamma\right]^{-\frac{3}{2}} & 0 \\ 0 & 0 & -\frac{1}{2}\left[1+\gamma\right]^{-\frac{3}{2}} \end{bmatrix} , \tag{2.102}$$

the velocity gradient is given by

$$\boldsymbol{l} = \dot{\boldsymbol{F}} \cdot \boldsymbol{F}^{-1} = \dot{\gamma} \begin{bmatrix} \left[1+\gamma\right]^{-1} & 0 & 0 \\ 0 & -\frac{1}{2}\left[1+\gamma\right]^{-1} & 0 \\ 0 & 0 & -\frac{1}{2}\left[1+\gamma\right]^{-1} \end{bmatrix} . \tag{2.103}$$

With eqs. (2.99) and (2.100), the plastic rate of deformation tensor

$$\boldsymbol{d}_{\mathrm{p}} = \frac{1}{2}\left[\boldsymbol{l} + \boldsymbol{l}^{\mathrm{t}}\right] = \boldsymbol{l} \tag{2.104}$$

then yields the equivalent plastic strain rate

$$\dot{\varepsilon}_{\mathrm{p}}^{\mathrm{eq}} = \sqrt{\frac{2}{3}}\, \|\boldsymbol{d}_{\mathrm{p}}\| = \frac{|\dot{\gamma}|}{1+\gamma} \tag{2.105}$$

which – assuming monotonic loading – integrates to the equivalent plastic strain

$$\varepsilon_{\mathrm{p}}^{\mathrm{eq}} = \left|\ln\left(1+\gamma\right)\right| \ . \tag{2.106}$$

Simple shear For the simple shear case, the deformation gradient reads

$$\boldsymbol{F} = \begin{bmatrix} 1 & \gamma & 0 \\ 0 & 1 & 0 \\ 0 & 0 & 1 \end{bmatrix} , \tag{2.107}$$

and the left Cauchy-Green tensor is given by

$$\boldsymbol{b} = \begin{bmatrix} 1+\gamma^2 & \gamma & 0 \\ \gamma & 1 & 0 \\ 0 & 0 & 1 \end{bmatrix} . \tag{2.108}$$

The spectral decomposition of this tensor yields the eigenvalues

$$\begin{aligned} \lambda_1^{(\boldsymbol{b})} &= 1 \ , \\ \lambda_2^{(\boldsymbol{b})} &= \frac{1}{2}\left[2+\gamma^2-\gamma\sqrt{4+\gamma^2}\right] \ , \\ \lambda_3^{(\boldsymbol{b})} &= \frac{1}{2}\left[2+\gamma^2+\gamma\sqrt{4+\gamma^2}\right] \end{aligned} \tag{2.109}$$

and eigenvectors

$$\begin{aligned}
\boldsymbol{n}_1^{(\boldsymbol{b})} &= \begin{bmatrix} 0 \\ 0 \\ 1 \end{bmatrix} \ , \\
\boldsymbol{n}_2^{(\boldsymbol{b})} &= \frac{1}{\sqrt{4 + \left[\gamma - \sqrt{4+\gamma^2}\right]^2}} \begin{bmatrix} \gamma - \sqrt{4+\gamma^2} \\ 2 \\ 0 \end{bmatrix} \ , \\
\boldsymbol{n}_3^{(\boldsymbol{b})} &= \frac{1}{\sqrt{4 + \left[\gamma + \sqrt{4+\gamma^2}\right]^2}} \begin{bmatrix} \gamma + \sqrt{4+\gamma^2} \\ 2 \\ 0 \end{bmatrix} \ .
\end{aligned} \tag{2.110}$$

By definition,

$$\boldsymbol{\varepsilon} = \frac{1}{2} \ln(\boldsymbol{b}) = \sum_i \frac{1}{2} \ln\left(\lambda_i^{(\boldsymbol{b})}\right) \boldsymbol{n}_i^{(\boldsymbol{b})} \otimes \boldsymbol{n}_i^{(\boldsymbol{b})} \ , \tag{2.111}$$

holds. The logarithmic strain tensor then reads

$$\boldsymbol{\varepsilon} = \frac{1}{2\sqrt{4+\gamma^2}} \begin{bmatrix} \gamma \ \mathrm{arctanh}\left(\dfrac{\gamma\sqrt{4+\gamma^2}}{2+\gamma^2}\right) & \ln\left(\dfrac{1}{4}\left[2+\gamma^2+\gamma\sqrt{4+\gamma^2}\right]^2\right) & 0 \\ \ln\left(\dfrac{1}{4}\left[2+\gamma^2+\gamma\sqrt{4+\gamma^2}\right]^2\right) & -\gamma \ \mathrm{arctanh}\left(\dfrac{\gamma\sqrt{4+\gamma^2}}{2+\gamma^2}\right) & 0 \\ 0 & 0 & 0 \end{bmatrix} . \tag{2.112}$$

With

$$\dot{\boldsymbol{F}} = \begin{bmatrix} 0 & \dot{\gamma} & 0 \\ 0 & 0 & 0 \\ 0 & 0 & 0 \end{bmatrix} \ , \tag{2.113}$$

and

$$\boldsymbol{F}^{-1} = \begin{bmatrix} 1 & -\gamma & 0 \\ 0 & 1 & 0 \\ 0 & 0 & 1 \end{bmatrix} \ , \tag{2.114}$$

the velocity gradient is given by

$$\boldsymbol{l} = \dot{\boldsymbol{F}} \cdot \boldsymbol{F}^{-1} = \begin{bmatrix} 0 & \dot{\gamma} & 0 \\ 0 & 0 & 0 \\ 0 & 0 & 0 \end{bmatrix} \ , \tag{2.115}$$

and the rate of deformation tensor reads

$$\boldsymbol{d} = \frac{1}{2}\left[\boldsymbol{l} + \boldsymbol{l}^{\mathrm{t}}\right] = \frac{1}{2}\begin{bmatrix} 0 & \dot{\gamma} & 0 \\ \dot{\gamma} & 0 & 0 \\ 0 & 0 & 0 \end{bmatrix} . \tag{2.116}$$

Using eqs. (2.99) and (2.100), the equivalent plastic strain rate is then obtained as

$$\dot{\varepsilon}_{\mathrm{p}}^{\mathrm{eq}} = \sqrt{\frac{2}{3}}\,\|\boldsymbol{d}\| = \frac{|\dot{\gamma}|}{\sqrt{3}} , \tag{2.117}$$

which integrates into

$$\varepsilon_{\mathrm{p}}^{\mathrm{eq}} = \frac{|\gamma|}{\sqrt{3}} . \tag{2.118}$$

2.3 Finite element method

Throughout this thesis, various physical problems will be stated in the framework of continuum mechanics described in section 2.1. To this end, a description of the geometrical region is combined with suitable initial conditions and boundary conditions for the independent variables $\boldsymbol{u}$, T, and $\boldsymbol{\xi}$, as well as a chosen material model. The solution of the physical problem is then given by the fields $\boldsymbol{u}(\boldsymbol{x}, t)$, $T(\boldsymbol{x}, t)$, and $\boldsymbol{\xi}(\boldsymbol{x}, t)$ satisfying the prescribed conditions.

Closed form solutions can be found for selected problems, especially for elastic material behaviour (see e.g. Timoshenko and Goodier [180]). In general however, the resulting partial differential equations are too complex to solve analytically. Instead, numerical methods are applied to approximate the solution. The finite element method is widely used in the field of computational mechanics for this task, and will be used extensively in this thesis. This section briefly introduces the underlying concepts with the aim to provide an intuitive understanding of the method. However, the reader is referred to the wide range of available textbooks on the matter, e.g. [168, 199], for a more comprehensive treatment.

Based on the loading of an arbitrary body shown in fig. 2.1, the following boundary value problem is considered. At the initial time t_0, the body occupies the region Ω_0 in space. The reference position of each particle and the initial temperature field are assumed to be known. The boundary of the region is split into two parts for each primary variable. Displacements $\boldsymbol{u}(\boldsymbol{X}, t)$ are prescribed on the boundary $\partial\Omega_t^{\boldsymbol{u}}$, while (spatial) tractions $\boldsymbol{t}(\boldsymbol{X}, t)$ are prescribed on $\partial\Omega_t^{\boldsymbol{t}}$. Similarly, the temperature $T(\boldsymbol{X}, t)$ and referential heat flux $\boldsymbol{q}(\boldsymbol{X}, t)$ are prescribed on $\partial\Omega_t^{T}$ and $\partial\Omega_t^{\boldsymbol{q}}$. Boundary conditions for the primary unknowns, i.e. displacements and temperature, are called Dirichlet conditions, while the remaining boundary conditions are called Neumann conditions. These are accompanied by initial velocity and temperature fields. Using the appropriate transformations, all loads can alternatively be expressed in the reference configuration.

A test function $\delta\boldsymbol{\varphi}$, representing a virtual displacement and satisfying the Dirichlet boundary conditions, is introduced, and multiplied by the local form (2.40), yielding

$$\delta\boldsymbol{\varphi} \cdot \left[\operatorname{div}(\boldsymbol{\sigma}) - \rho_t \left[\ddot{\boldsymbol{x}} - \boldsymbol{f}^{\mathrm{b}}\right]\right] = 0 \ . \tag{2.119}$$

Integration by parts of this expression after some manipulation yields

$$\int_{\Omega_t} \left[\boldsymbol{\sigma} : \operatorname{grad}\delta\boldsymbol{\varphi} - \rho_t \left[\boldsymbol{f}^{\mathrm{b}} - \ddot{\boldsymbol{x}}\right] \cdot \delta\boldsymbol{\varphi}\right] \mathrm{d}v - \int_{\partial\Omega_t^t} \boldsymbol{t} \cdot \delta\boldsymbol{\varphi} \, \mathrm{d}\boldsymbol{a} = 0 \ , \tag{2.120}$$

which is called the weak form of the balance of linear momentum [36]. Similarly, the temperature test function δT is introduced and multiplied with the first law of thermodynamics (eq. (2.47)) to yield

$$\delta T \ \left[\rho_t \, \dot{e} - \boldsymbol{\sigma} : \operatorname{grad}(\dot{\boldsymbol{x}}) + \operatorname{div}(\boldsymbol{q}) - \rho_t \, r\right] = 0 \ , \tag{2.121}$$

or, after integration,

$$\int_{\Omega_t} \left[\delta T \, \rho_t \, \dot{e} - \delta T \, \boldsymbol{\sigma} : \operatorname{grad}(\dot{\boldsymbol{x}}) - \operatorname{grad}(\delta T) \cdot \boldsymbol{q} - \delta T \, \rho_t \, r\right] \mathrm{d}v + \int_{\partial\Omega_t} \delta T \, \boldsymbol{q}\cdot\boldsymbol{n} \, \mathrm{d}a = 0 \ . \tag{2.122}$$

Alternatively, eqs. (2.120) and (2.122) can be expressed in the reference configuration, simplifying the integration.

The finite element method is fundamentally based on the approximation of the geometric domain by a set of finite cells, which are called the finite elements. In the Lagrangian description, the node points are attached to particles of the body, therefore the approximated geometry is directly obtained from the union of all finite elements. The solution variables stored at these nodes then describe the displacement $\boldsymbol{u}(\boldsymbol{X}, t)$ and temperature $T(\boldsymbol{X}, t)$ of these particles. In contrast, the Eulerian setting is based on a grid which is fixed in space, where the solution variables $\boldsymbol{u}(\boldsymbol{x}, t)$ and temperature $T(\boldsymbol{x}, t)$ are used. Additionally, a volume fraction variable can be used to describe the amount of material within each cell, and the geometry of the body is then approximated by interpolating this variable. A comparison of the geometrical approximation in the Lagrangian and Eulerian setting is shown in fig. 2.3.

When deformation becomes too large, the quality of Lagrangian finite element solutions deteriorates, and calculations may even abort. In contrast, Eulerian finite elements are able to accommodate practically unlimited deformations, but require a larger number of nodes and elements. Furthermore, some types of boundary conditions, such as non-zero surface tractions or heat fluxes, can not be applied to the interpolated boundaries in an Eulerian mesh. If these boundary conditions are not necessary, the Eulerian description can be a useful option to describe processes involving large deformations, especially when the focus lies on deformations in a comparatively small geometrical region, and flow of material out of the mesh can be accepted.

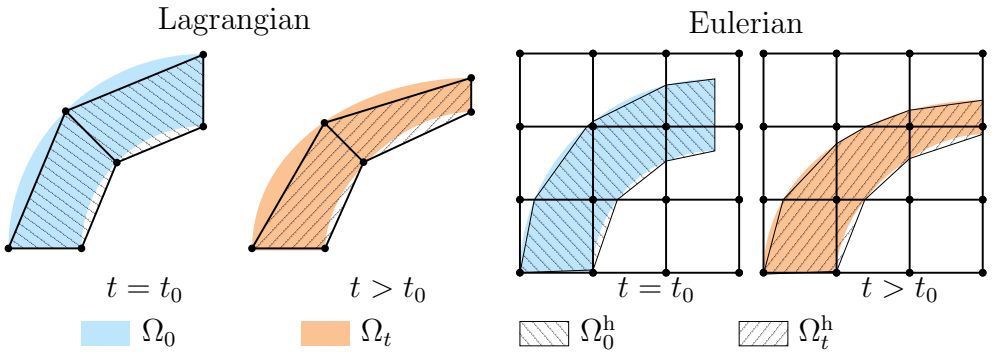

Figure 2.3: Two-dimensional example for the discretisation by finite elements. In the Lagrangian framework, the exact geometrical reference configuration Ω_0 is approximated as Ω_0^h by two quadrilateral finite elements. Two of the six node points are shared by the elements. At time t, the region Ω_t^h, defined by the deformed mesh, approximates the current configuration Ω_t. In the Eulerian framework, the grid is fixed in space, and the different configurations are described by different values of a variable indicating the amount of material within each cell. Based on an interpolation of this volume fraction, the boundaries of the body are approximated by an isosurface.

In general, the time-discrete weak balance equations are solved using either implicit or explicit time integration methods. Since the implicit time integration methods usually used are unconditionally stable, a relatively low number of time increments can be used. However, a nonlinear system of equations must be solved in each increment. The solvers therefore usually require the derivatives of the constitutive relations with respect to the primary variables, which can be tedious to derive. Explicit time integration on the other hand does not require local iterations, but is restricted by the magnitude of time increments to guarantee stability, and is therefore attractive especially for processes acting on shorter time scales.

A wide variety of implementations has been proposed for the finite element method, and specialised elements are often required for specific problems. The commercial finite element software Abaqus [33] is used for all finite element simulations presented in this thesis. Therefore, the reader is referred to works such as [36, 168, 199] for a detailed mathematical description of the method. Abaqus provides high-performance implementations of both Lagrangian and Eulerian formulations, as well as for various types of boundary conditions and contact algorithms. Furthermore, the Coupled Eulerian Lagrangian method (CEL) provided by Abaqus, which will be discussed in more detail later on, allows selective usage of Lagrangian and Eulerian description for two separate bodies within the same simulation [33]. Besides the material models already provided in the software, Fortran subroutines can be used to extend the simulation capabilities at defined interfaces, and within this thesis, multiple Fortran implementations for material models are presented. The usage of these defined interfaces allows for a clear separation between the implementation of the finite element method and the material models. In fact, material model subroutines can be combined with different finite element implementations within Abaqus.

3 Simulation of quenching

The following chapter, which is mainly based on the publication [54], presents a framework for the simulation of quenching during martensitic hardening processes, as described in section 1.2.

3.1 Introduction and objectives

$^{\text{qtd.}}_{[54]}\{$During this process, workpieces are heated in an austenitisation furnace above the austenitisation temperature, inducing a change from body-centered cubic (BCC) to face-centered cubic (FCC) lattice structure. They are then held at constant temperature for a defined time period, before being cooled down to induce the transformation to martensite. Depending on the cooling rate, a diffusive transformation of austenite to pearlite or bainite may begin before the onset of the martensite transformation, reducing the available fraction of austenite for the martensite transformation.$\}^{\text{qtd.}}_{[54]}$ The transformation kinetics are influenced not only by the thermal conditions, but also by the chemical composition of the workpiece material. $^{\text{qtd.}}_{[54]}\{$Although bainite was already discovered in the first half of the 20th century [34], the exact mechanisms of its formation are still subject to research [132, 149]. It is however generally accepted that bainite forms into different variants at different temperatures (upper and lower bainite).$\}^{\text{qtd.}}_{[54]}$

Since the product phases of a phase transformation do not necessarily have the same chemical composition as the parent phase, the composition of the parent phase can evolve during a transformation. One prominent example for this is carbon repartitioning during the formation of carbide-free bainite, where the carbon content of the product phase is significantly lower than in the parent phase, and therefore carbon enrichment of the parent phase takes place during the transformation [26].

In this section, a model for the simulation of the quenching process is presented to predict displacement and temperature fields as well as the volume fractions of the different steel phases.

3.2 State of the art

qtd. [54]{Extensive overviews on the modelling of quenching processes are given by Gür and Şimşir [63] and Şimşir and Gür [169]. Although Hunkel [82] recently showed that the martensite transformation is not solely dependent on the temperature, the assumption of an athermal martensite transformation is frequently and successfully used in the literature. A widely used class of models using this assumption is based on Koistinen and Marburger [99] and usually referred to as Koistinen-Marburger (KM) models. Various improvements of the model have been proposed for different applications, such as empirical formulae for composition-dependent model parameters to apply the model with reduced calibration effort [192]. It was shown that the agreement of simulation and experiment for individual cases can be improved by the introduction of additional parameters and terms in the model [84, 107, 112].

A popular model for the diffusive transformation was proposed individually by three different groups of researchers and is referred to as the JMAK model [10–12, 91, 100, 101]. While the original JMAK model is intended for the modelling of isothermal processes, it has been widely applied to general temperature paths based on the concept of fractional nucleation proposed by [158], also often referred to as additivity in this context. As for the KM model, various extensions and improvements have been published for the JMAK model, such as temperature-dependent parameters [28] or a dependency of the model parameters on the transformation state [88]. An extension including the influence of the austenite grain size on the transformation kinetics was proposed by Reti et al. [151]. The JMAK model has also been applied to the austenitisation, e.g. by Li et al. [110]. It should be noted that Leblond and Devaux [103] showed that the additivity rule is not generally valid when incomplete transformations are considered, and proposed a new model based on the equilibrium phase composition at each temperature. A dependency of the JMAK parameters on the cooling rate was found for high carbon steel by Rezaei et al. [153].

A drawback of the KM and JMAK models in their original form is the neglected interaction of microstructure evolution with mechanical load and deformation, most importantly the effect of transformation-induced plasticity (TRIP), for which an extensive overview was given by Taleb [178]. At the core, TRIP denotes the occurrence of a non-reversible strain during a phase transformation. It is widely accepted [52] that two different mechanisms cause these stresses: The Magee effect [116] describes the orientation of newly-formed crystallographic variants based on the stress state, while the Greenwood-Johnson effect [60] denotes the plastic yielding of the weaker phase due to the volumetric mismatch caused by the transformation strains, which can occur even in the absence of external loading.

Transformation plasticity has been incorporated into transformation models e.g. by Fischer [51], Ganghoffer and Simonsson [56], Leblond et al. [104, 105]. The Leblond model has been widely used, and was for example combined with a modified KM model to predict phase transformations in TRIP steels by Suwanpinij et al. [175]. However, it was

shown by Taleb and Petit [177] that the Leblond model is not able to capture all relevant interactions for the case of 15MND5 steel. An alternative macroscopic model, combining macroscopic plasticity and TRIP, was proposed by Mahnken et al. [118], Schneidt and Mahnken [161].

Another interaction between mechanical state and transformations are stress- and strain-induced transformations, which have been modelled e.g. by Hazar et al. [70], Tjahjanto et al. [181]. Furthermore, Mirhosseini et al. [124], Silva et al. [167] showed that a full coupling between transformation models and heat generation due to plastic dissipation and heat release is desirable for accurate predictions. The influence of the austenite grain size on the kinetics of phase transformations has already been considered in the classic Leblond model, but is still subject to research [111].

While phenomenological models have been successfully applied to many engineering applications, their consistency with physics is often questionable. Therefore, considerable research has been conducted to derive thermodynamically consistent phase transformation models and appropriate free energy functions [1, 22, 65, 86, 126, 134, 135, 156]. More recent models are often applied to phase transformations in shape memory alloys, where the transformations potentially occur frequently during the lifetime of a component [92, 102], or during additive manufacturing [131].

An overview of models which consider the bainite transformation as displacive was given by Santofimia et al. [157]. Especially the model by Ravi et al. [149] accounts for the redistribution of carbon during the formation of bainite, while Ravi et al. [150] investigates the influence of austenite-martensite interfaces as nucleation sites for bainite formation. The modelling of bainite formation is still an active topic of research [182, 191].

Effective (macroscopic) material properties are predicted from a given microstructure by homogenisation. Different methods are discussed by Andersson et al. [5], while Fernández-Pisón et al. [50] applied incremental mean-field homogenisation on martensite transformations. The microstructure is considered in detail by Amirmaleki et al. [3], who applied the representative volume element method to predict material properties, by Boccardo et al. [24], who used different representative volume elements to incorporate the morphology of the different phases into the transformation kinetics, and by Hellebrand et al. [72], who investigated the influence of the microstructure distribution in representative volume elements on residual stress distribution.}$^{\text{qtd.}}_{[54]}$

3.3 Finite element simulation framework

$^{\text{qtd.}}_{[54]}${A thermomechanically coupled finite element simulation is proposed to model the quenching process. The material model is able to predict the evolution of phase volume fractions, strains, stresses, and the carbon content of each phase under prescribed thermal and mechanical loading at the material point level.

This section presents the balance equations that are solved by the finite element model and specifies the models used for the calculation of stresses and strains, thermal flows, phase transformations, and carbon concentration. The mechanical problem is formulated in the geometrically linearised setting, assuming small deformations. Phenomenological models are used for the decomposition of austenite into martensite and bainite/austenite–martensite and austenite–bainite transformations due to the additional effort required for the calibration and solving of more complicated models.

The proposed model is based on the model proposed by de Oliveira et al. [35], but takes into account the carbon content of each individual phase, making these quantities available as variables in phase transformation models. Evolution equations for the carbon content are derived for transformations with and without carbon repartitioning.}$^{\text{qtd.}}_{[54]}$

3.3.1 Simulation framework

$^{\text{qtd.}}_{[54]}${For the study of boundary-value problems, the model proposed in this work is implemented in a quasi-static, thermodynamically coupled finite element framework. Assuming conservation of mass, the coupled problem is defined by the quasi-static balance of linear momentum

$$\nabla \cdot \boldsymbol{\sigma} + \rho\, \boldsymbol{f}^{\mathrm{b}} = \mathbf{0} \ , \tag{3.1}$$

and the first law of thermodynamics

$$\rho\, c_{\mathrm{p}}\, \dot{T} + \nabla \cdot \boldsymbol{q} - r = 0 \ , \tag{3.2}$$

where $\boldsymbol{\sigma}$ denotes the (Cauchy) stresses, $\boldsymbol{f}^{\mathrm{b}}$ represents mass-specific volumetric loads, ρ denotes the mass density, c_{p} denotes the specific heat capacity, $\boldsymbol{q}$ denotes the heat flux, r represents volume-specific heat sources, and the notation $\dot{\bullet}$ represents the time derivative of a quantity $\bullet$. In the following, eqs. (3.1) and (3.2) will be referred to as the *mechanical* and *thermal* problem, respectively.

At each material point, a coexistence of an austenite phase, a martensite phase, and a bainite phase is assumed, and their respective volume fractions are denoted by β_{A}, β_{M}, and β_{B}, respectively.

The material point represents a small homogeneous volume v with mass m. Denoting the density for each phase as ρ_i, the mass contribution of each phase can be expressed as

$$m_i = \rho_i\, \beta_i\, v \ . \tag{3.3}$$

The *metallurgical problem* is defined by the mass balance

$$\sum_i m_i = m \Leftrightarrow \sum_i \frac{\rho_i}{\rho}\, \beta_i = 1 \ . \tag{3.4}$$

A common assumption in the small strain setting is that the density changes between phases are small, i.e. $\rho_i \approx \rho$, which leads to

$$\sum_i \beta_i = 1 \ . \tag{3.5}$$

The *chemical problem* is defined by the mass balance for each element of the alloy. However, since the carbon content is expected to have the largest impact on the transformation kinetics, in this work only the carbon mass balance is considered. For the material point, the total mass of carbon is given by

$$m_\mathrm{C} = \rho\, v\, x_\mathrm{C} \ , \tag{3.6}$$

in terms of the nominal carbon content x_C, while the mass of carbon stored in each phase reads

$$\begin{aligned} m_\mathrm{C,A} &= \rho\, v\, \beta_\mathrm{A}\, x_\mathrm{C,A} \ , \\ m_\mathrm{C,M} &= \rho\, v\, \beta_\mathrm{M}\, x_\mathrm{C,M} \ , \\ m_\mathrm{C,B} &= \rho\, v\, \beta_\mathrm{B}\, x_\mathrm{C,B} \ , \end{aligned} \tag{3.7}$$

where $x_{\mathrm{C},i}$ denotes the carbon content of phase i. The carbon mass balance then reads

$$m_\mathrm{C} = m_\mathrm{C,A} + m_\mathrm{C,M} + m_\mathrm{C,B} \ . \tag{3.8}$$

Due to the limited time at elevated temperature, diffusional transport of carbon is neglected in the presented model. The primary global unknowns in the finite element problem are the displacement field $\boldsymbol{u}$ and therefore the temperature field T, while the volume fractions β_i and carbon contents $x_{\mathrm{C},i}$ represent (local) internal variables at each material point. Since the deformations associated with phase transformations are usually small in comparison with the part dimensions, the mechanical behaviour is modelled as *geometrically linear*, i.e. the strains $\boldsymbol{\varepsilon}$ are defined in terms of the displacement field $\boldsymbol{u}$ as

$$\boldsymbol{\varepsilon} = \frac{1}{2}\left[\nabla \boldsymbol{u} + [\nabla \boldsymbol{u}]^\mathrm{t}\right] \ . \tag{3.9}$$

Within the finite element framework, the material response must be defined in terms of appropriate constitutive models of the form

$$\boldsymbol{\sigma}\left(\boldsymbol{\varepsilon}, T, \beta_i, x_{\mathrm{C},i}\right) \ , \tag{3.10}$$

$$\boldsymbol{q}\left(\boldsymbol{\varepsilon}, T, \nabla T, \beta_i, x_{\mathrm{C},i}\right) \ , \tag{3.11}$$

$$r\left(\boldsymbol{\varepsilon}, T, \beta_i, x_{\mathrm{C},i}\right) \ , \tag{3.12}$$

together with heat capacity and evolution equations for all internal variables β_i and $x_{\mathrm{C},i}$. A graphical overview of the problems and interactions which are considered in the model is presented in fig. 3.1.}$^{\text{qtd.}}_{[54]}$

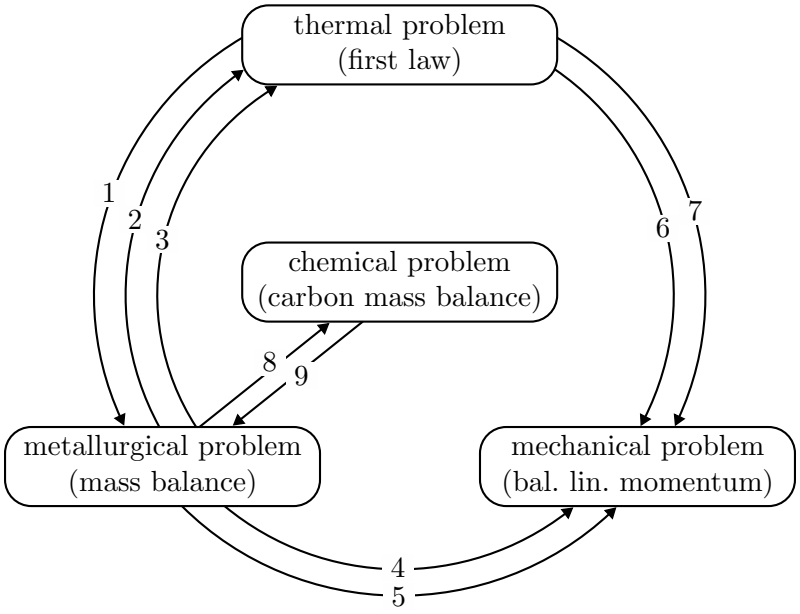

1 Thermal driving force for phase transformations
2 Phase-dependent thermal properties
3 Latent heat of transformations
4 Phase-dependent mechanical properties
5 Transformation strains
6 Thermal strains
7 Temperature-dependent mechanical properties
8 Carbon enrichment of austenite during bainitic transformation
9 Transformation laws dependent on carbon content

Figure 3.1: Overview of the problems and their interactions considered in the model. Under these assumptions, the mechanical problem does not influence the solution of the other three problems, and can therefore be solved individually as a post-processing step to the coupled solution of the thermal, chemical, and metallurgical problems. Dependencies which are considered constant during a simulation, e.g. the dependency of all material parameters on the overall chemical composition, are not depicted. *Figure reproduced from Furlan et al. [54] under the terms of the CC BY 4.0 license. The text font was updated to match the document text.*

3.3.2 Strains and stresses

qtd. [54] {In general, strains and stresses in different phases are expected to be non-uniform and need to be considered separately. For the sake of simplicity, the linear mixture rule is applied instead of a more rigorous homogenisation scheme, i.e. the model is formulated only in terms of effective macroscopic quantities which are obtained from the averaging of the respective quantities for the individual phases.

Following e.g. de Oliveira et al. [35], an additive decomposition for the strain increment $\mathrm{d}\boldsymbol{\varepsilon}$ is assumed and reads

$$\mathrm{d}\boldsymbol{\varepsilon} = \mathrm{d}\boldsymbol{\varepsilon}^{\mathrm{el}} + \mathrm{d}\boldsymbol{\varepsilon}^{\mathrm{th}} + \mathrm{d}\boldsymbol{\varepsilon}^{\mathrm{tv}} \ , \tag{3.13}$$

where $\mathrm{d}\boldsymbol{\varepsilon}^{\mathrm{el}}$ denotes the elastic strain increment, $\mathrm{d}\boldsymbol{\varepsilon}^{\mathrm{th}} = \alpha\, \boldsymbol{I}\, \mathrm{d}T$ denotes the thermal expansion due to the thermal expansion coefficient α and a temperature increment $\mathrm{d}T$[1], and $\mathrm{d}\boldsymbol{\varepsilon}^{\mathrm{tv}} = \mathrm{d}\gamma\, \boldsymbol{I}$ is a volumetric transformation strain increment, where the linear strain increment due to transformations is given by $\mathrm{d}\gamma$. Moreover, $\boldsymbol{I}$ represents the second-order identity tensor.

Following Hooke's law, the stresses $\boldsymbol{\sigma}$ are calculated as

$$\boldsymbol{\sigma} = \mathsf{E} : \varepsilon^{\mathrm{el}} \ , \tag{3.14}$$

where the (Cartesian) coefficients of the fourth-order elasticity tensor E read

$$\mathsf{E}_{ijkl} = \frac{E\,\nu}{[1+\nu][1-2\,\nu]}\,\delta_{ij}\,\delta_{kl} + \frac{E}{2[1+\nu]}\,[\delta_{ik}\,\delta_{jl} + \delta_{il}\,\delta_{jk}] \tag{3.15}$$

in terms of Young's modulus E, Poisson's ratio ν, and the Kronecker delta δ_{ij}. Considering an explicit dependency on the temperature T for all quantities in each individual phase, averaging by the linear mixture rule yields

$$E(T,\, \beta_i) = \sum_i \beta_i\, E_i(T) \ , \tag{3.16}$$

$$\nu(T,\, \beta_i) = \sum_i \beta_i\, \nu_i(T) \ , \tag{3.17}$$

$$\alpha(T,\, \beta_i) = \sum_i \beta_i\, \alpha_i(T) \ . \tag{3.18}$$

The transformation strain increment is computed based on the transformation strains γ_i for each phase as

$$\mathrm{d}\gamma(T,\, \beta_i) = \sum_i \gamma_i(T)\, \mathrm{d}\beta_i \ . \tag{3.19}$$

} qtd. [54]

[1] A reference temperature T_0 has to be chosen when evaluating the thermal strain in this formulation.

3.3.3 Heat transfer

$^{\text{qtd.}}_{[54]}\{$The well-established isotropic Fourier's law

$$\boldsymbol{q} = -\Lambda \nabla T \tag{3.20}$$

is assumed for the heat transfer problem, where the isotropic thermal conductivity Λ is considered to be a function of the temperature. Linear mixture is again applied to average the thermal parameters, i.e.

$$c_{\mathrm{p}}(T,\, \beta_i) = \sum_i \beta_i \, c_{\mathrm{p},i}(T) \ , \tag{3.21}$$

$$\Lambda(T,\, \beta_i) = \sum_i \beta_i \, \Lambda_i(T) \ . \tag{3.22}$$

Robin-type boundary conditions

$$-\boldsymbol{q} \cdot \boldsymbol{n} = h^{\mathrm{q}} \left[T - T_\infty\right] + e^{\mathrm{q}} \, k_{\mathrm{B}} \left[T^4 - T_\infty^4\right] \tag{3.23}$$

are used to model the heat flux from a surrounding medium of temperature T_∞ through a boundary with outward normal vector $\boldsymbol{n}$. Within the finite element framework, the surface heat flux enters the heat equation (3.20) as a surface contribution. Convectional heat exchange is governed by the temperature-dependent heat transfer coefficient (HTC), denoted by h^{q}, while heat exchange by radiation is determined by the emissivity e^{q} and the Boltzmann constant k_{B}.$\}^{\text{qtd.}}_{[54]}$

3.3.4 Evolution of carbon content

$^{\text{qtd.}}_{[54]}\{$After inserting eq. (3.7), the rate form of the diffusionless carbon mass balance (3.8) reads

$$\dot{\beta}_{\mathrm{A}} \, x_{\mathrm{C,A}} + \beta_{\mathrm{A}} \, \dot{x}_{\mathrm{C,A}} + \dot{\beta}_{\mathrm{M}} \, x_{\mathrm{C,M}} + \beta_{\mathrm{M}} \, \dot{x}_{\mathrm{C,M}} + \ \dot{\beta}_{\mathrm{B}} \, x_{\mathrm{C,B}} + \beta_{\mathrm{B}} \, \dot{x}_{\mathrm{C,B}} = 0 \ . \tag{3.24}$$

To derive evolution equations for the unknown carbon content in each phase, two additional assumptions are introduced. It is assumed that martensite always forms with the same amount of carbon that is currently present in the parent austenite phase, i.e.

$$\dot{m}_{\mathrm{C,M}} = \dot{m}_{\mathrm{M}} \, x_{\mathrm{C,A}} \ . \tag{3.25}$$

Using the product rule, this equation expands to

$$\dot{\beta}_{\mathrm{M}} \, x_{\mathrm{C,M}} + \beta_{\mathrm{M}} \, \dot{x}_{\mathrm{C,M}} = \dot{\beta}_{\mathrm{M}} \, x_{\mathrm{C,A}} \ . \tag{3.26}$$

The second assumption is that the carbon content in the bainite phase is constant and independent of the evolution in the parent phase, so that

$$\dot{x}_{\mathrm{C,B}} = 0 \tag{3.27}$$

holds. In the following, $x_{\mathrm{C,B}}$ is thus treated as a constant parameter. Inserting eqs. (3.26) and (3.27) into eq. (3.24) yields the evolution equation

$$\dot{x}_{\mathrm{C,A}} = -\frac{\dot{\beta}_{\mathrm{A}} x_{\mathrm{C,A}} + \dot{\beta}_{\mathrm{M}} x_{\mathrm{C,A}} + \dot{\beta}_{\mathrm{B}} x_{\mathrm{C,B}}}{\beta_{\mathrm{A}}} \ , \tag{3.28}$$

for the carbon content of the austenite phase. Using eq. (3.5), the evolution equation can also be expressed as

$$\dot{x}_{\mathrm{C,A}} = \frac{\dot{\beta}_{\mathrm{B}}}{\beta_{\mathrm{A}}} \left[x_{\mathrm{C,A}} - x_{\mathrm{C,B}} \right] \ . \tag{3.29}$$

The derived result does not depend on the reference volume introduced to motivate the equations, and is therefore directly applicable to the quadrature point level in the finite element model. It should be noted that eq. (3.29) reduces to $\dot{x}_{\mathrm{C,A}} = 0$ if $x_{\mathrm{C,B}} = x_{\mathrm{C,A}}$. In this case, all phases exhibit the same carbon content, and the carbon mass balance is trivially fulfilled.}$^{\text{qtd.}}_{[54]}$

3.3.5 Austenite-martensite transformation

$^{\text{qtd.}}_{[54]}${Martensite formation is modelled by the Koistinen–Marburger (KM) model [99]. The evolution of the martensite volume fraction is assumed to be dependent only on the temperature T and is given by the equation

$$\beta_{\mathrm{M}} = 1 - \exp\left(-k \left[M_{\mathrm{S}} - T \right]\right) \ , \tag{3.30}$$

where M_{S} denotes the martensite start temperature and k is called the rate parameter. Reformulating the original KM model as a rate equation, and interpreting the term $[1 - \beta_{\mathrm{M}}]$ as the remaining austenite volume fraction β_{A}, yields the expression

$$\begin{aligned} \dot{\beta}_{\mathrm{M}} &= -\exp\left(-k \left[M_{\mathrm{S}} - T \right]\right) k \dot{T} \\ &= -\left[1 - \beta_{\mathrm{M}}\right] k \dot{T} = -\beta_{\mathrm{A}} \, k \dot{T} \ , \end{aligned} \tag{3.31}$$

which remains valid even if competing diffusional transformations of austenite to bainite occur.

To ensure that the martensitic transformation takes place only below the martensite start temperature M_{S}, the term $\mathrm{H}\left(M_{\mathrm{S}} - T\right)$ is introduced, where H denotes the Heaviside function. Since the transformation of martensite back to austenite is not included in the model, another Heaviside term $\mathrm{H}\left(-\dot{T}\right)$ is introduced to restrict the transformation direction. After introducing an activation function

$$\zeta_{\mathrm{M}} = \mathrm{H}\left(M_{\mathrm{S}} - T\right) \mathrm{H}\left(-\dot{T}\right) \ , \tag{3.32}$$

which aggregates the conditions for an evolution, the final rate equation for the martensite volume fraction reads

$$\dot{\beta}_{\mathrm{M}} = -\zeta_{\mathrm{M}} \, \beta_{\mathrm{A}} \, k \dot{T} \ . \tag{3.33}$$

$\}^{\text{qtd.}}_{[54]}$

3.3.6 Austenite-bainite transformation

qtd. [54]{The transformation of austenite to bainite is modelled based on the classic JMAK model developed by Johnson and Mehl [17, 91], Avrami [10–12], and Kolmogorov [100, 101], which describes the isothermal transformation kinetics by an equation of the type

$$\beta_{\mathrm{B}} = \hat{\beta}_{\mathrm{B}} \left[1 - \exp\left(-b\, t^{N}\right)\right] \ , \tag{3.34}$$

where $\hat{\beta}_{\mathrm{B}}$ denotes the maximum reachable volume fraction of bainite. It is assumed that the model parameters b and N are functions of the temperature T. The transformation rate reads

$$\begin{aligned} \dot{\beta}_{\mathrm{B}} &= \hat{\beta}_{\mathrm{B}}\, N\, b\, t^{N-1} \exp\left(-b\, t^{N}\right) \\ &= N\, b\, t^{N-1} \left[\hat{\beta}_{\mathrm{B}} - \beta_{\mathrm{B}}\right] \ . \end{aligned} \tag{3.35}$$

Solving eq. (3.34) for the time t leads to the expression

$$t^{*} = \left[\frac{1}{b} \ln\left(\frac{\hat{\beta}_{\mathrm{B}}}{\hat{\beta}_{\mathrm{B}} - \beta_{\mathrm{B}}}\right)\right]^{\frac{1}{N}} \ , \tag{3.36}$$

which can be interpreted as the time required to reach a given bainite volume fraction β_{B} on an isothermal path, sometimes called the *fictitious time*. Inserting eq. (3.36) into eq. (3.35), and introducing an activation function

$$\zeta_{\mathrm{B}} = \mathrm{H}\left(B_{\mathrm{S}} - T\right) \ , \tag{3.37}$$

in terms of the bainite start temperature B_{S}, yields

$$\dot{\beta}_{\mathrm{B}} = \zeta_{\mathrm{B}}\, N\, b^{\frac{1}{N}} \left[\hat{\beta}_{\mathrm{B}} - \beta_{\mathrm{B}}\right] \left[\ln\left(\frac{\hat{\beta}_{\mathrm{B}}}{\hat{\beta}_{\mathrm{B}} - \beta_{\mathrm{B}}}\right)\right]^{\frac{N-1}{N}} \ , \tag{3.38}$$

eliminating the explicit time dependency.

Although the JMAK model is originally intended for isothermal applications, it can be employed for general temperature paths by assuming a series of isothermal steps at varying temperatures, as shown in e.g. de Oliveira et al. [35]. A parametrisation for the model parameters b and N dependent on the temperature is then required.

It is remarked that the JMAK model eq. (3.38) in rate form is valid only after the onset of the bainite transformation, since the rate for the bainite volume fraction is zero in case no bainite has been formed. Application of the time-dependent rate form eq. (3.35) requires tracking of the time of the onset of transformation. An alternative approach, based on the concept of fractional nucleation introduced in Scheil [158], is therefore used to model the incubation, i.e. the evolution of the first 1 % of bainite. Following

Scheil [158], the incubation for a general temperature path is assumed to be complete at temperature T_x if the condition

$$\int_{T_0}^{T_x} \frac{\mathrm{d}T}{\dot{T}\tau(T)} = 1 \tag{3.39}$$

is fulfilled, where T_0 is an equilibrium temperature at which no nucleation occurs, and $\tau(T)$ denotes the nucleation time for an isothermal path at temperature T, which can be acquired from e.g. isothermal time–temperature–transformation (TTT) diagrams. Given an explicit parametrisation $b(T)$ and $N(T)$, the nucleation time can be obtained from eq. (3.36) as

$$\tau\left(T\right) = \left[\frac{1}{b\left(T\right)} \ln\left(\frac{1}{0.99}\right)\right]^{\frac{1}{N(T)}} \quad . \tag{3.40}$$

Equation (3.39) is scaled to 1 % to represent the bainite fraction during incubation, leading to the expression

$$\beta_\mathrm{B} = 0.01 \int \frac{1}{\tau\left(T\right)} \,\mathrm{d}t \ , \tag{3.41}$$

or, in rate form,

$$\dot{\beta}_\mathrm{B} = 0.01 \, \frac{1}{\tau\left(T\right)} \ . \tag{3.42}$$

Combining the models for nucleation and further evolution of the bainite volume fraction yields

$$\dot{\beta}_\mathrm{B} = \begin{cases} 0.01\,\zeta_\mathrm{B}/\tau & \text{if } \beta_\mathrm{B} \leq 1\,\% \\ \zeta_\mathrm{B}\, N\, b^{\frac{1}{N}} \left[\hat{\beta}_\mathrm{B} - \beta_\mathrm{B}\right] \left[\ln\left(\frac{\hat{\beta}_\mathrm{B}}{\hat{\beta}_\mathrm{B}-\beta_\mathrm{B}}\right)\right]^{\frac{N-1}{N}} & \text{if } \beta_\mathrm{B} > 1\,\% \end{cases} \ . \tag{3.43}$$

To complete the model for the bainite evolution, the maximum reachable bainite fraction $\hat{\beta}_\mathrm{B}$ has to be specified. It is assumed that a function $\mathrm{f}(T, x_\mathrm{C,A})$ exists which describes the amount of bainite that will form from the current amount of austenite for a given temperature and carbon content. This function returns the value 1 if, assuming infinite transformation time, a complete transformation to bainite occurs. The maximum reachable bainite fraction then reads

$$\hat{\beta}_\mathrm{B} = \mathrm{f}(T, x_\mathrm{C,A})\, \beta_\mathrm{A} + \beta_\mathrm{B} \ , \tag{3.44}$$

where β_B denotes the bainite currently present.

For a given temperature T^*, current carbon content in the austenite phase $x_\mathrm{C,A}$, and prescribed carbon content in the bainite phase $x_\mathrm{C,B}$, the function f is chosen based on a

lever rule. Assuming a monotonous function $B_{\mathrm{S}}(x_{\mathrm{C,A}})$ for the bainite start temperature, $x^*_{\mathrm{C,A}} = B_{\mathrm{S}}^{-1}(T^*)$ describes the austenite phase carbon content at which no further bainite transformation occurs.

For a hypothetical isothermal evolution of only the current austenite phase to bainite, the resulting phase fractions are denoted by $\tilde{\beta}_{\mathrm{A}}$ and $\tilde{\beta}_{\mathrm{B}}$, respectively. During this hypothetical evolution, the mass balance yields

$$\tilde{\beta}_{\mathrm{A}} + \tilde{\beta}_{\mathrm{B}} = \beta_{\mathrm{A}} \ , \tag{3.45}$$

and the mass balance for the carbon initially bound in the austenite phase reads

$$\tilde{x}_{\mathrm{C,A}}\,\tilde{\beta}_{\mathrm{A}} + \tilde{x}_{\mathrm{C,B}}\,\tilde{\beta}_{\mathrm{B}} = x_{\mathrm{C,A}}\,\beta_{\mathrm{A}} \ , \tag{3.46}$$

where $\tilde{x}_{\mathrm{C,A}}$ and $\tilde{x}_{\mathrm{C,B}}$ describe the carbon content of the respective phases after the transformation. Assuming that $x_{\mathrm{C,B}}$ is constant, and that the transformation stops when the condition $\tilde{x}_{\mathrm{C,A}} = x^*_{\mathrm{C,A}}$ is fulfilled, inserting eq. (3.45) in eq. (3.46) yields

$$\mathrm{f}(T, x_{\mathrm{C,A}}) = \frac{\tilde{\beta}_{\mathrm{B}}}{\beta_{\mathrm{A}}} = \frac{x_{\mathrm{C,A}} - x^*_{\mathrm{C,A}}(T)}{x_{\mathrm{C,B}} - x^*_{\mathrm{C,A}}(T)} \ . \tag{3.47}$$

A graphical representation of these relations is shown in fig. 3.2.}$^{\text{qtd.}}_{[54]}$

3.3.7 Parametrisation of the bainite transformation model

$^{\text{qtd.}}_{[54]}${Time–temperature–transformation (TTT) diagrams are commonly used to visualise the temperature-dependent start and end times of isothermal transformations, usually in terms of lines for 1 % and 99 % transformation at each temperature. As stated in section 3.3.6, the parameters $b(T)$ and $N(T)$ must be temperature-dependent to model the impact of varying temperature on the transformation kinetics. In this work, the quadratic polynomial ansatz

$$\begin{aligned} \ln(b_p(T)) &= p_{b,0} + p_{b,1}\,T + p_{b,2}T^2 \ , \\ N_p(T) &= p_{N,0} + p_{N,1}T + p_{N,2}T^2 \end{aligned} \tag{3.48}$$

is used, where the vector $\boldsymbol{p} = [p_{b,0},\, p_{b,1},\, p_{b,2},\, p_{N,0},\, p_{N,1},\, p_{N,2}]^{\mathrm{t}}$ consists of the constant polynomial coefficients. The prediction for the bainite phase fraction in an isothermal transformation then reads

$$\beta_{\mathrm{B},p}(t, T) = 1 - \exp\left(-b_p(T)\, t^{N_p(T)}\right) \ . \tag{3.49}$$

A web-based plot digitising tool WebPlotDigitizer [155] was applied to a TTT–diagram of the bainite transformation for 100Cr6, which was published in Kaymak [93]. The times $t_{1,i}$ and $t_{99,i}$, at which the transformation to bainite reaches 1 % and 99 %, were extracted

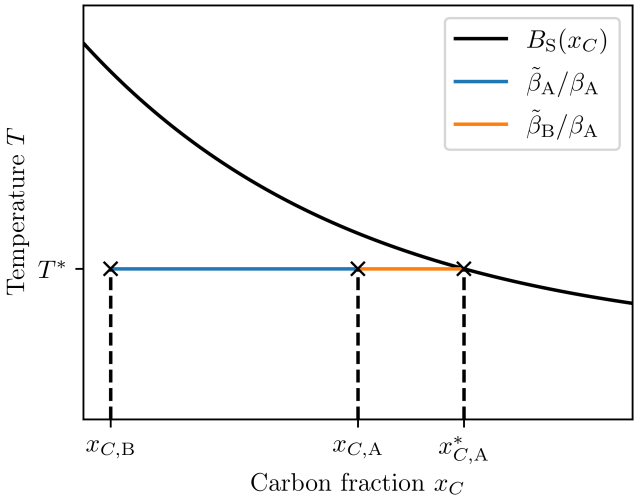

Figure 3.2: Graphical representation of the lever rule used to determine the maximum fraction of austenite transforming to bainite at a given temperature. At current temperature T^*, the austenite phase has the current carbon concentration $x_{\mathrm{C,A}}$. During a hypothetical isothermal transformation, bainite forms with the prescribed carbon content $x_{\mathrm{C,B}}$, inducing carbon enrichment of the remaining austenite. When the carbon content in the remaining austenite reaches the limit value $x^*_{\mathrm{C,A}}$, no further transformation takes place, i.e. the bainite phase fraction $\tilde{\beta}_{\mathrm{B}}$ with carbon concentration $x_{\mathrm{C,B}}$ and the austenite phase fraction $\tilde{\beta}_{\mathrm{A}}$ with carbon concentration $x^*_{\mathrm{C,A}}$ are in equilibrium. *Figure reproduced from Furlan et al. [54] under the terms of the CC BY 4.0 license. No changes were made.*

for a set of discrete temperatures T_i. Optimal parameters $\boldsymbol{p}^*$ were obtained from the nonlinear least-squares optimisation

$$\boldsymbol{p}^* = \arg\min_{\boldsymbol{p}} \sum_{i}^{m} \left[[\beta_{\mathrm{B},p}(t_{1,i}, T_i) - 0.01]^2 + [\beta_{\mathrm{B},p}(t_{99,i}, T_i) - 0.99]^2 \right] \ . \tag{3.50}$$

It is remarked that especially the choice of initial guess for the minimisation process is not trivial, and therefore discussed in more detail in Appendix A.1.1. The optimisation was implemented in Python, and the source code, along with the point data extracted from the diagram, is available in the github repository accompanying this work. An application to other materials, provided the TTT–diagram is available, as well as the application of a higher order polynomial ansatz, is straight-forward by using the provided code.}^{\text{qtd.}}_{[54]}

3.3.8 Composition-dependency of transformation parameters

qtd. [54]{In general, the transformation models described in sections 3.3.5 and 3.3.6 have to be calibrated for each material, i.e. for each chemical composition. However, calibration data such as TTT–diagrams is usually not available for every unique material. Especially the influence of slight changes in composition, such as the carbon enrichment during transformation to carbide-free bainite, can not directly be inferred from the available diagrams. For the proposed model, the JMAK parameters, i.e. b and N, are assumed to be independent of the carbon concentration, and to be identical for both materials under considerations. Therefore, a single TTT-diagram is used for the calibration procedure described in section 3.3.7.

For the dependency of the KM model parameters, the empirical equations

$$\begin{aligned} M_{\mathrm{S}}^{(1)} = {} & 530.2 - 290.3\,x_{\mathrm{C}} - 35.5\,x_{\mathrm{Mn}} - 6.8\,x_{\mathrm{Si}} - 20.8\,x_{\mathrm{Cr}} \\ & - 17.2\,x_{\mathrm{Ni}} - 10.4\,x_{\mathrm{Mo}} + 7.1\,x_{\mathrm{Al}} + 4.8\,x_{\mathrm{Co}} \\ & - 75\,\left[1 - \exp(-0.96\,x_{\mathrm{C}})\right]\ , \end{aligned} \tag{3.51}$$

proposed in Ingber and Kunert [85] for the martensite start temperature M_{S}, and

$$\begin{aligned} k^{(1)} = {} & \big[27.2 - 0.14\,x_{\mathrm{Mn}} - 0.21\,x_{\mathrm{Si}} - 0.11\,x_{\mathrm{Cr}} - 0.08\,x_{\mathrm{Ni}} \\ & - 0.05\,x_{\mathrm{Mo}} - 19.8\,\left[1 - \exp(-1.56\,x_{\mathrm{C}})\right]\big]/1000\ , \end{aligned} \tag{3.52}$$

given in van Bohemen [190] for the rate parameter k have been evaluated for the nominal chemical composition of 100Cr6 and 100CrMnSi6-4, defined by [42].}qtd. [54] Table 3.1 presents the assumed composition of the alloy, while the corresponding values obtained from eqs. (3.51) and (3.52) are presented in table 3.2.

qtd. [54]{While the resulting rate parameters $k = 0.0113$ and $k = 0.0110$ are in good agreement with the value $k = 0.0109$ estimated in Mustak et al. [127], the resulting martensite start temperatures $M_{\mathrm{S}} = 150.2\,^{\circ}\mathrm{C}$ and $M_{\mathrm{S}} = 102.1\,^{\circ}\mathrm{C}$ show a significant deviation from literature values. For 100Cr6, Kaymak [93] finds a value of $M_{\mathrm{S}} = 215\,^{\circ}\mathrm{C}$, and Hunkel [82] gives $M_{\mathrm{S}} = 212\,^{\circ}\mathrm{C}$. Depending on the austenitisation temperature, Cui et al. [31] provides values of approximately $M_{\mathrm{S}} = 190\,^{\circ}\mathrm{C}$ to $310\,^{\circ}\mathrm{C}$ for 100Cr6 and $M_{\mathrm{S}} = 190\,^{\circ}\mathrm{C}$ to $280\,^{\circ}\mathrm{C}$ for 100CrMnSi6-4.

Table 3.1: Mass fraction of chemical elements in 100Cr6 and 100CrMnSi6-4, following Deutsches Institut für Normung e.V. [42]. *Table reproduced from Furlan et al. [54] under the terms of the CC BY 4.0 license. The original table was split into two separate tables due to page size restrictions. The captions were altered accordingly.*

Material	x_{C}	x_{Si}	x_{Mn}	x_{Cr}	x_{Mo}	x_{Ni}	x_{Al}	x_{Co}
100Cr6	1.0 %	0.25 %	0.35 %	1.375 %	0.1 %	0.0 %	0.05 %	0.0 %
100CrMnSi6-4	1.0 %	0.6 %	1.55 %	1.525 %	0.1 %	0.0 %	0.05 %	0.0 %

Table 3.2: Martensite start temperature $M_S^{(1)}$ and rate coefficient $k^{(1)}$ for 100Cr6 and 100CrMnSi6-4, calculated by eqs. (3.51) and (3.52). *Table reproduced from Furlan et al. [54] under the terms of the CC BY 4.0 license. The original table was split into two separate tables due to page size restrictions. The captions were altered accordingly.*

Material	$M_S^{(1)}$	$k^{(1)}$
100Cr6	150.2 °C	0.0113 °C^{-1}
100CrMnSi6-4	102.1 °C	0.0110 °C^{-1}

Since the literature values suggest that the calculation of the transformation start temperature through eq. (3.51) is not accurate for the chemical compositions under consideration, the thermokinetic software package MatCalc 6 (version 6.04.1004) with the thermodynamic database mc_fe.tdb (version 2.060) was used to calculate the start temperatures M_S and B_S for the martensite and bainite transformations, for both 100Cr6 and 100CrMnSi6-4, and for varying carbon content x_C. For the calculations the so-called T0-principle was employed. This approach is based on the assumption that diffusionless transformations can only take place at temperatures below the temperature at which the initial and product phases with identical composition possess the same (value of) free energy. Depending on the amount of shear stress occurring during the transformation and the change in molar volume, an additional empirical term considering the necessary mechanical energy has to be added. For the results shown in fig. 3.3 an additional energy of 1400 J mol^{-1} was considered for martensite and 400 J mol^{-1} for bainite. Further details and a comparison of this approach with empirical equations for a steel with weight percentages $x_{Si} = 1.5\%$ and $x_{Mn} = 1.5\%$ can be found in Retzl et al. [152]. A linear regression shows good accordance with all data points for carbon contents between 0.5 % and 1.5 %, as presented in fig. 3.3.

For the final model, the start temperatures calculated in MatCalc are combined with eq. (3.52). All parametrisations are summarised in table 3.5.}$^{\text{qtd.}}_{[54]}$

3.3.9 Latent heat of transformations

$^{\text{qtd.}}_{[54]}${The latent heat associated with the transformations from austenite to martensite and from austenite to bainite is incorporated into eq. (3.2) in terms of the heat source r, as proposed in e.g. Denis et al. [39], Fernandes et al. [49], Woodard et al. [197], as

$$r = \rho \sum_i \dot{\beta}_i \, \Delta h_i \ , \tag{3.53}$$

where Δh_i is the specific enthalpy difference of phase i with respect to the austenite phase.}$^{\text{qtd.}}_{[54]}$

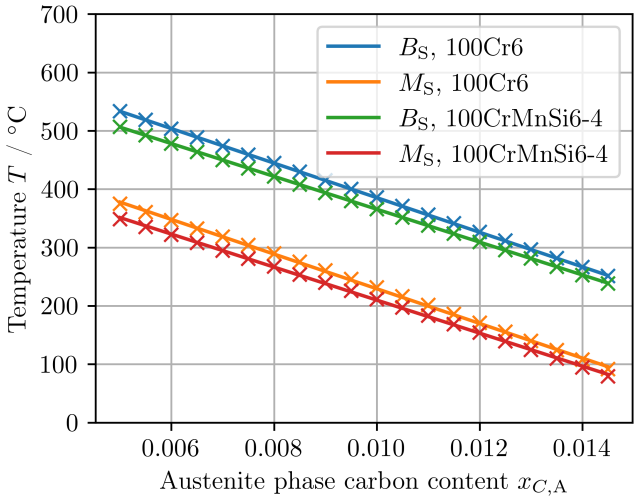

Figure 3.3: Martensite and bainite start temperatures for 100Cr6 and 100CrMnSi6-4 dependent on nominal carbon content x_C. Markers represent simulation results obtained from the software MatCalc, while solid lines show the linear regression for each of the data sets. *Figure reproduced from Furlan et al. [54] under the terms of the CC BY 4.0 license. No changes were made.*

3.4 Implementation

qtd. [54]{The proposed model is implemented in terms of a Fortran subroutine for the commercial finite element software Abaqus 2023 [33]. Based on the model structure shown in fig. 3.1, it would be possible to solve the thermal-metallurgical-chemical subproblem for all time steps, and to subsequently solve the mechanical problem. However, a fully coupled solution procedure is preferred in the implementation. This decision was made to simplify future additions to the model, which might introduce additional couplings, such as transformation plasticity. Implicit time integration was chosen due to the large time periods required for cooling to ambient temperature. Based on the choice of a time-implicit, thermo-mechanically coupled procedure, the model was implemented in Abaqus in terms of the Fortran user subroutines UMAT and UMATHT, which represent the mechanical and thermal material models at the quadrature point level.}qtd. [54]

3.4.1 Program structure

qtd. [54]{Every time an evaluation of the material model is required, Abaqus first calls the UMAT and subsequently the UMATHT subroutine. The implementation of a user material in the UMAT subroutine for a thermomechanically coupled problem requires the specification of the Cauchy stresses in Voigt notation $\boldsymbol{\sigma}_V$, the mechanical volumetric heat generation rate r_{pl}, and the updated internal variables $\boldsymbol{s}$ at the end of the time increment. Furthermore, the sensitivities of the stresses and heat generation rate with respect to

the strain increment in Voigt notation $\Delta\boldsymbol{\varepsilon}_V$ and the temperature T are required. In the following, the symbol $\boldsymbol{s}$ refers to the actual array stored by Abaqus for each integration point, while the symbol $\boldsymbol{\kappa}$ will denote the set of internal variables required to describe the current microstructure. The vector $\boldsymbol{s}$ includes $\boldsymbol{\kappa}$, but also additional quantities for post processing, as shown in table 3.3. During the call of the UMATHT subroutine, the thermal internal energy density e^T and the heat flux vector $\boldsymbol{q}$ must be set, and the state variables $\boldsymbol{s}$ can optionally be updated again. For both internal thermal energy and heat flux, the sensitivities with respect to the temperature T and the temperature gradient ∇T are required. Finally, a variable denoted $p_{\Delta\mathrm{t}}$ can be set in both subroutines to suggest the size of the next time increment if the automatic time step control is active. All variables to be defined are listed in table 3.4.}^{\text{qtd.}}_{[54]}

{}^{\text{qtd.}}_{[54]}\{Taking into account the dependencies on the internal variables $\boldsymbol{\kappa}$, the sensitivities read

$$\frac{\mathrm{d}\Delta\boldsymbol{\sigma}_V}{\mathrm{d}\Delta\boldsymbol{\varepsilon}_V} = \frac{\partial\Delta\boldsymbol{\sigma}_V}{\partial\Delta\boldsymbol{\varepsilon}_V} + \frac{\partial\Delta\boldsymbol{\sigma}_V}{\partial\boldsymbol{\kappa}} \cdot \frac{\mathrm{d}\boldsymbol{\kappa}}{\mathrm{d}\Delta\boldsymbol{\varepsilon}_V} \ , \tag{3.54}$$

$$\frac{\mathrm{d}\Delta\boldsymbol{\sigma}_V}{\mathrm{d}T} = \frac{\partial\Delta\boldsymbol{\sigma}_V}{\partial T} + \frac{\partial\Delta\boldsymbol{\sigma}_V}{\partial\boldsymbol{\kappa}} \cdot \frac{\mathrm{d}\boldsymbol{\kappa}}{\mathrm{d}T} \ , \tag{3.55}$$

$$\frac{\mathrm{d}r_{pl}}{\mathrm{d}\Delta\boldsymbol{\varepsilon}_V} = \frac{\partial r_{pl}}{\partial\Delta\boldsymbol{\varepsilon}_V} + \frac{\partial r_{pl}}{\partial\boldsymbol{\kappa}} \cdot \frac{\mathrm{d}\boldsymbol{\kappa}}{\mathrm{d}\Delta\boldsymbol{\varepsilon}_V} \ , \tag{3.56}$$

$$\frac{\mathrm{d}r_{pl}}{\mathrm{d}T} = \frac{\partial r_{pl}}{\partial T} + \frac{\partial r_{pl}}{\partial\boldsymbol{\kappa}} \cdot \frac{\mathrm{d}\boldsymbol{\kappa}}{\mathrm{d}T} \ . \tag{3.57}$$

A residual equation of the format

$$\boldsymbol{R}_{\boldsymbol{\kappa}}(\boldsymbol{\kappa}) = \boldsymbol{0} \tag{3.58}$$

will be solved to obtain the internal variables $\boldsymbol{\kappa}$, where $\boldsymbol{\kappa}$ and $\boldsymbol{R}_{\boldsymbol{\kappa}}$ are specified in section 3.4.3. Based on eq. (3.58), the implicit function theorem is applied to determine the derivatives

$$\frac{\mathrm{d}\boldsymbol{\kappa}}{\mathrm{d}\Delta\boldsymbol{\varepsilon}_V} = -\left[\frac{\partial\boldsymbol{R}_{\boldsymbol{\kappa}}}{\partial\boldsymbol{\kappa}}\right]^{-1} \cdot \frac{\partial\boldsymbol{R}_{\boldsymbol{\kappa}}}{\partial\Delta\boldsymbol{\varepsilon}_V} = \boldsymbol{0} \ , \tag{3.59}$$

$$\frac{\mathrm{d}\boldsymbol{\kappa}}{\mathrm{d}T} = -\left[\frac{\partial\boldsymbol{R}_{\boldsymbol{\kappa}}}{\partial\boldsymbol{\kappa}}\right]^{-1} \cdot \frac{\partial\boldsymbol{R}_{\boldsymbol{\kappa}}}{\partial T} \ , \tag{3.60}$$

where the local Jacobian $\partial\boldsymbol{R}_{\boldsymbol{\kappa}}/\partial\boldsymbol{\kappa}$ was already computed to solve the system of evolution equations. It was already exploited in eq. (3.59) that $\partial\boldsymbol{R}_{\boldsymbol{\kappa}}/\partial\Delta\boldsymbol{\varepsilon}_V = \boldsymbol{0}$ can be directly inferred from the coupling structure presented in fig. 3.1. The required derivatives of the local residual $\boldsymbol{R}_{\boldsymbol{\kappa}}$ are specified in Appendix A.1.2, the derivatives of the stress increment $\Delta\boldsymbol{\sigma}_V$ in Appendix A.1.3, and the derivatives of the heat generation rate r_{pl} in Appendix A.1.4.

A graphical overview of the data flow in the subroutine structure is shown in fig. 3.4, while the abstract steps in each of the subroutines are summarised in algorithms 1 and 2.}^{\text{qtd.}}_{[54]}

Table 3.3: Order of state variables $\boldsymbol{s}$ in user subroutines UMAT and UMATHT. The internal variables $\boldsymbol{\kappa}$ are extracted from the vector $\boldsymbol{s}$ for each subroutine call. Positions 7–9 are used to transfer the temperature derivatives of the internal variables $\boldsymbol{\kappa}$ from UMAT to UMATHT. *Table reproduced from Furlan et al. [54] under the terms of the CC BY 4.0 license. The text font was updated to match the font of the thesis.*

Position	Symbol	Description
1	β_M	Martensite volume fraction
2	β_B	Bainite volume fraction
3	β_A	Austenite volume fraction
4	$x_\mathrm{C,A}$	Austenite phase carbon content
5	$\int \alpha \, \mathrm{d}T$	Linear thermal strain
6	$\int \mathrm{d}\gamma$	Linear transformation strain
7	$\frac{\mathrm{d}\beta_\mathrm{M}}{\mathrm{d}T}$	Temperature derivative of martensite fraction
8	$\frac{\mathrm{d}\beta_\mathrm{B}}{\mathrm{d}T}$	Temperature derivative of bainite fraction
9	$\frac{\mathrm{d}x_\mathrm{C,A}}{\mathrm{d}T}$	Temperature derivative of austenite phase carbon content
10	f	Factor for incomplete bainite transformation

3.4.2 Regularised Heaviside function

$^{\text{qtd.}}_{[54]}\{$The activation functions for the phase transformations, i.e. ζ_M and ζ_B, are based on the Heaviside function H, which is non-continuous and therefore may cause convergence problems when the evolution equations are solved numerically. These problems are avoided by applying the approximation

$$\mathrm{H}\left(T\right) \approx \widetilde{\mathrm{H}} = \frac{1}{2}\left[\tanh\left(l\,T\right) + 1\right] \ , \tag{3.61}$$

where the parameter l governs the range over which the step function is regularised, and is chosen so that

$$\widetilde{\mathrm{H}}\left(T - 2\,^\circ\mathrm{C}\right) = 1\,\% \ , \quad \widetilde{\mathrm{H}}\left(T + 2\,^\circ\mathrm{C}\right) = 99\,\% \ . \tag{3.62}$$

The Heaviside function $\mathrm{H}\left(\dot{T}\right)$ in eq. (3.32) is implemented as an if-condition to avoid any martensite evolution during heating.$\}^{\text{qtd.}}_{[54]}$

Table 3.4: Output to be defined in the user material subroutines UMAT and UMATHT. *Table reproduced from Furlan et al. [54] under the terms of the CC BY 4.0 license. The text font was updated to match the font of the thesis.*

Variable name	Symbol	Description	Subroutine
STRESS	$\boldsymbol{\sigma}_V$	(Cauchy) stress tensor (Voigt notation)	UMAT
STAVEV	$\boldsymbol{s}$	Vector of state variables	UMAT, UMATHT
RPL	r_{pl}	Mechanical heat generation per volume and unit time	UMAT
DDSDDE	$\frac{\mathrm{d}\Delta\boldsymbol{\sigma}_V}{\mathrm{d}\Delta\boldsymbol{\varepsilon}_V}$	Sensitivity of stress increments w.r.t. strain increments	UMAT
DDSDDT	$\frac{\mathrm{d}\boldsymbol{\sigma}_V}{\mathrm{d}T}$	Sensitivity of stress increments w.r.t. temperature	UMAT
DRPLDE	$\frac{\mathrm{d}r_{pl}}{\mathrm{d}\Delta\boldsymbol{\varepsilon}_V}$	Sensitivity of heat generation w.r.t. strain increments	UMAT
DRPLDT	$\frac{\mathrm{d}r_{pl}}{\mathrm{d}T}$	Sensitivity of heat generation w.r.t. temperature	UMAT
U	e^T	Internal thermal energy per unit mass	UMATHT
DUDT	$\frac{\mathrm{d}e^T}{\mathrm{d}T}$	Sensitivity of e^T w.r.t. temperature	UMATHT
DUDG	$\frac{\mathrm{d}e^T}{\mathrm{d}\nabla T}$	Sensitivity of e^T w.r.t. temperature gradient	UMATHT
FLUX	$\boldsymbol{q}$	Heat flux vector	UMATHT
DFDT	$\frac{\mathrm{d}\boldsymbol{q}}{\mathrm{d}T}$	Sensitivity of heat flux w.r.t. temperature	UMATHT
DFDG	$\frac{\mathrm{d}\boldsymbol{q}}{\mathrm{d}\nabla T}$	Sensitivity of heat flux w.r.t. temperature gradient	UMATHT
PNEWDT	$p_{\Delta \mathrm{t}}$	Time increment ratio for automatic time stepping	UMAT, UMATHT

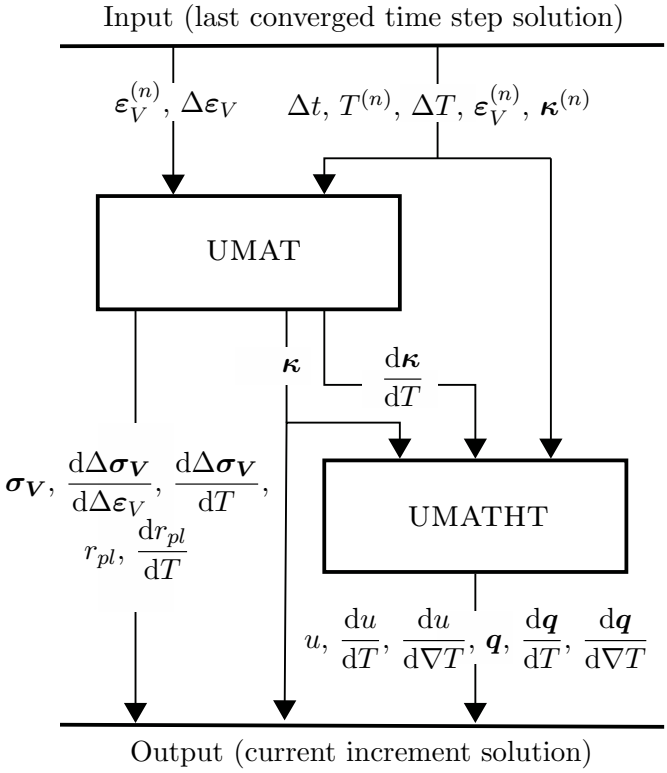

Figure 3.4: Data flow during the call of the user subroutines UMAT and UMATHT. Both $\boldsymbol{\kappa}$ and $\mathrm{d}\boldsymbol{\kappa}/\mathrm{d}T$ are passed from UMAT to UMATHT in the vector of state variables $\boldsymbol{s}$. *Figure reproduced from Furlan et al. [54] under the terms of the CC BY 4.0 license. The text font was updated to match the font of the thesis.*

Algorithm 1: Structure of user subroutine UMAT.
Terms which vanish for the proposed model are neglected here. *Algorithm reproduced from Furlan et al. [54] under the terms of the CC BY 4.0 license. The text font was updated to match the font of the thesis.*

Input: Δt, $T^{(n)}$, ΔT, $\boldsymbol{\varepsilon}_V^{(n)}$, $\Delta\boldsymbol{\varepsilon}_V$, $\boldsymbol{\sigma}_V^{(n)}$, $\boldsymbol{s}^{(n)}$

extract $\boldsymbol{\kappa}^{(n)}$ from $\boldsymbol{s}^{(n)}$

Step 1: Solve evolution equations for $\boldsymbol{\kappa}$

  Calculate $\boldsymbol{\kappa}$ so that $\boldsymbol{R}_{\boldsymbol{\kappa}} = \mathbf{0}$

  Calculate partial derivatives $\dfrac{\boldsymbol{R}_{\boldsymbol{\kappa}}}{\boldsymbol{\kappa}}$, $\dfrac{\boldsymbol{R}_{\boldsymbol{\kappa}}}{T}$

Step 2: Apply implicit function theorem

$$\frac{\mathrm{d}\boldsymbol{\kappa}}{\mathrm{d}T} = -\left[\frac{\partial \boldsymbol{R}_{\kappa}}{\partial \boldsymbol{\kappa}}\right]^{-1} \cdot \frac{\partial \boldsymbol{R}_{\kappa}}{\partial T}$$

Step 3: Evaluate mechanical constitutive model

  Calculate stresses $\boldsymbol{\sigma}_V$

  Calculate partial derivatives $\dfrac{\partial \Delta\boldsymbol{\sigma}_V}{\partial \Delta\boldsymbol{\varepsilon}_V}$, $\dfrac{\partial \Delta\boldsymbol{\sigma}_V}{\partial T}$, $\dfrac{\partial \Delta\boldsymbol{\sigma}_V}{\partial \boldsymbol{\kappa}}$

  Calculate rate of heat generation r_{pl}

  Calculate partial derivative $\dfrac{\partial r_{pl}}{\partial T}$, $\dfrac{\partial r_{pl}}{\partial \boldsymbol{\kappa}}$

Step 4: Compute sensitivities

$$\frac{\mathrm{d}(\bullet)}{\mathrm{d}\Delta\boldsymbol{\varepsilon}_V} = \frac{\partial(\bullet)}{\partial\Delta\boldsymbol{\varepsilon}_V}$$

$$\frac{\mathrm{d}(\bullet)}{\mathrm{d}T} = \frac{\partial(\bullet)}{\partial T} + \frac{\partial(\bullet)}{\partial \boldsymbol{\kappa}} \cdot \frac{\mathrm{d}\boldsymbol{\kappa}}{\mathrm{d}T}$$

Update $\boldsymbol{s}$ based on $\boldsymbol{\kappa}$ and $\mathrm{d}\boldsymbol{\kappa}/\mathrm{d}T$

Output: $\boldsymbol{\sigma}_V$, $\dfrac{\mathrm{d}\Delta\boldsymbol{\sigma}_V}{\mathrm{d}\Delta\boldsymbol{\varepsilon}_V}$, $\dfrac{\mathrm{d}\Delta\boldsymbol{\sigma}_V}{\mathrm{d}T}$, r_{pl}, $\dfrac{\mathrm{d}r_{pl}}{\mathrm{d}T}$, $\boldsymbol{s}$

Algorithm 2: Structure of user subroutine UMATHT.
Terms which vanish for the proposed model are neglected here. The derivatives $\partial e^T/\partial \boldsymbol{\kappa}$ and $\partial \boldsymbol{q}/\partial \boldsymbol{\kappa}$ arise from phase-dependent material parameters. *Algorithm reproduced from Furlan et al. [54] under the terms of the CC BY 4.0 license. The text font was updated to match the font of the thesis.*

Input: Δt, $T^{(n)}$, ΔT, $e^{T,(n)}$, $\boldsymbol{q}^{(n)}$, $\boldsymbol{s}^{(n)}$

extract $\boldsymbol{\kappa}^{(n)}$, $\boldsymbol{\kappa}$, and $\dfrac{\mathrm{d}\boldsymbol{\kappa}}{\mathrm{d}T}$ from $\boldsymbol{s}^{(n)}$

Step 1: Solve energy balance

  Update internal thermal energy e^T

  Calculate partial derivatives $\dfrac{\partial e^T}{\partial T}$, $\dfrac{\partial e^T}{\partial \nabla T}$, $\dfrac{\partial e^T}{\partial \boldsymbol{\kappa}}$

Step 2: Evaluate thermal constitutive law

  Calculate heat flux $\boldsymbol{q}$

  Calculate partial derivatives $\dfrac{\partial \boldsymbol{q}}{\partial T}$, $\dfrac{\partial \boldsymbol{q}}{\partial \nabla T}$, $\dfrac{\partial \boldsymbol{q}}{\partial \boldsymbol{\kappa}}$

Step 3: Compute Sensitivities

$$\frac{\mathrm{d}(\bullet)}{\mathrm{d}T} = \frac{\partial(\bullet)}{\partial T} + \frac{\partial(\bullet)}{\partial \boldsymbol{\kappa}} \cdot \frac{\mathrm{d}\boldsymbol{\kappa}}{\mathrm{d}T}$$

$$\frac{\mathrm{d}(\bullet)}{\mathrm{d}\nabla T} = \frac{\partial(\bullet)}{\partial \nabla T}$$

Output: e^T, $\dfrac{\mathrm{d}e^T}{\mathrm{d}T}$, $\dfrac{\mathrm{d}e^T}{\mathrm{d}\nabla T}$, $\boldsymbol{q}$, $\dfrac{\mathrm{d}\boldsymbol{q}}{\mathrm{d}T}$, $\dfrac{\mathrm{d}\boldsymbol{q}}{\mathrm{d}\nabla T}$

3.4.3 Solution of evolution equations

qtd. [54]{At any quadrature point in a finite element simulation, the local balance equations (3.5) and (3.8), as well as the evolution equations (3.33) and (3.43) for the volume fractions must be solved. Using the mass balance (3.5), the austenite volume fraction can be expressed as

$$\beta_{\mathrm{A}} = 1 - \beta_{\mathrm{M}} - \beta_{\mathrm{B}} \ . \tag{3.63}$$

The remaining internal variables at the quadrature point level are

$$\boldsymbol{\kappa} = \left[\beta_{\mathrm{M}},\, \beta_{\mathrm{B}},\, x_{\mathrm{C,A}}\right]^{\mathrm{t}} \ . \tag{3.64}$$

Restating eqs. (3.29), (3.33) and (3.38) in the rate form $\dot{\boldsymbol{\kappa}} = \boldsymbol{f}(\boldsymbol{\kappa})$ and introducing the abbreviation

$$A = \ln\left(\frac{\hat{\beta}_{\mathrm{B}}}{\hat{\beta}_{\mathrm{B}} - \beta_{\mathrm{B}}}\right) \tag{3.65}$$

leads to the coupled system of evolution equations

$$\dot{\beta}_{\mathrm{M}} = -\zeta_{\mathrm{M}}\left[1 - \beta_{\mathrm{M}} - \beta_{\mathrm{B}}\right] k\, \dot{T} \ , \tag{3.66a}$$

$$\dot{\beta}_{\mathrm{B}} = \begin{cases} 0.01\, \zeta_{\mathrm{B}}/\tau & \text{if } \beta_{\mathrm{B}} \leq 1\,\% \\ \zeta_{\mathrm{B}} N\, b^{\frac{1}{N}} \left[\hat{\beta}_{\mathrm{B}} - \beta_{\mathrm{B}}\right] A^{\frac{N-1}{N}} & \text{if } \beta_{\mathrm{B}} > 1\,\% \end{cases} \ , \tag{3.66b}$$

$$\dot{x}_{\mathrm{C,A}} = \frac{\dot{\beta}_{\mathrm{B}}}{1 - \beta_{\mathrm{M}} - \beta_{\mathrm{B}}}\left[x_{\mathrm{C,A}} - x_{\mathrm{C,B}}\right] \ . \tag{3.66c}$$

Inserting eq. (3.66b) into eq. (3.66c) yields the desired format, but is omitted here for readability.

Starting from increment n at time $t^{(n)}$, with known values $\boldsymbol{\kappa}^{(n)}$ and $T^{(n)}$, a time step $\Delta t = t^{(n+1)} - t^{(n)}$ to the next time increment $n+1$ is considered. The temperature $T^{(n+1)}$ is known at the material point level, but has to be taken into consideration when deriving the consistent tangent. Time discretisation is performed based on the implicit Euler integration scheme, i.e.

$$\dot{\boldsymbol{\kappa}} \approx \frac{\boldsymbol{\kappa}^{(n+1)} - \boldsymbol{\kappa}^{(n)}}{\Delta t} \ . \tag{3.67}$$

In the following the superscript $*^{(n+1)}$ will be omitted to improve readability. Applying the time discretisation to eq. (3.66) yields the discrete residual equation

$$\boldsymbol{R}_{\boldsymbol{\kappa}} = \left[R_{\beta_{\mathrm{M}}}\, R_{\beta_{\mathrm{B}}}\, R_{x_{\mathrm{C,A}}}\right]^{\mathrm{t}} = \boldsymbol{0} \tag{3.68}$$

with

$$R_{\beta_\mathrm{M}} = \beta_\mathrm{M} - \beta_\mathrm{M}^{(n)} + \zeta_\mathrm{M}\,[1 - \beta_\mathrm{M} - \beta_\mathrm{B}]\,k\Delta T\ , \tag{3.69a}$$

$$R_{\beta_\mathrm{B}} = \begin{cases} \beta_\mathrm{B} - \beta_\mathrm{B}^{(n)} - 0.01\,\zeta_\mathrm{B}\,\Delta t/\tau & \text{if } \beta_\mathrm{B}^{(n)} \leq 1\,\% \\ \beta_\mathrm{B} - \beta_\mathrm{B}^{(n)} - \Delta t \zeta_\mathrm{B} N\, b^{\frac{1}{N}} \left[\hat{\beta}_\mathrm{B} - \beta_\mathrm{B}\right] A^{\frac{N-1}{N}} & \text{if } \beta_\mathrm{B}^{(n)} > 1\,\% \end{cases}\ , \tag{3.69b}$$

$$R_{x_{\mathrm{C,A}}} = [1 - \beta_\mathrm{M} - \beta_\mathrm{B}] \left[x_{\mathrm{C,A}} - x_{\mathrm{C,A}}^{(n)}\right] - \left[\beta_\mathrm{B} - \beta_\mathrm{B}^{(n)}\right] [x_{\mathrm{C,A}} - x_{\mathrm{C,B}}]\ . \tag{3.69c}$$

Switching between nucleation and further evolution in eq. (3.69b) is implemented based on the last converged time step to improve numerical stability. A trust-region algorithm, provided in the Fortran version of the Intel MKL library, is used to solve the nonlinear equation eq. (3.68). The required Jacobian $\partial \boldsymbol{R}_{\boldsymbol{\kappa}}/\partial \boldsymbol{\kappa}$ is provided in Appendix A.1.2.}$^{\text{qtd.}}_{[54]}$

3.4.4 Stress update

$^{\text{qtd.}}_{[54]}${The time-discrete stress increment $\Delta\boldsymbol{\sigma}_V$ is obtained in a straight-forward manner from eq. (3.14) as

$$\Delta\boldsymbol{\sigma}_V = \mathbf{E}_V \cdot \left[\left[\boldsymbol{\varepsilon}_V^{\mathrm{el}}\right]^{(n)} + \Delta\boldsymbol{\varepsilon}_V^{\mathrm{el}}\right] - \boldsymbol{\sigma}_V^{(n)}\ , \tag{3.70}$$

where the elastic strain increment reads

$$\Delta\boldsymbol{\varepsilon}_V^{\mathrm{el}} = \Delta\boldsymbol{\varepsilon}_V - \alpha\,\Delta T\,\boldsymbol{I}_V - \Delta\gamma\,\boldsymbol{I}_V \tag{3.71}$$

with the second-order identity tensor in Voigt notation $\boldsymbol{I}_V$. By using eqs. (3.16) and (3.17), the elasticity tensor in Voigt notation can be computed as

$$\mathbf{E}_V = \sum_i \beta_i\,\mathbf{E}_{i,V}\ , \tag{3.72}$$

where the elasticity tensor $\mathbf{E}_{i,V}$ for each individual phase is computed following eq. (3.15), and the thermal expansion coefficient reads

$$\alpha = \sum_i \beta_i\,\alpha_i\ . \tag{3.73}$$

The discrete increment of the linear transformation strain is given by

$$\Delta\gamma = \sum_i \Delta\beta_i\,\gamma_i\ , \tag{3.74}$$

where $\Delta\beta_i$ denotes the increment in the respective volume fraction. Derivatives required for the FE implementation are specified in Appendix A.1.3.}$^{\text{qtd.}}_{[54]}$

3.4.5 Heat generation rate

qtd. [54] {The only part of the model contributing to the mechanical heat generation rate is the latent heat of the transformations, given by eq. (3.53), which is approximated as

$$r_{pl} = \frac{\beta_\mathrm{M} - \beta_\mathrm{M}^{(n)}}{\Delta t}\,\rho\,\Delta h_{\mathrm{A}\to\mathrm{M}} + \frac{\beta_\mathrm{B} - \beta_\mathrm{B}^{(n)}}{\Delta t}\,\rho\,\Delta h_{\mathrm{A}\to\mathrm{B}}\ . \tag{3.75}$$

Derivatives for the FE implementation are given in Appendix A.1.4.} qtd. [54]

Table 3.5: Parametrisation for the composition-dependent model parameters M_S, k, and B_S. The transformation start temperatures are obtained from MatCalc simulations, while the rate parameter is calculated based on eq. (3.52). *Table reproduced from Furlan et al. [54] under the terms of the CC BY 4.0 license. The text font was updated to match the font of the thesis.*

Parameter	Material	Parametrisation	Value at $x_\mathrm{C} = 1\,\%$
M_S	100Cr6	$526.29 - 29702.0\,x_\mathrm{C}$	229.28 °C
	100CrMnSi6-4	$492.71 - 28290.6\,x_\mathrm{C}$	209.80 °C
k	100Cr6	$7.14\,\mathrm{e}{-3} + 0.0198\,\exp\left(-156.0\,x_\mathrm{C}\right)$	0.0113
	100CrMnSi6-4	$6.88\,\mathrm{e}{-3} + 0.0198\,\exp\left(-156.0\,x_\mathrm{C}\right)$	0.0110
B_S	100Cr6	$681.51 - 29618.0\,x_\mathrm{C}$	385.33 °C
	100CrMnSi6-4	$646.95 - 28142.8\,x_\mathrm{C}$	365.52 °C

3.5 Representative simulation results

qtd. [54] {Representative finite element simulations have been performed to demonstrate the application of the proposed model. To demonstrate the coupling during the incomplete bainite transformation, a homogeneous, quasi-isothermal demonstration case above the martensite start temperature M_S is considered in section 3.5.2. Coupled evolution of martensite and bainite during cooling is considered in section 3.5.3 for a homogeneous problem, and in section 3.5.4 for the quenching of a complex axisymmetric workpiece.

All simulations presented in this work have been performed in the mm-g-ms unit system presented in table 3.6.} qtd. [54]

Table 3.6: Consistent mm-g-ms unit system, including units of selected derived quantities. *Table reproduced from Furlan et al. [54] under the terms of the CC BY 4.0 license. The text font was updated to match the font of the thesis.*

Quantity	Length	Mass	Time	Density	Force	Stress	Energy	Power
Unit	mm	g	ms	$\mathrm{g\,mm^{-3}}$	N	MPa	mJ	W

3.5.1 Choice of model parameters

qtd. [54]{All remaining model parameter choices for the representative simulations are summarised in this section. Table 3.7 gives an overview of all material parameters, except those for the phase transformation models, as functions of temperature T where applicable. Values for Young's modulus, Poisson's ratio, thermal expansion coefficient, specific heat capacity and thermal conductivity were published in Mustak et al. [127] for different phases of 100Cr6 and are adopted in this work for both material grades. As no specific values were available for 100Cr or 100CrMnSi6-4, the transformation strains and latent heat of transformation are chosen based on the values proposed in Denis et al. [38, 39] for 60NCD11 and XC80 steels. The overall mass density was approximated from general values for steel, since the differences between the phases are not considered as model parameters. The bainite phase carbon content was assumed as $x_{\mathrm{C,B}} = x_{\mathrm{C}} = 1.00\,\%$ for 100Cr6 and as $x_{\mathrm{C,B}} = 0.03\,\%$ for 100CrMnSi6-4.

To obtain the polynomial coefficients $\boldsymbol{p}$ for the temperature dependent JMAK model, see eq. (3.48), the optimisation described in section 3.3.7 was performed based on a TTT-diagram published in Kaymak [93]. Table 3.8 lists the optimal set of parameters $\boldsymbol{p}^*$. A comparison of the input data with the model prediction for the isothermal bainite transformation is presented in fig. 3.5 and shows good agreement between the model and the input data.

Following Gür and Tekkaya [64], the heat transfer coefficient for the quenching in water with a sink temperature of 20 °C and 60 °C is linearly interpolated from the values presented in table 3.9.}qtd. [54]

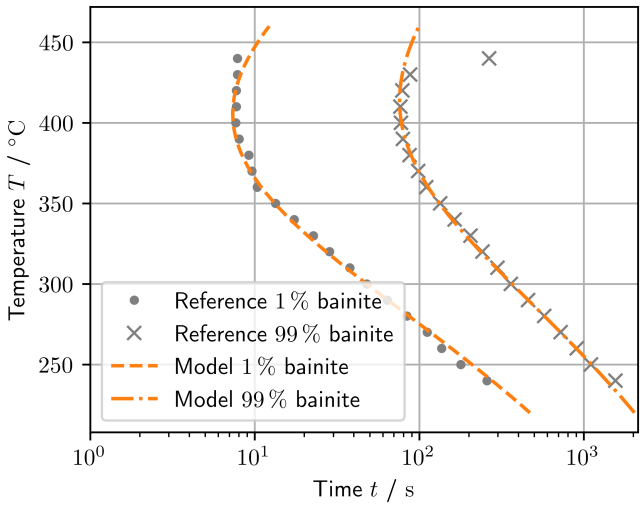

Figure 3.5: Comparison of input data and model prediction for the isothermal transformation from austenite to bainite. Grey markers represent points extracted from the TTT–diagram published in Kaymak [93], while orange lines show model prediction of transformation onset and finish after identification of polynomial parameters $\boldsymbol{p}^*$ for the temperature-dependent JMAK model. *Figure reproduced from Furlan et al. [54] under the terms of the CC BY 4.0 license. No changes were made.*

Table 3.7: Mechanical and thermal model parameters for each phase, based on (1) Mustak et al. [127], (2) Denis et al. [38], (3) Denis et al. [39]. All temperature-dependent expressions are given in terms of the dimensionless temperature $\tilde{T} = T/°\mathrm{C}$. *Table reproduced from Furlan et al. [54] under the terms of the CC BY 4.0 license. Formatting was slightly changed to fit the page width. The text font was updated to match the font of the thesis.*

Parameter	Symbol	Value	Unit	Source
Mass density	ρ	0.00785	$\mathrm{g\,mm^{-3}}$	
Young's modulus	E_A	$204000.0 - 91.0 \times \tilde{T}$	MPa	1
	E_M, E_B	$212000.0 - 52.7 \times \tilde{T}$	MPa	1
Poisson's ratio	ν_A	$0.223 + 0.00025 \times \tilde{T}$	–	1
	ν_M, ν_B	$0.344 + 0.00010 \times \tilde{T}$	–	1
Thermal expansion coefficient	α_A	$22.2\,\mathrm{e{-}6}$	$°\mathrm{C^{-1}}$	1
	α_M , α_B	$11.7\,\mathrm{e{-}6$	$°\mathrm{C^{-1}}$	1
Transformation strain	γ_A	0	–	
	γ_M	$1.11\,\mathrm{e{-}2}$	–	2
	γ_B	$5.0\,\mathrm{e{-}3}$	–	3
Specific heat capacity	$c_\mathrm{p,A}$	$448.67 + 0.3007 \times \tilde{T}$ $-2.49\,\mathrm{e{-}4} \times \tilde{T}^2$ $+1.42\,\mathrm{e{-}7} \times \tilde{T}^3$	$\mathrm{mJ\,g^{-1}\,°C^{-1}}$	1
	$c_\mathrm{p,M}$, $c_\mathrm{p,B}$	$336.51 + 0.4875 \times \tilde{T}$ $-6.16\,\mathrm{e{-}4} \times \tilde{T}^2$ $+ 1.62\,\mathrm{e{-}6} \times \tilde{T}^3$	$\mathrm{mJ\,g^{-1}\,°C^{-1}}$	1
Thermal conductivity	Λ_A	$1.68\,\mathrm{e{-}2} + 1.19\,\mathrm{e{-}5} \times \tilde{T}$	$\mathrm{W\,mm^{-1}\,°C^{-1}}$	1
	Λ_M, Λ_B	$3.93\,\mathrm{e{-}2} + 2.4\,\mathrm{e{-}5} \times \tilde{T}$ $-6.43\,\mathrm{e{-}8} \times \tilde{T}^2$	$\mathrm{W\,mm^{-1}\,°C^{-1}}$	1
Latent heat	$\rho\,\Delta h_{\mathrm{A}\to\mathrm{M}}$	$6.4\,\mathrm{e2}$	$\mathrm{mJ\,mm^{-3}}$	2
	$\rho\,\Delta h_{\mathrm{A}\to\mathrm{B}}$	$1.56\,\mathrm{e3} - 1.5 \times \tilde{T}$	$\mathrm{mJ\,mm^{-3}}$	3

Table 3.8: Optimal parameters $\boldsymbol{p}^*$ for the temperature-dependent JMAK model parameters $b_p(T)$ and $N_p(T)$ in eq. (3.48), based on least squares fit to the TTT–diagram published in Kaymak [93]. *Table reproduced from Furlan et al. [54] under the terms of the CC BY 4.0 license. The text font was updated to match the font of the thesis.*

$p^*_{b,0}$	$p^*_{b,1}$ / $°\mathrm{C^{-1}}$	$p^*_{b,2}$ / $°\mathrm{C^{-2}}$	$p^*_{N,0}$	$p^*_{N,1}$ / $°\mathrm{C^{-1}}$	$p^*_{N,2}$ / $°\mathrm{C^{-2}}$
$-1.8847\,\mathrm{e2}$	$8.1383\,\mathrm{e{-}1}$	$-1.0303\,\mathrm{e{-}3}$	$1.1313\,\mathrm{e1}$	$-4.5363\,\mathrm{e{-}2}$	$5.8965\,\mathrm{e{-}5}$

Table 3.9: Heat transfer coefficient $h^{\mathrm{q}}(T)$ for quenching in water at 20 °C and 60 °C, based on the data published by Gür and Tekkaya [64] and adapted to the unit system used. *Table reproduced from Furlan et al. [54] under the terms of the CC BY 4.0 license. The caption was adapted to specify change of unit system compared to [64]. The text font was updated to match the font of the thesis. A typo in the variable symbols was corrected.*

T / °C	h^{q} / W mm^{-2} °C^{-1}	
	$T_\infty = 20\,°\mathrm{C}$	$T_\infty = 60\,°\mathrm{C}$
0	0.00435	0.0001353
200	0.0082071	0.0020292
400	0.0119617	0.0028409
430	0.0134917	–
445	–	0.0032912
500	0.0125	0.003422
560	0.0102062	–
570	–	0.0026109
600	0.007793	0.002157
700	0.002507	–
800	0.0004371	0.0002302
900	0.0001352	0.0001352

3.5.2 Microstructure evolution under isothermal conditions

[54]qtd. {A homogeneous state of deformation, temperature, and microstructure is considered in three-dimensional simulations of a cube with an edge length of 1 mm. Constant ambient temperature conditions are assumed for this demonstration case, and are implemented either in terms of Dirichlet-type boundary conditions on all temperature degrees of freedom, or as convection boundary conditions on all faces of the cube. The initial temperature as well as the ambient temperature are chosen as 300 °C for this case, and the heat transfer coefficient is assumed to be constant at $h^{\mathrm{q}} = 1\,\mathrm{e}{-4}\,\mathrm{W\,mm^{-2}\,°C^{-1}}$. A fully austenitic initial microstructure is assumed, and no martensite evolution takes place since this temperature is above the martensite start temperature M_{S}. Figure 3.6 shows selected results for a total time span of 500 s.

Given enough time, the model predicts a final microstructure that is nearly 100 % bainitic for 100Cr6, where the implementation of the thermal conditions has a noticeable impact on the transformation rate. The Dirichlet-constraint problem assumes that the latent heat is immediately transported to the surrounding medium, while the retarded transport of heat due to convection leads to a temporary temperature increase of approximately 12 °C during the initial stage of the transformation. Faster transformation times in the elevated temperature regime lead to a faster completion of the bainite transformation when compared to the Dirichlet-constraint problem. As expected, the austenite phase carbon concentration remains constant for 100Cr6.

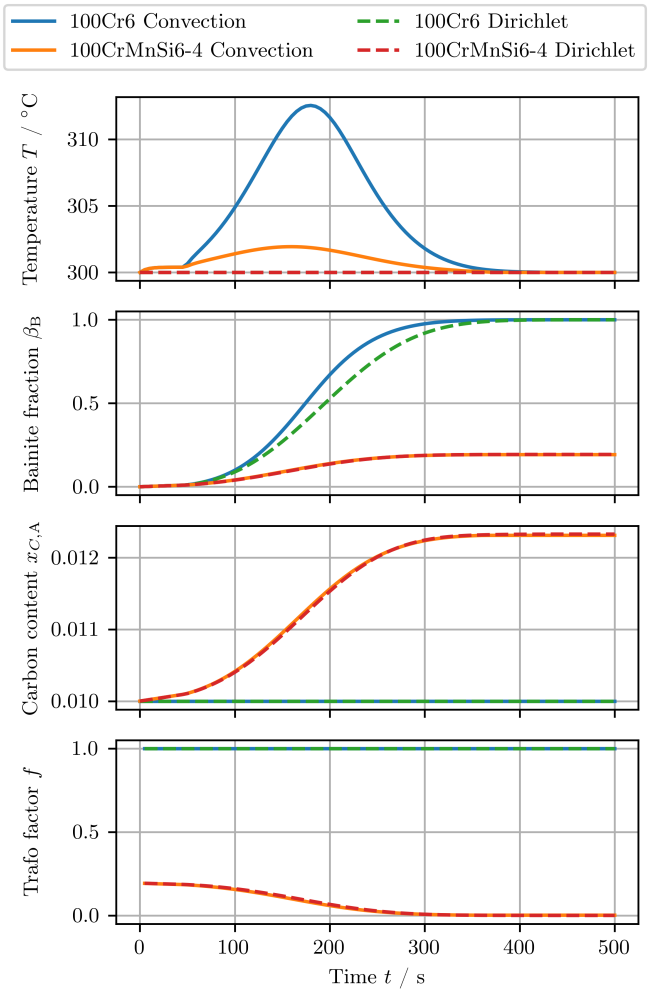

Figure 3.6: Homogeneous evolution of temperature T, bainite volume fraction β_B, austenite phase carbon content $x_{C,A}$, and incomplete bainite transformation function f, under constant ambient temperature of 300 °C. Both implementations of the thermal conditions are shown. *Figure reproduced from Furlan et al. [54] under the terms of the CC BY 4.0 license. No changes were made.*

For 100CrMnSi6-4, the expected austenite phase carbon content after the transformation can be obtained from fig. 3.3 as $x_{C,A} \approx 1.25\,\%$, which is in good accordance with the simulation results. Compared to 100Cr6, the temperature increase in the case of convection boundary conditions is lower at approximately 2 °C, which is in accordance with the lower transformation rates and therefore lower release of latent heat. Due to the small temperature increase, the differences in the evolution of the bainite volume fraction and austenite phase carbon content due to the different implementations of thermal conditions are negligible for 100CrMnSi6-4.}$^{\text{qtd.}}_{[54]}$

3.5.3 Microstructure evolution during homogeneous cooling

qtd. [54]{As in section 3.5.2, a homogeneous state is considered for the cube. From a fully austenitic initial microstructure and an initial temperature of 500 °C, convectional heat transfer with a transfer coefficient of $h^{\mathrm{q}} = 1\,\mathrm{e}{-5}\,\mathrm{W\,mm^{-2}\,°C^{-1}}$ to a surrounding medium at 60 °C is prescribed as the thermal boundary condition. The results for this example are presented in fig. 3.7.}qtd. [54]

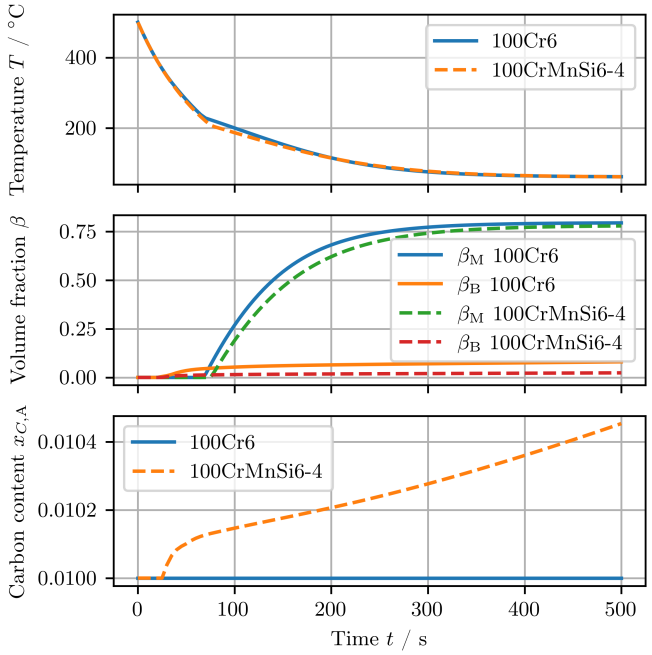

Figure 3.7: Homogeneous evolution of temperature T, bainite volume fraction β_{B}, austenite phase carbon content $x_{\mathrm{C,A}}$, and strain component ε_{11}, during cooling from 500 °C to 60 °C. *Figure reproduced from Furlan et al. [54] under the terms of the CC BY 4.0 license. No changes were made.*

qtd. [54]{Three stages of transformation can be observed in the results: During the initial stage of approximately 20 s, no evolution of the microstructure takes place, until the temperature reaches the bainite start temperature B_{S}. During the second stage, the transformation to bainite begins, while the temperature continues to drop towards the martensite start temperature M_{S}, which is reached at approximately 75 s. The third stage of the transformation is characterised by a simultaneous transformation of austenite to bainite and martensite, with the phase fractions saturating towards the end of the simulation.

A final microstructure of approximately 79.5 % martensite and 8 % bainite is reached in the case of 100Cr6, while for 100CrMnSi6-4 a martensite fraction of 78 % and a bainite fraction of 2.5 % can be observed. In line with the predominant transformation to martensite, the temperature graph does not visibly change at the onset of the bainite transformation after stage one, while a kink can be observed at the beginning of stage

three due to the latent heat release. Although the bainite transformation seems to be nearly complete after the simulation time of 500 s, the austenite phase carbon content $x_{\mathrm{C,A}}$ still evolves at this point in time. However, a longer simulation showed the expected saturation after approximately 5000 s without significant further impact on the final microstructure. This behaviour can be explained by the longer timescale of the bainite transformation at lower temperatures, while only a small amount of austenite remains to transform due to the competing growth of the martensite phase.

The normal strain at each temperature is shown in fig. 3.8. Since no external forces act on the cube, the resulting strain represents the addition of thermal strain and transformation strain. During the transformation-free initial stage, as expected due to the constant heat expansion coefficient, a linear correlation can be observed. The nonlinearity during the second stage, caused by the onset of bainite transformation and the corresponding transformation strain, is barely visible due to the low rate of transformation. However, the transformation strains during the third stage, dominated by the martensite transformation, are large enough to cause an expansion instead of further shrinkage.}$^{\text{qtd.}}_{[54]}$

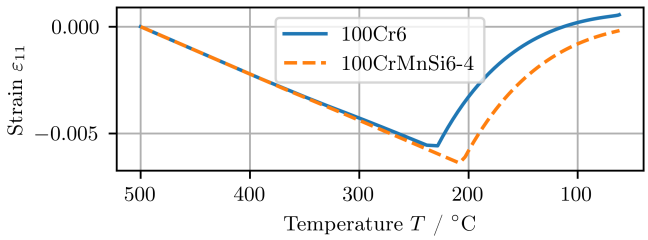

Figure 3.8: Evolution of strain in normal direction during cooling from 500 °C to 60 °C. *Figure reproduced from Furlan et al. [54] under the terms of the CC BY 4.0 license. No changes were made.*

3.5.4 Microstructure evolution during quenching

$^{\text{qtd.}}_{[54]}${The quench hardening of the inner race of a tapered roller bearing is considered as an example for the application of the proposed model to an industrial use case. Bearing components represent a typical application of the materials considered in this work, and the varying cross-section facilitates the development of an inhomogeneous microstructure distribution in the workpiece. While the example problem is of academic nature and has been chosen to demonstrate the capabilities of the proposed model, an effort is made to approximate realistic process conditions based on the literature. Fine-tuning the model parameters to mirror a specific real process and validating the model, e.g. through measurements of temperature curves and microstructure distributions, is beyond the scope of this work due to the required effort.

A rendering of the bearing race is presented along with the cross-section in fig. 3.9. Two element centroids, close to the centre points of the thinnest and thickest sections of the cross-section, are chosen as probing locations, denoted P_1 and P_2.

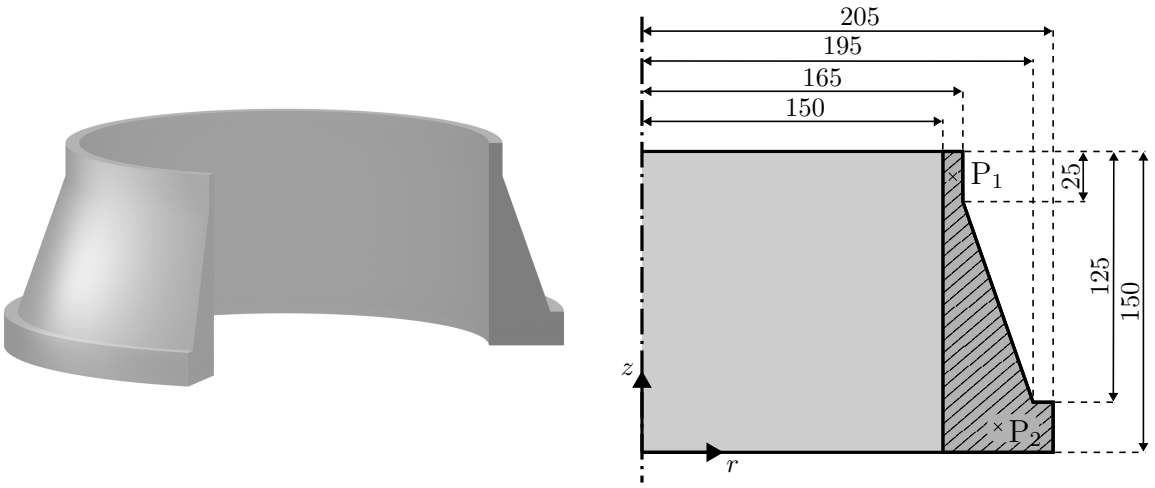

Figure 3.9: Rendering and sketch of the bearing race geometry. The 110° view cut reveals the cross-section, for which all dimensions are given in the sketch in mm. Time history will be shown for the locations marked in the sketch as P_1 and P_2. *Figure reproduced from Furlan et al. [54] under the terms of the CC BY 4.0 license. The composition was slightly altered to show the rendering besides the sketch instead of above it, as well as matching the font of the document.*

For all quenching simulations, a homogeneous initial microstructure of 100 % austenite at an initial temperature of 850 °C is prescribed. Water at either $T_\infty = 20\,°C$ or $T_\infty = 60\,°C$ is considered as the cooling medium, and the temperature-dependent transfer coefficients for convectional heat transfer, as proposed in Gür and Tekkaya [64], are presented in table 3.9. Simulations have been performed for both, 100Cr6 and 100CrMnSi6-4 with both quenching bath temperatures.

Since the workpiece exhibits rotational symmetry, axisymmetric quad elements of type CAX4T are used in Abaqus to reduce the computational cost. Rigid body motions are prevented by constraining displacements of a single node in z-direction. The quenching process is simulated for a total time interval of 11 min, after which the highest temperature in the workpiece deviates from the quenching bath temperature by less than 1.5 °C in all simulations.

Temperature, bainite fraction, martensite fraction and von Mises stresses at the end of the simulations are presented as contour plots over the deformed configuration of the workpiece cross-section in figs. 3.10 to 3.13.

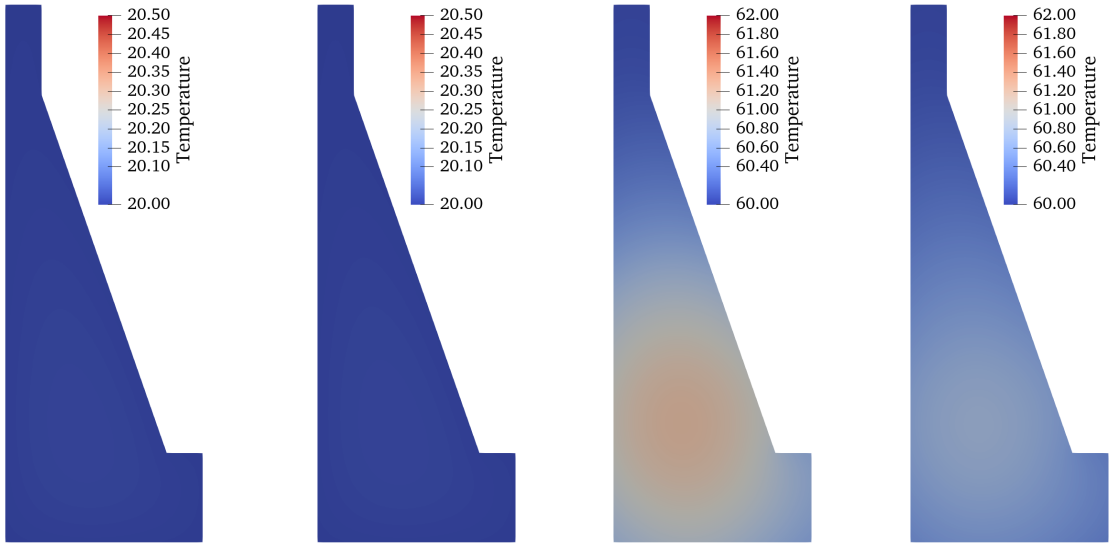

(a) 100Cr6, $T_\infty = 20\,^\circ\mathrm{C}$ **(b)** 100CrMnSi6-4, $T_\infty = 20\,^\circ\mathrm{C}$ **(c)** 100Cr6, $T_\infty = 60\,^\circ\mathrm{C}$ **(d)** 100CrMnSi6-4, $T_\infty = 60\,^\circ\mathrm{C}$

Figure 3.10: Contour plot of temperature distribution at the end of the simulation. *Figure reproduced from Furlan et al. [54] under the terms of the CC BY 4.0 license. The subcaption placement was adapted to the font and page size of this thesis.*

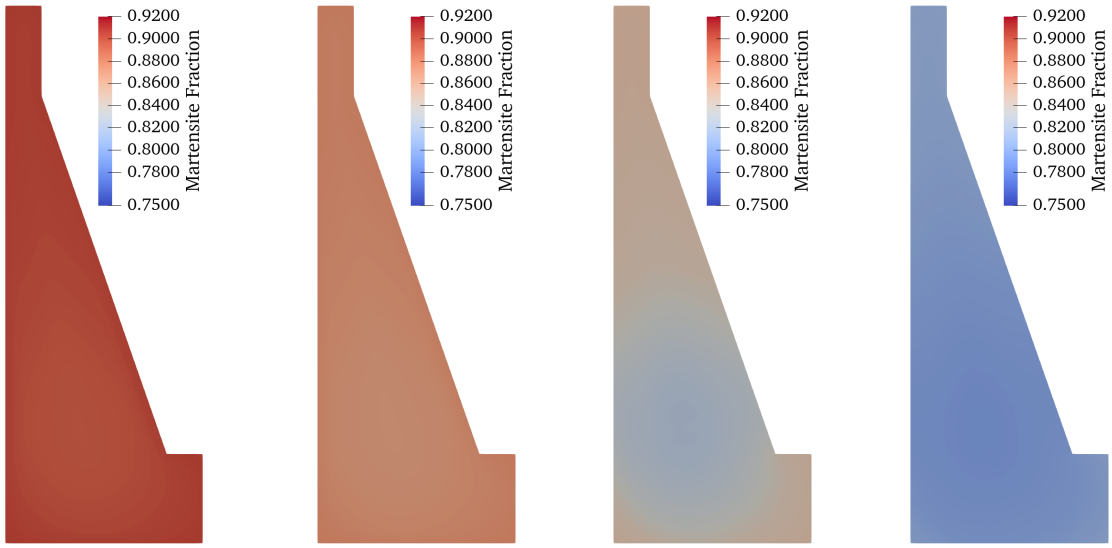

(a) 100Cr6, $T_\infty = 20\,^\circ\mathrm{C}$ **(b)** 100CrMnSi6-4, $T_\infty = 20\,^\circ\mathrm{C}$ **(c)** 100Cr6, $T_\infty = 60\,^\circ\mathrm{C}$ **(d)** 100CrMnSi6-4, $T_\infty = 60\,^\circ\mathrm{C}$

Figure 3.11: Contour plot of the distribution of martensite fraction at the end of the simulation. *Figure reproduced from Furlan et al. [54] under the terms of the CC BY 4.0 license. The subcaption placement was adapted to the font and page size of this thesis.*

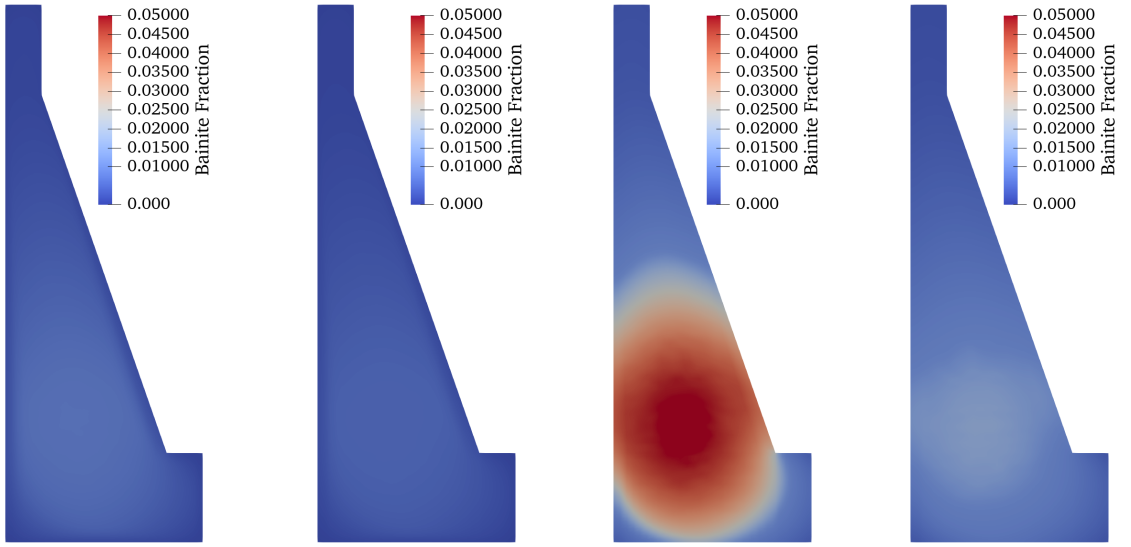

(a) 100Cr6, $T_\infty = 20\,^\circ\mathrm{C}$ **(b)** 100CrMnSi6-4, $T_\infty = 20\,^\circ\mathrm{C}$ **(c)** 100Cr6, $T_\infty = 60\,^\circ\mathrm{C}$ **(d)** 100CrMnSi6-4, $T_\infty = 60\,^\circ\mathrm{C}$

Figure 3.12: Contour plot of the distribution of bainite fraction at the end of the simulation. *Figure reproduced from Furlan et al. [54] under the terms of the CC BY 4.0 license. The subcaption placement was adapted to the font and page size of this thesis.*

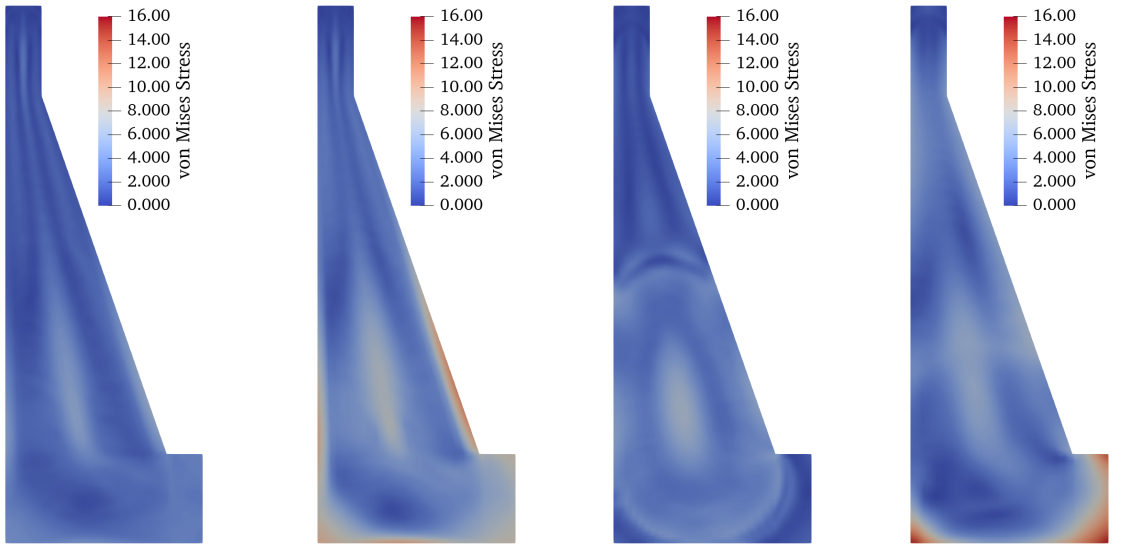

(a) 100Cr6, $T_\infty = 20\,^\circ\mathrm{C}$ **(b)** 100CrMnSi6-4, $T_\infty = 20\,^\circ\mathrm{C}$ **(c)** 100Cr6, $T_\infty = 60\,^\circ\mathrm{C}$ **(d)** 100CrMnSi6-4, $T_\infty = 60\,^\circ\mathrm{C}$

Figure 3.13: Contour plot of von Mises stress distribution at the end of the simulation. *Figure reproduced from Furlan et al. [54] under the terms of the CC BY 4.0 license. The subcaption placement was adapted to the font and page size of this thesis.*

It is clear from fig. 3.10 that the temperature distribution is close to uniform at the end of the simulations. In the case of a quenching bath temperature of $T_\infty = 20\,°C$, the maximum temperature difference in the workpiece is below $0.1\,°C$ for both materials, while the remaining temperature difference for $T_\infty = 60\,°C$ is approximately $1.2\,°C$ for 100Cr6 and $0.7\,°C$ for 100CrMnSi6-4. In all four cases, the warmer part of the workpiece is located towards the centre of gravity of the cross-section.

The variation of the martensite fraction throughout the workpiece is highest for the combination of $T_\infty = 60\,°C$ and 100Cr6 at approximately $4\,\%$. A variation of $1.7\,\%$ is found for $T_\infty = 60\,°C$ and 100CrMnSi6-4, while the variation is below $1\,\%$ for both materials when the quenching bath temperature is chosen as $T_\infty = 20\,°C$. The total value of the martensite fraction lies between approximately $80\,\%$ and $90\,\%$ for all simulations, where larger martensite fractions are achieved at $T_\infty = 20\,°C$. Accordingly, the bainite fraction at the end of the simulation is larger at $T_\infty = 60\,°C$, with approximately $5\,\%$ for 100Cr6 and $1.5\,\%$ for 100CrMnSi6-4, while at $T_\infty = 20\,°C$ the bainite fraction remains below $1\,\%$ for both materials.

The predicted residual stresses reach between approximately 6 MPa and 16 MPa, depending on the material and quenching bath temperature. Although the absolute values are relatively low, the distribution of the stresses within the workpiece is quite inhomogeneous. A typical quality measure for the heat treatment would be the achieved geometrical tolerances, especially of functional surfaces. The radial displacement over the length of the inner bore at the end of the simulation is shown in fig. 3.14 in comparison for all four cases. It should be noted that residual stresses and distortion are presented for demonstration purposes, but, as discussed in section 3.3.2, a model extension to include TRIP effects would be required to generate realistic results.

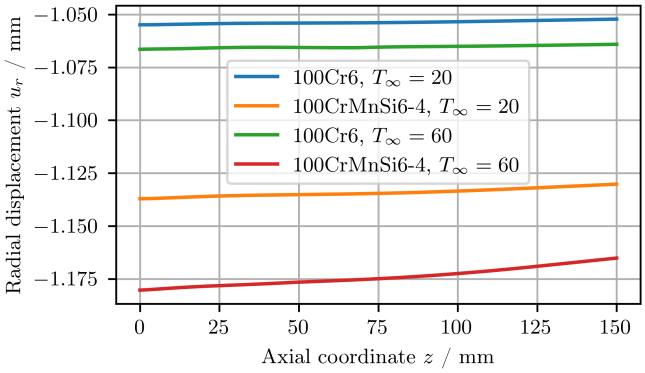

Figure 3.14: Comparison of radial displacements along the inner bore length. *Figure reproduced from Furlan et al. [54] under the terms of the CC BY 4.0 license. No changes were made.*

A slight conical shape of the inner bore can be observed for all four cases. However, lower absolute radial displacements as well as smaller displacement gradients along the

bore length are predicted for 100Cr6 compared to 100CrMnSi6-4. Quenching at $T_\infty = 20\,°C$ yields lower radial displacements than at $T_\infty = 60\,°C$ for both material grades.

The evolution of temperature and microstructure at the two probing points during the first 180 s is shown in figs. 3.15 and 3.16. While a faster cooling can be observed at the lower quenching bath temperature, the material choice has very little impact on the temperature history. At point P_1, a higher cooling rate is achieved compared to point P_2, which is due to the smaller cross-section.

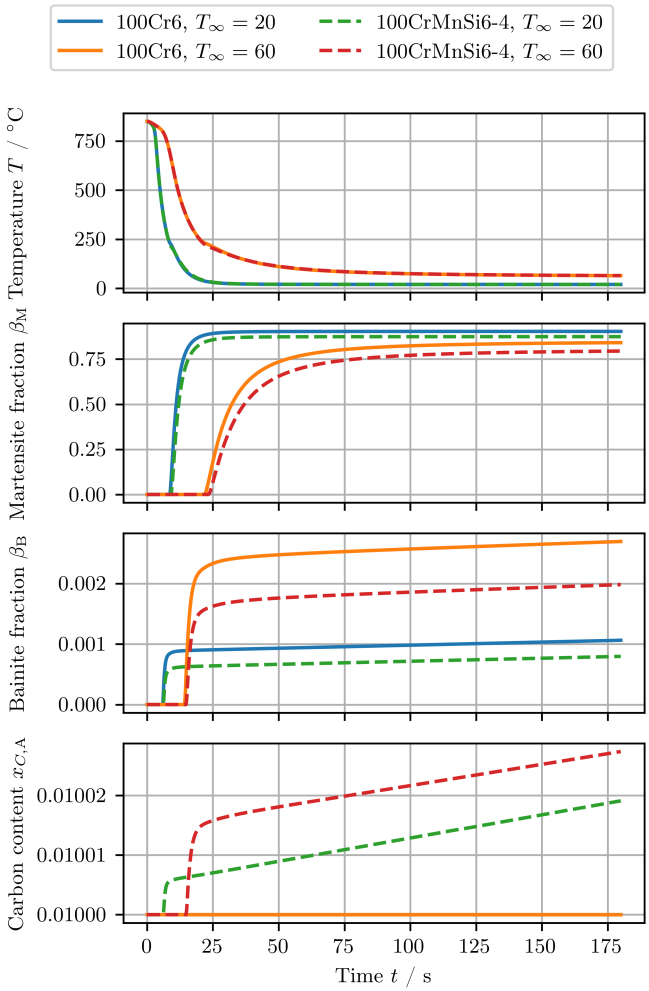

Figure 3.15: Evolution of temperature and microstructure at point P_1 during the first 180 s of the simulations. *Figure reproduced from Furlan et al. [54] under the terms of the CC BY 4.0 license. No changes were made.*

In summary, the proposed model was successfully applied in a finite element simulation of a complex boundary value problem to predict phase transformations, including the interactions of the austenite phase carbon content with the transformation paramet-

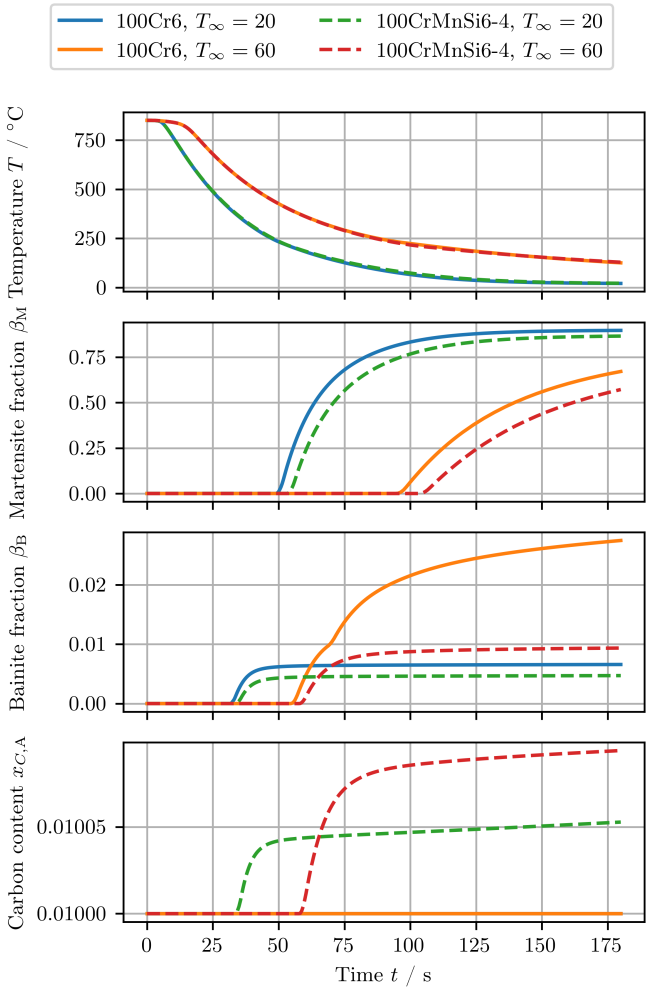

Figure 3.16: Evolution of temperature and microstructure at point P_2 during the first 180 s of the simulations. *Figure reproduced from Furlan et al. [54] under the terms of the CC BY 4.0 license. No changes were made.*

ers. It was possible to determine the impact of the material choice as well as different quenching temperatures on the evolution of the microstructure as well as the resulting geometry after quenching.}$^{\text{qtd.}}_{[54]}$

3.6 Conclusion

qtd. [54] {The model proposed in this work combines the classic phenomenological KM and JMAK phase transformation models with a newly proposed coupling between the austenite phase carbon content and the phase fractions to include the effects of an evolving chemical composition during incomplete formation of carbide-free bainite. An implementation of the model for the finite element software Abaqus, accessible at `https://github.com/InstituteOfMechanics/Phase_Trafos_Carbon_Repartitioning`, was successfully applied to simulate the quench hardening of a bearing component. It was demonstrated that the resulting microstructure can be predicted by the simulation for different process parameters.

A good calibration of all model components is crucial in order to obtain realistic predictions. For the presented examples, the calibration of the model was based on literature values, parameter fitting based on TTT–diagrams, and MatCalc simulations. The results clearly demonstrate that, for the application of the model to real-world problems, a detailed calibration and validation not only of the phase transformation models, but also of the model and boundary conditions for thermal conductance and heat transfer is crucial.

A possible improvement for future work is the application of more advanced models for the martensite and bainite transformations. Furthermore, the incorporation of plasticity and transformation-induced plasticity models is planned, which are considered essential for the prediction of realistic residual stresses and workpiece distortion.} qtd. [54]

4 Simulation of single grain cutting at mesoscopic scale

In this chapter, simulation approaches for the meso-scale cutting during grinding processes are presented. Parts of the research presented here have been published with permission in [53, 159, 160, 184–186], while the thermodynamically consistent material model is proposed in this thesis for the first time.

4.1 Introduction and objectives

Grinding processes are characterised by a large number of cutting edges, multiple of which can be engaged at the same time. In the following section, the cutting edge is usually thought of as part of a crystallographic grain, for example made of corundum or cubic boron nitride (cBN) [1]. However, the bonding material may also come into contact with the workpiece. Grinding is therefore categorised as cutting with geometrically undetermined cutting edges. Each individual cutting edge usually removes only a small amount of material, but does so at high cutting velocities (when compared to processes with geometrically defined cutting edges, such as turning or milling). In the following, this material removal by a single cutting edge will be referred to as cutting at the mesoscopic scale.

In general, any simulation of a grinding process has to account for this undetermined nature of the cutting edges. However, experimental investigations are challenging due to the geometric scale, the high cutting velocities, and the required precision of measurements. Simulations of the mesoscopic cutting process for individual cutting edges therefore provide a valuable tool to improve process understanding.

In the following, different simulation approaches for the mesoscopic cutting are introduced and compared. The commercial finite element software Abaqus [33] was used for all presented finite element simulations. This section therefore mainly focuses on the development and calibration of suitable material models. Furthermore, two different options are discussed to implement a representative boundary value problem for

[1] Depending on the context, the term 'single grain' is used instead of 'cutting edge'.

the engagement of individual grains. Based on these simulations, a surrogate model for the process force contributions of individual grains is presented, which takes the engagement situations and the cutting edge geometry into account. This model will be applied in macroscopic process simulations presented in chapter 5. Bearing steel 100Cr6 is considered as the workpiece material for the presented results. However, the proposed methods are expected to generalise well to other steel grades through recalibration of the underlying material models.

4.2 State of the art

In this section, the material behaviour of bearing steels like the considered grade 100Cr6 is reviewed with a focus on the effects which are expected to take place during (and influence the results of) mesoscopic cutting. Different simulation methods are discussed, with a focus on models for the aforementioned effects and different implementations of the finite element method. Finally, a brief review of experimental procedures to generate calibration data for these models is presented, and some calibration approaches are discussed.

4.2.1 Material behaviour

It is well known that for bearing steels such as 100Cr6 the mechanical properties, especially the flow stress, strongly depend on the temperature, the processing history, as well as the strain rate [16, 78]. However, the experimental characterisation of these properties does not always give insight into the underlying metallurgical and microstructural mechanisms. For 100Cr6, the flow stress generally reduces at elevated temperatures due to increased dislocation mobility [78] and, at higher temperatures, due to dynamic recrystallisation [16]. Since different crystallographic structures offer different levels of resistance to dislocation motions, transformations of ferrite, cementite, or martensite to austenite also reduce the flow stress, and at the same time increase the strain-rate sensitivity [78]. Furthermore, carbide spheroidisation and dissolution can contribute to thermal softening [83]. The increase of flow stress with plastic strain is called strain hardening or work hardening. For single crystals, the resulting flow curve is characterised by three distinctive sections, see e.g. [59]. Initially, dislocations travel comparatively long distances along the primary slide system, and only a small increase of yield strength is caused by a small number of pinned dislocations. A steeper yield curve in the second section is caused by a reduced dislocation mobility due to interactions with secondary slide systems, as well as a general increase of dislocation density, for example through Frank-Read sources. In the third section, the slope of the yield curve reduces, as especially screw dislocations start to circumvent obstacles by changes of the sliding system, and dynamic recovery processes remove some of the obstacles for dislocation movement. Due to the time- and temperature-dependency of these recovery processes,

the flow curve is especially sensitive to both variables in the third section. However, interactions at the interfaces between individual single-crystal grains impose restrictions on the displacements and strains in polycrystals. Therefore, the flow stress observed in experiments with polycrystals is generally considerably higher than for single crystals. In particular, dislocation motion is constrained by grain boundaries, leading to dislocation pileups. Grain refinement, which can be caused by plastic deformation, therefore further constrains the movement of dislocations and increases strength, which is called grain boundary strengthening or Hall-Petch strengthening [67, 139]. Another mechanism for strain hardening is the generation of so-called geometrically necessary dislocations (GNDs), which is caused by inhomogeneous plastic deformation, for example through bending [7]. This brief review does not capture all details of strain hardening, and the reader is referred to [98] for an extensive discussion of the topic.

The hardness of bearing steel components is mainly dictated by the phase composition, especially the amount of martensite, and the microstructure of the material. High local thermal and mechanical loads can influence this microstructure, for example by the decomposition of cementite precipitates [140], and therefore further influence the material properties. Besides hardness, the performance of machined parts, especially resistance to wear and fatigue, is reported to be related to the phase composition of the surface, which can vary due to work hardening and phase transformations under thermal loads generated from inelastic heating and friction [68]. For 100Cr6, the formation of so-called white layers is reported during machining. While the formation of these layers is not completely understood, it is supposedly caused by local grain refinement due to plastic strain at lower strain rates, while phase transformations are reported as the dominant effect for their formation at elevated strain rates and temperatures [143]. Furthermore, different types of white layers exist, which do not always have a detrimental impact on the part performance [95, 171]. A clear positive influence on the fatigue life is reported for compressive residual stress state due to phase transformations during the machining process [68, 171].

The nucleation, growth, and coalescence of voids during loading is often referred to as ductile damage, and can play a crucial role when material fails. While Rice and Tracey [154] found – based on theoretical considerations – that the growth rate of the voids was approximately proportional to a factor which depends exponentially on the triaxiality factor, Bao and Wierzbicki [15] showed for aluminium that this failure occurs at different equivalent plastic strains depending on the average triaxiality during loading, which was attributed to different failure mechanisms. A model for the fracture strain that also includes a dependency on temperature and strain rate was proposed by Johnson and Cook [90]. However, the authors stated that the additional variables had less influence on the fracture strain than pressure. They also proposed an implementation where damage was accumulated based on the fraction of equivalent plastic strain and current fracture strain, introducing a path dependency. In particular, Bao and Wierzbicki [15] identified three distinct fracture branches: Shear fracture at negative triaxialities, fracture due to void growth and coalescence at large positive triaxialities, and a mixture of both at

moderate positive triaxialities. Six different models for the equivalent plastic strain at failure for St12 steel, all similar to the one by Bao and Wierzbicki [15] and based on the idea of three failure branches, were compared by Asadi et al. [6], Hosseinpour et al. [81]. These studies also emphasise the experimental effort for calibration, especially for models with a large number of parameters. More recently, Noell et al. [130] extended this point of view by introducing a total of seven independent mechanisms of ductile rupture.

4.2.2 Calibration of material models

The calibration of material models suitable for mesoscopic cutting of bearing steels presents multiple challenges. In general, the experimental procedures required to capture the calibration data are time-consuming and expensive. Besides classic tension, compression and torsion tests, the split Hopkinson pressure bar (SHPB) test is widely used to capture stress-strain data at high strain rates [125], for example in the seminal work by Johnson and Cook [89]. Although flow curves and models calibrated to these are available for 100Cr6 in multiple publications, they can not always be safely transferred to other applications. For example, the metallurgical state, especially phase composition due to different heat treatments, can significantly alter the mechanical properties of the material. Furthermore, the reported properties are often obtained from tests which do not reproduce the strain state in the application. To tackle these problems, Shatla et al. [164] proposed a cutting-specific calibration procedure for the Johnson-Cook model, based on comparison with an analytical cutting model [136]. This procedure was applied by Ramesh and Melkote [144] to 100Cr6. One of the most comprehensive studies on the mechanical behaviour of 100Cr6 during large deformations was performed by Hor et al. [78]. Therein, compression tests as well as SHPB tests were used to obtain flow curves at various temperatures and strain rates. A special type of specimen was used in the SHPB tests to trigger shear deformation, and therefore include a second deformation mode in the study. Similar specimens made of S355 steel were subjected to extensive characterisation by Jentzsch et al. [87], where digital image correlation was performed to validate simulation results. Additional flow stress data for 100Cr6 at elevated temperatures but at low strain rates was obtained by [16].

Based on tensile tests, Guo and Liu [62] examined the mechanical properties of 100Cr6 at different temperatures. They found that while the material was brittle at room temperature, ductility significantly increased at elevated temperatures, and thermal softening dominated strain hardening at temperatures above 400 °C.

4.2.3 Simulation methods and material modelling

Due to the popularity of steel as a material, a wide variety of material models has been proposed, ranging from purely phenomenological models to very detailed modelling of microstructural effects. For plasticity of metals, the classic yield criterion proposed by

von Mises [194] and further formalised by Hill [73] is still widely used. In this framework, the flow stress is usually expressed as a function of different variables. For example, phenomenological models for strain hardening can be expressed as a dependency of the flow stress on the equivalent plastic strain. Examples include the power law model by Swift [176] and the exponential function based model by Voce [193].

Although various models have been proposed which consider the physical phenomena behind changes in yield stress in more detail, phenomenological models are still widely used for simulations of metal cutting processes. One of the most widely used flow stress models for cutting simulations is the classic Johnson-Cook model [89], which accounts for the dependency of the flow stress on temperature, plastic strain, and plastic strain rate phenomenologically. However, to the best of the author's knowledge, it has not been shown that von Mises plasticity in combination with the Johnson-Cook flow stress is thermodynamically consistent, which is due to the strain rate sensitivity of the yield surface. The same problem holds true for the Zerilli-Armstrong model [203], where a flow stress model similar to the one by Johnson and Cook [89] was introduced, but where the specific form is based on considerations of dislocation mechanics.

An approach to include a rate-dependent material behaviour in a thermodynamically consistent viscoplastic model was introduced by Perzyna [138]. Therein, the strict requirement that the equivalent stress must be smaller or equivalent to the flow stress was relaxed, introducing an overstress. The viscous behaviour of the material was then modelled by coupling the plastic evolution to the overstress. One of the various modifications that have been published based on [138] is the model proposed by Mareau [119], which uses an exponential ansatz for the coupling of the overstress to the evolution of the equivalent plastic strain, and thereby leads to a form that is very similar to the original Johnson-Cook model.

Another class of models including the rate dependency is based on the model by Duvaut and Lions [48], which introduces a relaxation of the stress towards the flow stress. For example, Mahnken et al. [117] combines this approach with a ductile damage model.

Finally, so-called consistency models, introduced by Wang et al. [196], actually introduce a yield surface changing with the strain rate in a thermodynamically consistent manner. A comparison to the Perzyna ansatz is given by Heeres et al. [71].

Various models have been proposed to account for additional physical phenomena of 100Cr6 in cutting applications. For example, Umbrello et al. [189] extended the Johnson-Cook model by a hardness dependency to account for the influence of thermal processing on the machinability of the material. Hardness dependency was included in a consistent material model together with the consideration of martensite-austenite-martensite transformations in Cheng and Mahnken [29], Uhlmann et al. [188], and extended to incorporate the Zerilli-Armstrong model instead of the Johnson-Cook model [30].

In the framework of continuum damage mechanics, material degradation is usually described by a scalar variable and treated as a change of macroscopic material behaviour based on this variable. Microscopic processes, such as void nucleation and growth, as

well as crack initiation, are not considered directly but incorporated into the evolution of the damage variable. A phenomenological approach based on the concept of effective stress and coupling of the damage evolution to the evolution of equivalent plastic strain was proposed by Lemaitre [108], and a comprehensive overview of this approach is given in Lemaitre [109]. For a review of more advanced models, especially incorporating anisotropic damage effects and the introduction of separate yield surfaces for plasticity and damage, the reader is referred to [123, 173] and the references cited therein.

In terms of simulation setup, the simulation of mesoscopic cutting processes during grinding is similar to the simulation of cutting processes with geometrically defined cutting edges, since a deterministic cutting edge shape has to be assumed for each simulation. In general, the large deformations occurring during chip formation and material removal require specialised simulation techniques, since a standard Lagrangian finite element mesh would be deformed during the deformation, leading to the degeneration of elements and therefore to the termination of the analysis. Therefore, if the Lagrangian approach is applied to cutting simulations, the mesh has to be updated during the simulation. The Arbitrary Lagrangian Eulerian (ALE) method [33] keeps the connectivity of the old mesh intact, and updates only the node positions. While this approach is computationally efficient due to the low effort of updating the mesh, it is naturally restricted to moderate to large deformations. In contrast, adaptive remeshing is the process of replacing the current mesh with a new mesh for parts of or the complete simulation domain. Besides the control of mesh distortion, adaptive remeshing can significantly improve performance due to adaptive mesh density.

Since usually no analytical reference solution is known, it can be useful to estimate the error of the finite element solution to adapt the mesh density during remeshing. One widely used estimator was proposed by Zienkiewicz and Zhu [204], where a so-called recovered solution is obtained for quantities such as stress or strain by interpolating integration point values to node points and subsequently using the finite element shape functions to interpolate these values. The recovered field is generally more accurate than the field at the integration points, and is used as a stand-in for the missing reference when judging the accuracy of the finite element solution. In contrast to error estimators, error indicators yield experience-based information on where a finer mesh is required. For example, Diaz et al. [44] introduced an indicator based on the variation of the velocity within each element, which is equivalent to the indicator proposed by Batra and K.-I. Ko [18] if the velocity field is smooth. Other indicators include the maximum difference in effective plastic strains for metal forming [14], plastic work in each element for evolution of slip bands in ductile single crystals [32], and plastic work rate for high-speed machining [122]. Usually, an equidistribution of the error indicator is desired [43]. Due to the numerical effort, data structures for efficient grid generation are a prerequisite for the implementation of adaptive remeshing [115].

The generation of a new mesh is generally followed by a mapping of solution variables from the old mesh to the new one. A procedure for the derivation of consistent transfer operators was derived by Ortiz and Quigley IV [133], and combined with a remeshing

procedure to model the penetration of metallic targets by Camacho and Ortiz [27]. A similar model was applied for two-dimensional simulations of orthogonal cutting by Marusich and Ortiz [122], incorporating full thermo-mechanical coupling and fracture.

Further investigations into the application of adaptive remeshing to cutting simulations were performed by Hortig and Svendsen [80]. Based on [79, 80], a framework for the modelling of the mesoscopic engagement of individual grains in grinding processes was developed [23, 77, 162], and incorporated in a multi-scale simulation system in terms of a surrogate model for the heat generation. Based on the same model, a surrogate model for the process force contributions of individual grains during grinding processes was proposed by Holtermann [76], which is parametrised by undeformed chip thickness and an approximation of the rake angle.

An alternative to adaptive remeshing is the use of the Eulerian finite element method, where by design the elements do not deform, and where the solution variables describe the material motion through the mesh. While the Lagrangian formulation offers more efficient resolution of critical regions, especially when these regions move in space, the Eulerian formulation avoids the need for remeshing even for large deformations. However, the Eulerian description has inherent problems when contact is considered, since the boundaries of a body are not explicitly discretised [4].

The finite element software Abaqus implements the so-called Coupled Eulerian Lagrangian method (CEL), which combines the Eulerian and Lagrangian approaches [33]. Boundaries are interpolated from the volume fraction of material in an Eulerian mesh, and the resulting surfaces are taken into account in the contact algorithm which also includes Lagrangian bodies. This method has been applied to cutting simulations by various researchers by modelling the workpiece material as Eulerian and the cutting edge as a Lagrangian body. For example, CEL was applied to simulations of orthogonal cutting in two dimensions by Bergs et al. [19], Ducobu et al. [45], Peng et al. [137] and in three dimensions by Ducobu et al. [47], and was applied to three-dimensional simulations of milling by Vovk et al. [195]. The option to include multiple material phases in the Eulerian domain of a CEL simulation was used by Klocke et al. [96] to model the influence of a high-pressure cooling medium on the chip formation. $^{\text{qtd.}}_{[53]}\{$CEL-based three-dimensional simulations for single grain cutting experiments were proposed in [198]. However, the model is not directly applicable to internal grinding due to the linear kinematics, and no chip formation was shown.$\}^{\text{qtd.}}_{[53]}$

$^{\text{qtd.}}_{[53]}\{$A comparison of the classic Lagrangian and the Arbitrary Lagrangian Eulerian finite element method, smooth particle hydrodynamics (SPH), and the particle finite element method (PFEM) for the simulation of cutting identified SPH and PFEM as promising alternatives to the classic FE approaches since they maintain better distortion control and element quality under large deformations and include chip separation without techniques such as element deletion [174].$\}^{\text{qtd.}}_{[53]}$ In a comparison study for the cutting of Ti6Al4V, Ducobu et al. [46] found that a CEL based model performed better than the

Lagrangian-based commercial packages Deform and AdvantEdge for the prediction of process forces.

In general, finite element simulations incorporating local damage models suffer from localisation effects and therefore yield mesh-dependent results. This means that damage parameters for such models can only be fitted for a specific mesh. The mesh dependency can be reduced by various methods. A viscous regularisation of the damage evolution can reduce the mesh dependency, but introduces rate-dependency. Non-local approaches, such as gradient enhanced damage, can completely remove the mesh dependency, but incur the cost of solving an additional field equation.

4.3 Constitutive modelling

In this section, multiple material models for 100Cr6 steel are presented. All of the models are formulated for logarithmic strains, which is the default strain measure used by Abaqus for finite strain simulations with explicit time integration. The model presented in section 4.3.1, which was used in Holtermann et al. [74], combines a Johnson-Cook type plasticity with a Lemaitre type damage model. Although this model was successfully applied in simulations of mesoscopic cutting, it cannot be shown to fulfil the second law of thermodynamics. Furthermore, the damage model used is rather basic. Therefore, a thermodynamically consistent viscoplasticity model with similar properties is derived in section 4.3.2.

4.3.1 Johnson-Cook model with damage

This section briefly outlines the material model which was used for all simulations presented by Tsagkir Dereli et al. [185]. The model was not developed by the author of this thesis, but was rather adopted from Holtermann [76], and will be considered as a reference for the newly proposed model in this thesis.

Constitutive model

Based on the elastic logarithmic strain tensor $\boldsymbol{\varepsilon}$, the Cauchy stresses are calculated as

$$\boldsymbol{\sigma} = \mathbf{E} : \varepsilon \ , \tag{4.1}$$

where the fourth-order elasticity tensor $\mathbf{E}$ is calculated based on temperature-dependent values for Young's modulus and Poisson's ratio.

For the inelastic deformation, a model based on standard von Mises plasticity is used. Slightly adapted from the original Johnson-Cook model [89], the flow stress is modelled

based on the temperature T, the equivalent plastic strain $\varepsilon_{\mathrm{p}}^{\mathrm{eq}}$, and the equivalent plastic strain rate $\dot{\varepsilon}_{\mathrm{p}}^{\mathrm{eq}}$ by the equation

$$\sigma_{\mathrm{y}}^{\mathrm{JC}} = \left[A_{\mathrm{JC}} + B_{\mathrm{JC}}\left[1 - \exp\left(-\varepsilon_{\mathrm{p}}^{\mathrm{eq}} N_{\mathrm{JC}}\right)\right]\right]\left[1 + C_{\mathrm{JC}} \ln\left(1 + \frac{\dot{\varepsilon}_{\mathrm{p}}^{\mathrm{eq}}}{\dot{\varepsilon}_{0,\mathrm{JC}}^{\mathrm{p}}}\right)\right]\left[1 - \langle T_{\mathrm{JC}}^{*}\rangle^{M_{\mathrm{JC}}}\right] , \tag{4.2}$$

with the homologous temperature

$$T_{\mathrm{JC}}^{*} = \frac{T - T_{0,\mathrm{JC}}}{T_{\mathrm{m,JC}} - T_{0,\mathrm{JC}}} . \tag{4.3}$$

Therein, the material parameter A_{JC} denotes the static yield stress at reference temperature $T_{0,\mathrm{JC}}$. The hardening term proposed by Johnson and Cook [89] is replaced by an exponential hardening law based on Voce [193], where B_{JC} is the limit value of hardening stress for static conditions, and N_{JC} governs the hardening rate. The rate dependency of the flow stress, also slightly altered with respect to the original Johnson-Cook model to be valid at a plastic strain rate of zero, is controlled by the reference strain rate $\dot{\varepsilon}_{0,\mathrm{JC}}^{\mathrm{p}}$ and the parameter C_{JC}. Finally, the temperature dependency is governed by the melting temperature $T_{\mathrm{m,JC}}$ and the parameter M_{JC}. In the thermal contribution, $\langle\bullet\rangle$ denotes Macaulay brackets.

A local, scalar damage variable

$$d \in [0, 1) \tag{4.4}$$

is introduced to incorporate ductile damage into the material model. The evolution of the damage variable is coupled to the equivalent plastic strain by the equation

$$\dot{d} = \vartheta_{d,JC}\left\langle \varepsilon_{\mathrm{p}}^{\mathrm{eq}} - \varepsilon_{\mathrm{p},0}^{\mathrm{JC}}\right\rangle \left[d - \bar{d}_{\mathrm{JC}}\right] \dot{\varepsilon}_{\mathrm{p}}^{\mathrm{eq}} , \tag{4.5}$$

where $\vartheta_{d,JC}$ is a parameter controlling the rate of damage evolution, $\varepsilon_{\mathrm{p},0}^{\mathrm{JC}}$ is an equivalent plastic strain threshold for the onset of damage evolution, and $\bar{d}_{\mathrm{JC}}$ is a limit value for the damage variable.

The final Cauchy yield stress is the obtained from

$$\sigma_{\mathrm{y}} = [1 - d]\ \sigma_{\mathrm{y}}^{\mathrm{JC}} . \tag{4.6}$$

Within this framework, the elastic properties remain intact during damage evolution.

To the best of the author's knowledge, no proof for the thermodynamic consistency of the Johnson-Cook model is available. Although this raises questions about the physical validity of the model, it is one of the most widely applied phenomenological models for metal plasticity, and was shown to yield accurate results for a wide variety of use cases.

Implementation

Due to the structure of eq. (4.5), for a chosen set of parameters, the value of d can be pre-calculated based on the value of $\varepsilon_{\mathrm{p}}^{\mathrm{eq}}$. It is therefore possible to pre-calculate the value of σ_{y} for given triples $(T, \varepsilon_{\mathrm{p}}^{\mathrm{eq}}, \dot{\varepsilon}_{\mathrm{p}}^{\mathrm{eq}})$. The model is implemented in Abaqus by interpolating the flow stress on such a table, which was kindly provided by Raphael Holtermann based on [76].

4.3.2 Viscoplasticity with local damage

In this section, an improved material model, based on the model presented in section 4.3.1, is derived. To this end, the plasticity framework presented in section 2.1.4 based on de Souza Neto et al. [36] is combined with a thermodynamically consistent ansatz for local damage and viscoplasticity, based on Mareau [119].

Constitutive model

As described in section 2.1.4, the proposed constitutive model is derived by specifying a free energy density $\psi(\boldsymbol{\varepsilon}, T, \boldsymbol{\varepsilon}_{\mathrm{p}}, \boldsymbol{\xi})$ and evolution equations for the internal state variables $\boldsymbol{\xi}$, including the plastic strain tensor $\boldsymbol{\varepsilon}_{\mathrm{p}}$.

Specifically, the set of internal variables is chosen as

$$\boldsymbol{\xi} = \{\boldsymbol{\varepsilon}_{\mathrm{p}}, \alpha, \kappa_{\mathrm{d}}\} \ , \tag{4.7}$$

where

$$\alpha \in [0, \infty) \tag{4.8}$$

is a strain-like variable representing isotropic hardening, and

$$\kappa_{\mathrm{d}} \in [0, 1] \tag{4.9}$$

is a damage variable describing the progress of material failure.

Following Lemaitre [108], continuum damage mechanics can be motivated by the following (hypothetical and simplified) thought experiment. A small control volume of material under load is considered. Initially, the load is distributed equally, and all of the material carries an equal share of the load. At some point, damage starts to initiate, e.g. by nucleation of small voids in the material. Any representative cross-section of the control volume now contains some of the voids, reducing the load-carrying cross-section. The void fraction in the cross section is thought of as the measure of damage, and described by the variable d. Therefore, the remaining fraction of load-carrying material is given by

$$f_{\mathrm{d}} = 1 - d \ . \tag{4.10}$$

This fraction will be referred to as the (damage) integrity in the following. As proposed by Lemaitre [108], the effective Kirchhoff stress is introduced as

$$\boldsymbol{\tau}_{\mathrm{eff}} = \frac{\boldsymbol{\tau}}{f_{\mathrm{d}}} \ . \tag{4.11}$$

If the control volume from the thought experiment macroscopically experiences a given stress $\boldsymbol{\tau}$, the effective stress can be thought of as the stress carried by the remaining undamaged material in the cross-section.

Any damage integrity function satisfying

$$f_{\mathrm{d}}\left(\kappa_{\mathrm{d}}\right) : [0,1] \to [0,1] \ , \quad f'_{\mathrm{d}}\left(\kappa_{\mathrm{d}}\right) < 0 \ \forall \ 0 \leq \kappa_{\mathrm{d}} \leq 1 \tag{4.12}$$

can be used with the proposed framework. In the following, the damage-related integrity is modelled as

$$f_{\mathrm{d}}\left(\kappa_{\mathrm{d}}\right) = 1 - d_{\mathrm{i}} - \left[d_{\mathrm{f}} - d_{\mathrm{i}}\right] \ \kappa_{\mathrm{d}} \ , \tag{4.13}$$

where d_{i} and d_{f} are model parameters. The initial damage is defined by d_{i}, while $1 - d_{\mathrm{f}}$ defines a (numerical) residual stiffness fraction for a failing material.

Free energy density Using the integrity function, the free energy density is chosen as

$$\psi\left(\boldsymbol{\varepsilon}, T, \boldsymbol{\varepsilon}_{\mathrm{p}}, \alpha, \kappa_{\mathrm{d}}\right) = f_{\mathrm{d}}\left(\kappa_{\mathrm{d}}\right) \ \psi_{\mathrm{e}}\left(\boldsymbol{\varepsilon}, \boldsymbol{\varepsilon}_{\mathrm{p}}\right) + \psi_{\mathrm{c}}\left(T\right) + \psi_{\mathrm{p}}\left(\alpha\right) \ , \tag{4.14}$$

where ψ_{e}, ψ_{c} and ψ_{p} refer to the elastic, caloric, and plastic contributions.

It is assumed that the plastic deformation of the material is volume preserving, which motivates the split of the elastic free energy density into volumetric and isochoric parts

$$\psi_{\mathrm{e}}^{(\mathrm{vol})} = \frac{9 \, K_{\mathrm{e}}}{2 \, \rho_0} \, \varepsilon_{\mathrm{m}}^2 \tag{4.15}$$

and

$$\psi_{\mathrm{e}}^{(\mathrm{iso})} = \frac{G_{\mathrm{e}}}{\rho_0} \ \left[\boldsymbol{\varepsilon}^{(\mathrm{iso})} - \boldsymbol{\varepsilon}_{\mathrm{p}}\right] : \left[\boldsymbol{\varepsilon}^{(\mathrm{iso})} - \boldsymbol{\varepsilon}_{\mathrm{p}}\right] \ , \tag{4.16}$$

where K_{e} and G_{e} denote the bulk and shear moduli, and where ε_{m} and $\boldsymbol{\varepsilon}^{(\mathrm{iso})}$ are obtained from the volumetric-deviatoric decomposition (2.15) of the strain tensor. Since the logarithmic strains are used, this simple quadratic form fulfils the physical requirements

$$\psi_{\mathrm{e}} \xrightarrow{J \to 0} \infty \ , \quad \psi_{\mathrm{e}} \xrightarrow{J \to \infty} \infty \ . \tag{4.17}$$

The caloric free energy density is chosen based on the model parameters c_T and T_0 as

$$\psi_\mathrm{c} = c_T \left[T - T_0 - T \, \ln\left(\frac{T}{T_0}\right) \right] \ . \tag{4.18}$$

Based on the classic hardening model by Voce [193] and its implementation within the modified Johnson-Cook model used in section 4.3.1, the plastic free energy density is chosen as

$$\psi_\mathrm{p} = \frac{1}{\rho_0} B_\mathrm{p} \left[\alpha + \frac{1}{n_\mathrm{p}} \left[\exp\left(-n_\mathrm{p} \, \alpha\right) - 1 \right] \right] \ , \tag{4.19}$$

where B_p and n_p are material parameters.

The volumetric and isochoric parts of the Kirchhoff stresses follow from the constitutive relation (2.79) as

$$\boldsymbol{\tau}^\mathrm{vol} = \rho_0 \, f_\mathrm{d} \, \frac{\partial \psi_\mathrm{e}^{(\mathrm{vol})}}{\partial \boldsymbol{\varepsilon}} = 3 \, f_\mathrm{d} \, K_\mathrm{e} \, \varepsilon_\mathrm{m} \, \boldsymbol{I} \ , \tag{4.20}$$

$$\boldsymbol{\tau}^\mathrm{iso} = \rho_0 \, f_\mathrm{d} \, \frac{\partial \psi_\mathrm{e}^{(\mathrm{iso})}}{\partial \boldsymbol{\varepsilon}} = 2 \, f_\mathrm{d} \, G_\mathrm{e} \, \left[\boldsymbol{\varepsilon}^{(\mathrm{iso})} - \boldsymbol{\varepsilon}_\mathrm{p} \right] \ , \tag{4.21}$$

i.e. they are scaled by the integrity function. From eq. (4.11), the effective stresses follow as

$$\boldsymbol{\tau}_\mathrm{eff}^\mathrm{vol} = \frac{\boldsymbol{\tau}^\mathrm{vol}}{f_\mathrm{d}} = \rho_0 \, \frac{\partial \psi_\mathrm{e}^{(\mathrm{vol})}}{\partial \boldsymbol{\varepsilon}} = 3 \, K_\mathrm{e} \, \varepsilon_\mathrm{m} \, \boldsymbol{I} \ , \tag{4.22}$$

$$\boldsymbol{\tau}_\mathrm{eff}^\mathrm{iso} = \frac{\boldsymbol{\tau}^\mathrm{iso}}{f_\mathrm{d}} = \rho_0 \, \frac{\partial \psi_\mathrm{e}^{(\mathrm{iso})}}{\partial \boldsymbol{\varepsilon}} = 2 \, G_\mathrm{e} \, \left[\boldsymbol{\varepsilon}^{(\mathrm{iso})} - \boldsymbol{\varepsilon}_\mathrm{p} \right] \ . \tag{4.23}$$

The entropy density and its rate are given by

$$s = -\frac{\partial \psi}{\partial T} = c_T \, \ln\left(\frac{T}{T_0}\right) \tag{4.24}$$

and

$$\dot{s} = c_T \, \frac{\dot{T}}{T} \ . \tag{4.25}$$

Accordingly, for this model eq. (2.75) can also be stated as

$$\rho_0 \, c_T \, \dot{T} = \mathcal{D}_{0,\mathrm{mech}}^\mathrm{red} + \rho_0 \, r - J \, \mathrm{div}\left(\boldsymbol{q}\right) \tag{4.26}$$

or, in the absence of external heat sources and heat transfer,

$$\rho_0 \, c_T \, \dot{T} = \mathcal{D}_{0,\mathrm{mech}}^\mathrm{red} \ . \tag{4.27}$$

The driving forces for the internal variables, defined in eq. (2.81), follow as

$$\boldsymbol{g}_{\boldsymbol{\varepsilon}_\mathrm{p}} = -\rho_0 \, \frac{\partial \psi}{\partial \boldsymbol{\varepsilon}_\mathrm{p}} = \boldsymbol{\tau}^\mathrm{iso} \ , \tag{4.28}$$

$$g_\alpha = -\rho_0 \, \frac{\partial \psi}{\partial \alpha} = -B_\mathrm{p} \, \left[1 - \exp\left(-n_\mathrm{p} \, \alpha\right)\right] \ , \tag{4.29}$$

$$g_{\kappa_\mathrm{d}} = -\rho_0 \, \frac{\partial \psi}{\partial \kappa_\mathrm{d}} = -\frac{\partial f_\mathrm{d}}{\partial \kappa_\mathrm{d}} \, \rho_0 \, \psi_\mathrm{e} \ , \tag{4.30}$$

where the derivative of the integrity function is given by

$$\frac{\partial f_\mathrm{d}}{\partial \kappa_\mathrm{d}} = -\left[d_\mathrm{f} - d_\mathrm{i}\right] \ . \tag{4.31}$$

Plastic evolution For material under quasi-static loading, the (static) yield stress is modelled by

$$\tau_\mathrm{y} = \left[A_\mathrm{p} - g_\alpha\right] \, f_\mathrm{T} \ , \tag{4.32}$$

where the material parameter A_p describes the initial yield stress at reference temperature, and the thermal integrity function

$$f_\mathrm{T}\left(T\right) : \left[T_{0,\mathrm{abs}}, \infty\right) \to \left[0, \infty\right) \tag{4.33}$$

describes thermal softening as a function of temperature T, where $T_{0,\mathrm{abs}}$ denotes the absolute zero temperature. For example, the temperature term used in the Johnson-Cook model (see eq. (4.2)) can be interpreted as the thermal integrity function

$$f_\mathrm{T} = 1 - \left\langle T^*_\mathrm{JC} \right\rangle^{M_\mathrm{JC}} \ . \tag{4.34}$$

Since the effective stresses describe the stress state in the remaining load-carrying fraction of the material, the yield function is defined as

$$\phi_\mathrm{p} = \tau^\mathrm{eq} - \tau_\mathrm{y} \, f_\mathrm{d} \ , \tag{4.35}$$

where elastic loading is identified by states fulfilling

$$\phi_\mathrm{p} < 0 \ . \tag{4.36}$$

Based on the classic associative format, the evolution equations for the rate of deformation and the rate of the hardening variable are chosen as

$$\tilde{\boldsymbol{d}}_\mathrm{p} = \dot{\lambda}_\mathrm{p} \, \frac{\partial \phi_\mathrm{p}}{\partial \boldsymbol{g}_{\boldsymbol{\varepsilon}_\mathrm{p}}} = \sqrt{\frac{3}{2}} \, \dot{\lambda}_\mathrm{p} \, \boldsymbol{\nu}_\mathrm{p} \ , \quad \boldsymbol{\nu}_\mathrm{p} = \frac{\boldsymbol{\tau}^\mathrm{iso}}{\left\| \boldsymbol{\tau}^\mathrm{iso} \right\|} \ , \tag{4.37}$$

$$\dot{\alpha} = \dot{\lambda}_\mathrm{p} \, \frac{\partial \phi_\mathrm{p}}{\partial g_\alpha} = \dot{\lambda}_\mathrm{p} \, f_\mathrm{T} \, f_\mathrm{d} \ , \tag{4.38}$$

where $\dot{\lambda}_\mathrm{p}$ denotes the plastic multiplier. The equivalent plastic strain rate then reads

$$\dot{\varepsilon}_\mathrm{p}^\mathrm{eq} = \dot{\lambda}_\mathrm{p} \ . \tag{4.39}$$

Similar to the classic viscoplasticity model by Perzyna [138], a viscoplastic flow rule for the plastic multiplier is chosen based on the ansatz proposed by Mareau [119] as

$$\dot{\lambda}_\mathrm{p} = \dot{\varepsilon}_{\mathrm{p},0}^\mathrm{eq} \left[\exp\left(\frac{\langle \phi_\mathrm{p} \rangle}{C_\mathrm{p}\, \tau_\mathrm{y}} \right) - 1 \right] = \exp\left(\frac{\langle \phi_\mathrm{p} \rangle}{C_\mathrm{p}\, \tau_\mathrm{y}} + \ln\left(\dot{\varepsilon}_{\mathrm{p},0}^\mathrm{eq} \right) \right) - \dot{\varepsilon}_{\mathrm{p},0}^\mathrm{eq} \tag{4.40}$$

with material parameters C_p and $\dot{\varepsilon}_{\mathrm{p},0}^\mathrm{eq}$. Rearranging this equation yields the form

$$\langle \phi_\mathrm{p} \rangle = \langle \tau^\mathrm{eq} - \tau_\mathrm{y}\, f_\mathrm{d} \rangle = \tau_\mathrm{y}\, f_\mathrm{d}\, C_\mathrm{p}\, \ln\left(1 + \frac{\dot{\lambda}_\mathrm{p}}{\dot{\varepsilon}_{\mathrm{p},0}^\mathrm{eq}} \right) \ , \tag{4.41}$$

revealing the similarity to the Johnson-Cook model.

In this formulation, the classic loading-unloading conditions are generally not fulfilled, i.e. states with $\phi_\mathrm{p} > 0$ are admissible. This results in a viscous overstress which drives the evolution of the plastic strain.

Damage evolution The remaining component for the model at this point is an evolution equation for the damage variable κ_d. From experimental data, it is well-known that ductile damage is influenced by the temperature T, the equivalent plastic strain rate $\dot{\varepsilon}_\mathrm{p}^\mathrm{eq}$, and the stress triaxiality

$$\eta = \frac{\tau^\mathrm{m}}{\tau^\mathrm{eq}} \ . \tag{4.42}$$

In the proposed model, it is assumed that damage initialises at an equivalent plastic strain $\varepsilon_{\mathrm{p,i}}^\mathrm{eq}\left(\dot{\varepsilon}_\mathrm{p}^\mathrm{eq}, T, \eta\right)$, and failure occurs at another equivalent plastic strain $\varepsilon_{\mathrm{p,f}}^\mathrm{eq}\left(\dot{\varepsilon}_\mathrm{p}^\mathrm{eq}, T, \eta\right)$.

The (linear) progress of plastic straining

$$s_\mathrm{p}\left(\varepsilon_\mathrm{p}^\mathrm{eq}, \dot{\varepsilon}_\mathrm{p}^\mathrm{eq}, T, \eta\right) = \begin{cases} 0 & \varepsilon_\mathrm{p}^\mathrm{eq} \leq \varepsilon_{\mathrm{p,i}}^\mathrm{eq} \\ \left[\varepsilon_\mathrm{p}^\mathrm{eq} - \varepsilon_{\mathrm{p,i}}^\mathrm{eq}\right] / \left[\varepsilon_{\mathrm{p,f}}^\mathrm{eq} - \varepsilon_{\mathrm{p,i}}^\mathrm{eq}\right] & \varepsilon_{\mathrm{p,i}}^\mathrm{eq} \leq \varepsilon_\mathrm{p}^\mathrm{eq} \leq \varepsilon_{\mathrm{p,f}}^\mathrm{eq} \\ 1 & \varepsilon_{\mathrm{p,f}}^\mathrm{eq} < \varepsilon_\mathrm{p}^\mathrm{eq} \end{cases} \tag{4.43}$$

describes the fraction of equivalent plastic strain between damage initiation and failure which would have occurred at constant equivalent plastic strain rate, temperature, and stress triaxiality for the given equivalent plastic strain. It is mapped by an appropriate function $S_\mathrm{d}\left(s_\mathrm{p}\right)$ to a theoretical damage progress $\bar{\kappa}$, i.e.

$$\bar{\kappa}\left(\varepsilon_\mathrm{p}^\mathrm{eq}, \dot{\varepsilon}_\mathrm{p}^\mathrm{eq}, T, \eta\right) = S_\mathrm{d}\left(s_\mathrm{p}\left(\varepsilon_\mathrm{p}^\mathrm{eq}, \dot{\varepsilon}_\mathrm{p}^\mathrm{eq}, T, \eta\right)\right) \ . \tag{4.44}$$

If $S_\mathrm{d}\left(s_\mathrm{p}\right) = s_\mathrm{p}$ is chosen, the theoretical damage evolves linearly with equivalent plastic strain. Other options, such as a smooth step function, can be used to change the shape of the flow curve in the damage regime.

The viscous evolution law

$$\dot{\kappa}_\mathrm{d} = \frac{1}{t_\mathrm{d}} \left\langle \bar{\kappa} - \kappa_\mathrm{d} \right\rangle \ , \tag{4.45}$$

based on relaxation time parameter t_d, is chosen for the damage variable. Similar to the concept of overstress for plasticity, the difference between the theoretical and actual damage values drives the evolution of the damage variable. Therefore, the theoretical damage value is reached only in the limit case. In addition to the ease of implementation, viscous damage evolution is known to reduce the mesh-sensitivity of finite element simulations with local damage models (see e.g. [129, 170]).

The damage model is completed by suitable choices for the model functions $\varepsilon_\mathrm{p,i}^\mathrm{eq}\left(\dot{\varepsilon}_\mathrm{p}^\mathrm{eq}, T, \eta\right)$ and $\varepsilon_\mathrm{p,f}^\mathrm{eq}\left(\dot{\varepsilon}_\mathrm{p}^\mathrm{eq}, T, \eta\right)$.

Thermodynamic consistency For the proposed model, the reduced mechanical dissipation per unit reference volume (eq. (2.82)) reads

$$\mathcal{D}_\mathrm{0,mech}^\mathrm{red} = \boldsymbol{\tau}^\mathrm{iso} : \tilde{\boldsymbol{d}}_\mathrm{p} + g_\alpha \, \dot{\alpha} + g_{\kappa_\mathrm{d}} \, \dot{\kappa}_\mathrm{d} \ . \tag{4.46}$$

Inserting the evolution equations (4.37) and (4.38) yields

$$\begin{aligned} \mathcal{D}_\mathrm{0,mech} &= \sqrt{\frac{3}{2}} \, \dot{\lambda}_\mathrm{p} \, \boldsymbol{\tau}^\mathrm{iso} : \boldsymbol{\nu}_\mathrm{p} + g_\alpha \, \dot{\lambda}_\mathrm{p} \, f_\mathrm{T} \, f_\mathrm{d} + g_{\kappa_\mathrm{d}} \, \dot{\kappa}_\mathrm{d} \\ &= \left[\tau^\mathrm{eq} + g_\alpha \, f_\mathrm{T} \, f_\mathrm{d}\right] \, \dot{\lambda}_\mathrm{p} + g_{\kappa_\mathrm{d}} \, \dot{\kappa}_\mathrm{d} \\ &= \left[\phi_\mathrm{p} + A_\mathrm{p} \, f_\mathrm{T} \, f_\mathrm{d}\right] \, \dot{\lambda}_\mathrm{p} + g_{\kappa_\mathrm{d}} \, \dot{\kappa}_\mathrm{d} \ . \end{aligned} \tag{4.47}$$

The viscous ansatz functions eqs. (4.41) and (4.45) guarantee non-negative $\dot{\alpha}$ and $\dot{\kappa}_\mathrm{d}$. As long as the damage integrity function f_d satisfies condition (4.12), the last term of eq. (4.47) is non-negative (see eq. (4.30)). It is clear from eq. (4.31) that this is the case for the presented model if $\varepsilon_\mathrm{p,f}^\mathrm{eq} > \varepsilon_\mathrm{p,i}^\mathrm{eq}$ holds. Since either $\phi_\mathrm{p} > 0$ or $\dot{\lambda}_\mathrm{p} = 0$ holds, the first term is also non-negative. Therefore, the mechanical dissipation is shown to be non-negative, and the second law of thermodynamics – given by eq. (2.84) – is fulfilled by the proposed model.

Implementation

The proposed material model was implemented in the commercial finite elements package Abaqus in terms of the Fortran user subroutine VUMAT, which can be used with the explicit time integration procedures, including the Coupled Eulerian Lagrangian approach. Since the balance equations are integrated explicitly to obtain the unknown nodal values of displacements $\boldsymbol{u}$ and temperature T, no material tangent is required.

The VUMAT subroutine defines the update of the stresses, internal variables, and energy contributions during a discrete time increment Δt from ${}^{(\mathrm{n})}t$ to ${}^{(\mathrm{n+1})}t$, where the left-hand superscripts will be used to denote quantities belonging to the respective time values. All quantities at the beginning of the increment are known, especially ${}^{(\mathrm{n})}\boldsymbol{\varepsilon}$, ${}^{(\mathrm{n})}T$, ${}^{(\mathrm{n})}\boldsymbol{\varepsilon}_\mathrm{p}$, ${}^{(\mathrm{n})}\alpha$, ${}^{(\mathrm{n})}\kappa_\mathrm{d}$, and ${}^{(\mathrm{n})}\boldsymbol{\sigma}$. In addition, the strain ${}^{(\mathrm{n+1})}\boldsymbol{\varepsilon}$ and temperature ${}^{(\mathrm{n+1})}T$ at the end of the increment are known from the explicit global time integration. Based on these quantities, the VUMAT subroutine computes the updated values ${}^{(\mathrm{n+1})}\boldsymbol{\varepsilon}_\mathrm{p}$, ${}^{(\mathrm{n+1})}\alpha$, and ${}^{(\mathrm{n+1})}\kappa_\mathrm{d}$ of the internal variables, as well as the corresponding Cauchy stress ${}^{(\mathrm{n+1})}\boldsymbol{\sigma}$. In the following, the notation $\Delta(\bullet) = {}^{(\mathrm{n+1})}(\bullet) - {}^{(\mathrm{n})}(\bullet)$ is used for the increment of any quantity $(\bullet)$.

The time integration scheme used in Abaqus for explicit procedures is based on a corotational frame, decoupling rigid body motions of the element from the constitutive equations. By stating the constitutive equations in the coordinate system of the strain tensor, this rotation is implicitly accounted for by the proposed implementation.

In the following, an efficient algorithm for the time integration of the evolution equations is presented. The structure of the global integration scheme, specifically the fact that ${}^{(\mathrm{n+1})}\boldsymbol{\varepsilon}$ and ${}^{(\mathrm{n+1})}T$ are known a priori, is exploited to reduce the nonlinear system of evolution equations to a single scalar equation for the determination of the plastic multiplier $\dot{\lambda}_\mathrm{p}$. Based on the solution for $\dot{\lambda}_\mathrm{p}$, all other quantities can be explicitly updated.

Integration of temperature Two options are available in Abaqus to implement the thermal material behaviour for the presented model. The most flexible option is the implementation of a second Fortran user subroutine (VUMATHT). Alternatively, built-in models for heat flux and thermal storage can be combined with the VUMAT user subroutine by coupling the temperature increase (neglecting heat flow and additional heat sources) to the inelastic work as

$$c\,\dot{T} = \beta^{\mathrm{TQ}}\,\mathcal{P}^{\mathrm{inelas}}\,, \tag{4.48}$$

where β^{TQ} denotes the empirical Taylor-Quinney factor, c is the specific heat capacity, and $\mathcal{P}^{\mathrm{inelas}}$ is a specific heat source representing the heat generated by inelastic deformation (which the VUMAT subroutine then has to calculate), and which is integrated into the inelastic energy $\mathcal{I}^{\mathrm{inelas}}$

From the comparison of eq. (4.48) and eq. (4.27), and recognising that

$$\mathcal{P}^{\mathrm{inelas}} = \frac{1}{\rho_0}\,\mathcal{D}^{\mathrm{red}}_{0,\mathrm{mech}} \tag{4.49}$$

it is evident that, if $c_T = c$ and $\beta^{\mathrm{TQ}} = 1$, this approach is consistent with the presented model. The implementation of a VUMATHT subroutine is therefore not necessary. The Taylor-Quinney factor is included in the model as a phenomenological fitting coefficient to account for stored energy due to microstructural changes, which is therefore not converted to heat. Energy storage due to hardening is however already included in the

model and reduces the dissipation, which should be taken into account when choosing the value for β^{TQ}.

Time-discrete evolution equations An exponential map is applied for the time integration of the evolution equation (4.37) for the plastic strain. It was shown by de Souza Neto et al. [36] that this approach yields an update of the type

$$ {}^{(\mathrm{n+1})}\boldsymbol{\varepsilon}_{\mathrm{e}} = {}^{(\mathrm{tr})}\boldsymbol{\varepsilon}_{\mathrm{e}} - \dot{\lambda}_{\mathrm{p}}\,\Delta t\,{}^{(\mathrm{n+1})}\left[\frac{\partial \phi_{\mathrm{p}}}{\partial \boldsymbol{\tau}}\right] , \tag{4.50} $$

where the elastic trial strain ${}^{(\mathrm{tr})}\boldsymbol{\varepsilon}_{\mathrm{e}}$ assumes that plastic deformation remains constant within the increment. Under the assumptions of the presented model, especially the additive decomposition (2.85) of the logarithmic strain tensor, the time-discrete update for the plastic strain tensor can then be obtained as

$$ \Delta\boldsymbol{\varepsilon}_{\mathrm{p}} = \dot{\lambda}_{\mathrm{p}}\,\Delta t\,{}^{(\mathrm{n+1})}\left[\frac{\partial \phi_{\mathrm{p}}}{\partial \boldsymbol{\tau}}\right] = \sqrt{\frac{3}{2}}\,\dot{\lambda}_{\mathrm{p}}\,\Delta t\;{}^{(\mathrm{n+1})}\boldsymbol{\nu}_{\mathrm{p}} . \tag{4.51} $$

It is remarked that this integration algorithm fulfils plastic incompressibility, since the increment of plastic strain is deviatoric, see eq. (2.18).

The remaining (scalar) evolution equations (4.38), (4.39) and (4.45) are integrated by an implicit Euler scheme, resulting in the updates

$$ \Delta\varepsilon_{\mathrm{p}}^{\mathrm{eq}} = \dot{\lambda}_{\mathrm{p}}\,\Delta t , \tag{4.52} $$

$$ \Delta\alpha = f_{\mathrm{T}}\left({}^{(\mathrm{n+1})}T\right)\,f_{\mathrm{d}}\left({}^{(\mathrm{n+1})}\kappa_{\mathrm{d}}\right)\,\dot{\lambda}_{\mathrm{p}}\,\Delta t , \tag{4.53} $$

$$ \Delta\kappa_{\mathrm{d}} = \frac{\Delta t}{t_{\mathrm{d}}}\left\langle {}^{(\mathrm{n+1})}\bar{\kappa} - {}^{(\mathrm{n+1})}\kappa_{\mathrm{d}}\right\rangle . \tag{4.54} $$

From the expansion

$$ \frac{\Delta t}{t_{\mathrm{d}}}\left\langle {}^{(\mathrm{n+1})}\bar{\kappa} - {}^{(\mathrm{n})}\kappa_{\mathrm{d}} - \Delta\kappa_{\mathrm{d}}\right\rangle \tag{4.55} $$

of eq. (4.54), it is evident that

$$ \Delta\kappa_{\mathrm{d}} = 0 \quad \Leftrightarrow \quad \left\langle {}^{(\mathrm{n+1})}\bar{\kappa} - {}^{(\mathrm{n})}\kappa_{\mathrm{d}}\right\rangle = 0 \tag{4.56} $$

holds. Therefore, eq. (4.54) can be restated as

$$ \Delta\kappa_{\mathrm{d}} = \frac{\Delta t}{\Delta t + t_{\mathrm{d}}}\left\langle {}^{(\mathrm{n+1})}\bar{\kappa} - {}^{(\mathrm{n})}\kappa_{\mathrm{d}}\right\rangle . \tag{4.57} $$

The update is completed by the time-discrete version

$$ \left\langle {}^{(\mathrm{n+1})}\tau^{\mathrm{eq}} - {}^{(\mathrm{n+1})}\tau_{\mathrm{y}}\;{}^{(\mathrm{n+1})}f_{\mathrm{d}}\right\rangle = {}^{(\mathrm{n+1})}\tau_{\mathrm{y}}\;{}^{(\mathrm{n+1})}f_{\mathrm{d}}\,C_{\mathrm{p}}\,\ln\left(1 + \frac{\dot{\lambda}_{\mathrm{p}}}{\dot{\varepsilon}_{\mathrm{p,0}}^{\mathrm{eq}}}\right) \tag{4.58} $$

of the viscoplastic flow rule (4.41), yielding a coupled system of nonlinear equations.

Elastic trial step An elastic trial step is performed under the assumption that no evolution of plasticity takes place. Due to the explicit time integration, the volumetric and isochoric strains can directly be computed as

$$ {}^{(\mathrm{n}+1)}\boldsymbol{\varepsilon}^{(\mathrm{vol})} = {}^{(\mathrm{n}+1)}\varepsilon_{\mathrm{m}}\,\boldsymbol{I}\ , \quad {}^{(\mathrm{n}+1)}\varepsilon_{\mathrm{m}} = \frac{1}{3}\,\mathrm{tr}\left({}^{(\mathrm{n}+1)}\boldsymbol{\varepsilon}\right)\ , \tag{4.59} $$

$$ {}^{(\mathrm{n}+1)}\boldsymbol{\varepsilon}^{(\mathrm{iso})} = {}^{(\mathrm{n}+1)}\boldsymbol{\varepsilon} - {}^{(\mathrm{n}+1)}\boldsymbol{\varepsilon}^{(\mathrm{vol})}\ . \tag{4.60} $$

Following eq. (2.18) the determinant of the deformation gradient is obtained from

$$ {}^{(\mathrm{n}+1)}J = \exp\left(3\ {}^{(\mathrm{n}+1)}\varepsilon_{\mathrm{m}}\right)\ . \tag{4.61} $$

The volumetric part of the effective strain does not depend on internal variables, and can therefore directly be computed as

$$ {}^{(\mathrm{n}+1)}\boldsymbol{\tau}_{\mathrm{eff}}^{\mathrm{vol}} = {}^{(\mathrm{n}+1)}\tau_{\mathrm{eff}}^{\mathrm{m}}\,\boldsymbol{I}\ , \quad {}^{(\mathrm{n}+1)}\tau_{\mathrm{eff}}^{\mathrm{m}} = 3\,K_{\mathrm{e}}\ {}^{(\mathrm{n}+1)}\varepsilon_{\mathrm{m}}\ . \tag{4.62} $$

Since no plastic evolution is assumed in the trial step, the isochoric part of the effective trial stress reads

$$ {}^{(\mathrm{tr})}\boldsymbol{\tau}_{\mathrm{eff}}^{\mathrm{iso}} = 2\,G_{\mathrm{e}}\left[{}^{(\mathrm{n}+1)}\boldsymbol{\varepsilon}^{(\mathrm{iso})} - {}^{(\mathrm{n})}\boldsymbol{\varepsilon}_{\mathrm{p}}\right]\ , \tag{4.63} $$

and the corresponding equivalent trial stress is given by

$$ {}^{(\mathrm{tr})}\tau_{\mathrm{eff}}^{\mathrm{eq}} = \sqrt{\frac{3}{2}}\left\|{}^{(\mathrm{tr})}\boldsymbol{\tau}_{\mathrm{eff}}^{\mathrm{iso}}\right\|\ . \tag{4.64} $$

With the same assumption, the trial yield stress is computed as

$$ {}^{(\mathrm{tr})}\tau_{\mathrm{y}} = \tau_{\mathrm{y}}\left({}^{(\mathrm{n})}\alpha\right)\ . \tag{4.65} $$

Even for an elastic step, the viscous damage evolution allows for evolving damage. Assuming all other internal variables are frozen, the damage variable evolves according to

$$ {}^{(\mathrm{tr})}\kappa_{\mathrm{d}} = {}^{(\mathrm{n})}\kappa_{\mathrm{d}} + \frac{\Delta t}{\Delta t + t_{\mathrm{d}}}\left\langle \bar{\kappa}\left(\dot{\varepsilon}_{\mathrm{p}}^{\mathrm{eq}} = 0, {}^{(\mathrm{n})}\varepsilon_{\mathrm{p}}^{\mathrm{eq}}, {}^{(\mathrm{n}+1)}T, {}^{(\mathrm{n})}\eta\right) - {}^{(\mathrm{n})}\kappa_{\mathrm{d}}\right\rangle\ . \tag{4.66} $$

Based on eq. (4.35), if the condition

$$ {}^{(\mathrm{tr})}\phi_{\mathrm{p}} = {}^{(\mathrm{tr})}\tau^{\mathrm{eq}} - {}^{(\mathrm{tr})}\tau_{\mathrm{y}}\,f_{\mathrm{d}}\left({}^{(\mathrm{tr})}\kappa_{\mathrm{d}}\right) \leq 0 \tag{4.67} $$

holds, $\dot{\lambda}_{\mathrm{p}} = 0$ holds, and the step is elastic. If ${}^{(\mathrm{tr})}\phi_{\mathrm{p}} > 0$, eq. (4.41) is solved for $\dot{\lambda}_{\mathrm{p}}$ in the corrector step described below.

Corrector step The updated isochoric part of the Kirchhoff stress can be expressed as

$$ {}^{(\mathrm{n}+1)}\boldsymbol{\tau}_{\mathrm{eff}}^{\mathrm{iso}} = 2\,G_{\mathrm{e}} \left[{}^{(\mathrm{n}+1)}\boldsymbol{\varepsilon}^{(\mathrm{iso})} - {}^{(\mathrm{n})}\boldsymbol{\varepsilon}_{\mathrm{p}} - \Delta\boldsymbol{\varepsilon}_{\mathrm{p}} \right] , \tag{4.68} $$

which – using eqs. (4.51) and (4.63) – is restated as

$$ {}^{(\mathrm{n}+1)}\boldsymbol{\tau}_{\mathrm{eff}}^{\mathrm{iso}} = {}^{(\mathrm{tr})}\boldsymbol{\tau}_{\mathrm{eff}}^{\mathrm{iso}} - 2\,G_{\mathrm{e}} \sqrt{\frac{3}{2}}\,\dot{\lambda}_{\mathrm{p}}\,\Delta t\,\frac{{}^{(\mathrm{n}+1)}\boldsymbol{\tau}_{\mathrm{eff}}^{\mathrm{iso}}}{\left\| {}^{(\mathrm{n}+1)}\boldsymbol{\tau}_{\mathrm{eff}}^{\mathrm{iso}} \right\|} . \tag{4.69} $$

Expressing every tensor by its amplitude and direction yields

$$ \tau_{\mathrm{eff}\,n+1}^{\mathrm{eq}}\,\frac{\boldsymbol{\tau}_{\mathrm{eff}\;n+1}^{\mathrm{iso}}}{\left\|\boldsymbol{\tau}_{\mathrm{eff}\;n+1}^{\mathrm{iso}}\right\|} = \tau_{\mathrm{eff}\,\mathrm{tr}}^{\mathrm{eq}}\,\frac{\boldsymbol{\tau}_{\mathrm{eff}\;\mathrm{tr}}^{\mathrm{iso}}}{\left\|\boldsymbol{\tau}_{\mathrm{eff}\;\mathrm{tr}}^{\mathrm{iso}}\right\|} - 3\,G_{\mathrm{e}}\,\dot{\lambda}_{\mathrm{p}}\,\Delta t\,\frac{\boldsymbol{\tau}_{\mathrm{eff}\;n+1}^{\mathrm{iso}}}{\left\|\boldsymbol{\tau}_{\mathrm{eff}\;n+1}^{\mathrm{iso}}\right\|} , \tag{4.70} $$

or, separately for directions and amplitudes,

$$ \boldsymbol{\nu}_{\mathrm{p}\,n+1} = \frac{\boldsymbol{\tau}_{\mathrm{eff}\;n+1}^{\mathrm{iso}}}{\left\|\boldsymbol{\tau}_{\mathrm{eff}\;n+1}^{\mathrm{iso}}\right\|} = \frac{\boldsymbol{\tau}_{\mathrm{eff}\;\mathrm{tr}}^{\mathrm{iso}}}{\left\|\boldsymbol{\tau}_{\mathrm{eff}\;\mathrm{tr}}^{\mathrm{iso}}\right\|} = \frac{{\boldsymbol{\varepsilon}^{(\mathrm{iso})}}_{n+1} - \boldsymbol{\varepsilon}_{\mathrm{p}\,n}}{\left\|{\boldsymbol{\varepsilon}^{(\mathrm{iso})}}_{n+1} - \boldsymbol{\varepsilon}_{\mathrm{p}\,n}\right\|} \tag{4.71} $$

and

$$ \tau_{\mathrm{eff}\,n+1}^{\mathrm{eq}} = \tau_{\mathrm{eff}\,\mathrm{tr}}^{\mathrm{eq}} - 3\,G_{\mathrm{e}}\,\dot{\lambda}_{\mathrm{p}}\,\Delta t . \tag{4.72} $$

Since the stresses and effective stresses are coaxial, the plastic flow direction ${}^{(\mathrm{n}+1)}\boldsymbol{\nu}_{\mathrm{p}}$ is completely determined by the trial step, and the equivalent effective stress ${}^{(\mathrm{n}+1)}\tau_{\mathrm{eff}}^{\mathrm{eq}}$ depends only on the plastic multiplier $\dot{\lambda}_{\mathrm{p}}$.

Based on eq. (4.52), the equivalent plastic strain rate

$$ {}^{(\mathrm{n}+1)}\dot{\varepsilon}_{\mathrm{p}}^{\mathrm{eq}} = \dot{\lambda}_{\mathrm{p}} \tag{4.73} $$

and equivalent plastic strain

$$ {}^{(\mathrm{n}+1)}\varepsilon_{\mathrm{p}}^{\mathrm{eq}} = {}^{(\mathrm{n})}\varepsilon_{\mathrm{p}}^{\mathrm{eq}} + \dot{\lambda}_{\mathrm{p}}\,\Delta t \tag{4.74} $$

are also expressed as a function of only the plastic multiplier.

By expressing the stress triaxiality in the effective stress space as

$$ {}^{(\mathrm{n}+1)}\eta = \frac{{}^{(\mathrm{n}+1)}\tau^{\mathrm{m}}}{{}^{(\mathrm{n}+1)}\tau^{\mathrm{eq}}} = \frac{{}^{(\mathrm{n}+1)}\tau_{\mathrm{eff}}^{\mathrm{m}}}{{}^{(\mathrm{n}+1)}\tau_{\mathrm{eff}}^{\mathrm{eq}}} , \tag{4.75} $$

and recognising the dependency structure

$$ {}^{(\mathrm{n}+1)}\varepsilon_{\mathrm{p,i}}^{\mathrm{eq}} = \varepsilon_{\mathrm{p,i}}^{\mathrm{eq}} \left({}^{(\mathrm{n}+1)}\dot{\varepsilon}_{\mathrm{p}}^{\mathrm{eq}}, {}^{(\mathrm{n}+1)}T, {}^{(\mathrm{n}+1)}\eta \right) , \tag{4.76} $$

$$ {}^{(\mathrm{n}+1)}\varepsilon_{\mathrm{p,f}}^{\mathrm{eq}} = \varepsilon_{\mathrm{p,f}}^{\mathrm{eq}} \left({}^{(\mathrm{n}+1)}\dot{\varepsilon}_{\mathrm{p}}^{\mathrm{eq}}, {}^{(\mathrm{n}+1)}T, {}^{(\mathrm{n}+1)}\eta \right) , \tag{4.77} $$

the theoretical damage progress can be expressed by a reduced function $\bar{\kappa}^{\mathrm{red}}$ as

$$
\begin{aligned}
{}^{(\mathrm{n}+1)}\bar{\kappa} &= \bar{\kappa}\left({}^{(\mathrm{n}+1)}\dot{\varepsilon}_{\mathrm{p}}^{\mathrm{eq}}(\dot{\lambda}_{\mathrm{p}}), {}^{(\mathrm{n}+1)}\varepsilon_{\mathrm{p}}^{\mathrm{eq}}(\dot{\lambda}_{\mathrm{p}}), {}^{(\mathrm{n}+1)}T, {}^{(\mathrm{n}+1)}\eta(\dot{\lambda}_{\mathrm{p}})\right) && (4.78)\\
&= \bar{\kappa}^{\mathrm{red}}\big({}^{(\mathrm{n}+1)}T, \dot{\lambda}_{\mathrm{p}}\big) \ . && (4.79)
\end{aligned}
$$

The discrete update (4.57) of the damage variable then reads

$${}^{(\mathrm{n}+1)}\kappa_{\mathrm{d}} = {}^{(\mathrm{n})}\kappa_{\mathrm{d}} + \frac{\Delta t}{\Delta t + t_{\mathrm{d}}}\left\langle {}^{(\mathrm{n}+1)}\bar{\kappa} - {}^{(\mathrm{n})}\kappa_{\mathrm{d}}\right\rangle \ , \tag{4.80}$$

and – taking into account that the updated temperature ${}^{(\mathrm{n}+1)}T$ is known – is dependent solely on $\dot{\lambda}_{\mathrm{p}}$. Finally, the update of the hardening variable given by eq. (4.53) can be expressed by the reduced function α^{red} as

$$
\begin{aligned}
{}^{(\mathrm{n}+1)}\alpha &= {}^{(\mathrm{n})}\alpha + f_{\mathrm{T}}\left({}^{(\mathrm{n}+1)}T\right)\ f_{\mathrm{d}}\left({}^{(\mathrm{n}+1)}\kappa_{\mathrm{d}}\right)\ \dot{\lambda}_{\mathrm{p}}\,\Delta t && (4.81)\\
&= \alpha^{\mathrm{red}}\big({}^{(\mathrm{n}+1)}T, \dot{\lambda}_{\mathrm{p}}\big) \ . && (4.82)
\end{aligned}
$$

Since the static yield stress – see eq. (4.32) – is given by

$${}^{(\mathrm{n}+1)}\tau_{\mathrm{y}} = \left[A_{\mathrm{p}} - g_{\alpha}\left(\alpha^{\mathrm{red}}\big({}^{(\mathrm{n}+1)}T, \dot{\lambda}_{\mathrm{p}}\big)\right)\right]\ f_{\mathrm{T}}\left({}^{(\mathrm{n}+1)}T\right) \ , \tag{4.83}$$

the viscoplastic flow rule can be expressed as the nonlinear, scalar residual equation

$$R\left(\dot{\lambda}_{\mathrm{p}}\right) = {}^{(\mathrm{n}+1)}\tau_{\mathrm{eff}}^{\mathrm{eq}} - {}^{(\mathrm{n}+1)}\tau_{\mathrm{y}}\left[1 + C_{\mathrm{p}}\ \ln\left(1 + \frac{\dot{\lambda}_{\mathrm{p}}}{\dot{\varepsilon}_{\mathrm{p},0}^{\mathrm{eq}}}\right)\right] = 0 \tag{4.84}$$

of only the plastic multiplier $\dot{\lambda}_{\mathrm{p}}$. The Newton-Raphson scheme

$$\dot{\lambda}_{\mathrm{p}} \leftarrow \dot{\lambda}_{\mathrm{p}} - \frac{R\left(\dot{\lambda}_{\mathrm{p}}\right)}{R'\left(\dot{\lambda}_{\mathrm{p}}\right)} \quad \text{until} \quad \left|R\left(\dot{\lambda}_{\mathrm{p}}\right)\right| < \epsilon_{\mathrm{N}} \tag{4.85}$$

is used to solve eq. (4.83), where the first derivative of R with respect to $\dot{\lambda}_{\mathrm{p}}$ is denoted as $R'(\dot{\lambda}_{\mathrm{p}})$, and ϵ_{N} represents a numerical tolerance. The derivatives required for the Newton-Raphson scheme are given in appendix A.2.1. Since $\dot{\lambda}_{\mathrm{p}}$ is strictly positive, if a Newton iteration yields a negative value for $\dot{\lambda}_{\mathrm{p}}$, the step size is recursively reduced until a positive multiplier is obtained. This approach ensures that all functions are evaluated with admissible inputs.

Based on the solution for $\dot{\lambda}_{\mathrm{p}}$, the updates of all internal variables can be performed explicitly, and the isochoric Kirchhoff stress ${}^{(\mathrm{n}+1)}\boldsymbol{\tau}^{\mathrm{iso}}$ is computed. Using eq. (4.61), the

Kirchhoff stress is mapped to the Cauchy stress – which is required as output by the Abaqus subroutine – by

$$^{(\mathrm{n+1})}\boldsymbol{\sigma} = \frac{1}{^{(\mathrm{n+1})}J}\ ^{(\mathrm{n+1})}\boldsymbol{\tau}\ . \tag{4.86}$$

Finally, based on eq. (4.47), the increment of inelastic energy is computed as

$$\Delta\mathcal{I}^{\mathrm{inelas}} = \left[^{(\mathrm{n+1})}\tau^{\mathrm{eq}} + {}^{(\mathrm{n+1})}g_{\alpha}\ {}^{(\mathrm{n+1})}f_{\mathrm{T}}\ {}^{(\mathrm{n+1})}f_{\mathrm{d}}\right]\ \dot{\lambda}_{\mathrm{p}}\,\Delta t + {}^{(\mathrm{n+1})}g_{\kappa_{\mathrm{d}}}\,\Delta\kappa_{\mathrm{d}}\ . \tag{4.87}$$

A high degree of flexibility is retained for the model since the functions $f_{\mathrm{d}}(\kappa_{\mathrm{d}})$, $f_{\mathrm{T}}\,(T)$, $\varepsilon^{\mathrm{eq}}_{\mathrm{p,i}}(\dot{\varepsilon}^{\mathrm{eq}}_{\mathrm{p}}, T, \eta)$, $\varepsilon^{\mathrm{eq}}_{\mathrm{p,f}}(\dot{\varepsilon}^{\mathrm{eq}}_{\mathrm{p}}, T, \eta)$, and $S_{\mathrm{d}}\,(s_{\mathrm{p}})$ can be chosen independently (from the respective admissible function spaces), while maintaining the scalar structure of the update equation. Specific choices for the mesoscopic cutting of 100Cr6 are presented in section 4.3.2.

Algorithmic overview An overview of the model implementation as algorithmic boxes is presented in algorithm 3 for the elastic trial step, and in algorithm 4 for the corrector step.

Algorithm 3: Elastic trial step

Input: ${}^{(n+1)}\boldsymbol{\varepsilon}$, ${}^{(n+1)}T$, ${}^{(n)}\boldsymbol{\varepsilon}_\mathrm{p}$, ${}^{(n)}\varepsilon_\mathrm{p}^\mathrm{eq}$, ${}^{(n)}\alpha$, ${}^{(n)}\kappa_\mathrm{d}$, Δt

Output: ${}^{(n+1)}\boldsymbol{\varepsilon}_\mathrm{p}$, ${}^{(n+1)}\varepsilon_\mathrm{p}^\mathrm{eq}$, ${}^{(n+1)}\alpha$, ${}^{(n+1)}\kappa_\mathrm{d}$, ${}^{(n+1)}\boldsymbol{\sigma}$, ${}^{(n+1)}\mathcal{I}^\mathrm{inelas}$, ${}^{(n+1)}g_\alpha$, ${}^{(n+1)}g_{\kappa_\mathrm{d}}$

${}^{(n+1)}f_\mathrm{T} \leftarrow f_\mathrm{T}({}^{(n+1)}T)$

${}^{(n+1)}\varepsilon_\mathrm{m} \leftarrow \frac{1}{3}\,\mathrm{tr}({}^{(n+1)}\boldsymbol{\varepsilon})$

${}^{(n+1)}\boldsymbol{\varepsilon}^{(\mathrm{vol})} \leftarrow {}^{(n+1)}\varepsilon_\mathrm{m}\boldsymbol{I}$

${}^{(n+1)}\boldsymbol{\varepsilon}^{(\mathrm{iso})} \leftarrow {}^{(n+1)}\boldsymbol{\varepsilon} - {}^{(n+1)}\boldsymbol{\varepsilon}^{(\mathrm{vol})}$

${}^{(n+1)}\tau_\mathrm{eff}^\mathrm{m} \leftarrow 3\,K_\mathrm{e}\,{}^{(n+1)}\varepsilon_\mathrm{m}$

${}^{(n+1)}J \leftarrow \exp\left(3\,{}^{(n+1)}\varepsilon_\mathrm{m}\right)$

${}^{(n+1)}\boldsymbol{\tau}_\mathrm{eff}^\mathrm{vol} \leftarrow {}^{(n+1)}\tau_\mathrm{eff}^\mathrm{m}\boldsymbol{I}$

${}^{(\mathrm{tr})}\boldsymbol{\tau}_\mathrm{eff}^\mathrm{iso} \leftarrow 2\,G_\mathrm{e}\left[{}^{(n+1)}\boldsymbol{\varepsilon}^{(\mathrm{iso})} - {}^{(n)}\boldsymbol{\varepsilon}_\mathrm{p}\right]$

${}^{(\mathrm{tr})}\tau_\mathrm{eff}^\mathrm{eq} \leftarrow \sqrt{3/2}\,\left\|{}^{(\mathrm{tr})}\boldsymbol{\tau}_\mathrm{eff}^\mathrm{iso}\right\|$

${}^{(\mathrm{tr})}\eta \leftarrow {}^{(n+1)}\tau_\mathrm{eff}^\mathrm{m}/\,{}^{(\mathrm{tr})}\tau_\mathrm{eff}^\mathrm{eq}$

${}^{(\mathrm{tr})}\bar{\kappa} \leftarrow \bar{\kappa}\left(\dot{\varepsilon}_\mathrm{p}^\mathrm{eq} = 0, {}^{(n)}\varepsilon_\mathrm{p}^\mathrm{eq}, {}^{(n+1)}T, {}^{(\mathrm{tr})}\eta\right)$

${}^{(\mathrm{tr})}\kappa_\mathrm{d} \leftarrow {}^{(n)}\kappa_\mathrm{d} + \Delta t/\left[\Delta t + t_\mathrm{d}\right]\left\langle {}^{(\mathrm{tr})}\bar{\kappa} - {}^{(n)}\kappa_\mathrm{d}\right\rangle$

${}^{(\mathrm{tr})}f_\mathrm{d} \leftarrow f_\mathrm{d}({}^{(\mathrm{tr})}\kappa_\mathrm{d})$

${}^{(\mathrm{tr})}g_\alpha \leftarrow g_\alpha({}^{(n)}\alpha)$

${}^{(\mathrm{tr})}\tau_\mathrm{y} \leftarrow \left(A_\mathrm{p} - {}^{(\mathrm{tr})}g_\alpha\right){}^{(n+1)}f_\mathrm{T}$

${}^{(\mathrm{tr})}\phi_\mathrm{p} \leftarrow {}^{(\mathrm{tr})}\tau_\mathrm{eff}^\mathrm{eq} - {}^{(\mathrm{tr})}\tau_\mathrm{y}\,{}^{(\mathrm{tr})}f_\mathrm{d}$

if ${}^{(\mathrm{tr})}\phi_\mathrm{p} < 0$ **then**

`/* elastic step */`

${}^{(n+1)}\boldsymbol{\varepsilon}_\mathrm{p} \leftarrow {}^{(n)}\boldsymbol{\varepsilon}_\mathrm{p}$

${}^{(n+1)}\varepsilon_\mathrm{p}^\mathrm{eq} \leftarrow {}^{(n)}\varepsilon_\mathrm{p}^\mathrm{eq}$

${}^{(n+1)}\alpha \leftarrow {}^{(n)}\alpha$

${}^{(n+1)}\kappa_\mathrm{d} \leftarrow {}^{(\mathrm{tr})}\kappa_\mathrm{d}$

${}^{(n+1)}f_\mathrm{d} \leftarrow {}^{(\mathrm{tr})}f_\mathrm{d}$

${}^{(n+1)}\boldsymbol{\tau}_\mathrm{eff}^\mathrm{iso} \leftarrow {}^{(\mathrm{tr})}\boldsymbol{\tau}_\mathrm{eff}^\mathrm{iso}$

${}^{(n+1)}\boldsymbol{\sigma} \leftarrow \left[{}^{(n+1)}f_\mathrm{d}/\,{}^{(n+1)}J\right]\,\left[{}^{(n+1)}\boldsymbol{\tau}_\mathrm{eff}^\mathrm{vol} + {}^{(n+1)}\boldsymbol{\tau}_\mathrm{eff}^\mathrm{iso}\right]$

${}^{(n+1)}g_\alpha \leftarrow g_\alpha({}^{(n)}\alpha)$

${}^{(n+1)}g_{\kappa_\mathrm{d}} \leftarrow g_{\kappa_\mathrm{d}}({}^{(\mathrm{tr})}\kappa_\mathrm{d})$

${}^{(n+1)}\mathcal{I}^\mathrm{inelas} \leftarrow {}^{(n)}\mathcal{I}^\mathrm{inelas} + {}^{(n+1)}g_{\kappa_\mathrm{d}}\left[{}^{(n+1)}\kappa_\mathrm{d} - {}^{(n)}\kappa_\mathrm{d}\right]$

else

`/* viscoplastic step */`

Perform viscoplastic corrector step given in algorithm 4

end

Algorithm 4: Viscoplastic corrector step

Input: ${}^{(n+1)}\boldsymbol{\varepsilon}^{(\mathrm{iso})}$, ${}^{(n+1)}T$, ${}^{(n+1)}f_{\mathrm{T}}$, ${}^{(n)}\boldsymbol{\varepsilon}_{\mathrm{p}}$, ${}^{(n)}\varepsilon_{\mathrm{p}}^{\mathrm{eq}}$, ${}^{(n)}\alpha$, ${}^{(n)}\kappa_{\mathrm{d}}$, ${}^{(n)}\dot{\varepsilon}_{\mathrm{p}}^{\mathrm{eq}}$, ${}^{(\mathrm{tr})}\boldsymbol{\tau}_{\mathrm{eff}}^{\mathrm{iso}}$, ${}^{(\mathrm{tr})}\tau_{\mathrm{eff}}^{\mathrm{eq}}$, ${}^{(n+1)}\tau_{\mathrm{eff}}^{\mathrm{m}}$, Δt

Output: ${}^{(n+1)}\boldsymbol{\varepsilon}_{\mathrm{p}}$, ${}^{(n+1)}\varepsilon_{\mathrm{p}}^{\mathrm{eq}}$, ${}^{(n+1)}\alpha$, ${}^{(n+1)}\kappa_{\mathrm{d}}$, ${}^{(n+1)}\boldsymbol{\sigma}$, ${}^{(n+1)}\mathcal{I}^{\mathrm{inelas}}$, ${}^{(n+1)}g_{\alpha}$, ${}^{(n+1)}g_{\kappa_{\mathrm{d}}}$

$i \leftarrow 0$

$\dot{\lambda}_{\mathrm{p}} \leftarrow {}^{(n)}\dot{\varepsilon}_{\mathrm{p}}^{\mathrm{eq}}$

while $i \leq n_{\mathrm{iter,max}}$ **do**

  ${}^{(n+1)}\dot{\varepsilon}_{\mathrm{p}}^{\mathrm{eq}} \leftarrow \dot{\lambda}_{\mathrm{p}}$

  ${}^{(n+1)}\varepsilon_{\mathrm{p}}^{\mathrm{eq}} \leftarrow {}^{(n)}\varepsilon_{\mathrm{p}}^{\mathrm{eq}} + \dot{\lambda}_{\mathrm{p}}\Delta t$

  ${}^{(n+1)}\tau_{\mathrm{eff}}^{\mathrm{eq}} \leftarrow {}^{(\mathrm{tr})}\tau_{\mathrm{eff}}^{\mathrm{eq}} - 3G_{\mathrm{e}}\dot{\lambda}_{\mathrm{p}}\Delta t$

  ${}^{(n+1)}\eta \leftarrow {}^{(n+1)}\tau_{\mathrm{eff}}^{\mathrm{m}} / {}^{(n+1)}\tau_{\mathrm{eff}}^{\mathrm{eq}}$

  ${}^{(n+1)}\bar{\kappa} \leftarrow \bar{\kappa}\left({}^{(n+1)}\dot{\varepsilon}_{\mathrm{p}}^{\mathrm{eq}}, {}^{(n+1)}\varepsilon_{\mathrm{p}}^{\mathrm{eq}}, {}^{(n+1)}T, {}^{(n+1)}\eta\right)$

  ${}^{(n+1)}\kappa_{\mathrm{d}} \leftarrow {}^{(n)}\kappa_{\mathrm{d}} + \Delta t/\left[\Delta t + t_{\mathrm{d}}\right]\left\langle {}^{(n+1)}\bar{\kappa} - {}^{(n)}\kappa_{\mathrm{d}}\right\rangle$

  ${}^{(n+1)}f_{\mathrm{d}} \leftarrow f_{\mathrm{d}}({}^{(n+1)}\kappa_{\mathrm{d}})$

  ${}^{(n+1)}\alpha \leftarrow {}^{(n)}\alpha + {}^{(n+1)}f_{\mathrm{T}}\ {}^{(n+1)}f_{\mathrm{d}}\,\dot{\lambda}_{\mathrm{p}}\,\Delta t$

  ${}^{(n+1)}g_{\alpha} \leftarrow g_{\alpha}({}^{(n+1)}\alpha)$

  ${}^{(n+1)}\tau_{\mathrm{y}} \leftarrow \left[A_{\mathrm{p}} - {}^{(n+1)}g_{\alpha}\right]{}^{(n+1)}f_{\mathrm{T}}$

  $R \leftarrow \left\langle {}^{(n+1)}\tau_{\mathrm{eff}}^{\mathrm{eq}} - {}^{(n+1)}\tau_{\mathrm{y}}\right\rangle - C_{\mathrm{p}}\,{}^{(n+1)}\tau_{\mathrm{y}}\ln(1 + \dot{\lambda}_{\mathrm{p}}/\dot{\varepsilon}_{\mathrm{p},0}^{\mathrm{eq}})$

  `/* Convergence check */`

  if $|R| < \mathrm{tol}$ **then**

    exit loop

  end

  $R' \leftarrow R'\left(\dot{\lambda}_{\mathrm{p}}\right)$

  $\Delta\dot{\lambda}_{\mathrm{p}} \leftarrow -R/R'$

  `/* Avoid negative multipliers even in iterations */`

  while $\dot{\lambda}_{\mathrm{p}} + \Delta\dot{\lambda}_{\mathrm{p}} < 0$ **do**

    $\Delta\dot{\lambda}_{\mathrm{p}} \leftarrow \Delta\dot{\lambda}_{\mathrm{p}}/2$

  end

  $\dot{\lambda}_{\mathrm{p}} \leftarrow \dot{\lambda}_{\mathrm{p}} + \Delta\dot{\lambda}_{\mathrm{p}}$

end

${}^{(n+1)}\boldsymbol{\nu}_{\mathrm{p}} \leftarrow {}^{(\mathrm{tr})}\boldsymbol{\tau}_{\mathrm{eff}}^{\mathrm{iso}} / \left\| {}^{(\mathrm{tr})}\boldsymbol{\tau}_{\mathrm{eff}}^{\mathrm{iso}} \right\|$

${}^{(n+1)}\boldsymbol{\varepsilon}_{\mathrm{p}} \leftarrow {}^{(n)}\boldsymbol{\varepsilon}_{\mathrm{p}} + \sqrt{3/2}\,\dot{\lambda}_{\mathrm{p}}\,\Delta t\ {}^{(n+1)}\boldsymbol{\nu}_{\mathrm{p}}$

${}^{(n+1)}\boldsymbol{\tau}_{\mathrm{eff}}^{\mathrm{iso}} \leftarrow 2\,G_{\mathrm{e}}\left[{}^{(n+1)}\boldsymbol{\varepsilon}^{(\mathrm{iso})} - {}^{(n+1)}\boldsymbol{\varepsilon}_{\mathrm{p}}\right]$

${}^{(n+1)}\boldsymbol{\sigma} \leftarrow \left[{}^{(n+1)}f_{\mathrm{d}} / {}^{(n+1)}J\right]\left[{}^{(n+1)}\boldsymbol{\tau}_{\mathrm{eff}}^{\mathrm{vol}} + {}^{(n+1)}\boldsymbol{\tau}_{\mathrm{eff}}^{\mathrm{iso}}\right]$

${}^{(n+1)}g_{\kappa_{\mathrm{d}}} \leftarrow g_{\kappa_{\mathrm{d}}}({}^{(n+1)}\kappa_{\mathrm{d}})$

${}^{(n+1)}\mathcal{I}^{\mathrm{inelas}} \leftarrow {}^{(n)}\mathcal{I}^{\mathrm{inelas}} + {}^{(n+1)}g_{\kappa_{\mathrm{d}}}\left[{}^{(n+1)}\kappa_{\mathrm{d}} - {}^{(n)}\kappa_{\mathrm{d}}\right]$

Model calibration

In the following, a calibration procedure for the model proposed in section 4.3.2 for 100Cr6 is presented. Specifically, suitable model functions are proposed for $f_\mathrm{T}(T)$, $\varepsilon_\mathrm{p,i}^\mathrm{eq}(\dot{\varepsilon}_\mathrm{p}^\mathrm{eq}, T, \eta)$, and $\varepsilon_\mathrm{p,f}^\mathrm{eq}(\dot{\varepsilon}_\mathrm{p}^\mathrm{eq}, T, \eta)$, and values for all model parameters are obtained from a combination of engineering approximations and mathematical optimisation.

The procedure combines two different datasets as references, and individual model components are calibrated separately. This approach is possible due to the interpretable nature of the different model components. Since no original experimental data is available to the author of this thesis, the resulting calibration of the model should be understood as an academic demonstration rather than as the best possible fit for any specific application. In general, the attempt to properly calibrate a material model of the proposed complexity highlights the need for experimental validation, as well as experimental procedure to generate the correct kind of calibration data in the first place.

Review of experimental data One of the most comprehensive studies on the plastic behaviour of 100Cr6 was performed by Hor et al. [78]. Compression tests with cylindrical specimens were performed at strain rates up to $1\,\mathrm{e}2\,\mathrm{s}^{-1}$ and temperatures between 20 °C and 1000 °C. In addition, hat-shaped specimens were subjected to compression and split-Hopkinson pressure bar tests to cover shear deformation as well as higher strain rates.

Some of the stress-strain curves for 100Cr6 from Hor et al. [78] are reproduced in fig. 4.1 to give an overview on the influence of the different variables. From fig. 4.1a, a general decrease of flow stress with increasing temperature is evident. However, this relation is not monotonic, i.e. the flow stress at 400 °C is slightly higher than at 200 °C. This behaviour was verified by Hor et al. [78] through additional tests, and is explained by ageing dynamics.

The strain rate sensitivity of the flow stress can be observed for 20, 600, and 1000 °C in figs. 4.1b to 4.1d, and is more pronounced at higher temperatures. The compression tests with cylindrical and hat-shaped specimens are designed to produce deformations which are – at least in theory – very close to those prescribed in the homogeneous deformation examples presented in section 2.2.

In general, not only the level but also the shape of the stress-strain curves show some variation. It is not obvious which of these variations are due to physical phenomena especially at certain temperature levels. Furthermore, the temperature evolution during the testing is unknown. It is therefore not feasible to capture every detail of the flow curves in a material model. Instead, the model should reproduce the general trends and average stress levels.

Plastic flow curves are presented by Hor et al. [78] using two different stress and strain measures. For the compression tests with cylindrical specimens, Hor et al. [78] present their results as effective stress over plastic strain, where the 'plastic strain' ϵ^p is calculated from the effective stress σ and Young's modulus E as

$$\epsilon^p = \epsilon - \sigma / E(T) \ , \tag{4.88}$$

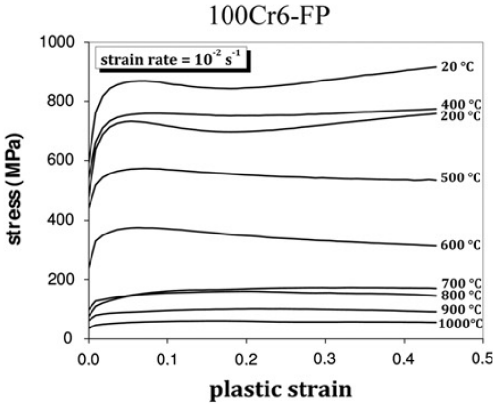

(a) Fig. 8c from Hor et al. [78].

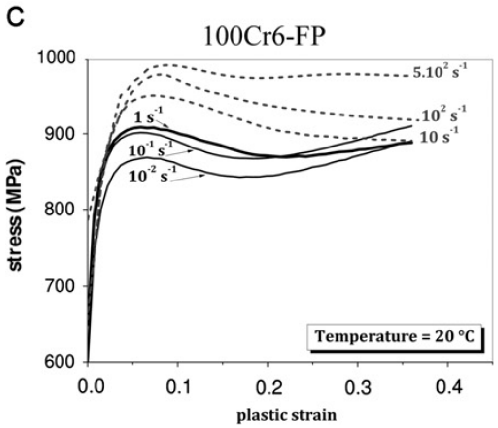

(b) Fig. 10c from Hor et al. [78].

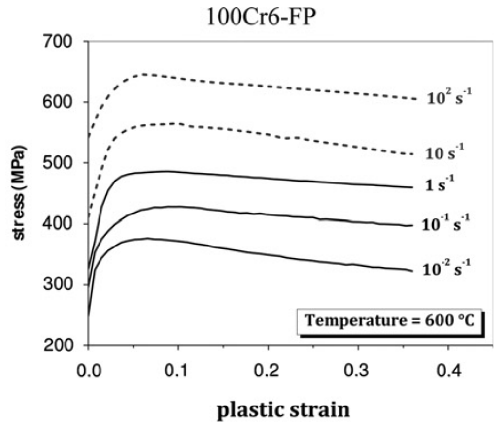

(c) Fig. 15c from Hor et al. [78].

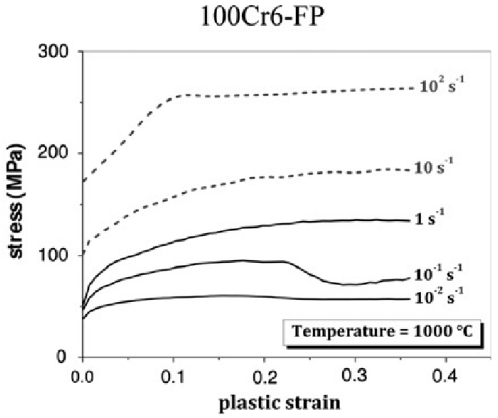

(d) Fig. 17c from Hor et al. [78].

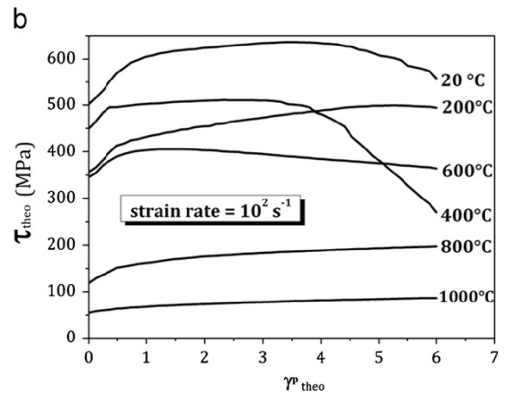

(e) Fig. 9b from Hor et al. [78].

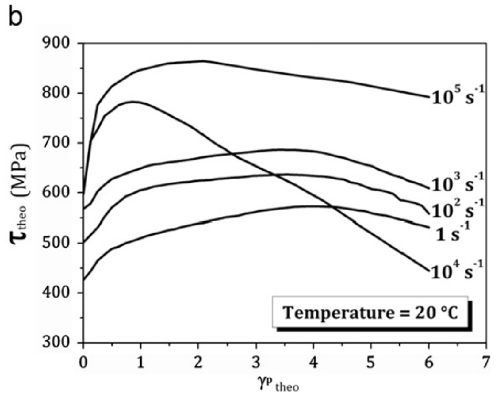

(f) Fig. 14b from Hor et al. [78].

Figure 4.1: Experimental stress-strain curves for annealed 100Cr6, reproduced from Hor et al. [78] with kind permission.

where E includes the machine stiffness, and ε is referred to as the 'positive true strain'. In the case of the hat-shape specimens, the results are presented based on an idealised deformation of the shear zone of the specimens, assuming that only shear deformation is present in this zone. The theoretical shear stress

$$\tau_{\text{theo}} = \frac{F}{\pi\, h \left[\dfrac{d_i + d_e}{2}\right]} \tag{4.89}$$

is obtained by assuming that the total force F is evenly distributed over a hypothetical cylinder, which lies within the shear zone with length h and average diameter $[d_i + d_e]/2$. In the same spirit, the theoretical shear strain is calculated from the axial displacement Δl and the width of the shear zone W as

$$\gamma_{\text{theo}} = \frac{\Delta l}{W} \ . \tag{4.90}$$

For the calibration of the material model, it is desirable to transform all experimental results to equivalent (logarithmic) plastic strain and equivalent Kirchhoff stress. To this end, the kinematic approximations derived in section 2.2 will be exploited. Although it is acknowledged that these relations are not exact, additional accuracy is not judged necessary for the unification of experimental results, whose repeatability is described as 'generally low' by the authors.

For the compression tests, it is assumed that 'true plastic strain' refers to the absolute value of the axial component of the logarithmic strain tensor $\boldsymbol{\varepsilon}_{\text{p}}$, i.e.

$$\gamma = \exp\left(-\varepsilon^p\right) - 1 \ . \tag{4.91}$$

From the comparison to the uniaxial tension/compression example (see section 2.2), it is evident from eq. (2.106) that the corresponding equivalent plastic strain is simply given by

$$\varepsilon_{\text{p}}^{\text{eq}} = \left|\varepsilon^p\right| \ . \tag{4.92}$$

Since it is assumed from the shape of the stress-strain curve in Hor et al. [78] that the provided stress σ is given per unit of deformed area, the Kirchhoff stress tensor is given by

$$\boldsymbol{\tau} = \begin{bmatrix} \sigma & 0 & 0 \\ 0 & 0 & 0 \\ 0 & 0 & 0 \end{bmatrix} \ . \tag{4.93}$$

The equivalent Kirchhoff stress then simply reads

$$\tau^{\text{eq}} = \sqrt{\frac{3}{2}}\, \left\|\boldsymbol{\tau}^{\text{iso}}\right\| = \sigma \ . \tag{4.94}$$

For the shear tests, the equivalent plastic strain is approximated based on the shear angle by eq. (2.118) as

$$\varepsilon_{\mathrm{p}}^{\mathrm{eq}} = \frac{\gamma}{\sqrt{3}} \ , \tag{4.95}$$

approximating the deformation as purely plastic.

On the other hand, the stress tensor is approximated as

$$\boldsymbol{\tau} = \begin{bmatrix} 0 & \tau_{\mathrm{theo}} & 0 \\ \tau_{\mathrm{theo}} & 0 & 0 \\ 0 & 0 & 0 \end{bmatrix} \ , \tag{4.96}$$

leading to the equivalent stress

$$\tau^{\mathrm{eq}} = \sqrt{3}\,\tau_{\mathrm{theo}} \ . \tag{4.97}$$

This approximation is justified by considering that the stress initially develops during the (small) elastic deformation. While it is acknowledged that this approximation does not hold true for large values of γ, it provides a convenient scalar measure to compare stress values relative to each other for the calibration of rate dependency.

Hor et al. [78] state that the experiments are performed at constant strain rates. Presumably, this statement refers to a constant stroke velocity especially for the compression tests. However, the rate dependency for the proposed model is formulated in terms of the equivalent plastic strain rate, which is obtained from the quantities used in [78] based on eqs. (2.105) and (2.117) as

$$\dot{\varepsilon}_{\mathrm{p}}^{\mathrm{eq}} = \frac{\dot{\epsilon}^p}{1+\epsilon^p} \tag{4.98}$$

for the compression tests, and as

$$\dot{\varepsilon}_{\mathrm{p}}^{\mathrm{eq}} = \frac{\dot{\gamma}_{\mathrm{theo}}}{\sqrt{3}} \tag{4.99}$$

for the shear tests.

The stress-strain curves presented by Hor et al. [78] in Fig. 10c and Fig. 14b have been converted to tabular data by using the website WebPlotDigitizer [155], and were converted to the space of equivalent (logarithmic) plastic strain and equivalent Kirchhoff stress as described above. Exemplary curves for strain rates $1.0\,\mathrm{s}^{-1}$ and $100.0\,\mathrm{s}^{-1}$ are presented in fig. 4.2.

While the maximum equivalent stress values reached in compression and shear are quite close, it becomes obvious from this representation that the modelling of the stress-strain relationship based solely on equivalent plastic strain cannot fully reproduce the experimental results.

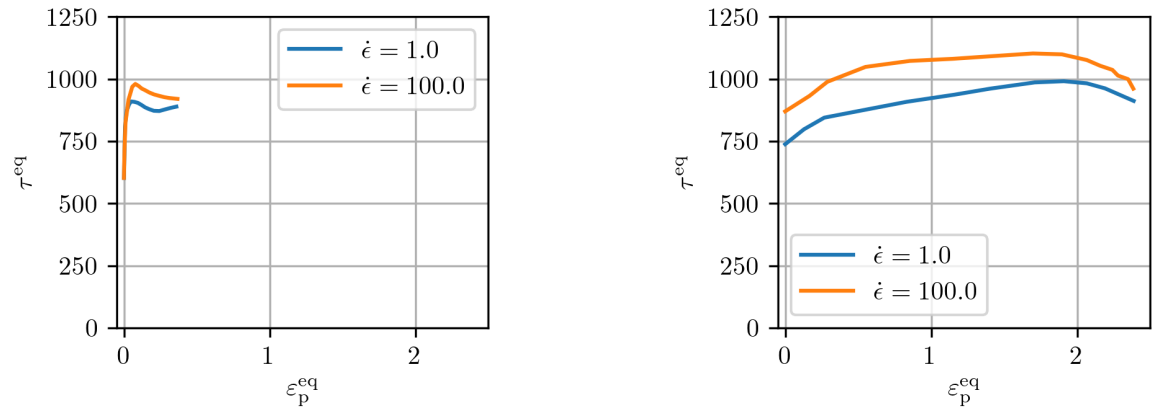

(a) Transformation of Fig. 10c (compression test).

(b) Transformation of Fig. 14b (shear test).

Figure 4.2: Stress-strain curves from Hor et al. [78], converted to equivalent plastic strain and equivalent Kirchhoff stress. Only the curves for strain rates obtained from both experiment types are shown.

Tensile tests were performed by Guo and Liu [62] on specimens made of 100Cr6 steel quench-hardened to 62 HRC. The authors of the study present stress-strain curves for temperatures of 20 °C, 200 °C, 400 °C, 600 °C, 800 °C, and 1000 °C. No rate dependent data is presented in the study, since the authors state that rate dependence was found to be negligible in comparison to the influence of temperature. In addition, the true yield strength, tensile strength (i.e. strength at the initiation of necking), and fracture strength, as well as the corresponding true strain values are given.

As for the data obtained by Hor et al. [78], the stress-strain curves from Guo and Liu [62] were converted to tabular data through WebPlotDigitizer [155], and the engineering stress and strain values were transformed to equivalent strain and equivalent Kirchhoff stress. A comparison of the reproduced curves is presented in fig. 4.3. Based on the table provided by Guo and Liu [62], the point of yield and the point of ultimate tensile strength are marked with a dot and a triangle marker. Since the material showed brittle behaviour at room temperature, i.e. fracture occurred before necking, no ultimate tensile strength marker is given for this curve. The transformation from brittle to ductile behaviour in the range from 20 °C to 200 °C is also reflected in the fact that Guo and Liu [62] determined the yield point by deviation from the linear slope at 20 °C, but used the 0.2 % offset strain method for the remaining curves.

Excluding the values at room temperature, both yield stress and ultimate tensile stress decrease monotonically for increasing temperature. However, the corresponding strain values are not ordered monotonically. Since the temperature dependency of the stresses and strains, especially at yield and at fracture, is of interest for model calibration, the values obtained by Guo and Liu [62] are visualised in fig. 4.4.

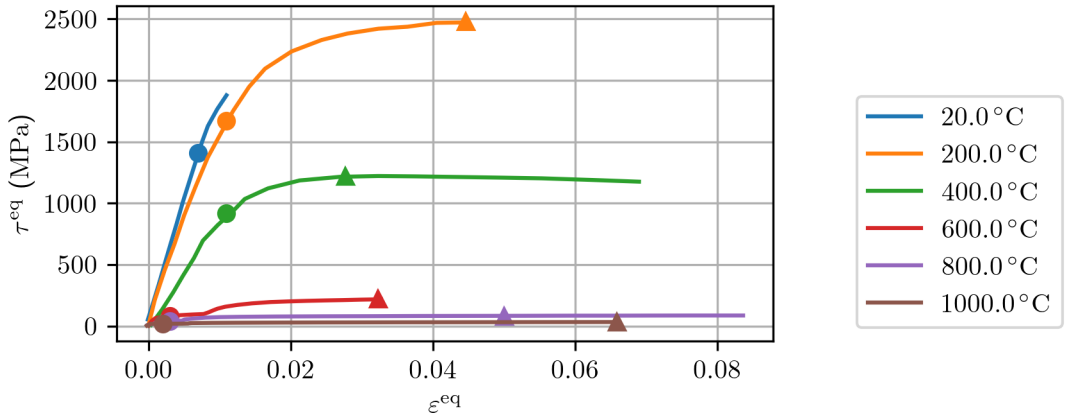

Figure 4.3: Stress-strain curves from Guo and Liu [62], converted to equivalent strain and equivalent Kirchhoff stress. Dot markers show the yield points identified by the authors, while triangle markers show the location of ultimate tensile strain and strength. The curves were reproduced approximately by digitising the original plots with WebPlotDigitizer [155], while the markers are based on Table 4 of the same publication.

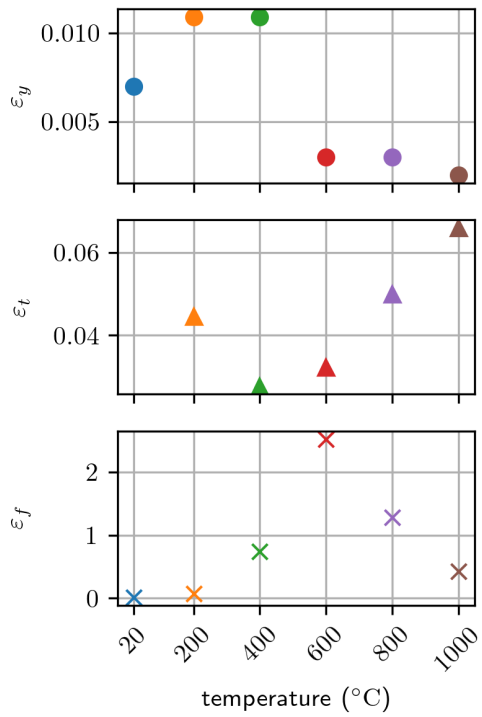

(a) Logarithmic strain at yield, ultimate tensile strength, and fracture.

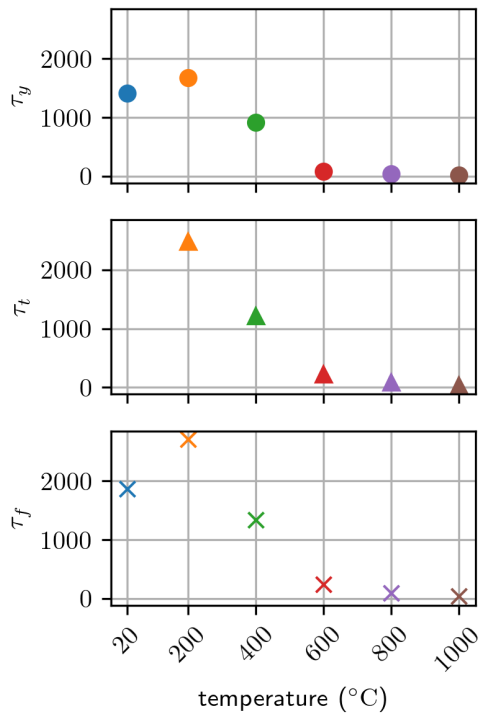

(b) Kirchhoff yield strength, ultimate tensile strength, and fracture strength.

Figure 4.4: Values given by Guo and Liu [62] for yield stress and strain (τ_y, ε_y), ultimate tensile strength and strain (τ_t, ε_t), and fracture stress and strain (τ_f and ε_f).

Calibration procedure The following assumptions are adopted for the calibration of the material model:

- The equivalent plastic strain is approximated for each curve by subtracting the strain at yield.
- It is sufficient to calibrate the temperature dependency based on the yield stress.
- Ductile damage evolution occurs over a prescribed (temperature and rate independent) range of equivalent plastic strain.
- Damage initiation and failure are independent of the strain rate.

Based on these assumptions, the following calibration procedure was devised:

1. Choose constant values for Young's modulus E, Poisson's ratio ν, and mass density ρ_0
2. Choose temperature integrity function $f_\mathrm{T}(T)$ and calibrate based on values for τ_y from Guo and Liu [62]
3. Choose model function for equivalent plastic strain at damage initiation and calibrate based on values for ε_t from Guo and Liu [62]
4. Choose model function for equivalent plastic strain at failure and calibrate based on values for ε_f from Guo and Liu [62]
5. Calibrate hardening parameters based on one or multiple curves from Guo and Liu [62]
6. Calibrate rate dependency based on Hor et al. [78]

Calibration of temperature dependency In the following, the model ansatz

$$f(T) = A \exp\left(-\left[\frac{T-B}{C}\right]^2\right) \tag{4.100}$$

is used for the temperature dependencies, where A, B, and C are parameters. This ansatz reflects the non-monotonous data, while enforcing a strictly positive value if A is positive. The symmetric nature of the ansatz function does not reflect physical intuition, but should be understood as a purely empirical model for the temperature range above room temperature.

Specifically, the temperature integrity function is modelled as

$$f_\mathrm{T}(T) = A_T \exp\left(-\left[\frac{T-B_T}{C_T}\right]^2\right) , \tag{4.101}$$

and optimal values $\boldsymbol{p}_{\mathrm{T}}^{*}$ for the parameters

$$\boldsymbol{p}_{\mathrm{T}} = [A_T, B_T, C_T]^{\mathrm{t}} \tag{4.102}$$

are obtained based on the data at n_{temp} different temperatures from the least squares fit

$$\boldsymbol{p}_{\mathrm{T}}^{*} = \arg\min_{\boldsymbol{p}_{\mathrm{T}}} \left\{ \sum_{i=1}^{n_{\mathrm{temp}}} \frac{1}{2} \left[f_{\mathrm{T}}\left(T_i, \boldsymbol{p}_{\mathrm{T}}\right) - \tau_{\mathrm{y}}\left(T_i\right) / \tau_{\mathrm{y}}\left(20\,^{\circ}\mathrm{C}\right) \right]^2 \right\} , \tag{4.103}$$

where the yield stress $\tau_{\mathrm{y}}(T_i)$ at the different temperatures is obtained from [62]. The resulting parameters are presented in table 4.1, and a graphical representation of the result is presented in fig. 4.5.

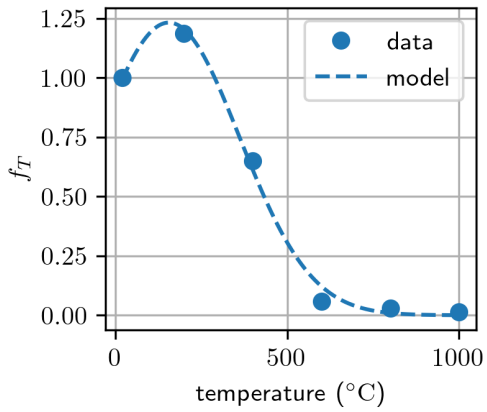

Figure 4.5: Results of least squares fit (4.103) based on the data published in [62]. The resulting parameters are given in table 4.1.

Table 4.1: Resulting parameter set $\boldsymbol{p}_{\mathrm{T}}^{*}$ from optimisation (4.103).

Parameter	A_T	B_T	C_T
Value	1.23	156.13	291.60
Unit	-	°C	°C

Calibration of damage model The equivalent plastic strain at failure is modelled by the same ansatz as the temperature dependency as

$$\varepsilon_{\mathrm{p,f}}^{\mathrm{eq}}\left(T, \dot{\varepsilon}_{\mathrm{p}}^{\mathrm{eq}}, \eta\right) = A_{\mathrm{d,f}} \exp\left(- \left[\frac{T - B_{\mathrm{d,f}}}{C_{\mathrm{d,f}}} \right]^2 \right) w_\eta\left(\eta\right) , \tag{4.104}$$

where $w_\eta\left(\eta\right)$ is a weighting function based on the stress triaxiality.

The calibration of the weighting function requires experimental data at different triaxialities, which are therefore usually obtained from different experiments. A procedure to obtain such data – and, in fact, to model the equivalent plastic strain at failure based on this data – was developed by Bao and Wierzbicki [15] for aluminium. Unfortunately, as far as the author of this thesis is aware, no similar dataset is available for steel grades comparable to 100Cr6. In the following, the simplification

$$w_\eta(\eta) = 1 \tag{4.105}$$

is therefore assumed, although it is to be mentioned that this simplification could (and should) be revised in the future based on improved calibration data.

Since no calibration data is available for the onset of ductile damage either, this value is modelled based on the equivalent plastic strain at failure as

$$\varepsilon_{\mathrm{p,i}}^{\mathrm{eq}}\left(T, \dot{\varepsilon}_{\mathrm{p}}^{\mathrm{eq}}, \eta\right) = A_{\mathrm{d,i}}\, \varepsilon_{\mathrm{p,f}}^{\mathrm{eq}}\left(T, \dot{\varepsilon}_{\mathrm{p}}^{\mathrm{eq}}, \eta\right) \ , \tag{4.106}$$

where the parameter $A_{\mathrm{d,i}} = 0.9$ is chosen. This approach ensures that the relation

$$\varepsilon_{\mathrm{p,f}}^{\mathrm{eq}} > \varepsilon_{\mathrm{p,i}}^{\mathrm{eq}} \tag{4.107}$$

holds at any time. The optimal values $\boldsymbol{p}_{\mathrm{d,f}}^{*}$ for the parameters

$$\boldsymbol{p}_{\mathrm{d,f}} = \left[A_{\mathrm{d,f}}, B_{\mathrm{d,f}}, C_{\mathrm{d,f}}\right]^{\mathrm{t}} \tag{4.108}$$

are then obtained from the least squares fit

$$\boldsymbol{p}_{\mathrm{d,f}}^{*} = \arg\min_{\boldsymbol{p}_{\mathrm{d,f}}} \left\{ \sum_{i=1}^{n_{\mathrm{temp}}} \frac{1}{2} \left[\varepsilon_{\mathrm{p,f}}^{\mathrm{eq}}\left(T_i, \boldsymbol{p}_{\mathrm{d,f}}\right) - \varepsilon_{\mathrm{f}}\left(T_i\right)\right]^2 \right\} \ , \tag{4.109}$$

where the failure strains $\varepsilon_{\mathrm{f}}\left(T_i\right)$ at the different temperatures are obtained from [62].

A graphic representation of the resulting fit for eq. (4.109) is shown in fig. 4.6, while the corresponding parameters values are presented in table 4.2.

Table 4.2: Resulting parameter set $\boldsymbol{p}_{\mathrm{d,f}}^{*}$ from optimisation (4.109).

Parameter	$A_{\mathrm{d,f}}$	$B_{\mathrm{d,f}}$	$C_{\mathrm{d,f}}$
Value	2.53	631.88	214.42
Unit	-	°C	°C

Calibration of hardening model Assuming isothermal evolution during quasi-static loading, integration of the evolution law for the hardening variable α yields

$$\alpha\left(T, \varepsilon_{\mathrm{p}}^{\mathrm{eq}}\right) = f_{\mathrm{T}}\, \varepsilon_{\mathrm{p}}^{\mathrm{eq}} \ , \tag{4.110}$$

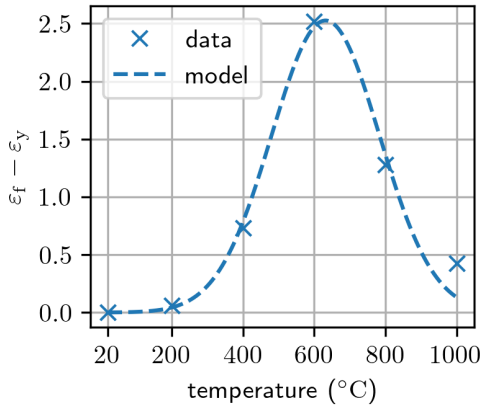

Figure 4.6: Results of least squares fit eq. (4.109) based on the data published in [62]. The resulting parameters are given in table 4.2.

and therefore the static yield stress of the proposed material model is described by

$$\tau_y\left(T, \varepsilon_p^{eq}\right) = \left[A_p + B_p\left[1 - \exp\left(-n_p\, f_T\left(T\right)\, \varepsilon_p^{eq}\right)\right]\right]\, f_T\left(T\right)\ . \tag{4.111}$$

The flow curves obtained by Guo and Liu [62] are each cut off at the ultimate tensile strain, and then resampled onto a regular spaced grid of n_{points} pairs of equivalent plastic strain ${\varepsilon_p^{eq}}_{i,j}$ and corresponding flow stress $\tau_{y\,i,j}$. Therein, the index i refers to the discrete value of temperature in the experiments, and the index j refers to the j^{th} point in the resampled curve at that temperature.

Similar to the temperature dependency, the parameters

$$\boldsymbol{p}_p = \left[A_p, B_p, n_p\right]^t \tag{4.112}$$

are introduced, and the optimal values $\boldsymbol{p}_p^*$ are obtained from the least squares fit

$$\boldsymbol{p}_p^* = \arg\min_{\boldsymbol{p}_p}\left\{\sum_{i=1}^{n_{temp}}\sum_{j=1}^{n_{points}}\frac{1}{2}\left[\tau_y\left(T_i, {\varepsilon_p^{eq}}_{i,j}\right) - \tau_{y\,i,j}\right]^2\right\}\ , \tag{4.113}$$

taking all flow curves into account.

The optimal parameters $\boldsymbol{p}_p^*$ are listed in table 4.3, and the resulting fit of the flow curves is presented in fig. 4.7.

Table 4.3: Resulting parameter set $\boldsymbol{p}_p^*$ from the optimisation (4.113)

Parameter	A_p	B_p	n_p
Value	1444.63	541.75	265.92
Unit	MPa	MPa	-

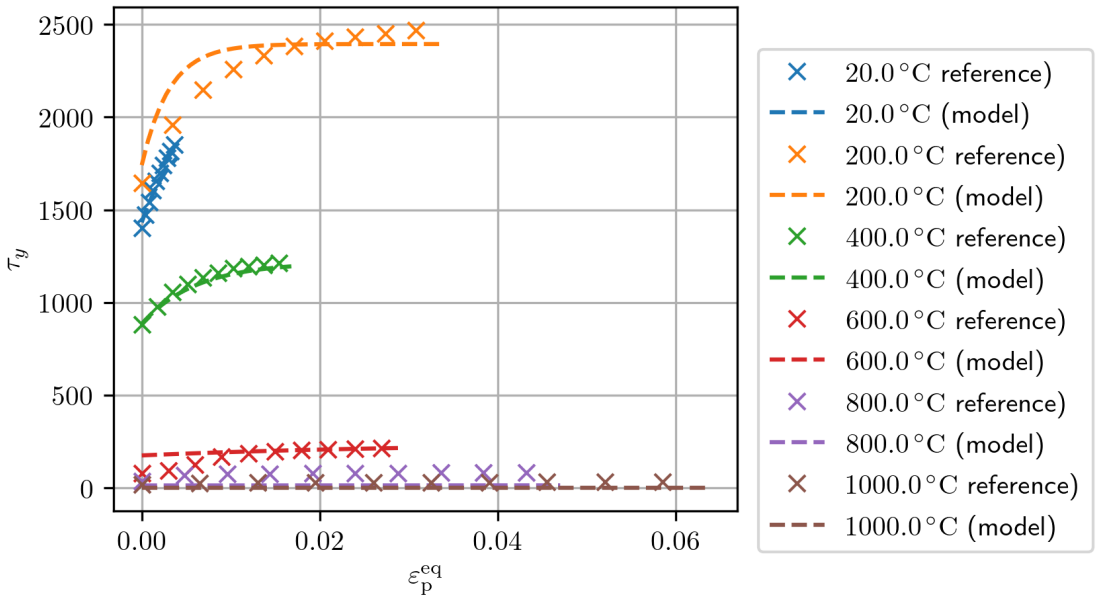

Figure 4.7: Results of least squares fit (4.113), based on the data published in [62]. The parameters corresponding to both results are given in table 4.3.

The general trends are predicted by the model in good accordance with the data. However, some deviations can be observed. At 200 °C, the rate of hardening predicted by the model is higher than observed experimentally, and the ultimate tensile strength is slightly underestimated. The strong nonlinearity of the flow curve at 600 °C, attributed by Guo and Liu [62] to a possible phase transformation, is – as expected due to the chosen ansatz functions – not captured by the model. Finally, the strength at temperature above 800 °C is underestimated. This results from the fact that the temperature integrity function $f_T(T)$ predicts this temperature range less accurately.

Given the nature of the proposed phenomenological model, the predictions are judged to be sufficiently accurate. In particular, the proposed ansatz for the temperature dependency is able to catch the nonlinear transformation from brittle to ductile behaviour, which would not be possible with the original Johnson-Cook model. The inaccuracies in the high-temperature range are not expected to significantly impact the predictions for cutting simulations, since material in these temperature regions does not significantly contribute to the stresses.

Calibration of rate dependency Calibrating the rate-dependency parameters based on the already identified plastic parameters would be preferable if data for the same material were available. Unfortunately, no data for high strain rates is given by Guo and Liu [62]. Therefore, the flow curves published by Hor et al. [78] are used as the reference to calibrate the rate dependency.

When large plastic deformations occur in high strain rate experiments, the specimens heat up due to the dissipated work. The coupling between temperature and mechanical material properties will in turn influence the evolution of hardening and therefore the further heating as well as the stress state. For this reason, only a selected interval of the flow curves is used to calibrate the rate dependency. Ideally, the calibration would consider only yield strain, since the elastic deformation is assumed to not induce notable temperature changes. However, the exact point of yield is not easily identified, especially at higher strain rates. Therefore, the range $0 \leq \varepsilon_{\mathrm{p}}^{\mathrm{eq}} \leq 0.1$ is considered in the following for all stress-strain curves.

Since the model for τ_{y} was calibrated on a different dataset and is therefore not applicable to the calibration data for the rate dependency, an unknown (average) yield stress is introduced for each considered temperature. The set of parameters for the calibration is then given by

$$\boldsymbol{p}_{\mathrm{r}} = \left[C_{\mathrm{p}}, \dot{\varepsilon}_{\mathrm{p},0}^{\mathrm{eq}}, \tau_{\mathrm{y}}^{(20)}, \tau_{\mathrm{y}}^{(600)}, \tau_{\mathrm{y}}^{(1000)}\right]^{\mathrm{t}} , \tag{4.114}$$

where for example $\tau_{\mathrm{y}}^{(20)}$ refers to the unknown yield stress at 20 °C. If no damage occurs, which is assumed for this part of the flow curves, the evolution equation yields

$$\tau^{\mathrm{eq}}\left(T, \dot{\varepsilon}_{\mathrm{p}}^{\mathrm{eq}}, \boldsymbol{p}_{\mathrm{r}}\right) = \tau_{\mathrm{y}}^{(T)} \left[1 + C_{\mathrm{p}} \ln\left(1 + \frac{\dot{\varepsilon}_{\mathrm{p}}^{\mathrm{eq}}}{\dot{\varepsilon}_{\mathrm{p},0}^{\mathrm{eq}}}\right)\right] . \tag{4.115}$$

For each flow curve i, the average values $\bar{\dot{\varepsilon}}_{\mathrm{p}}^{\mathrm{eq}}$ and $\bar{\tau}^{\mathrm{eq}}$ of plastic strain rate and equivalent stress are computed in the selected interval, resulting in n_{points} points $(T_i, \bar{\dot{\varepsilon}}_{\mathrm{p}\ i}^{\mathrm{eq}}, \bar{\tau}_i^{\mathrm{eq}})$. Based on these points, the least squares optimisation

$$\boldsymbol{p}_{\mathrm{r}}^{*} = \arg\min_{\boldsymbol{p}_{\mathrm{r}}} \left\{ \sum_{i=1}^{n_{\mathrm{points}}} \frac{1}{2} \left[\tau^{\mathrm{eq}}\left(T_i, \bar{\dot{\varepsilon}}_{\mathrm{p}\ i}^{\mathrm{eq}}, \boldsymbol{p}_{\mathrm{r}}\right) - \bar{\tau}_i^{\mathrm{eq}}\right]^2 \right\} \tag{4.116}$$

is performed. The auxiliary parameters $\tau_{\mathrm{y}}^{(T_i)}$ are disregarded, and the remaining parameters C_{p} and $\dot{\varepsilon}_{\mathrm{p},0}^{\mathrm{eq}}$ are used for the proposed material model. Their values are given in table 4.4, and a graphic representation of the least squares fit is presented in fig. 4.8.

Table 4.4: Resulting parameter set $\boldsymbol{p}_{\mathrm{r}}^{*}$ from the optimisation (4.116)

Parameter	C_{p}	$\dot{\varepsilon}_{\mathrm{p},0}^{\mathrm{eq}}$
Value	4.17 e−2	1.16 e−3
Unit	-	ms^{-1}

The rate dependency at 20 °C is captured well, whereas the influence of the equivalent plastic strain rate is underestimated at elevated temperatures. While it is acknowledged that a better fit might be possible with a more elaborate calibration method, the transferability to hardened 100Cr6 material, as used by Guo and Liu [62], is questionable. The presented result is therefore accepted for the proposed model.

An overview of all model parameters and their values is presented in table 4.5

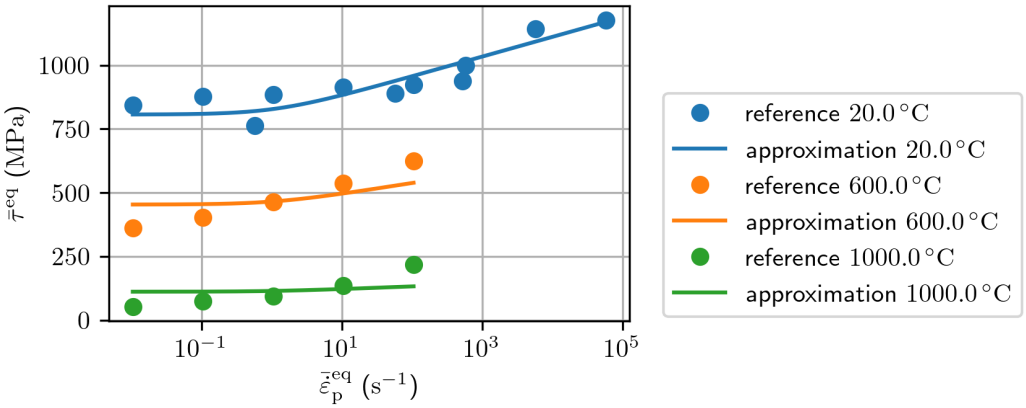

Figure 4.8: Results of least squares fit (4.116), based on the data published in [78]. The parameters corresponding to both results are given in table 4.4.

Table 4.5: Material parameters used for the viscoplastic model with damage. The kg-mm-ms unit system – leading to GPa, J, kW – is used for all presented examples, although any consistent unit system can be used. The values for heat capacity and thermal conductivity as well as the Taylor-Quinney coefficient are estimated based on literature values.

	Parameter	Value	Unit
Mass density	ρ_0	7.83 e−6	$\mathrm{kg\,mm^{-3}}$
Elasticity	E	210.00	GPa
	ν	0.30	-
Plasticity	A_{p}	1.44	GPa
	B_{p}	0.54	GPa
	n_{p}	265.92	-
Rate dependency	C_{p}	4.17 e−2	-
	$\dot{\varepsilon}_{\mathrm{p},0}^{\mathrm{eq}}$	1.16 e−3	$\mathrm{ms^{-1}}$
Damage	d_{i}	0.00	-
	d_{f}	0.99	-
	t_{d}	0.10	ms
	$A_{\mathrm{d,i}}$	0.90	-
	$A_{\mathrm{d,f}}$	2.53	-
	$B_{\mathrm{d,f}}$	631.88	°C
	$C_{\mathrm{d,f}}$	214.42	°C
Thermal softening	A_T	1.23	-
	B_T	156.13	°C
	C_T	291.60	°C
Thermal coupling	c_T	470.00	$\mathrm{J\,kg^{-1}\,K^{-1}}$
	k_t	4.5 e−5	$\mathrm{kW\,mm^{-1}\,K^{-1}}$
	β^{TQ}	0.95	-

4.3.3 Homogeneous deformation examples

In this section, the behaviour of the model proposed in section 4.3.2 (which is referred to as the 'viscoplastic model' in the following) is demonstrated by some representative results for the homogeneous deformation problems introduced in section 2.2. One element tests with a single quadrature point are implemented to investigate the example problems with the same finite element framework which is used for the solution of actual boundary value problems. Specifically, the model prediction of temperature and rate dependent effects is discussed, and the implications of the chosen viscous damage evolution law on the results are investigated. Furthermore, the results for the viscoplastic model are compared to the table-based implementation of the damage-enhanced Johnson-Cook model presented in section 4.3.1 (referred to as the 'JC model' in the following).

Results for the simple shear and uniaxial tension examples under isothermal conditions, obtained with the viscoplastic model, are presented in fig. 4.9. The development of equivalent Kirchhoff stress τ^{eq}, equivalent plastic strain $\varepsilon_{\mathrm{p}}^{\mathrm{eq}}$, hardening variable α, and damage variable κ_{d} with load factor γ is compared for different initial temperatures in fig. 4.9a for the simple shear case, and in fig. 4.9b for uniaxial tension. As expected from the model equations, the equivalent plastic strain is (nearly) independent of the temperature for a given deformation path.

The equivalent stress shows the expected behaviour as well: A brittle response is produced at 20 °C, where the onset of ductile damage occurs nearly instantaneously after the material yields. At 200 °C, an increased yield strength in combination with a more ductile response can be observed, delaying the onset of damage. Finally, at 400 °C, no damage is observed in the presented strain regime, since the material is even more ductile. However, the general level of equivalent stress is lower, since thermal softening takes place. Hardening is constrained by the evolution of ductile damage, therefore the resulting curves for the hardening variables flatten with the onset of damage.

The influence of the strain rate on the same quantities for the simple shear test is shown in figs. 4.9c and 4.9d.

These results are presented over both, the load parameter γ as well as time t, to demonstrate that the evolution of the damage variable has a characteristic shape, governed by the time scale parameter t_{d}: Even for the brittle case, where the material fails nearly directly after reaching the yield limit, the viscous damage evolution law results in a smooth transition to the residual stiffness. This effect is especially obvious in the graph for the damage variable, which does not saturate for the highest strain rate – but would do so, given enough time.

As expected, the ultimate strength of the material increases with higher strain rates, while the ductility (measured by the onset of damage) is unaffected. However, since the relaxation behaviour of the damage variable is tied to a specific time scale, a pseudo-increase in ductility is visible in fig. 4.9c, which is different for each strain rate. It is evident from fig. 4.9d that after damage initiates, it evolves very similarly for all strain rates in the time domain.

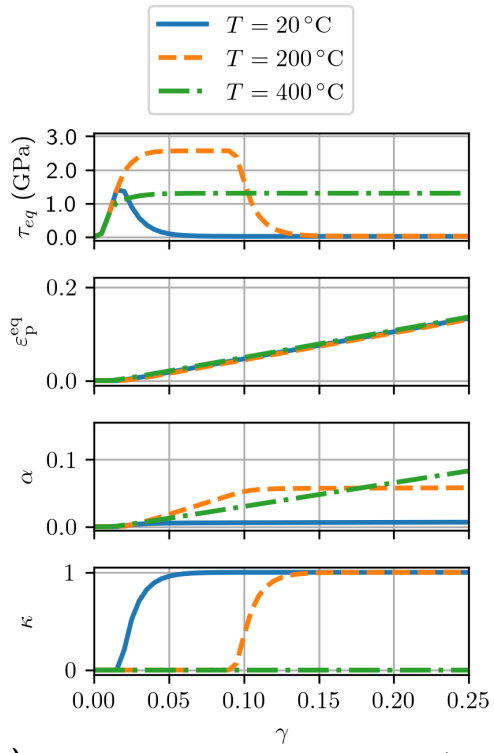

(a) Results for simple shear with different (initial) temperatures at $\dot{\gamma} = 0.1\,\mathrm{ms}^{-1}$.

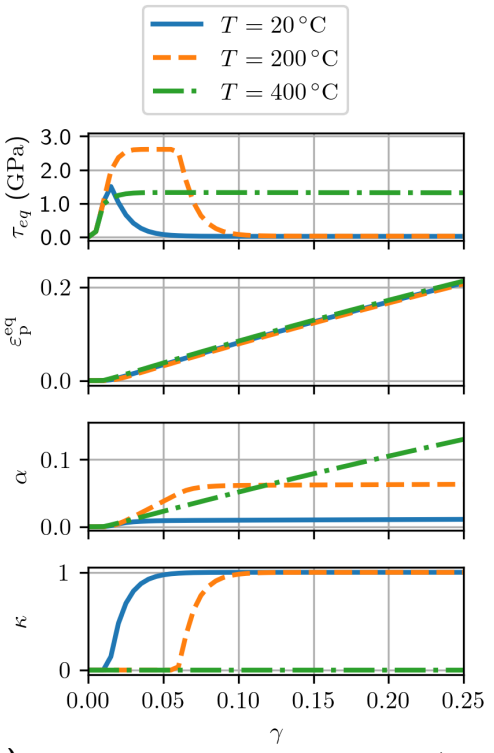

(b) Results for uniaxial tension with different (initial) temperatures at $\dot{\gamma} = 0.1\,\mathrm{ms}^{-1}$.

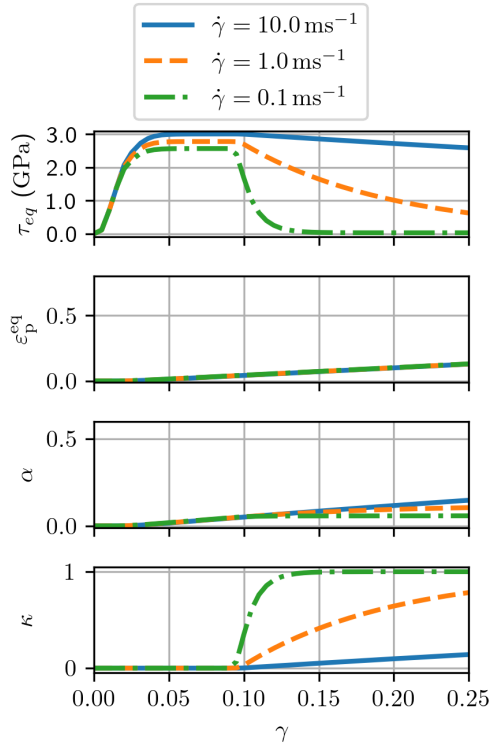

(c) Results for uniaxial tension with different strain rates at $T = 200\,°C$.

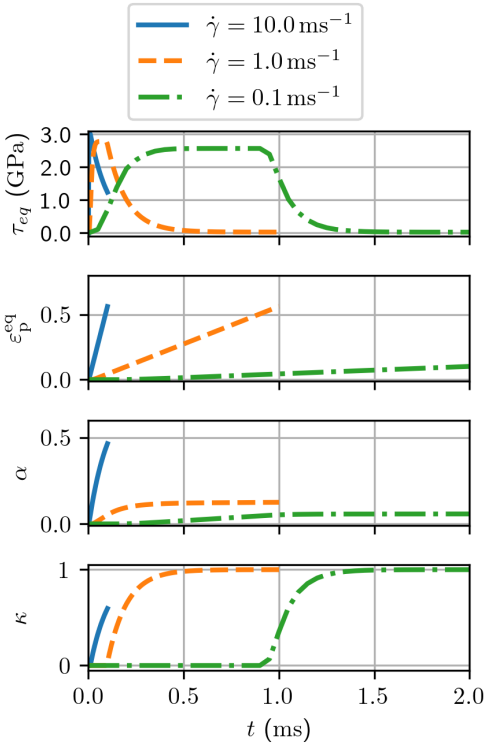

(d) Results for simple shear with different strain rates at $T = 200\,°C$.

Figure 4.9: Homogeneous problem results under isothermal conditions, obtained from the model proposed in section 4.3.2.

For the simple shear problem, the influence of adiabatic heating is presented in fig. 4.10. All results correspond to $\dot{\gamma} = 0.1\,\mathrm{ms}^{-1}$. Adiabatic and isothermal results are shown for an initial temperature of 20 °C in fig. 4.10a and for an initial temperature of 200 °C in fig. 4.10b.

The resulting stress curves for an initial temperature of 20 °C are nearly identical, since the adiabatic heating only induces a temperature change of approximately 5 °C before the material fails. On the other hand, a temperature increase of nearly 50 °C is observed for an initial temperature of 200 °C, which in turn increases the material's ductility, and delays the onset of damage.

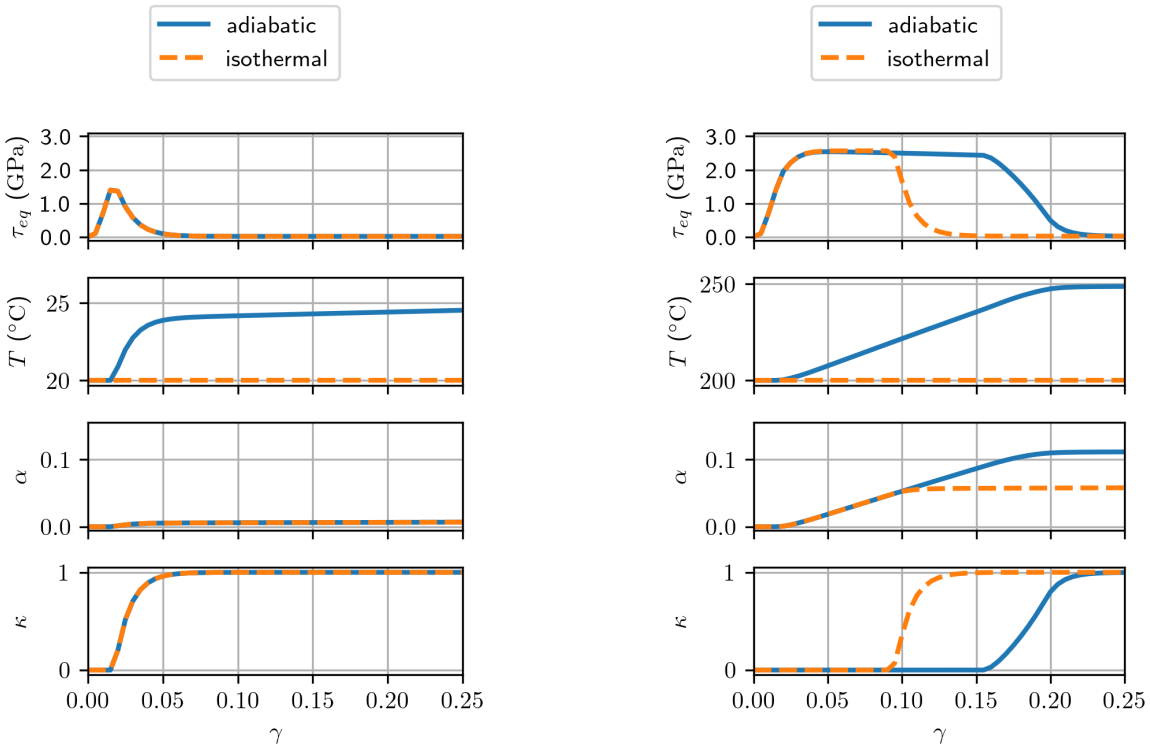

(a) Initial temperature of 20 °C.

(b) Initial temperature of 200 °C.

Figure 4.10: Influence of adiabatic heating simple shear. All curves correspond to $\dot{\gamma} = 0.1\,\mathrm{ms}^{-1}$.

While these results nicely demonstrate the implementation of the thermo-mechanical coupling, they also show a drawback of the proposed calibration strategy, as no validation data is available for the temperature increase. It is generally accepted that the heat generated during the large plastic deformation of steel specimens will incur a temperature change. Nonetheless, such data is rarely reported in experimental studies. For the proposed model, a validation of the predicted temperature increase (and the changes in mechanical behaviour due to this coupling) remains to be addressed in future work.

In the following, the viscoplastic model is compared to the JC model. Both equivalent stress and temperature evolution, based on different initial temperatures T_0, are compared for deformations up to $\gamma = 5$ in fig. 4.11.

The transition from brittle to ductile behaviour at elevated temperature, which is evident from the flow curves of the viscoplastic model presented in fig. 4.11a, is not captured by the JC model shown in fig. 4.11b. Furthermore, the temperature dependency of the flow stress is much more pronounced for the viscoplastic model than for the JC model. This difference arises from the proposed nonlinear model of the temperature dependency, which captures the nearly complete thermal softening reported by Guo and Liu [62] already at temperatures around 1000 °C. On the other hand, the thermal softening term used in the traditional Johnson-Cook model (and therefore in the JC model implementation) assumes that complete softening occurs at the melting temperature – which typically lies between 1350 °C and 1550 °C – and linearly interpolates.

It is to be mentioned that, even in the damaged state, a numerical residual stiffness is prescribed in the JC model, which amounts to a residual equivalent stress of approximately 100 MPa.

While the general shape of the flow curves is quite different, the rate dependency is predicted very similar by both models. Flow curves obtained at an initial temperature of $T_0 = 600\,°\mathrm{C}$ are presented in fig. 4.12 for three different loading rates $\dot{\gamma}$. The comparison of the stress levels close to the yield point – where different thermal softening behaviour does not play a crucial role – reveals quite similar relative stress levels for both models.

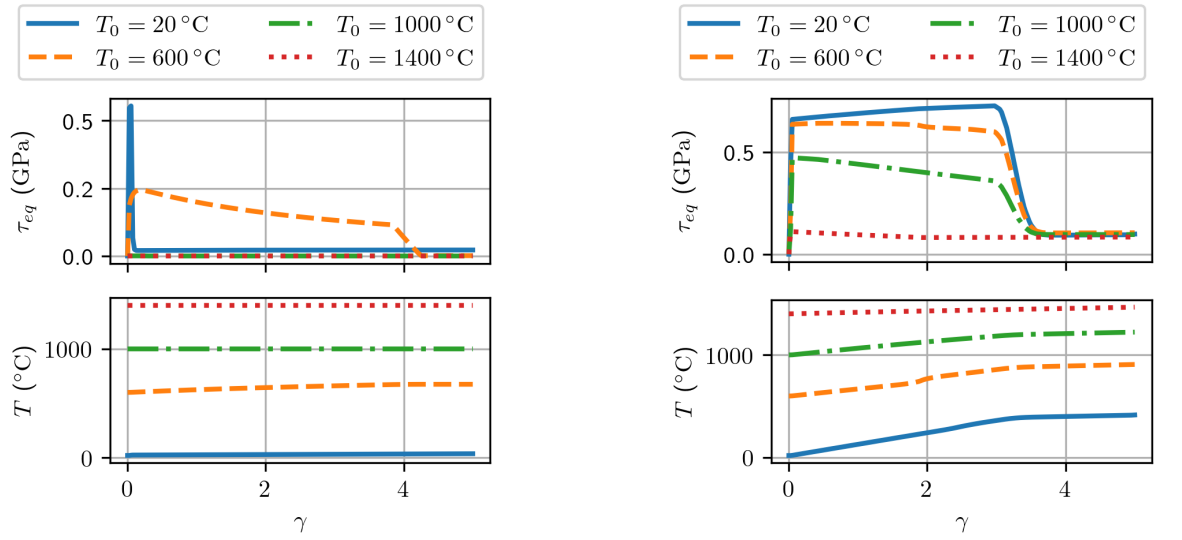

(a) Results obtained from the VUMAT implementation.

(b) Results obtained from the table-based Johnson-Cook implementation.

Figure 4.11: Exemplary results for the simple shear test with adiabatic heating at different initial temperatures T_0. All results were obtained at a loading rate of $\dot{\gamma} = 0.1\,\mathrm{ms}^{-1}$

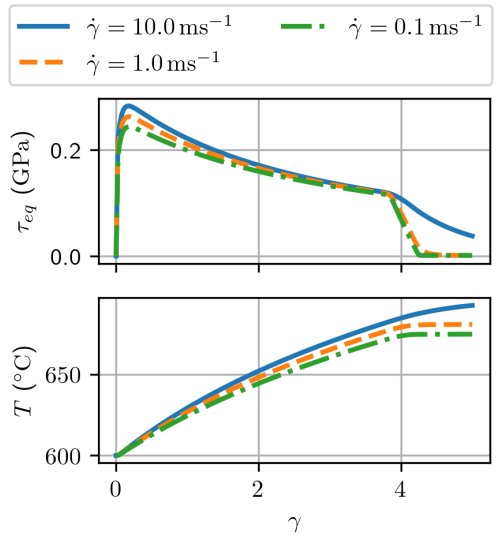

(a) Results obtained from the VUMAT implementation.

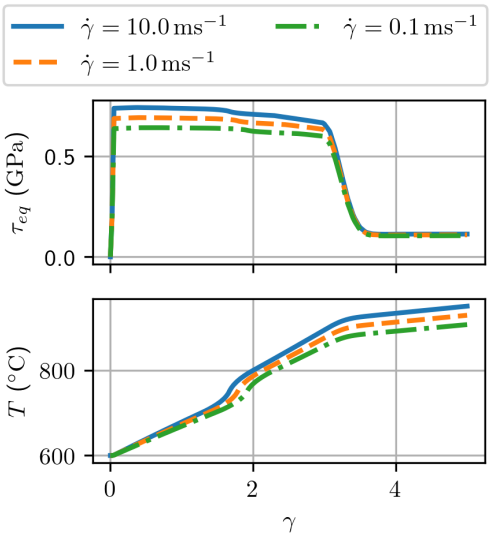

(b) Results obtained from the table-based Johnson-Cook implementation.

Figure 4.12: Exemplary results for the simple shear test with adiabatic heating at different loading rates $\dot{\gamma}$. All results were obtained at an initial temperature of $T_0 = 200\,°\mathrm{C}$.

Overall, although both models have been developed for 100Cr6, the predicted material behaviour shows significant differences. It could be speculated that the calibration of the JC model to cutting simulations, cf. [144], yields a material model which results in a good average prediction of the resulting forces under typical process conditions, while the influence of specific variables is not necessarily captured in detail.

On the other hand, more specific data was taken into account for the calibration of the proposed viscoplastic model, which is therefore more sensitive to temperature changes especially in the range below 1000 °C. However, the accordance of cutting forces predicted based on this model remains to be investigated.

4.4 Simulation frameworks

In this section, two different options to simulate the engagement of a single cutting edge during the grinding of 100Cr6 are discussed. All simulations are based on the material models presented in section 4.3, and were implemented in the finite element software Abaqus.

The framework presented in section 4.4.1 is based on a Lagrangian description of both grain and workpiece. In contrast, a new framework based on the Coupled Eulerian Lagrangian method – which avoids the need for a remeshing scheme – is proposed in section 4.4.2. Both frameworks are then applied to example problems in section 4.5 to demonstrate their respective performance.

4.4.1 Remeshing-based simulation framework

The remeshing-based simulation model described in this section is largely based on the model proposed by Holtermann et al. [75], Holtermann [76], which was kindly made available to the author of this thesis. Although a comprehensive description is provided in Holtermann et al. [75], the key points are presented here for completeness.

A parametrised finite element model for the engagement of a cBN grain during grinding of 100Cr6 material was implemented. The underlying boundary value problem is depicted in fig. 4.13. The model contains a single grain, idealised as a trapezoid, while only a flat section of the workpiece material is considered, assuming that the actual workpiece geometry can be neglected, and that it is sufficient to consider material which moves close to the cutting zone during the process.

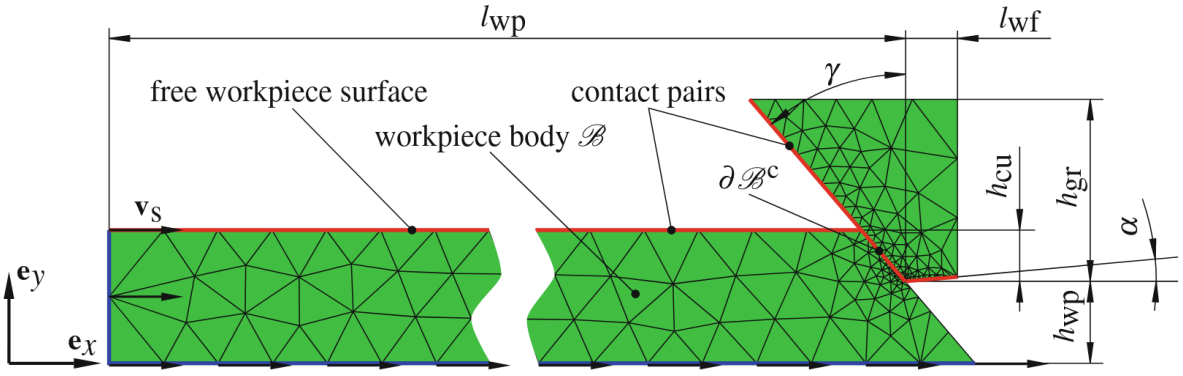

Figure 4.13: Boundary value problem for the parametrised meso-scale cutting simulations. Blue lines represent Dirichlet boundary conditions of the workpiece domain $\mathscr{B}$, while red lines represent surfaces which are potentially part of the contact surface $\partial\mathscr{B}^c$. For the studies presented in this thesis, the rake angle γ_s and undeformed chip thickness h_{cu}^s were varied, while the remaining parameters were either kept constant or chosen as multiples of the undeformed chip thickness. Figure reproduced from Holtermann et al. [75] with kind permission. The caption was replaced. It is remarked, that the rake angle γ_s is negative in this sketch.

In addition, simplified kinematics of the grain engagement are assumed, which resemble an orthogonal cutting process. Instead of considering the velocities of workpiece and grain, the combined relative velocity v_s is prescribed as a Dirichlet boundary condition for the workpiece, while all nodes of the grain are kept at a fixed position. Optionally the elastic deformation of the grain can be considered, however, this can introduce instabilities in the remeshing scheme, while the predicted average forces are nearly unaffected. The modelled length of the workpiece l_wp is chosen so that the cutting edge stays in contact with the workpiece material during the simulation, and no boundary effects occur at the end of the cut. Grain height h_gr and flank face length l_wf are chosen as multiples of the undeformed chip thickness h_cu, and the clearance angle α is kept constant for all simulations.

Both workpiece and grain are initialised at a given initial temperature, which evolves due to inelastic heating, friction, and heat conduction, i.e. the model is fully thermomechanically coupled.

Since no specific data is available for the friction between tool and workpiece, especially considering the interaction with the cooling medium, Coulomb friction with a coefficient of 0.1 is applied, which was shown in [75] to yield good results for a similar process.

Both grain and workpiece are modelled as Lagrangian bodies, and a remeshing scheme is applied periodically during each simulation to accommodate the large deformations of the workpiece domain $\mathscr{B}$ during chip formation. The remeshing allows for mesh refinement and coarsening, and is based on the comparison of the equivalent plastic strain field with a recovered solution obtained from the Zienkiewicz-Zhu error estimator [204]. All parameters related to the remeshing were chosen according to [75, 76].

4.4.2 CEL-based simulation framework

The Coupled Eulerian Lagrangian (CEL) method allows large deformations without the need for remeshing. Since the mesh remains unchanged, the advection algorithm for the state variables is more efficient compared to the periodic adaptive remeshing used in section 4.4.1. Furthermore, CEL is directly available in Abaqus, reducing both the required complexity and implementation effort for the simulation framework.

To make use of the CEL capabilities of Abaqus, the geometric domain close to the cutting edge is discretised by an Eulerian grid. A volume fraction variable describes the amount of workpiece material in each element, and the boundary of the workpiece is approximated by the 50 % isosurface of this variable. This surface is available in Abaqus for contact interactions with the Lagrangian body describing the cutting edge, however, unfortunately not for general thermal boundary conditions such as heat convection. Since the surfaces are recalculated in each increment, CEL naturally includes separation of material from the workpiece.

The same material models and subroutines as in (explicit) Lagrangian Abaqus simulations can be used for the Eulerian material in CEL, so that the simulation framework can

be combined with both models presented in section 4.3.1 and section 4.3.2. Although no heat transport at boundaries of the workpiece can be prescribed, heat transport within each body, as well as heat exchange between workpiece and cutting edge, is included in the model, which therefore is thermodynamically fully coupled.

A sketch of the boundary value problem for a cutting edge with a rake angle of $\gamma_s = -20°$ is shown in fig. 4.14.

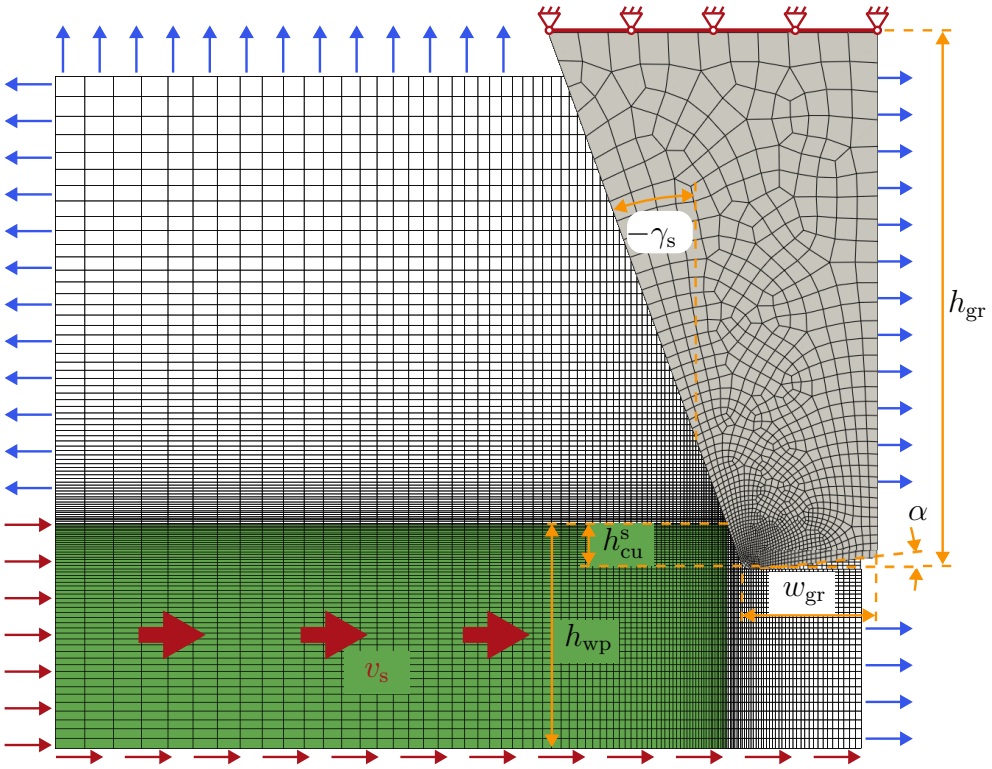

Figure 4.14: Boundary value problem for the CEL simulation of meso-scale cutting with a rake angle of $\gamma_s = -20°$. The Lagrangian body representing the cutting edge is shown in grey, and is kinematically fully constrained on the upper edge (marked by red symbols). Optionally, all displacements of the grain nodes can be fixed. In the Eulerian domain, green colour indicates elements initially filled with workpiece material, while white colour is used for initially empty elements. A non-uniform element size ensures good geometric approximation near the cutting zone, while a reduced accuracy is accepted at larger distances to reduce computational effort. The prescribed relative velocity v_s is applied at the boundary regions marked by red arrows, while blue arrows represent boundaries where workpiece material is allowed to freely exit the Eulerian domain. An initial velocity condition compatible with the external velocity constraints is applied to all Eulerian elements, symbolised by the large red arrows.

Adiabatic boundary conditions are prescribed on all boundaries of cutting edge and workpiece. While a convection condition on the chip surface would be physically reasonable, this is unfortunately not supported by the CEL implementation. Heat is transported into and out of the Eulerian domain by the flow of workpiece material, which enters the domain at room temperature and exits at a non-homogeneous temperature. Since no

two-dimensional implementation is available for CEL, a single layer of hexahedral elements is used, and boundary conditions on the front and back side enforce a plane strain setting. These surfaces are also modelled as adiabatic. The flow velocity is prescribed at the inflow and bottom part of the Eulerian mesh, while free material outflow is possible at the other surfaces which are not in the x-y-plane.

To reduce the computational cost, a graded mesh density was prescribed for the Eulerian domain, with the minimum element size at the contact zone between workpiece and cutting edge. The improved performance comes at the cost of reduced resolution of geometric workpiece and chip features at larger distances from the cutting zone.

Self contact of workpiece material in the Eulerian description joins the separate flows, so that the chip would merge back into the workpiece. To avoid this problem, a rigid plane shell is placed above the workpiece material flowing towards the cutting edge (not depicted in fig. 4.14). Instead of self contact, the chip establishes contact with this separator part, approximating the influence of the contact. However, since the separator does not move, any tangential force acting on the chip due to the self contact is neglected.

4.5 Comparison of frameworks

To evaluate the simulation frameworks, the engagement of a cutting edge with an undeformed chip thickness of $h_{\mathrm{cu}}^{\mathrm{s}} = 10\,\mu\mathrm{m}$ and a rake angle of $\gamma_{\mathrm{s}} = -20°$ is considered. A cutting velocity of $75\,\mathrm{m\,s^{-1}}$ was chosen for the example, and rigid grains were used in both frameworks.

Simulations were performed with both material models (Johnson-Cook model presented in section 4.3.1 and consistent model proposed in section 4.3.2) in the CEL framework. Only the Johnson-Cook model was used in the remeshing framework due to the required effort to combine the existing code with the new model.

For an initial temperature of 100 °C, the chip morphology obtained at a defined time of $t = 2\,\mu\mathrm{s}$ with both frameworks using the Johnson-Cook model is shown[2] in fig. 4.15.

Both frameworks predict a segmented chip structure resulting from shear band formation. While the segmentation is clearly visible near the cutting zone, the chip shape becomes smoother at larger distances. This – clearly unphysical – effect is caused by the reduced geometric precision due to the different element sizes, see fig. 4.14. Besides the geometric shape, the solution fields such as the equivalent plastic strain are smoothed as well.

[2] All contour plots in this section were created in ParaView [13]. To visualise the workpiece in the CEL framework, the workpiece material volume fraction was extrapolated to the nodes of the Eulerian mesh, and subsequently subjected to an isovolume filter. The export of the simulation data from Abaqus to the `vtu` file format used by ParaView was performed by using the free and open source Python package Paraqus [55], which was co-developed by the author of this thesis.

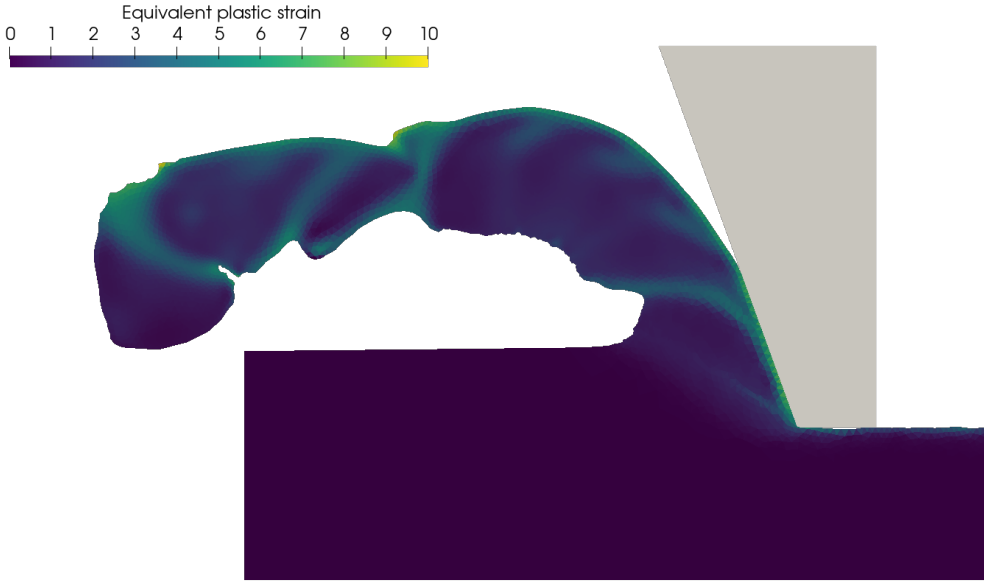

(a) Result from remeshing framework.

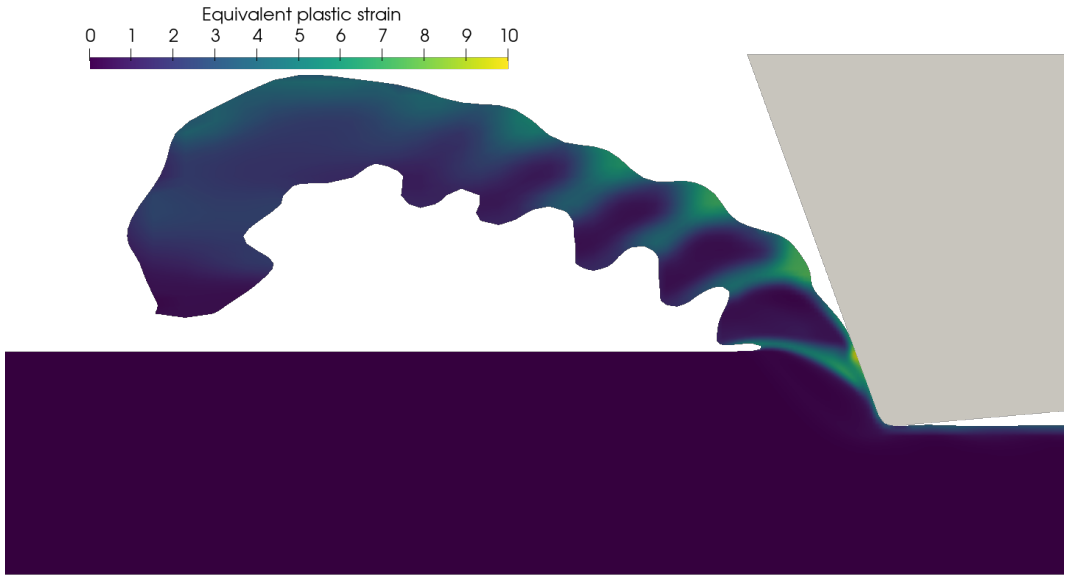

(b) Result from CEL framework.

Figure 4.15: Predicted chip morphology and equivalent plastic strain $\varepsilon_{\mathrm{p}}^{\mathrm{eq}}$ at $t \approx 2\,\mu\mathrm{s}$, obtained using the Johnson-Cook model. Both plots have been cropped to focus on the chip, and the colour legend has been clipped at $\varepsilon_{\mathrm{p}}^{\mathrm{eq}} = 10.0$.

A more regular shear banding pattern and chip shape is predicted near the cutting edge by the CEL framework, while not all shear bands result in fully formed segmentation in the remeshing framework. However, an acceptable overall agreement is obtained from both frameworks, especially given the expected inaccuracies and mesh dependencies.

A plot of the forces predicted during the chip formation by both frameworks is shown in fig. 4.16. The results are normalised to an undeformed chip width (i.e. the chip width normal to the x-y-plane) of 1 mm. Due to the different implementations, a higher number of time steps was exported for the remeshing framework. In general, the exported forces represent instantaneous values, and do not accurately represent vibrations due to the sampling.

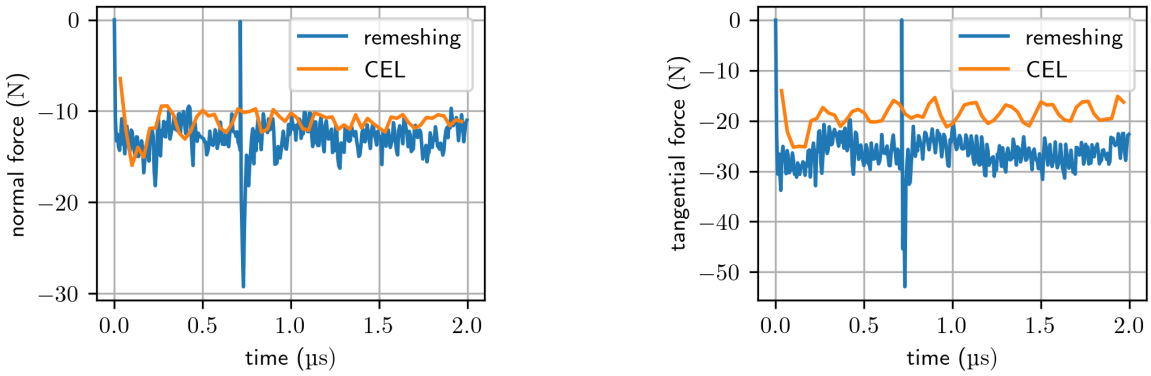

(a) Normal force F_n.

(b) Tangential force F_t.

Figure 4.16: Comparison of normal and tangential forces obtained from the remeshing and CEL frameworks using the Johnson-Cook based model. All forces are given for a unit thickness of 1 mm.

While a good agreement can be observed in the normal force component, the tangential forces predicted by the CEL framework are consistently lower than for the remeshing framework. This is in accordance with the prediction of a lower chip thickness and more regular shear bands shown in fig. 4.15. It is to be mentioned that some of the oscillations in the remeshing results can be attributed to shocks induced by incompatibilities in the mapped stress and strain fields after remeshing, especially the distinct spike at $t \approx 0.7\,\mu\mathrm{s}$.

In the following, the material models presented in section 4.3.1 and section 4.3.2 are compared by using the same example problem described above. However, the cutting edge was modelled as elastic instead of rigid in these simulations. In addition, a second initial temperature of 50 °C was considered to investigate the temperature dependency in the context of the chip formation simulations. Since the consistent material model proposed in section 4.3.2 was not combined with the remeshing framework, all simulations in this section were performed with the CEL framework.

The chip morphology after a defined time is shown in fig. 4.17 for both initial temperatures and both material models. Colouring of the workpiece material represents the value of equivalent plastic strain.

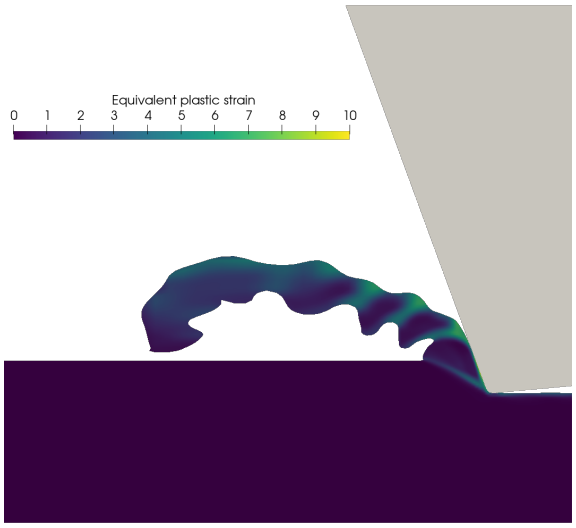

(a) Johnson-Cook model, $T_0 = 50\,^{\circ}\mathrm{C}$.

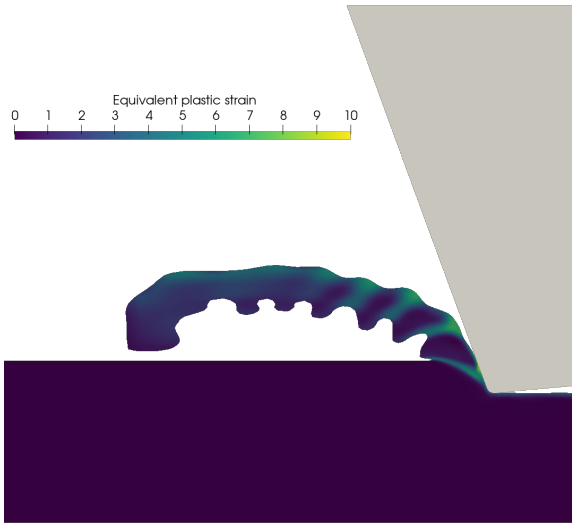

(b) Johnson-Cook model, $T_0 = 100\,^{\circ}\mathrm{C}$.

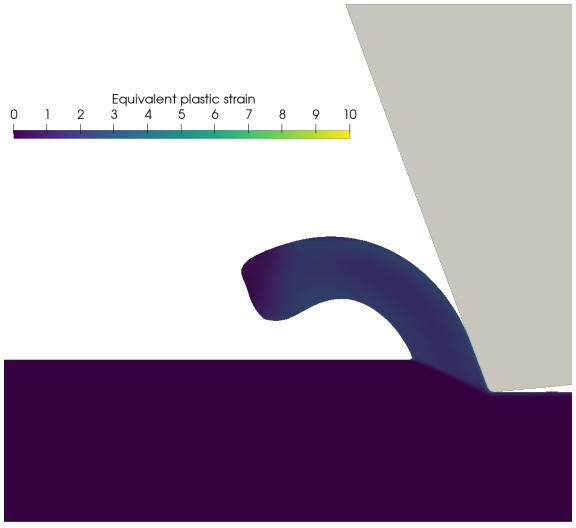

(c) Consistent model, $T_0 = 50\,^{\circ}\mathrm{C}$.

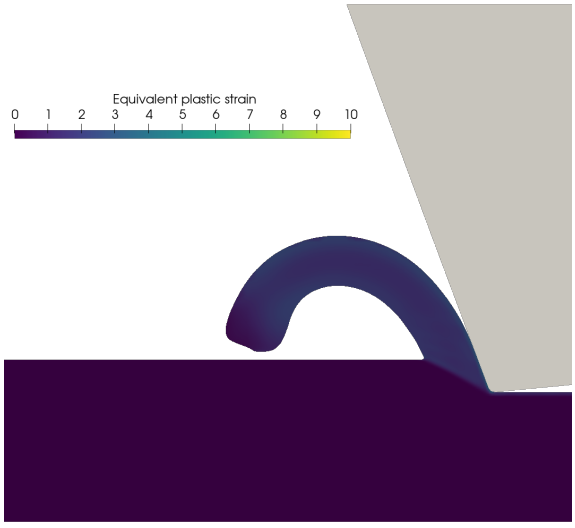

(d) Consistent model, $T_0 = 100\,^{\circ}\mathrm{C}$.

Figure 4.17: Predicted chip morphology and equivalent plastic strain $\varepsilon_{\mathrm{p}}^{\mathrm{eq}}$ at $t \approx 2\,\mu\mathrm{s}$, obtained using the CEL framework.

The Johnson-Cook model leads to the segmentation of the chip shown in fig. 4.15 at both temperatures (figs. 4.17a and 4.17b). However, no segmentation is visible in the results obtained with the consistent viscoplastic model (figs. 4.17c and 4.17d). While the chip morphology is quite similar for both initial temperatures when using the Johnson-Cook model, a reduction of chip thickness can be observed for the consistent model at 100 °C when compared to 50 °C. This observation is in line with the more pronounced temperature dependency of the consistent model, cf. fig. 4.12.

The sum of the reaction forces at the Dirichlet-constrained nodes of the cutting edge for each case is presented in fig. 4.18, with fig. 4.18a showing the force component F_y normal to the relative velocity, and fig. 4.18b showing the tangential component F_x.

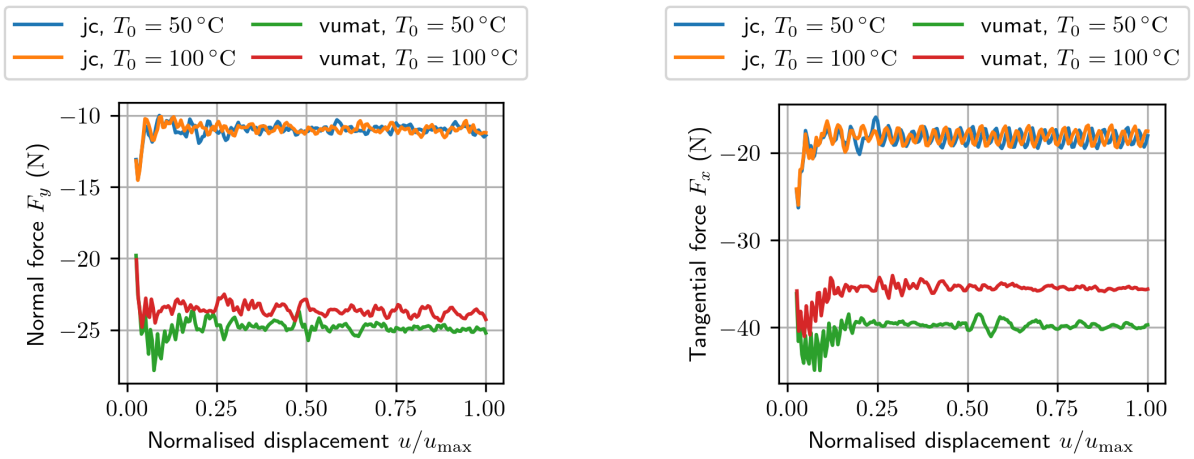

(a) Normal force F_n.

(b) Tangential force F_t.

Figure 4.18: Normal and tangential force components during the chip formation obtained from the Johnson-Cook model (jc) and the VUMAT implementation of the proposed consistent model (vumat). Results are shown for initial temperatures of $T_0 = 50\,°C$ and 100 °C. All force curves consist of force values exported at 200 equidistant time values, which were smoothed with a moving average filter, and are given for a unit thickness of 1 mm.

All force curves show a transient phase at the beginning of the cut, followed by a quasi-stationary response with a lower amplitude. The shear bands which lead to the segmentation of the chip when using the Johnson-Cook model are reflected in periodic fluctuations of the quasi-stationary force response, especially in the tangential component. Normal and tangential forces predicted by using the Johnson-Cook model are lower than those obtained with the consistent model at the initial temperatures considered. While the forces are nearly unaffected by the change in initial temperature for the Johnson-Cook model, a reduced force amplitude can be observed for the consistent model at 100 °C compared to 50 °C.

In summary, both frameworks yield similar predictions for chip morphology and forces when the Johnson-Cook model is used. In comparison to the remeshing framework, which offers a high degree of flexibility, the CEL framework reduces the need for expert

knowledge as well as the complexity of the overall simulation system. Furthermore, the computational effort required by the CEL framework scales linearly with the simulated time period. In contrast, a larger workpiece model is required in the remeshing framework for larger time periods, introducing an above linear scaling of the required computational time. However, the remeshing framework is more flexible with regard to thermal boundary conditions, where the CEL framework only allows adiabatic free workpiece surfaces.

To obtain accurate predictions, the choice of a well-suited material model is paramount. The differences of the two models considered in this thesis outweigh the influences of the different simulation frameworks, underlining the importance of a well calibrated model for specific applications. It would therefore be beneficial to evaluate the presented models based on experimental data at the meso-scale, if this data becomes available in the future.

4.6 Conclusion

In this chapter, a thermodynamically consistent material model for 100Cr6 in the hardened state was proposed. Based on one element tests and examples resulting in a homogeneous state of deformation, the new model was compared to the modified Johnson-Cook model used in e.g. [75, 76] for the same material. It was shown that the new model is able to reproduce the transition from brittle to ductile behaviour between 20 °C and 200 °C, which is evident in the data published by Guo and Liu [62].

Furthermore, a simulation framework for the mesoscopic cutting of single grains during grinding processes, based on the Coupled Eulerian Lagrangian method, was implemented, which allows very large deformations without the need for a remeshing scheme. It was shown that the CEL-based framework predicts process forces and chip morphology similar to the remeshing-based approach used in e.g. [74, 75]. Since no remeshing is required, the CEL-based framework has less meta-parameters and is easier to apply to new problems. However, it is suitable only for relatively fast cutting processes, as it requires a larger number of degrees of freedom, and only adiabatic boundary conditions can be used on free surfaces.

Overall, the discrepancies between published datasets and model parameters also highlight the need to adapt the model for mesoscopic cutting simulations to the specific microstructure of the product under consideration. A comprehensive evaluation of modelling approaches would greatly benefit from reliable experimental reference data for meso-scale cutting processes, which is currently not available.

5 Simulation of internal traverse grinding

In the following chapter of this thesis, which is mainly based on the publications [159] and [185], a framework for the simulation of internal traverse grinding processes is presented.

5.1 Introduction and objectives

As described in section 1.3, the kinematics of traverse grinding lead to a constantly changing engagement situation between grinding tool and workpiece. These changes are reflected by variations of process forces, and therefore – since the machining system has a finite stiffness – variations of the resulting contour.

Specifically, the proposed framework was applied to the simulation of high-performance internal traverse grinding of bearing rings with electroplated cBN tools, where characteristic step-like contour errors can occur at both ends of the bore.

The proposed framework is based on the multi-scale simulation system developed by Holtermann et al. [75] and further extended by Schumann [163]. The original framework consists of three main components: The heat generation and process force contributions during the engagement of individual grains are predicted by a surrogate model, which was calibrated through finite element simulations of single grain engagements. A digital grinding wheel model is intersected with a model of the workpiece in a geometric kinematic simulation (GKS) to simulate the actual engagements during the grinding process. Finally, a macro-scale finite element simulation was used to include clamping-related deformation of the workpiece as well as thermal effects.

The proposed framework incorporates methods proposed by Siebrecht et al. [165], Siebrecht [166] for the modelling of the grains, which allows incorporating grain geometries obtained from measuring real grinding wheels instead of artificially generating the geometries. Furthermore, a simplified compliance model is presented, which was calibrated based on a static analogy test. The process forces are calculated directly in the GKS based on an efficient surrogate model for the mesoscopic single grain engagements.

Two separate reference settings were considered for the machining of bearing rings: A 'laboratory' setting at the Institute of Machining Technology at TU Dortmund University, and an 'industry' setting in collaboration with *Schaeffler Technologies AG & Co. KG*. While both settings required specific treatment especially from the experimental point of view, the treatment of both in the proposed simulation system is very similar. Attention therefore especially focuses on the industrial use case in the following. It is hereby mentioned that the experimental investigations were further supported by *August Rüggeberg GmbH & Co. KG*, who provided the tools used in the study.

5.2 State of the art

The simulation of grinding processes poses significant challenges due to complex interactions over multiple scales. In general, the material removal is realised on the meso-scale by an unknown – and changing – number of cutting edges simultaneously. Each cutting edge has a different geometry, and the local conditions under which material is removed, such as temperature, workpiece surface shape, and hardening state of the workpiece material, change even between successive engagements of the same cutting edge. Furthermore, the collective mechanical load from the process results in an elastic deformation of the machining system, which is reflected in the engagement situation.

Finite element simulations have been applied with great success to the simulation of cutting processes with geometrically defined edges for example in [46, 113, 144]. It is however unfeasible to apply this approach directly to the simulation of grinding due to the required geometrical resolution and the resulting computational cost. Various other types of grinding simulations have been proposed, for example for the prediction of process forces [148] and tool deflections [9, 37].

qtd. [53] {An overview on the modelling of grinding processes is given in [25], where models are classified into seven categories: artificial neural networks, regression models, rule-based models, fundamental analytical models, kinematic models, finite elements based models, and molecular dynamics models. It is concluded that kinematic models provide the highest flexibility for different grinding operations or tools and, together with models based on finite elements or molecular dynamics, facilitate a higher level of understanding of the processes.} qtd. [53]

A specific type of kinematic model, so-called geometrically physically-based simulations (GPS), have been applied very successfully to the simulation of milling and grinding [2, 25]. This approach is characterised by high-precision geometric approximation of tool and workpiece geometry, and therefore the geometrical engagement situation, as well as the possibility to simulate a complete machining process efficiently.

qtd. [185] {Mesoscopic simulations, which model the interaction between the workpiece and the complete grinding wheel down to the engagement of every single grain, were presented for grinding processes [8, 25, 147], including internal traverse grinding [163], but are in practice limited to the simulation of a few grinding wheel rotations because of the much

higher computational effort that is required.}$^{\text{qtd.}}_{[185]}$ $^{\text{qtd.}}_{[185]}${An enhanced method developed by Siebrecht [166] for face grinding [165, 166] is computationally more efficient than older approaches and well suited to incorporate the changes in grain shapes due to wear.}$^{\text{qtd.}}_{[185]}$

A multi-scale simulation system was proposed by Holtermann et al. [75]. Therein, grains made of cubic boron nitride (cBN) on an electroplated grinding wheel were modelled based on geometric primitives through constructive solid geometry (CSG). Based on meso-scale finite element simulations of the engagement of individual grains, surrogate models were calibrated to predict the force contributions and heat generation of individual grains based on the undeformed chip thickness and rake angle, which were identified as the most important parameters. A geometrical physically-based simulation was used to model the engagement of the individual grains during the grinding process, and to calculate the resulting macroscopic mechanical and thermal loading. While the evaluation of the rake angle based on the CSG models was directly possible, the approach is not directly transferable to general grain geometries. Finally, a macro-scale finite element simulation was used to account for deformations arising from thermal expansion, elastic compliance, as well as clamping, and to predict the final workpiece contour after grinding. Although the thermal and mechanical loads were predicted based on average values obtained from the GPS, they did not account for the current engagement situation (other than the material removal rate).

$^{\text{qtd.}}_{[185]}${A similar simulation approach, incorporating the spindle compliances in a meta model of the process, was proposed in [163], highlighting the relevance of the compliances for the accurate prediction of process results.}$^{\text{qtd.}}_{[185]}$ In contrast to the FE based approach in Holtermann et al. [75], Schumann [163] applied a force model which was experimentally calibrated.

Since the contributions of the author of this thesis are related primarily to the compliance and force models, these aspects of the new simulation system will be discussed comprehensively in the following, while the interested reader is referred to Tsagkir Dereli et al. [185] for any details of the GPS which are not presented here.

5.3 Machining system compliance

A model for the elastic compliance of the machining system is required to account for elastic deflections during the grinding process based on the forces obtained from the surrogate force model.

In the following, a static analogy test is presented which was used to obtain experimental compliance data. The compliance model used in the GPS is then presented, together with the calibration procedure based on the experimental data.

5.3.1 Static analogy test

A static analogy test was used to measure the stiffness of different parts of the machining system. The discussion in this thesis focuses on the general approach, and the interested reader is referred to the publications [159, 185] for a comprehensive description of the experimental procedure.

A force measurement platform was used to record forces in the analogy test for the laboratory setting, while in the analogy test for the industrial setting, the workpiece holder was replaced by a custom construction including a piezoelectric force sensor. Eddy-current sensors were additionally positioned at the headstock, as well as along the tool. The tool was initially positioned so that a gap of approximately 5 µm remained between tool and workpiece. It was then radially moved towards the workpiece in 30 increments of 0.5 µm through the machine control without tool rotation, and subsequently moved back to its original position.

An exemplary measurement of measured distance d at the headstock and corresponding normal force F_n is presented in fig. 5.1. $\overset{\text{qtd.}}{\underset{[185]}{}}\{$The headstock moves approximately 10 µm away from the sensor at zero force (grey dots), until contact with the workpiece holder is established. Any additional movement of the headstock results in a deflection of the system and in a corresponding increase of the normal force (blue dots). Although the loading and unloading paths can be visually distinguished, a reasonable approximation of the effective system compliance c was obtained from a linear regression of the force-distance-data, neglecting data points where the measured force does not exceed a threshold of $F_0 = 3\,\mathrm{N}.\}^{\text{qtd.}}_{[185]}$

5.3.2 Compliance model

The static analogy test described in section 5.3.1 was performed 68 times for the laboratory setting and 25 times for the industry setting, covering three different positions of the grinding wheel along the bore of the workpiece in each setting. For the industrial setting compliance values between different contact positions varied by as much as 100 %. This was judged unrealistically high, and attributed to possible movements of the workpiece in the holder. In contrast, only a minor influence (below 5 %) was found for the laboratory setting.

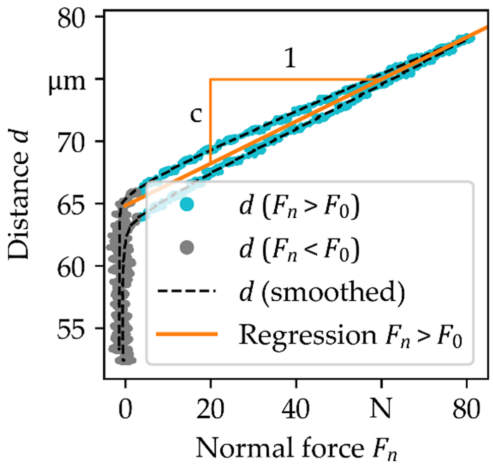

Figure 5.1: Exemplary evaluation of the effective machine compliance c, based on headstock distance d and normal force F_n. *Figure reproduced from Tsagkir Dereli et al. [185] under the terms of the CC BY 4.0 license. Only subfigure a) is reproduced here with an altered caption.*

The effective machining system compliance was therefore simply modelled as the average

$$\bar{c} = \frac{1}{n} \sum_{i=1}^{n} c_i \tag{5.1}$$

of n values obtained from the static analogy test, whereas only one contact position was included for the industrial setting.

5.4 Cutting force model

An efficient surrogate model for the process force contribution of individual grains is required to include elastic deflection in the geometrical physically-based simulation. Such a model – based on fitting a phenomenological function to the results of finite element simulations of single grain engagements – was proposed by Holtermann [76], who identified the undeformed chip thickness h_cu^s and rake angle γ_s as the most important parameters.

In this section, finite element simulations of single grain engagements, similar to those used by Holtermann [76], are presented. Based on the evaluation of these simulations, a new surrogate model is proposed for contributions of the individual grain to normal and tangential forces.

5.4.1 Finite element simulations

Single grain engagements were simulated by using the remeshing-based finite element simulation framework presented in section 4.4.1. The Johnson-Cook based material model presented in section 4.3.1 was used for these simulations. It is, however, to be mentioned that a similar force model can be derived by using the alternative CEL framework presented in section 4.4.2, and that this framework allows a straightforward combination with the new material model proposed in section 4.3.2.

A selection of representative force-displacement curves is presented in fig. 5.2, where the forces were obtained from the reaction forces of the grain nodes subject to Dirichlet boundary conditions. The displacement of the grain, which is calculated from the relative cutting velocity v_s as

$$u^\mathrm{s} = v_\mathrm{s}\, t \ , \tag{5.2}$$

is normalised by the undeformed chip thickness h^s_cu.

qtd. [185] { To compare the forces for varying undeformed chip thicknesses h^s_cu, specific values per theoretical material removal rate Q^s_w of the single grain were calculated, i.e.

$$\tilde{F}^\mathrm{s}_\mathrm{n/t} = \frac{F^\mathrm{s}_\mathrm{n/t}}{Q^\mathrm{s}_\mathrm{w}} \ , \tag{5.3}$$

where the material removal rate is calculated based on unit width b, the undeformed chip thickness and on the relative cutting speed v_s for the single grain engagement as

$$Q^\mathrm{s}_\mathrm{w} = v_\mathrm{s}\, b\, h^\mathrm{s}_\mathrm{cu} \ . \tag{5.4}$$

A pronounced dependency of the specific forces on the rake angle γ_s can be observed: Large negative rake angles produce higher values for both normal and tangential forces. However, no significant influence of the undeformed chip thickness on the specific forces was found. Although only some exemplary curves are shown in fig. 5.2, these trends held true for all simulations conducted.

The force curves for rake angles closer to 0° show oscillations around an approximately constant value. Larger negative values of γ_s lead to a reduced number of oscillations, and values below a certain threshold do not show any oscillations at all. This observation is linked to the emergence of shear bands in the workpiece material and resulting chip formation. Figure 5.3 shows exemplary deformed workpiece geometries to demonstrate this effect. The segmented chip obtained for $\gamma_\mathrm{s} = -40°$ coincides with the oscillations in the corresponding force curves. Only one distinct chip emerged for $\gamma_\mathrm{s} = -60°$ before the simulation terminated because chip separation was not included in the model. For $\gamma_\mathrm{s} = -80°$, no chip formation was observed in the simulations. } qtd. [185]

As shown in fig. 5.2, when considering the specific force generation per material removal rate, the undeformed chip thickness h^s_cu has no significant impact. Based on this result, the proposed surrogate model for the single grain force contributions was

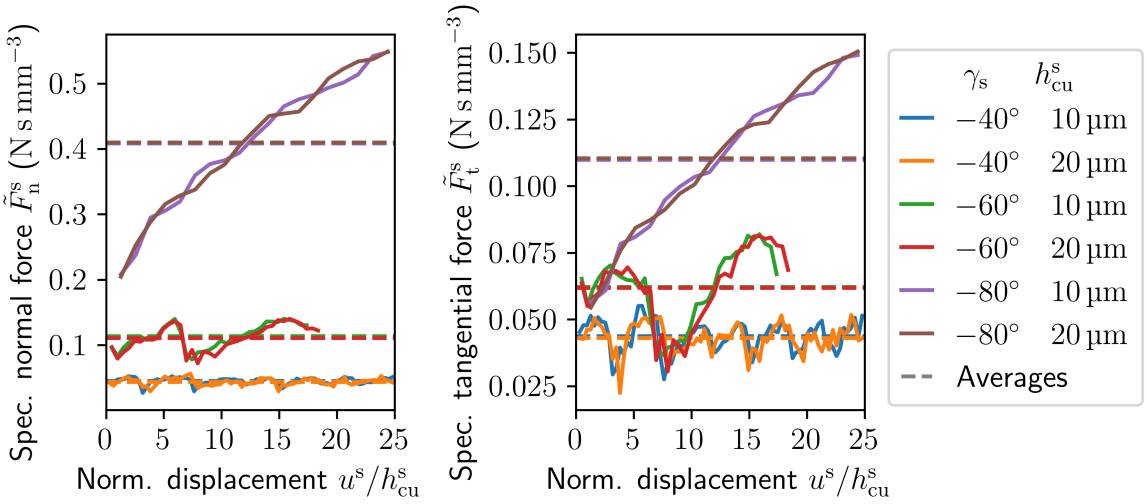

Figure 5.2: Exemplary specific normal and tangential force curves, for multiple combinations of rake angle γ_s and undeformed chip thickness h_cu^s, obtained from single grain FE simulations. The displacements are normalised by h_cu^s. Dashed lines indicate average values for each curve. *Figure reproduced from Tsagkir Dereli et al. [185] under the terms of the CC BY 4.0 license. Based on the original data, the subplot size was updated, and symbols were adapted to the notation used in this thesis. A single figure is presented instead of subplots a) and b).*

parametrised only in terms of the rake angle γ_s (apart from scaling the results by the material removal rate). It is hereby mentioned that real-world experience suggests that a size effect does indeed exist for small values of the undeformed chip thickness, but is not captured by this model.

5.4.2 Surrogate force model

$\overset{\text{qtd.}}{\scriptstyle[185]}\{$A parameter study was conducted for a constant value of $h_\mathrm{cu}^\mathrm{s} = 10\,\mu\mathrm{m}$ and $-20° \geq \gamma_\mathrm{s} \geq -82°$. Based on [163], it was assumed that predominantly large negative rake angles occur in the ITG process, and therefore the parameter study was focused on rake angles $\gamma_\mathrm{s} \leq -40°$. The restriction to angles $\gamma_\mathrm{s} \geq -82°$ is due to numerical instabilities occurring in the single grain simulations past this value. $\}^{\text{qtd.}}_{[185]}$

Empirical ansatz functions were used for the surrogate model for the single grain forces, where the function parameters were obtained from a least squares fit to the data obtained from the meso-scale finite element simulations. $\overset{\text{qtd.}}{\scriptstyle[185]}\{$For the normal forces, the exponential ansatz function

$$\tilde{F}_\mathrm{n}^\mathrm{s,exp}\left(\gamma_\mathrm{s}\right) = b_0 \exp\left(b_1\left[\gamma_\mathrm{s} - b_2\right]\right) + b_3 \tag{5.5}$$

was used, whereas for the tangential forces the functions

$$\tilde{F}_\mathrm{t}^\mathrm{s,exp}\left(\gamma_\mathrm{s}\right) = c_0 \exp\left(c_1\left[\gamma_\mathrm{s} - c_2\right]\right) + c_3 \tag{5.6}$$

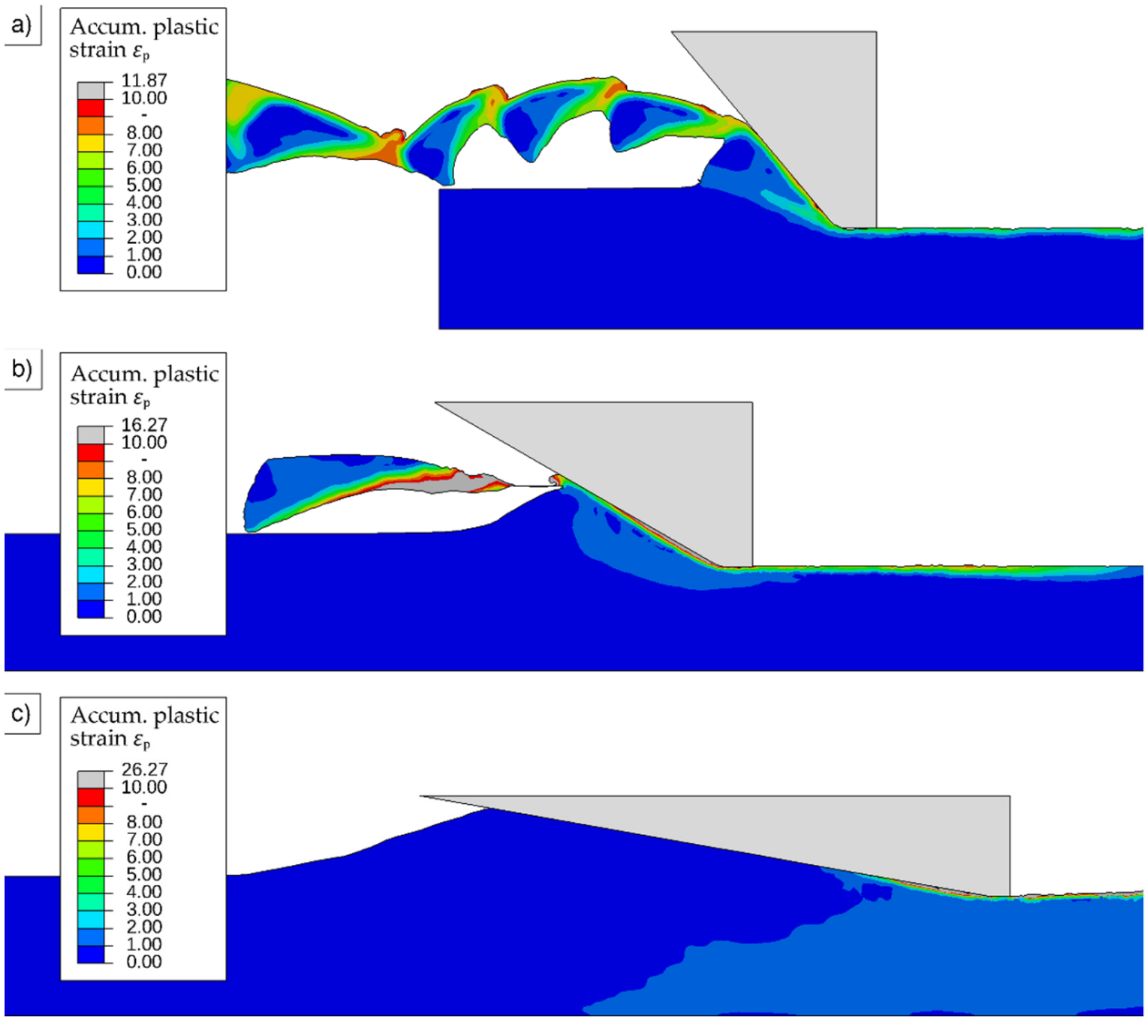

Figure 5.3: Chip formation for different rake angles γ_s: **a)** $\gamma_s = -40°$, **b)** $\gamma_s = -60°$ and **c)** $\gamma_s = -80°$. Colour plot indicates the accumulated plastic strain. *Figure reproduced from Tsagkir Dereli et al. [185] under the terms of the CC BY 4.0 license. No changes were made.*

and

$$\tilde{F}_t^{s,\tanh}(\gamma_s) = d_0 \tanh\left(d_1\left[\gamma_s - d_2\right]\right) + d_3 \tag{5.7}$$

were compared.

The results of the parameter study, as well as the force models resulting from the curve fits, are shown in fig. 5.4, and the coefficients obtained for each ansatz function are presented in table 5.1.

It should be mentioned that, since the force curves did not saturate for large negative rake angles in the single grain simulations, a systematic underestimation of the predicted

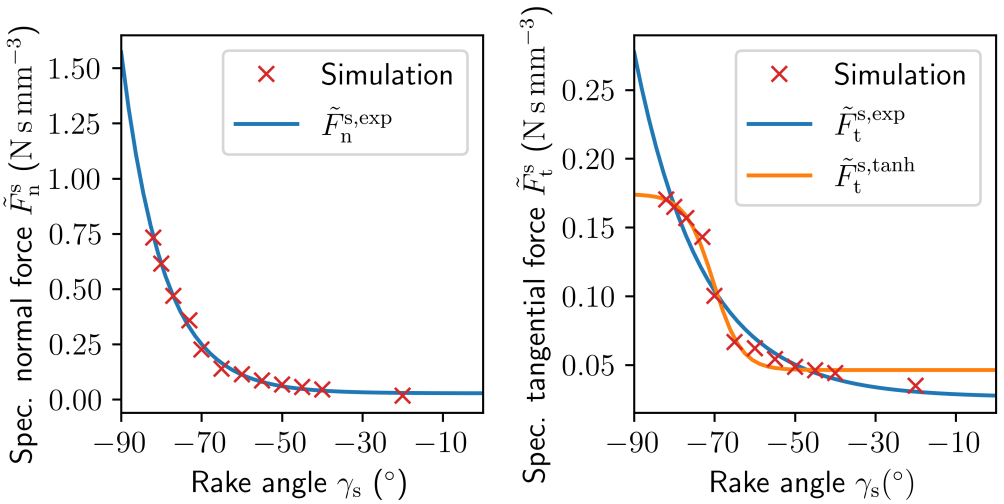

Figure 5.4: Specific normal and tangential single grain cutting forces obtained from the parameter study, and approximation by the proposed force models. *Figure reproduced from Tsagkir Dereli et al. [185] under the terms of the CC BY 4.0 license. Figure reproduced from the original data with updated fonts and symbols matching this thesis. The caption was altered to reflect the presentation as one figure instead of two subplots.*

Table 5.1: Optimal force model coefficients based on results of the parameter study. *Table reproduced from Tsagkir Dereli et al. [185] under the terms of the CC BY 4.0 license. A typo in the unit column was corrected.*

Model	Parameter	Value	Unit
$\tilde{F}_\mathrm{n}^{\mathrm{s,exp}}$	b_0	0.00469046	N s mm^{-3}
	b_1	−0.096 937 84	1/°
	b_2	−30.204 010 38	°
	b_3	0.027 645 13	N s mm^{-3}
$\tilde{F}_\mathrm{t}^{\mathrm{s,exp}}$	c_0	0.00134135	N s mm^{-3}
	c_1	−0.058 788 25	1/°
	c_2	−1.014 632 76	°
	c_3	0.026 431 51	N s mm^{-3}
$\tilde{F}_\mathrm{t}^{\mathrm{s,tanh}}$	d_0	0.06397807	N s mm^{-3}
	d_1	−0.144 203 48	1/°
	d_2	−70.291 281 12	°
	d_3	0.110 259 13	N s mm^{-3}

forces at large negative rake angles is expected. Not all simulations covered the same displacements due to numerical difficulties, e.g. chip separation as shown above.}[qtd. [185]]

While the exponential ansatz function (5.5) accurately reproduces the simulation-based data for the specific normal forces, the corresponding ansatz (5.6) for the specific tangential forces does not capture the saturation for large negative rake angles, leading to a significant over-estimation in this regime. In contrast, the ansatz (5.7) reproduces the saturating behaviour for large negative rake angles, but results in a slightly worse fit for rake angles closer to 0°.

Since predominantly large negative rake angles are expected to occur during the grinding process, eq. (5.5) and eq. (5.7) were chosen for the single grain force surrogate model.

It is remarked that the surrogate model is not specifically calibrated to the use case presented, but is mainly based on the underlying FE simulation of the mesoscopic cutting process, and especially on the chosen material model. It is therefore reasonable to expect this approach to generalise well to other applications, given suitable calibration data for the workpiece material.

5.5 Multi-scale simulation system

A new multi-scale framework for the simulation of high-performance internal traverse grinding of 100Cr6 bearing rings is presented in this section. It combines elements of the simulation systems proposed by Holtermann et al. [75] and Schumann [163] with an efficient point-based modelling approach based on Siebrecht [166]. Furthermore, since the characteristic shape deviations at both ends of the bearing rings are attributed mainly to elastic deflection (as opposed to thermal deformation), the macroscopic FE simulation proposed by Holtermann et al. [75] was not implemented. Instead, the GPS was extended to directly consider the elastic deflection based on a compliance model for the machining system and a surrogate model for the single grain force contributions. After calibration of the force surrogate model, this approach allows the simulation of the complete grinding process in the GPS, combining the geometric accuracy of the method with the consideration of elastic deflections, which previously required an additional model. Furthermore, an improved prediction quality is expected for the process forces, because the engagement situation in different stages of the process is explicitly modelled and considered.

5.5.1 Digital grinding wheel

One of the main differences of the proposed simulation framework to the methods proposed by Holtermann et al. [75] and Schumann [163] is the geometric description of the cutting edges. Instead of geometric primitives, a database of triangulations of real grain geometries was created, and these triangulations were used to populate the digital

grinding wheel. qtd. [185]{For the grinding tools, 3D-printed shell containers were produced, and filled with the fast-curing two-part silicon rubber compound RepliSet-GF1 (Struers) to prepare high resolution 3D replicas of the tools, see fig. 5.5 a). The grinding wheel replica was measured across the roughing and finishing zone widths by using the light microscope Alicona Infinite Focus G5. From the visualised measurement data, individual grains were manually masked, see fig. 5.5 b). The height data of each grain were extracted and converted into a mesh to create a database of realistic grain geometries (fig. 5.5 c)). Because these meshes are based on evenly spaced vertices in a 2D projection, i.e. the top view, the 3D meshes exhibit elements with very small angles especially where the grains show large gradients in height. The open source software gmsh [58] was used to perform a remeshing of these 3D shell meshes, yielding near-uniform triangle meshes of a prescribed element size (fig. 5.5 d)). The individual grains have been randomly rotated and placed on the surface of the grinding wheel model according to a Poisson disk sampling [201] to reach a realistic grain concentration [166].}qtd. [185] The digital grinding wheel model represents each triangle as a point in the tool heightfield (fig. 5.5 e)), which is then used in the GPS (fig. 5.5 f)).

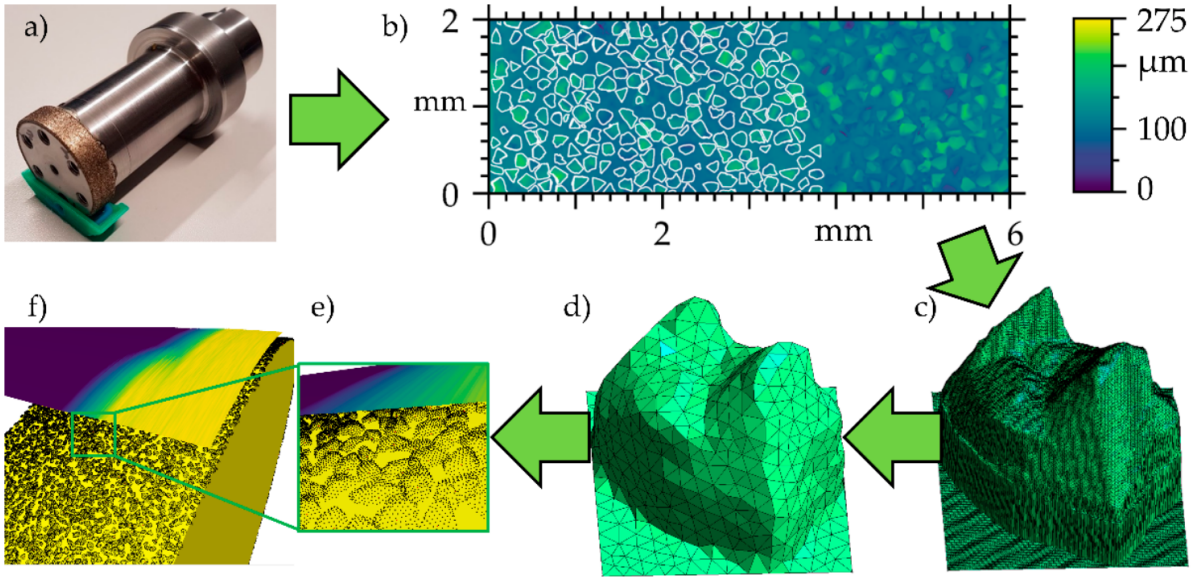

Figure 5.5: **a)** Preparation of a grinding wheel topography replica with silicon rubber compound, **b)** Manual preparation of masks for grain segmentation, **c)** Grain mesh based on the digitalised grinding wheel containing distorted triangles, **d)** Remeshing of the grain using the software gmsh yields nearly uniform triangles, **e)** Topography of the grinding wheel model, **f)** Geometric physically-based grinding simulation for ITG. *Figure reproduced from Tsagkir Dereli et al. [185] under the terms of the CC BY 4.0 license. No changes were made.*

5.5.2 Geometric physically-based simulation

Since the workpieces considered for this study are cylindrical, the geometrical physically-based simulation is based on a workpiece height field in cylindrical coordinates. For each time step, the volume of removed material is then calculated by a subtraction of the grain height fields from the current workpiece height field, which makes use of a predefined number of sub-steps. Since the author of the present thesis did not actively develop the proposed GPS, the interested reader is referred to Tsagkir Dereli et al. [185] and Siebrecht [166] for a more comprehensive description of the mathematical operations. It is hereby mentioned that this approach directly allows the approximation of the current material removal rate $Q_{\mathrm{w}}^{\mathrm{s}}$ as well as undeformed chip thickness $h_{\mathrm{cu}}^{\mathrm{s}}$ for each grain currently engaged with the workpiece.

Based on the rotational symmetry of the workpieces, only a selected circumferential section of the workpiece – which, due to the process kinematics, is engaged periodically by the grinding wheel– was modelled in the GPS, as shown in fig. 5.6. Since the calculated forces are representative only when the grinding wheel is fully engaged with the workpiece, results are considered only for the part of the workpiece model denoted as the 'stable section' in fig. 5.6 b).

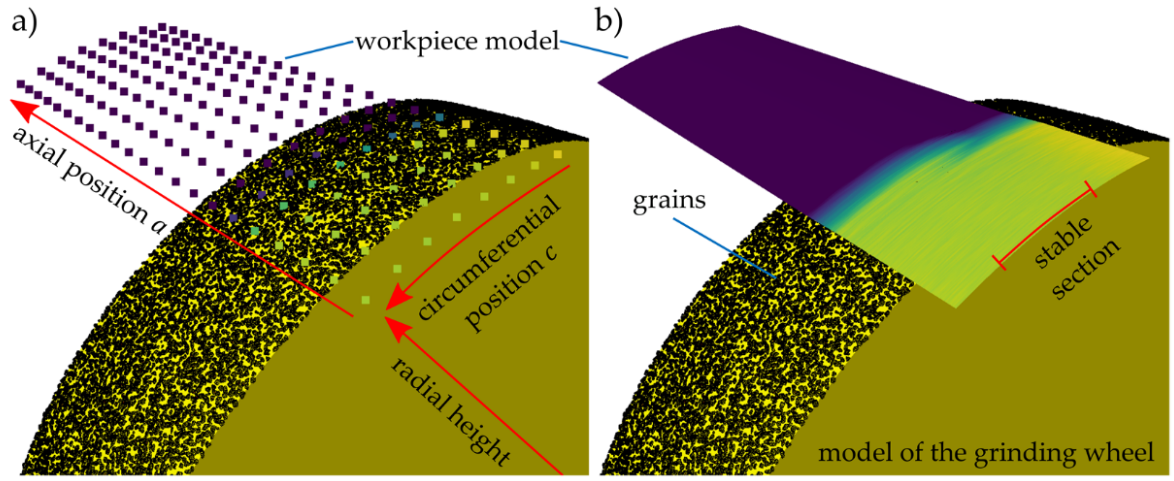

Figure 5.6: Visualisation of the tool and workpiece models. **a)** Only every 200th point in every dimension of the grid is visible, **b)** Every height value is rendered. *Figure reproduced from Tsagkir Dereli et al. [185] under the terms of the CC BY 4.0 license. No changes were made.*

An approximation of the (effective) rake angle γ_{s} is required for each engaged grain to calculate the cutting force contributions from the surrogate model presented in section 5.4.2. The proposed approximation method, which is based on the triangulation of the grain geometries, is visualised in fig. 5.7.

qtd. [185] {The triangles of the grain mesh, which are assumed to be engaged for a cutting direction $\boldsymbol{e}_{\mathrm{c}}$, are depicted in fig. 5.7 a) and b) for two different undeformed chip thicknesses $h_{\mathrm{cu}}^{\mathrm{s}}$. Triangles are considered only if they face in cutting direction, i.e. the

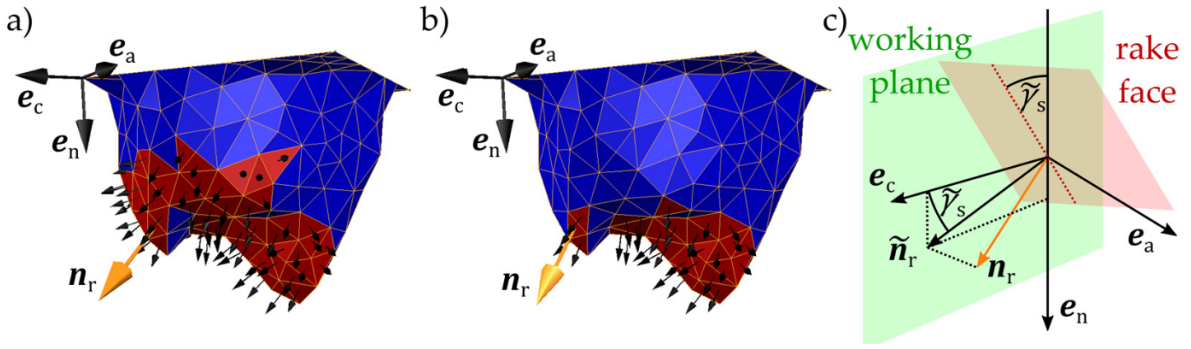

Figure 5.7: Calculation of the approximated rake angle $\tilde{\gamma}_\mathrm{s}$ for a single grain. **a)** Averaging of normal vectors in cutting direction for a higher value of the undeformed chip thickness h_cu^s. **b)** Averaging of normal vectors for a smaller value of h_cu^s. **c)** Schematic projection of the average normal vector $\boldsymbol{n}_\mathrm{r}$ into the working plane and calculation of the approximated rake angle $\tilde{\gamma}_\mathrm{s}$. *Figure reproduced from Tsagkir Dereli et al. [185] under the terms of the CC BY 4.0 license. No changes were made.*

projection of their normal onto the cutting direction $\boldsymbol{e}_\mathrm{c}$ is positive. The effective normal vector $\boldsymbol{n}_\mathrm{r}$ of a (virtual) plane rake face, see fig. 5.7, is approximated by averaging the normals of the engaged triangles. The effective rake angle γ_s is then approximated as

$$\gamma_\mathrm{s} \approx \tilde{\gamma}_\mathrm{s} = -\cos^{-1}\left(\frac{\tilde{\boldsymbol{n}}_\mathrm{r}}{\|\tilde{\boldsymbol{n}}_\mathrm{r}\|}\cdot\boldsymbol{e}_\mathrm{c}\right) \tag{5.8}$$

based on the projection $\tilde{\boldsymbol{n}}_\mathrm{r} = \boldsymbol{n}_\mathrm{r} - \boldsymbol{n}_\mathrm{r}\cdot\boldsymbol{e}_\mathrm{a}\,\boldsymbol{e}_\mathrm{a}$ of the effective normal vector into the working plane. To speed up the simulation, $\tilde{\gamma}_\mathrm{s}\left(h_\mathrm{cu}^\mathrm{s}\right)$ is calculated in steps of 0.011 mm the first time a grain is engaged and interpolated linearly for the exact h_cu^s of each engagement of the grain occurring during the entire grinding process.}$^{\text{qtd.}}_{[185]}$

Based on eqs. (5.5) and (5.7), the single grain force contributions can then be calculated by scaling the specific force contributions by the material removal rate, i.e.

$$F_\mathrm{n}^\mathrm{s} = \tilde{F}_\mathrm{n}^{\mathrm{s,exp}}\left(\tilde{\gamma}_\mathrm{s}\left(h_\mathrm{cu}^\mathrm{s}\right)\right)\, Q_\mathrm{w}^\mathrm{s}\ , \tag{5.9}$$

$$F_\mathrm{t}^\mathrm{s} = \tilde{F}_\mathrm{t}^{\mathrm{s,tanh}}\left(\tilde{\gamma}_\mathrm{s}\left(h_\mathrm{cu}^\mathrm{s}\right)\right)\, Q_\mathrm{w}^\mathrm{s}\ , \tag{5.10}$$

and the total process forces F_n and F_t are given by the sum of the single grain contributions. It is hereby mentioned that this approach is directly applicable for nearly arbitrary cutting edge geometries, and is therefore considered to be well suited for the application in other grinding processes as well.

With the process forces available, the compliance model presented in section 5.3.2 can be evaluated to calculate the elastic reduction Δa_e of the effective depth of cut $a_\mathrm{e,eff}$ as

$$\Delta a_\mathrm{e}\left(F_\mathrm{n}\right) \approx \bar{c}\, F_\mathrm{n}\ , \tag{5.11}$$

where $\bar{c}$ is the effective compliance of the machining system (cf. eq. (5.1)). In the GPS, the tool is radially offset from the workpiece by Δa_e. Whereas the dynamics of the interaction between tool and workpiece are not resolved, a numerical damping is applied to the elastic deflection to avoid spurious results.

5.6 Exemplary results

Internal traverse grinding tests were conducted which serve as a reference for the forces and final workpiece contours predicted by the simulations. The process parameters and experimental conditions are presented in table 5.2. While both settings (laboratory and industrial) were investigated, the comparison of the results is out of the scope of this thesis, and attention is focused on the industrial case in the following to demonstrate the capabilities of the proposed simulation system.

Table 5.2: Experimental conditions for grinding investigations. *Table reproduced from Tsagkir Dereli et al. [185] under the terms of the CC BY 4.0 license. The table formatting was updated to fit the style of this thesis.*

	Industrial Setup	**Laboratory Setup**
Tool spindle:	HV-P 120-45.000/18	HV-P 120-40.000/18
Grinding tool:	Electroplated cBN, B181, $D = 39\,\mathrm{mm}$, $\chi = 3°$	
Workpiece:	100Cr6/AISI 52100, $63 \pm 1\,\mathrm{HRC}$	
	Cylindrical: $D = 53\,\mathrm{mm}$, $d = 47\,\mathrm{mm}$, $w = 31.4\,\mathrm{mm}$	
Cooling medium:	Grinding oil, $\nu = 5\,\mathrm{mm^2\,s^{-1}}$	
Grinding tool velocity:	$v_\mathrm{t} = 80\,\mathrm{m\,s^{-1}}$	$v_\mathrm{t} = 75\,\mathrm{m\,s^{-1}}$
Workpiece velocity:	$v_\mathrm{w} = 1.33\,\mathrm{m\,s^{-1}}$	$v_\mathrm{w} = 1.25\,\mathrm{m\,s^{-1}}$
Axial feed rate:	$v_\mathrm{fa} = 120,\ 240,\ 360,\ 480, 600\,\mathrm{mm\,min^{-1}}$	
Total radial stock removal:	$a_\mathrm{e,tot} = 0.125\,\mathrm{mm}$	

A comparison of measured and simulated process forces in the industrial setting is presented in fig. 5.8. $^{\text{qtd.}}_{[185]}\{$A strong increase of the process forces was observed in the simulated as well as the experimentally recorded forces in the tool entry section. Whereas the simulation predicted a subsequent quasi-stationary phase in both normal and tangential forces, the measured normal force decreased in this phase.

The measured and simulated forces show good agreement at the tool exit, where all forces drop back to zero. The increase and drop of forces at the entry and exit zone are related to the progressive engagement and disengagement of the tool. Figure 5.8 b) displays the maximum process forces for all tested feed rates. A linear increase depending on the feed rate was observed. Whereas the normal forces exhibited a difference between 21.7 N and 33.5 N, a good agreement was observed for the maximum tangential forces between simulation and experiment with a difference between 1.6 N and 2.4 N.$\}^{\text{qtd.}}_{[185]}$

The comparison of measured and predicted inner workpiece contours, presented in fig. 5.9, shows good qualitative accordance. Shape deviations caused by the elastic deflections are visible as a reduction of the achieved stock removal from the set value of 0.125 mm. Accordingly, the lowest deviation is observed at the tool exit zone, where the set radial stock removal is nearly achieved, while no step-shaped deviations occur in

the tool entry zone. This is correctly predicted by the presented simulation framework, showcasing the ability to incorporate the elastic deflections directly in the GPS. However, the simulation consistently underestimates the elastic deflection, and therefore the reduction of stock removal.

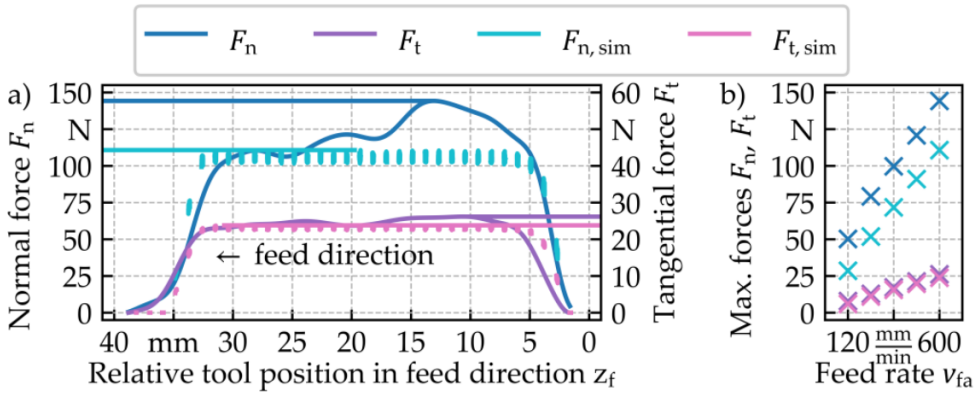

Figure 5.8: **a)** Comparison of metrologically recorded and simulated ITG process forces in the industrial setting at $v_{fa} = 600\,\mathrm{mm\,min^{-1}}$. **b)** Maxima of tangential and normal forces depending on feed rate. Process conditions are given in table 5.2. *Figure reproduced from Tsagkir Dereli et al. [185] under the terms of the CC BY 4.0 license. No changes were made.*

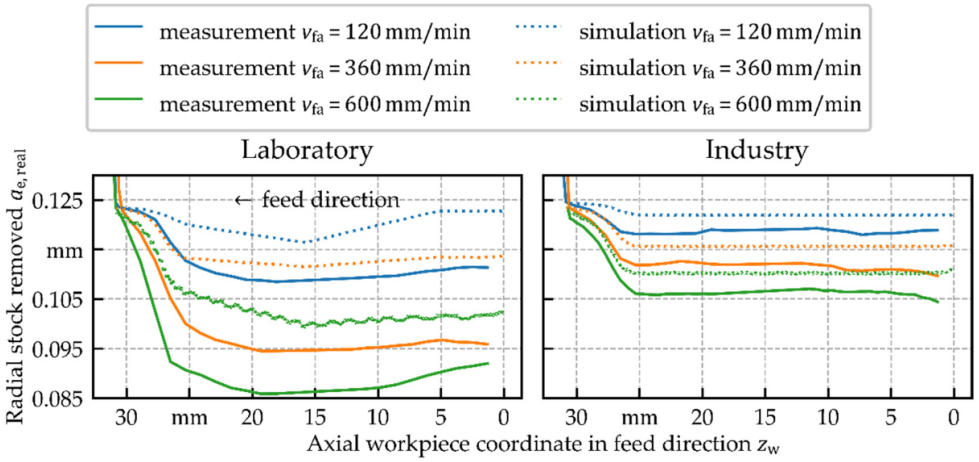

Figure 5.9: Comparison of measured and simulated workpiece contours after internal traverse grinding for lab and industrial environment. *Figure reproduced from Tsagkir Dereli et al. [185] under the terms of the CC BY 4.0 license. No changes were made.*

5.7 Conclusion

There are multiple possible reasons for the remaining discrepancies between simulation and experimental data. The single grain force model does not account for the actual shape of the cutting edge, but relies on a simplified parametrisation. An improved version of the surrogate force model could be based on three-dimensional single grain simulations, but would require additional parameters, as well as an efficient way to calculate these parameters in the GPS. Such a model would naturally account for material repositioning without removal, such as ploughing. Furthermore, the direct comparison of the meso-scale cutting simulations with experimental data would be desirable. In this context, a systematic investigation of the interplay of material softening and mesh sensitivities should be performed. However, obtaining reliable experimental data for high-speed cutting at the meso-scale is a challenging task, and to the best of the knowledge of the author of this thesis, no such data is currently available.

Additional validation is also desirable for the compliance model, especially for the industrial setting, as the unrealistically high variations in measured machining system compliance indicate a possible problem with the force measurement, such as an inaccuracy of the sensor in the custom clamping device. Another possible improvement of the compliance model is the inclusion of dynamical effects.

Although an improvement of the prediction accuracy of the simulation system is desirable, it was demonstrated that the extension of the geometrical physically-based simulation by a compliance model and a surrogate force model results in a powerful simulation system, which is able to combine information from multiple scales and to correctly predict interactions based on elastic deflections. Since no additional model is used at the macro-scale, the result directly includes information on the topography of the ground surfaces, which represents a major improvement.

Based on the predicted contours, optimisations of process strategies and NC paths are possible to reduce the characteristic shape deviations. While no final results for this approach are available at the publication date of this thesis, preliminary work shows promising results in this regard.

6 Concluding remarks

As described in chapter 1, the development and adoption of more specialised production processes leads to increased productivity, reduced resource usage, as well as to higher product performance. However, process control plays a crucial role to ensure both productivity and process stability. Variations of product properties within and in between different batches have to be taken into account to minimise the number of rejects, and to achieve the best performance of the finished products possible. By taking into account interdependencies between different stages of the process chain, an additional level of complexity is introduced. At the same time, additional improvements in efficiency and performance are expected when considering the process chain in a holistic manner.

The concept of a digital twin, consisting of the physical product, a virtual product, and bi-directional data transfer, is a promising approach to monitor and improve product quality over the complete life cycle. However, it relies on the availability of high-fidelity simulations in the digital domain – taking into account all relevant physical effects – as well as data measured in the physical domain.

This thesis is a contribution towards the development of such a digital twin for the manufacturing of bearing components made of 100Cr6 steel. It focuses on the development of simulations for the heat treatment and grinding of the workpieces. In contrast to black-box models often used in digital twins, the simulation approaches developed in this thesis incorporate a high degree of physical information. They can therefore be applied to help analyse processes in detail and to improve the understanding of the relevant physical phenomena and interactions. Furthermore, they might aid in the selection of state characteristics for more efficient surrogate models used in a future digital twin.

6.1 Summary and conclusion

A finite element simulation framework for the quenching during the heat treatment of bearing components is proposed in chapter 3. Based on the classic Koistinen-Marburger and Johnson-Mehl-Avrami-Kolmogorov models, the athermal transformation of austenite to martensite as well as the diffusive transformation of austenite to bainite are considered in the metallurgical problem, and an extension to additional diffusive transformations is straightforward.

The metallurgical problem is coupled to the thermal and mechanical problems since the phase transformations are temperature dependent, and lead to a release of latent heat as well as a volume change. Furthermore, overall mechanical and thermal properties of the continuum are calculated based on the individual volume fractions of each phase.

Finally, the influence of the chemical composition on the phase transformations is included. The mass balance of carbon is included as a local balance equation, and a repartitioning of carbon during the formation of carbide-free bainite is modelled, causing a carbon-enrichment in the remaining austenite. Since carbon content was identified as the primary influence on transformation behaviour, the parameters of the phase transformation models are parametrised based on the current carbon content. The calibration of the model parameters is based on a combination of literature values, mathematical optimisation based on published transformation diagrams, and MatCalc simulations.

The material model proposed in this chapter was implemented as a Fortran user material subroutine for the commercial finite element package Abaqus, and was made available as open source software at github.

A fully thermo-mechanically coupled solver with implicit time integration is used in Abaqus to simulate illustrative problems at a single material point to demonstrate the general model behaviour, as well as an exemplary boundary value problem, based on the quenching of a bearing component with varying wall thickness. It was shown that the framework is capable of predicting the resulting phase fractions as well as the temperature and deformation fields.

For the simulation of grinding, an existing simulation framework was adapted and further developed, which is presented in chapter 5. The original framework consists of three components: meso-scale finite element simulations of single-grain cutting, a geometric simulation of grain engagements, and a finite element simulation at process level. In contrast, the framework presented in this thesis relies on a geometric simulation of the process. This approach is enabled by the performance improvements of the current implementation, as well as the fact that thermal deformations were found to play a secondary role compared to elastic deflections for the use cases considered in this thesis.

The remeshing-based mesoscopic simulation approach for the single grain cutting simulations was adopted from the original framework. However, a novel surrogate model for the process force contributions of individual grain engagements during grinding was proposed. This model is based on an approximation of the engaged grain as a geometric primitive, and parametrised in terms of the material removal rate and the rake angle.

Another key point is the use of measured grain geometries from real grinding wheels instead of artificially created grains in the physical kinematic simulation. The evaluation of the process force surrogate model for these geometries is enabled by the proposed approximation for the rake angle of an engaged grain, which is based on a triangulation of the grain, the cutting direction, and the undeformed chip thickness.

The framework is completed by a compliance model for the machine system. A simple but effective procedure was proposed to calibrate this compliance model based on data obtained from static analogy tests. By combining the compliance and process

force models, the elastic deflection between tool and workpiece is taken into account in the geometric physically-based simulation, and the impact of these deflections on the resulting workpiece contour and surface can be investigated.

The proposed framework was applied to the simulation of the internal traverse grinding process introduced in section 1.3, and it was shown that the predicted process forces were in good accordance with their measured counterparts. Furthermore, while a quantitative difference remained for the compliance-induced reduction of the achieved radial stock removal, the characteristic shape deviation at the tool entry and exit zones of the workpiece can be predicted by using the simulation framework.

In addition to the process simulations, a new material model for finite element simulations of mesoscopic cutting of 100Cr6 steel is proposed in chapter 4. It is based on the classic and widely used Johnson-Cook model, but formulated in a thermodynamically consistent manner, and includes a local damage model inspired by viscoplasticity. Based on flow stress data available in the literature, an incremental calibration procedure is presented, which takes data from multiple sources into account. The new model is compared to the material model used in the original framework for mesoscopic cutting of the same material, and it is shown that only the new model is able to reproduce the transition from brittle to ductile failure observed in 100Cr6 between 20 °C and 200 °C.

A new framework for the single grain cutting simulations is also proposed in chapter 4, which is based on the Coupled Eulerian Lagrangian method. The new framework therefore avoids the remeshing applied in the original framework, and significantly reduced the complexity of the model.

6.2 Outlook

One of the most exciting aspects of research is that every answered question gives rise to two new ones. In this spirit, some possible extensions and improvements of the simulation models proposed in this thesis are discussed below.

The model proposed in chapter 3 for the microstructure evolution during the quenching process neglects some effects which do in fact influence the resulting microstructure and stress state.

For each phase, only a single variant is considered in the model. However, it is well known that the same phase can form different variants in real microstructures. For example, martensite typically forms microstructures resembling plates or needles, which are therefore not isotropic. The volume change assigned to the transformation in the proposed model is therefore a macroscopic average of local deformations, which are not purely volumetric.

A natural next step for the development of a comprehensive model for quenching is the incorporation of transformation plasticity. Mechanical loading favours formation of product phases at specific orientations, which is called the Magee effect [116], while the Greenwood-Johnson effect [60] describes local yielding of a weaker phase during

formation of a strong phase such as martensite. Depending on the application, the incorporation of stress-induced transformations is another option for future work.

While the simple volume averaging used in the proposed model has been shown to yield good results, a more advanced homogenisation approach could yield better accuracy, especially when product phase interactions such as transformation plasticity are taken into account.

Another area of possible improvement is the incorporation of diffusion into the carbon mass balance. The purely local repartitioning of carbon is a simplifying model assumption, which does not hold true in reality. However, the introduction of another global solution field would be necessary to incorporate this effect, which presents a challenge especially when working with closed-source codes such as Abaqus.

Besides carbon, chromium and silicon are described in the literature as especially relevant for the transformation behaviour, and a repartitioning of chromium was described by Bhadeshia [21]. Incorporating mass balances for additional elements could therefore further improve the model.

A natural approach to further improve the simulation of internal traverse grinding is the improvement of the meso-scale cutting simulations. However, the evaluation of the proposed approaches is limited by the lack of reference data. Experimental investigations are difficult due to the combination of small length scales, high relative velocities, and the geometrically undefined cutting edge geometry. The same problems make it challenging to generate reference data for flow stress and damage models. Therefore, the development of experimental procedures to generate better reference data is seen as the most pressing research direction for this topic by the author of this thesis.

However, some of the drawbacks of the currently used finite element implementations demand further improvements as well. Non-local models are widely viewed as a promising approach to avoid mesh dependency of results when material softening is present. However, such models are usually not available in commercial finite element software. On the other hand, in-house codes are typically outperformed by the contact algorithms and general performance of commercial software. It would therefore be desirable to extend the functionalities of finite element codes such as Abaqus to incorporate non-local damage models, especially for explicit time integration.

Besides the improvement of the presented models, the remaining stages of the process chain have to be taken into account to reach the objective of a true digital twin. Special attention is required to combine results obtained for individual stages of the process, and to develop a set of state characteristics which remains valid throughout all stages of the manufacturing process. Finally, the integration of the models with sensor data from the manufacturing environment is crucial to the vision of a real-time replica of the product during manufacturing.

A Appendix

Additional material for two different chapters of this thesis is provided in the following. Appendix A.1 provides supplementary material for chapter 3, whereas Appendix A.2 pertains to chapter 4.

A.1 Simulation of quenching processes

The following appendices provide additional details and derivations for the simulation of quenching processes, which is discussed in chapter 3.

A.1.1 Initial guess for the bainite transformation model parameters

qtd. [54]{As described in section 3.3.7, the choice of initial guess for the nonlinear least squares fit presented in eq. (3.50) is not trivial. Recall that the input data obtained from the TTT–diagram consists of m discrete temperatures T_i and the corresponding times $t_{1,i}$ and $t_{99,i}$ required for the formation of 1 % and 99 % martensite. Introducing constant parameters b_i and N_i, the JMAK model for the isothermal transformation at temperature T_i reads

$$\beta_{\mathrm{B},i}(t) = 1 - \exp\left(- b_i \, t^{N_i} \right) \, , \tag{A.1}$$

or, solved for t,

$$t(\beta_{\mathrm{B},i}) = \left[\frac{1}{b_i} \ln\left(\frac{1}{1-\beta_{\mathrm{B},i}} \right) \right]^{\frac{1}{N_i}} \, , \tag{A.2}$$

where b_i and N_i are determined for each temperature individually by the nonlinear optimisation

$$(\hat{b}_i, \hat{N}_i) = \arg\min_{b_i, N_i} \left\{ \left[\beta_{\mathrm{B},i}(t_{1,i}) - 0.01 \right]^2 + \left[\beta_{\mathrm{B},i}(t_{99,i}) - 0.99 \right]^2 \right\} \, . \tag{A.3}$$

It is remarked that, as shown in e.g. Tzitzelkov et al. [187], in the isothermal case with only two lines in the diagram, a unique solution to eq. (A.3) exists for each temperature, which will be denoted as the *isothermal fit* in the following. Inserting the isothermal

solution into eq. (A.2), and evaluating for $\beta_{\mathrm{B},i} = 1\,\%$ and $\beta_{\mathrm{B},i} = 99\,\%$, the data points in the input data are recovered up to numerical tolerances.

Given the discrete pairs $(T_i, \hat{b}_i)$ and $(T_i, \hat{N}_i)$, the polynomial ansatz

$$\ln\left(b_p(T)\right) = p_{b,0} + p_{b,1}\,T + p_{b,2}T^2\ , \tag{A.4}$$

$$N_p(T) = p_{N,0} + p_{N,1}T + p_{N,2}T^2\ , \tag{A.5}$$

is considered to approximate the temperature dependence of the parameters, and the vectors $\boldsymbol{p}_b = [p_{b,0},\, p_{b,1},\, p_{b,2}]^{\mathrm{t}}$ and $\boldsymbol{p}_N = [p_{N,0},\, p_{N,1},\, p_{N,2}]^{\mathrm{t}}$ are introduced. The least squares problems

$$\tilde{\boldsymbol{p}}_b = \arg\min_{\boldsymbol{p}_b} \left\{ \sum_i^m \left[\log_{10}\left(b_p(T_i)\right) - \log_{10}\left(\hat{b}_i\right) \right]^2 \right\}\ , \tag{A.6}$$

$$\tilde{\boldsymbol{p}}_N = \arg\min_{\boldsymbol{p}_N} \left\{ \sum_i^m \left[N_p(T_i) - \hat{N}_i \right]^2 \right\} \tag{A.7}$$

yield the optimal parameters $\tilde{\boldsymbol{p}}_b$ and $\tilde{\boldsymbol{p}}_N$ and the corresponding polynomials $\tilde{b}_p(T)$ and $\tilde{N}_p(T)$. The evaluation of the JMAK model based on these parameters will be denoted the *parameter fit* in the following.

The solution $\tilde{\boldsymbol{p}} = [\tilde{p}_{b,0},\, \tilde{p}_{b,1},\, \tilde{p}_{b,2},\, \tilde{p}_{N,0},\, \tilde{p}_{N,1},\, \tilde{p}_{N,2}]^{\mathrm{t}}$ is then used as the initial guess for the parameter identification based on the JMAK model, described in section 3.3.7 and referred to as the *model fit* in the following, yielding the optimal set of parameters $\boldsymbol{p}^*$. It is remarked that the parameter sets $\tilde{\boldsymbol{p}}$ and $\boldsymbol{p}^*$ can produce very similar results, but that they are in general not identical since they represent solutions to two different minimisation problems.

Table A.1 lists the optimised coefficients for both, the parameter fit and the model fit whereas fig. A.1 shows the approximation of the temperature-discrete isothermal fit by the continuous parameter fit and model fit. While both fits yield similar parabolic progressions for b_p, a significant difference can be observed in N_p, where the parameter fit yields a nearly linear function, while the model fit leads to a pronounced parabolic shape.

Table A.1: Comparison of optimal polynomial coefficients based on the parameter fit and model fit strategies. *Table reproduced from Furlan et al. [54] under the terms of the CC BY 4.0 license. The font was adapted to the style of this thesis.*

Strategy	$p_{b,0}$	$p_{b,1}$ / $^\circ\mathrm{C}^{-1}$	$p_{b,2}$ / $^\circ\mathrm{C}^{-2}$	$p_{N,0}$	$p_{N,1}$ / $^\circ\mathrm{C}^{-1}$	$p_{N,2}$ / $^\circ\mathrm{C}^{-2}$
parameter fit	−3.5399 e1	1.4467 e−1	−1.6688 e−4	4.8917	−6.7588 e−3	1.9972 e−6
model fit	−4.7912 e1	2.1736 e−1	−2.7056 e−4	1.1313 e1	−4.5363 e−2	5.8965 e−5

The original TTT–diagram data and the recovered values from the isothermal fit, along with the predictions for the 1 % and 99 % lines based on the parameter fit and the model fit, are presented in fig. A.2. As expected, the isothermal fit exactly reproduces the

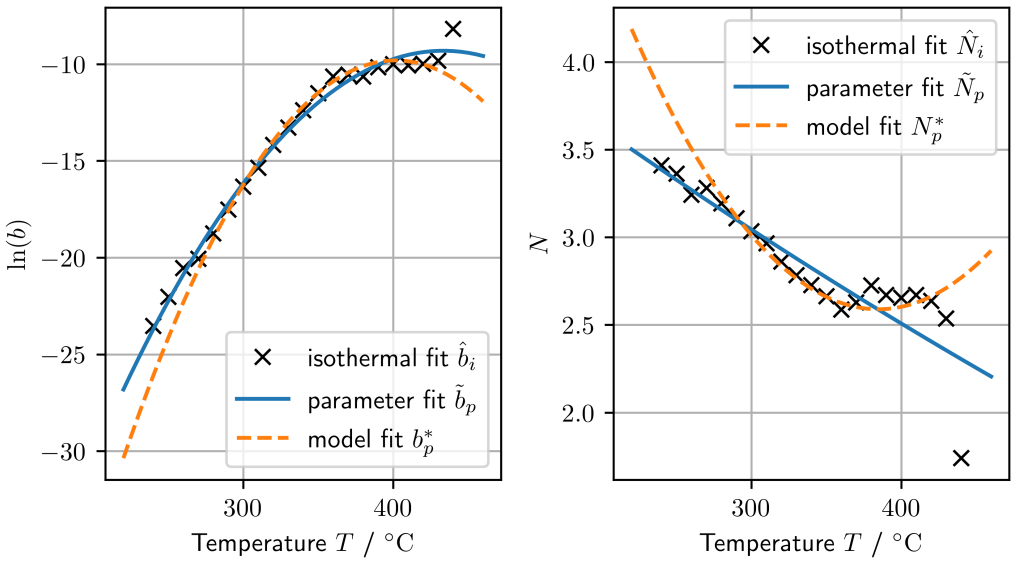

Figure A.1: JMAK model parameters b and N obtained from different fitting strategies. The isothermal fit recovers the original diagram data up to numerical tolerances, but is only available for discrete temperatures. The parameter fit and the model fit are based on a second-order polynomial ansatz for the temperature-dependency of the parameters b and N, and represent the optimal fit of the polynomials based on the isothermal parameters and on the predicted phase fractions, respectively. *Figure reproduced from Furlan et al. [54] under the terms of the CC BY 4.0 license. No changes were made.*

reference values. Both the parameter fit and the model fit are in good agreement with the original data. While the parameter fit is in slightly better agreement with values for relatively low and high temperatures, the model fit shows slightly better performance in between. Since the model fit strategy minimises a physically more meaningful error functional, it was chosen for the implementation in this work. However, based on the simulated TTT–diagram, no significant differences should be expected when applying the simpler parameter fit strategy.}$^{\text{qtd.}}_{[54]}$

A.1.2 Derivatives of the evolution equations

$^{\text{qtd.}}_{[54]}${For the solution of the evolution equations (3.68), the Jacobian

$$\frac{\partial \boldsymbol{R}_{\boldsymbol{\kappa}}}{\partial \boldsymbol{\kappa}} = \begin{bmatrix} \frac{\partial R_{\beta_\mathrm{M}}}{\partial \beta_\mathrm{M}} & \frac{\partial R_{\beta_\mathrm{M}}}{\partial \beta_\mathrm{B}} & \frac{\partial R_{\beta_\mathrm{M}}}{\partial x_{\mathrm{C,A}}} \\ \frac{\partial R_{\beta_\mathrm{B}}}{\partial \beta_\mathrm{M}} & \frac{\partial R_{\beta_\mathrm{B}}}{\partial \beta_\mathrm{B}} & \frac{\partial R_{\beta_\mathrm{B}}}{\partial x_{\mathrm{C,A}}} \\ \frac{\partial R_{x_{\mathrm{C,A}}}}{\partial \beta_\mathrm{M}} & \frac{\partial R_{x_{\mathrm{C,A}}}}{\partial \beta_\mathrm{B}} & \frac{\partial R_{x_{\mathrm{C,A}}}}{\partial x_{\mathrm{C,A}}} \end{bmatrix}, \tag{A.8}$$

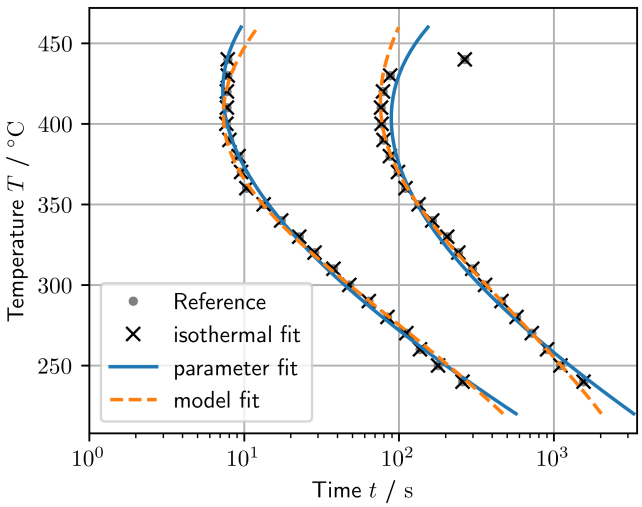

Figure A.2: TTT–diagram with isolines for 1 % and 99 % bainite phase fraction. The reference data is obtained from the TTT–diagram published in Kaymak [93], and is recovered exactly by the isothermal fit of the JMAK parameters b and N for each discrete temperature. Parameter fit and model fit strategies, based on a quadratic polynomial ansatz for the temperature-dependency of the parameters b and N, show good agreement with the data. *Figure reproduced from Furlan et al. [54] under the terms of the CC BY 4.0 license. No changes were made.*

is required. Furthermore, for the application of the implicit function theorem, the derivatives of the residual with respect to the strain increment and the temperature are necessary. Since the evolution equations do not depend on the mechanical state, as shown in fig. 3.1, the relation

$$\frac{\partial \boldsymbol{R}_{\boldsymbol{\kappa}}}{\partial \Delta \boldsymbol{\varepsilon}_V} = \mathbf{0} \tag{A.9}$$

holds, while the temperature derivatives

$$\frac{\partial \boldsymbol{R}_{\boldsymbol{\kappa}}}{\partial T} = \left[\frac{\partial R_{\beta_\mathrm{M}}}{\partial T} \quad \frac{\partial R_{\beta_\mathrm{B}}}{\partial T} \quad \frac{\partial R_{x_{\mathrm{C,A}}}}{\partial T} \right]^\mathrm{t} \tag{A.10}$$

are specified in the following section together with the Jacobian contributions for each evolution equation.}$^{\text{qtd.}}_{[54]}$

Martensite evolution

$^{\text{qtd.}}_{[54]}${The evolution equation for martensite, eq. (3.69a), reads

$$R_{\beta_\mathrm{M}} = \beta_\mathrm{M} - \beta_\mathrm{M}^{(n)} + \zeta_\mathrm{M} \left[1 - \beta_\mathrm{M} - \beta_\mathrm{B}\right] k \, \Delta T \ , \tag{A.11}$$

resulting in the Jacobian contributions

$$\frac{\partial R_{\beta_\mathrm{M}}}{\partial \beta_\mathrm{M}} = 1 - \zeta_\mathrm{M}\, k\, \Delta T \ , \tag{A.12}$$

$$\frac{\partial R_{\beta_\mathrm{M}}}{\partial \beta_\mathrm{B}} = -\zeta_\mathrm{M}\, k\, \Delta T \ , \tag{A.13}$$

$$\frac{\partial R_{\beta_\mathrm{M}}}{\partial x_\mathrm{C,A}} = \left[1 - \beta_\mathrm{M} - \beta_\mathrm{B}\right] \Delta T \left[\zeta_\mathrm{M} \frac{\mathrm{d}k}{\mathrm{d}x_\mathrm{C,A}} + \frac{\mathrm{d}\zeta_\mathrm{M}}{\mathrm{d}x_\mathrm{C,A}}\, k\right] \ , \tag{A.14}$$

and the temperature derivative

$$\frac{\partial R_{\beta_\mathrm{M}}}{\partial T} = \left[1 - \beta_\mathrm{M} - \beta_\mathrm{B}\right] k \left[\frac{\mathrm{d}\zeta_\mathrm{M}}{\mathrm{d}T} \Delta T + \zeta_\mathrm{M}\right] \ . \tag{A.15}$$

Inserting the derivatives of the activation function, i.e.

$$\frac{\partial \widetilde{\mathrm{H}}\left(T\right)}{\partial T} = \frac{l}{2\cosh\left(lT\right)^2} \ , \tag{A.16}$$

$$\begin{aligned} \frac{\mathrm{d}\zeta_\mathrm{M}}{\mathrm{d}x_\mathrm{C,A}} &= \frac{\partial \zeta_\mathrm{M}}{\partial M_\mathrm{S}} \frac{\mathrm{d}M_\mathrm{S}}{\mathrm{d}x_\mathrm{C,A}} \\ &= \mathrm{H}\left(-\dot{T}\right) \frac{l}{2\cosh\left(l\left[M_\mathrm{S} - T\right]\right)^2} \frac{\mathrm{d}M_\mathrm{S}}{\mathrm{d}x_\mathrm{C,A}} \ , \end{aligned} \tag{A.17}$$

$$\frac{\mathrm{d}\zeta_\mathrm{M}}{\mathrm{d}T} = \frac{\partial \zeta_\mathrm{M}}{\partial T} = -\mathrm{H}\left(-\dot{T}\right) \frac{l}{2\cosh\left(l\left[M_\mathrm{S} - T\right]\right)^2} \ , \tag{A.18}$$

leaves only the terms $\mathrm{d}M_\mathrm{S}/\mathrm{d}x_\mathrm{C,A}$ and $\mathrm{d}k/\mathrm{d}x_\mathrm{C,A}$ to be specified, which result directly from the polynomial parametrisation of the model parameters.$\}^{\text{qtd.}}_{[54]}$

Bainite evolution

$^{\text{qtd.}}_{[54]}\{$The derivatives for the bainite evolution equation will be given individually based on whether the bainite fraction has already reached the value of 1 %, starting with the case that $\beta_\mathrm{B}^{(n)} \leq 1\,\%$. The residual evolution equation (3.69b) then reads

$$R_{\beta_\mathrm{B}} = \beta_\mathrm{B} - \beta_\mathrm{B}^{(n)} - 0.01\, \zeta_\mathrm{B}\, \Delta t/\tau \ , \tag{A.19}$$

and the derivatives with respect to the internal variables are given by

$$\frac{\partial R_{\beta_\mathrm{B}}}{\partial \beta_\mathrm{M}} = 0 \ , \tag{A.20}$$

$$\frac{\partial R_{\beta_\mathrm{B}}}{\partial \beta_\mathrm{B}} = 1 \ , \tag{A.21}$$

$$\frac{\partial R_{\beta_\mathrm{B}}}{\partial x_\mathrm{C,A}} = -0.01 \frac{\Delta t}{\tau} \frac{\mathrm{d}\zeta_\mathrm{B}}{\mathrm{d}x_\mathrm{C,A}} \ , \tag{A.22}$$

while the temperature derivative reads

$$\frac{\partial R_{\beta_\mathrm{B}}}{\partial T} = -0.01\frac{\Delta t}{\tau}\left[\frac{\mathrm{d}\zeta_\mathrm{B}}{\mathrm{d}T} + \zeta_\mathrm{B}\left[\frac{1}{N^2}\ln\left(\frac{1}{b}\ln\left(\frac{1}{0.99}\right)\right)\frac{\mathrm{d}N}{\mathrm{d}T} + \frac{1}{b\,N}\frac{\mathrm{d}b}{\mathrm{d}T}\right]\right] . \tag{A.23}$$

After the nucleation is complete, i.e. when $\beta_\mathrm{B}^{(n)} > 1\,\%$, eq. (3.69b) reads

$$R_{\beta_\mathrm{B}} = \beta_\mathrm{B} - \beta_\mathrm{B}^{(n)} - \Delta t\,\zeta_\mathrm{B}\,N\,b^{\frac{1}{N}}\,\left[\hat{\beta}_\mathrm{B} - \beta_\mathrm{B}\right]\,A^{\frac{N-1}{N}} , \tag{A.24}$$

where the abbreviation

$$A = \ln\left(\frac{\hat{\beta}_\mathrm{B}}{\hat{\beta}_\mathrm{B} - \beta_\mathrm{B}}\right) \tag{A.25}$$

was used to simplify the expression. In this case, the derivatives with respect to the internal variables read

$$\frac{\partial R_{\beta_\mathrm{B}}}{\partial \beta_\mathrm{M}} = -\Delta t\,\zeta_\mathrm{B}\left[\frac{b}{A}\right]^{\frac{1}{N}}\left[NA - [N-1]\,\frac{\beta_\mathrm{B}}{\hat{\beta}_\mathrm{B}}\right]\frac{\mathrm{d}\hat{\beta}_\mathrm{B}}{\mathrm{d}\beta_\mathrm{M}} , \tag{A.26}$$

$$\begin{aligned}\frac{\partial R_{\beta_\mathrm{B}}}{\partial \beta_\mathrm{B}} =& 1 - \Delta t\,\zeta_\mathrm{B}\left[\frac{b}{A}\right]^{\frac{1}{N}}\left[N - 1 - NA\right.\\ &\left.+\left[NA - [N-1]\,\frac{\beta_\mathrm{B}}{\hat{\beta}_\mathrm{B}}\right]\frac{\mathrm{d}\hat{\beta}_\mathrm{B}}{\mathrm{d}\beta_\mathrm{B}}\right] ,\end{aligned} \tag{A.27}$$

$$\begin{aligned}\frac{\partial R_{\beta_\mathrm{B}}}{\partial x_{\mathrm{C,A}}} =& -\Delta t\left[\frac{b}{A}\right]^{\frac{1}{N}}\left[\left[NA - [N-1]\,\frac{\beta_\mathrm{B}}{\hat{\beta}_\mathrm{B}}\right]\zeta_\mathrm{B}\frac{\mathrm{d}\hat{\beta}_\mathrm{B}}{\mathrm{d}x_{\mathrm{C,A}}}\right.\\ &\left.+ NA\left[\hat{\beta}_\mathrm{B} - \beta_\mathrm{B}\right]\frac{\mathrm{d}\zeta_\mathrm{B}}{\mathrm{d}x_{\mathrm{C,A}}}\right] .\end{aligned} \tag{A.28}$$

The temperature derivative for this case is given by

$$\begin{aligned}\frac{\partial R_{\beta_\mathrm{B}}}{\partial T} =& -\Delta t\left[\frac{b}{A}\right]^{\frac{1}{N}}\left[NA\left[\hat{\beta}_\mathrm{B} - \beta_\mathrm{B}\right]\frac{\mathrm{d}\zeta_\mathrm{B}}{\mathrm{d}T}\right.\\ &+ \zeta_\mathrm{B}A\left[\hat{\beta}_\mathrm{B} - \beta_\mathrm{B}\right]\left[1 + \frac{1}{N}\ln\left(\frac{A}{b}\right)\right]\frac{\mathrm{d}N}{\mathrm{d}T}\\ &+ \zeta_\mathrm{B}\frac{A}{b}\left[\hat{\beta}_\mathrm{B} - \beta_\mathrm{B}\right]b^{\frac{1}{N}-1}\frac{\mathrm{d}b}{\mathrm{d}T}\\ &\left.+ \zeta_\mathrm{B}\left[AN - [N-1]\,\frac{\beta_\mathrm{B}}{\hat{\beta}_\mathrm{B}}\right]\frac{\mathrm{d}\hat{\beta}_\mathrm{B}}{\mathrm{d}\beta_\mathrm{B}}\right] .\end{aligned} \tag{A.29}$$

Simplification of the expressions requires the derivatives

$$\frac{\partial A}{\partial \beta_{\mathrm{M}}} = -\frac{\beta_{\mathrm{B}}}{\hat{\beta}_{\mathrm{B}}\left[\hat{\beta}_{\mathrm{B}} - \beta_{\mathrm{B}}\right]} \frac{\mathrm{d}\hat{\beta}_{\mathrm{B}}}{\mathrm{d}\beta_{\mathrm{M}}} \,, \tag{A.30}$$

$$\frac{\partial A}{\partial \beta_{\mathrm{B}}} = \frac{1}{\hat{\beta}_{\mathrm{B}} - \beta_{\mathrm{B}}} - \frac{\beta_{\mathrm{B}}}{\hat{\beta}_{\mathrm{B}}\left[\hat{\beta}_{\mathrm{B}} - \beta_{\mathrm{B}}\right]} \frac{\mathrm{d}\hat{\beta}_{\mathrm{B}}}{\mathrm{d}\beta_{\mathrm{B}}} \,, \tag{A.31}$$

$$\frac{\mathrm{d}A}{\mathrm{d}x_{\mathrm{C,A}}} = -\frac{\beta_{\mathrm{B}}}{\hat{\beta}_{\mathrm{B}}\left[\hat{\beta}_{\mathrm{B}} - \beta_{\mathrm{B}}\right]} \frac{\mathrm{d}\hat{\beta}_{\mathrm{B}}}{\mathrm{d}x_{\mathrm{C,A}}} \,, \tag{A.32}$$

$$\frac{\mathrm{d}A}{\mathrm{d}T} = -\frac{\beta_{\mathrm{B}}}{\hat{\beta}_{\mathrm{B}}\left[\hat{\beta}_{\mathrm{B}} - \beta_{\mathrm{B}}\right]} \frac{\mathrm{d}\hat{\beta}_{\mathrm{B}}}{\mathrm{d}T} \,, \tag{A.33}$$

$$\begin{aligned} \frac{\mathrm{d}\tau}{\mathrm{d}T} &= \frac{\partial \tau}{\partial N}\frac{\mathrm{d}N}{\mathrm{d}T} + \frac{\partial \tau}{\partial b}\frac{\mathrm{d}b}{\mathrm{d}T} \\ &= -\frac{\tau}{N^2}\ln\left(\frac{1}{b}\ln\left(\frac{1}{0.99}\right)\right)\frac{\mathrm{d}N}{\mathrm{d}T} - \frac{\tau}{b\,N}\frac{\mathrm{d}b}{\mathrm{d}T} \,. \end{aligned} \tag{A.34}$$

To complete the implementation, the derivatives of the maximum reachable bainite fraction

$$\frac{\mathrm{d}\hat{\beta}_{\mathrm{B}}}{\mathrm{d}\beta_{\mathrm{M}}} = -\,\mathrm{f} \,, \tag{A.35}$$

$$\frac{\mathrm{d}\hat{\beta}_{\mathrm{B}}}{\mathrm{d}\beta_{\mathrm{B}}} = 1 - \mathrm{f} \,, \tag{A.36}$$

$$\frac{\mathrm{d}\hat{\beta}_{\mathrm{B}}}{\mathrm{d}x_{\mathrm{C,A}}} = \beta_{\mathrm{A}}\,\frac{\mathrm{d}\,\mathrm{f}}{\mathrm{d}x_{\mathrm{C,A}}} = -\beta_{\mathrm{A}}\,\frac{x^*_{\mathrm{C,A}}}{x_{\mathrm{C,B}} - x^*_{\mathrm{C,A}}} \,, \tag{A.37}$$

$$\begin{aligned} \frac{\mathrm{d}\hat{\beta}_{\mathrm{B}}}{\mathrm{d}T} &= \beta_{\mathrm{A}}\,\frac{\mathrm{d}\,\mathrm{f}}{\mathrm{d}T} = \beta_{\mathrm{A}}\,\frac{\mathrm{d}\,\mathrm{f}}{\mathrm{d}x^*_{\mathrm{C,A}}}\frac{\mathrm{d}x^*_{\mathrm{C,A}}}{\mathrm{d}T} \\ &= \beta_{\mathrm{A}}\,\frac{x_{\mathrm{C,A}} - x_{\mathrm{C,B}}}{\left[x_{\mathrm{C,B}} - x^*_{\mathrm{C,A}}\right]^2}\frac{p_{B_{\mathrm{S}},0}}{p_{B_{\mathrm{S}},1}} \,, \end{aligned} \tag{A.38}$$

and of the activation function

$$\frac{\mathrm{d}\zeta_{\mathrm{B}}}{\mathrm{d}\beta_{\mathrm{M}}} = 0 \ , \tag{A.39}$$

$$\frac{\mathrm{d}\zeta_{\mathrm{B}}}{\mathrm{d}\beta_{\mathrm{B}}} = 0 \ , \tag{A.40}$$

$$\frac{\mathrm{d}\zeta_{\mathrm{B}}}{\mathrm{d}x_{\mathrm{C,A}}} = \frac{\partial\zeta_{\mathrm{B}}}{\partial B_{\mathrm{S}}}\frac{\mathrm{d}B_{\mathrm{S}}}{\mathrm{d}x_{\mathrm{C,A}}} = \frac{l}{2\cosh\left(l\left[B_{\mathrm{S}}-T\right]\right)^2}\frac{\mathrm{d}B_{\mathrm{S}}}{\mathrm{d}x_{\mathrm{C,A}}} \ , \tag{A.41}$$

$$\begin{aligned}\frac{\mathrm{d}\zeta_{\mathrm{B}}}{\mathrm{d}T} &= \frac{\partial\zeta_{\mathrm{B}}}{\partial T} + \frac{\partial\zeta_{\mathrm{B}}}{\partial B_{\mathrm{S}}}\frac{\mathrm{d}B_{\mathrm{S}}}{\mathrm{d}T} \\ &= \frac{l}{2\cosh\left(l\left[B_{\mathrm{S}}-T\right]\right)^2}\left[\frac{\mathrm{d}B_{\mathrm{S}}}{\mathrm{d}x_{\mathrm{C,A}}} - 1\right]\end{aligned} \tag{A.42}$$

are required.}$^{\text{qtd.}}_{[54]}$

Evolution of austenite phase carbon content

$^{\text{qtd.}}_{[54]}${Based on the residual format of the carbon mass balance presented in eq. (3.69c), i.e.

$$R_{x_{\mathrm{C,A}}} = \left[1-\beta_{\mathrm{M}}-\beta_{\mathrm{B}}\right]\left[x_{\mathrm{C,A}} - x_{\mathrm{C,A}}^{(n)}\right] - \left[\beta_{\mathrm{B}} - \beta_{\mathrm{B}}^{(n)}\right]\left[x_{\mathrm{C,A}} - x_{\mathrm{C,B}}\right] \ , \tag{A.43}$$

the Jacobian contributions read

$$\frac{\partial R_{x_{\mathrm{C,A}}}}{\partial\beta_{\mathrm{M}}} = -\left[x_{\mathrm{C,A}} - x_{\mathrm{C,A}}^{(n)}\right] \tag{A.44}$$

$$\frac{\partial R_{x_{\mathrm{C,A}}}}{\partial\beta_{\mathrm{B}}} = -\left[x_{\mathrm{C,A}} - x_{\mathrm{C,A}}^{(n)}\right] - \left[x_{\mathrm{C,A}} - x_{\mathrm{C,B}}\right] \tag{A.45}$$

$$\frac{\partial R_{x_{\mathrm{C,A}}}}{\partial x_{\mathrm{C,A}}} = \left[1-\beta_{\mathrm{M}}-\beta_{\mathrm{B}}\right] - \left[\beta_{\mathrm{B}} - \beta_{\mathrm{B}}^{(n)}\right] \ , \tag{A.46}$$

while the temperature derivative is given by

$$\frac{\partial R_{x_{\mathrm{C,A}}}}{\partial T} = 0 \ . \tag{A.47}$$

}$^{\text{qtd.}}_{[54]}$

A.1.3 Derivatives of stresses

qtd. [54] {For the finite element implementation, the derivatives of the stress increment $\Delta\boldsymbol{\sigma}_V$ with respect to the strain increment $\Delta\boldsymbol{\varepsilon}_V$, the temperature T and the internal variables $\boldsymbol{\kappa}$ are required.

Recalling eqs. (3.70) and (3.71), i.e.

$$\begin{aligned}\Delta\boldsymbol{\sigma}_V &= \mathbf{E}_V \cdot \left[\left[\boldsymbol{\varepsilon}_V^{\mathrm{el}}\right]^{(n)} + \Delta\boldsymbol{\varepsilon}_V^{\mathrm{el}}\right] - \boldsymbol{\sigma}_V^{(n)} \\ &= \mathbf{E}_V \cdot \boldsymbol{\varepsilon}_V^{\mathrm{el}} - \boldsymbol{\sigma}_V^{(n)}\end{aligned} \tag{A.48}$$

and

$$\Delta\boldsymbol{\varepsilon}_V^{\mathrm{el}} = \Delta\boldsymbol{\varepsilon}_V - \alpha\Delta T\boldsymbol{I}_V - \Delta\gamma\boldsymbol{I}_V \ , \tag{A.49}$$

the partial derivative with respect to the strain increment reads

$$\frac{\partial\Delta\boldsymbol{\sigma}_V}{\partial\Delta\boldsymbol{\varepsilon}_V} = \mathbf{E}_V \ . \tag{A.50}$$

The temperature derivative is given by

$$\frac{\partial\Delta\boldsymbol{\sigma}_V}{\partial T} = \frac{\partial\mathbf{E}_V}{\partial T}\cdot\boldsymbol{\varepsilon}_V^{\mathrm{el}} + \mathbf{E}_V\cdot\frac{\partial\Delta\boldsymbol{\varepsilon}_V^{\mathrm{el}}}{\partial T} \ , \tag{A.51}$$

where the temperature derivative of the elastic tensor is given by

$$\frac{\partial\mathbf{E}_V}{\partial T} = \sum_i\left[\frac{\partial\mathbf{E}_V}{\partial E_i}\frac{\mathrm{d}E_i}{\mathrm{d}T} + \frac{\partial\mathbf{E}_V}{\partial\nu_i}\frac{\mathrm{d}\nu_i}{\mathrm{d}T}\right] \tag{A.52}$$

with

$$\frac{\partial\mathsf{E}_{ijkl}}{\partial E} = \frac{\nu}{[1-\nu][1-2\nu]}\,\delta_{ij}\,\delta_{kl} + \frac{1}{2(1+\nu)}\left[\delta_{ik}\,\delta_{jl} + \delta_{il}\,\delta_{jk}\right] \ , \tag{A.53}$$

$$\frac{\partial\mathsf{E}_{ijkl}}{\partial\nu} = E\frac{2\nu^2+1}{2\nu^2+\nu-1}\,\delta_{ij}\,\delta_{kl} - \frac{E}{2[1+\nu]^2}\left[\delta_{ik}\,\delta_{jl} + \delta_{il}\,\delta_{jk}\right] \ . \tag{A.54}$$

Derivation of the elastic strain increment with respect to the temperature yields

$$\frac{\partial\Delta\boldsymbol{\varepsilon}_V}{\partial T} = -\left[\alpha + \sum_i\beta_i\frac{\partial\alpha_i}{\partial T}\Delta T + \sum_i\beta_i\frac{\partial\gamma_i}{\partial T}\right]\boldsymbol{I}_V \ . \tag{A.55}$$

The derivatives $\mathrm{d}E_i/\mathrm{d}T$, $\mathrm{d}\nu_i/\mathrm{d}T$, $\mathrm{d}\alpha_i/\mathrm{d}T$, and $\mathrm{d}\gamma_i/\mathrm{d}T$ are obtained from the respective polynomial parametrisations.

For the derivative with respect to the internal variables $\boldsymbol{\kappa}$, which has the structure

$$\frac{\partial\Delta\boldsymbol{\sigma}_V}{\partial\boldsymbol{\kappa}} = \left[\frac{\partial\Delta\boldsymbol{\sigma}_V}{\partial\beta_{\mathrm{M}}} \quad \frac{\partial\Delta\boldsymbol{\sigma}_V}{\partial\beta_{\mathrm{B}}} \quad \frac{\partial\Delta\boldsymbol{\sigma}_V}{\partial x_{\mathrm{C,A}}}\right] \ , \tag{A.56}$$

the individual terms read

$$\frac{\partial \Delta \boldsymbol{\sigma}_V}{\partial \beta_\mathrm{M}} = \frac{\partial \mathbf{E}_V}{\partial \beta_\mathrm{M}} \cdot \boldsymbol{\varepsilon}_V^\mathrm{el} + \mathbf{E}_V \cdot \frac{\partial \Delta \boldsymbol{\varepsilon}_V^\mathrm{el}}{\partial \beta_\mathrm{M}} \ , \tag{A.57}$$

$$\frac{\partial \Delta \boldsymbol{\sigma}_V}{\partial \beta_\mathrm{B}} = \frac{\partial \mathbf{E}_V}{\partial \beta_\mathrm{B}} \cdot \boldsymbol{\varepsilon}_V^\mathrm{el} + \mathbf{E}_V \cdot \frac{\partial \Delta \boldsymbol{\varepsilon}_V^\mathrm{el}}{\partial \beta_\mathrm{B}} \ , \tag{A.58}$$

$$\frac{\partial \Delta \boldsymbol{\sigma}_V}{\partial x_\mathrm{C,A}} = \mathbf{0} \ , \tag{A.59}$$

with

$$\frac{\partial \mathbf{E}_V}{\partial \beta_\mathrm{M}} = \mathbf{E}_{\mathrm{M},V} - \mathbf{E}_{\mathrm{A},V} \ , \tag{A.60}$$

$$\frac{\partial \mathbf{E}_V}{\partial \beta_\mathrm{B}} = \mathbf{E}_{\mathrm{B},V} - \mathbf{E}_{\mathrm{A},V} \ , \tag{A.61}$$

$$\frac{\partial \Delta \boldsymbol{\varepsilon}_V^\mathrm{el}}{\partial \beta_\mathrm{M}} = -\left[\alpha_\mathrm{M} - \alpha_\mathrm{A}\right] \Delta T \, \boldsymbol{I}_V - \left[\gamma_\mathrm{M} - \gamma_\mathrm{A}\right] \boldsymbol{I}_V \ , \tag{A.62}$$

$$\frac{\partial \Delta \boldsymbol{\varepsilon}_V^\mathrm{el}}{\partial \beta_\mathrm{B}} = -\left[\alpha_\mathrm{B} - \alpha_\mathrm{A}\right] \Delta T \, \boldsymbol{I}_V - \left[\gamma_\mathrm{B} - \gamma_\mathrm{A}\right] \boldsymbol{I}_V \ . \tag{A.63}$$

}$^{\text{qtd.}}_{[54]}$

A.1.4 Derivatives of the heat generation rate

$^{\text{qtd.}}_{[54]}${The discrete heat generation rate was derived in eq. (3.75) as

$$r_{pl} = \frac{\beta_\mathrm{M} - \beta_\mathrm{M}^{(n)}}{\Delta t} \, \rho \, \Delta h_{\mathrm{A}\to\mathrm{M}} + \frac{\beta_\mathrm{B} - \beta_\mathrm{B}^{(n)}}{\Delta t} \, \rho \, \Delta h_{\mathrm{A}\to\mathrm{B}} \ , \tag{A.64}$$

so derivation with respect to the strain increment trivially yields

$$\frac{\partial r_{pl}}{\partial \Delta \boldsymbol{\varepsilon}_V} = \mathbf{0} \ . \tag{A.65}$$

The temperature derivative is given by

$$\frac{\partial r_{pl}}{\partial T} = \frac{\beta_\mathrm{M} - \beta_\mathrm{M}^{(n)}}{\Delta t} \frac{\mathrm{d}(\rho \, \Delta h_{\mathrm{A}\to\mathrm{M}})}{\mathrm{d}T} + \frac{\beta_\mathrm{B} - \beta_\mathrm{B}^{(n)}}{\Delta t} \frac{\mathrm{d}(\rho \, \Delta h_{\mathrm{A}\to\mathrm{B}})}{\mathrm{d}T} \ , \tag{A.66}$$

while the derivation with respect to the internal variables yields

$$\frac{\partial r_{pl}}{\partial \beta_\mathrm{M}} = \frac{\rho \, \Delta h_{\mathrm{A}\to\mathrm{M}}}{\Delta t} \ , \tag{A.67}$$

$$\frac{\partial r_{pl}}{\partial \beta_\mathrm{B}} = \frac{\rho \, \Delta h_{\mathrm{A}\to\mathrm{B}}}{\Delta t} \ , \tag{A.68}$$

$$\frac{\partial r_{pl}}{\partial x_\mathrm{C,A}} = 0 \ . \tag{A.69}$$

All remaining temperature derivatives, i.e. $\mathrm{d}(\rho \, \Delta h_{\mathrm{A}\to\mathrm{M}})/\mathrm{d}T$ and $\mathrm{d}(\rho \, \Delta h_{\mathrm{A}\to\mathrm{B}})/\mathrm{d}T$, follow from the polynomial parametrisations.}$^{\text{qtd.}}_{[54]}$

A.2 Simulation of single grain cutting

In the following, additional material related to chapter 4 is presented.

A.2.1 Derivatives for viscoplasticity model

The following derivatives are required to calculate the tangent $R'\left(\dot{\lambda}_\mathrm{p}\right)$ for the Newton-Raphson scheme (4.85). To improve readability, any quantities evaluated at the end of the increment are denoted as $(\bullet)$ instead of ${}^{(\mathrm{n+1})}(\bullet)$. Distinctions between elastic and plastic cases are dropped here, but should be implemented.

$$\frac{\mathrm{d}R}{\mathrm{d}\dot{\lambda}_\mathrm{p}} = \frac{\partial \tau_\mathrm{eff}^\mathrm{eq}}{\partial \dot{\lambda}_\mathrm{p}} - \frac{\partial \tau_\mathrm{y}}{\partial \dot{\lambda}_\mathrm{p}} \left[1 + C_\mathrm{p} \ln\left(1 + \frac{\dot{\lambda}_\mathrm{p}}{\dot{\varepsilon}_\mathrm{p,0}^\mathrm{eq}}\right)\right] - \frac{\tau_\mathrm{y}\, C_\mathrm{p}}{\dot{\lambda}_\mathrm{p} + \dot{\varepsilon}_\mathrm{p,0}^\mathrm{eq}} \tag{A.70}$$

$$\frac{\mathrm{d}\tau_\mathrm{eff}^\mathrm{eq}}{\mathrm{d}\dot{\lambda}_\mathrm{p}} = -3\, G_\mathrm{e}\, \Delta t \tag{A.71}$$

$$\frac{\mathrm{d}\tau_\mathrm{y}}{\mathrm{d}\dot{\lambda}_\mathrm{p}} = -f_\mathrm{T}\, g'_\alpha\left(\alpha\right) \frac{\mathrm{d}\alpha}{\mathrm{d}\dot{\lambda}_\mathrm{p}} \tag{A.72}$$

$$\frac{\mathrm{d}\alpha}{\mathrm{d}\dot{\lambda}_\mathrm{p}} = f_\mathrm{T}\, \dot{\lambda}_\mathrm{p}\, \Delta t\, f'_\mathrm{d}\left(\kappa_\mathrm{d}\right) \frac{\mathrm{d}\kappa_\mathrm{d}}{\mathrm{d}\dot{\lambda}_\mathrm{p}} + f_\mathrm{T}\, f_\mathrm{d}\, \Delta t \tag{A.73}$$

$$\frac{\mathrm{d}\kappa_\mathrm{d}}{\mathrm{d}\dot{\lambda}_\mathrm{p}} = \frac{\Delta t}{\Delta t + t_\mathrm{d}}\, \bar{\kappa}'\left(s_\mathrm{p}\right) \frac{\mathrm{d}s_\mathrm{p}}{\mathrm{d}\dot{\lambda}_\mathrm{p}} \tag{A.74}$$

$$\frac{\mathrm{d}s_\mathrm{p}}{\mathrm{d}\dot{\lambda}_\mathrm{p}} = \frac{\partial s_\mathrm{p}}{\partial \varepsilon_\mathrm{p}^\mathrm{eq}} \frac{\mathrm{d}\varepsilon_\mathrm{p}^\mathrm{eq}}{\mathrm{d}\dot{\lambda}_\mathrm{p}} + \frac{\partial s_\mathrm{p}}{\partial \varepsilon_\mathrm{p,i}^\mathrm{eq}} \frac{\mathrm{d}\varepsilon_\mathrm{p,i}^\mathrm{eq}}{\mathrm{d}\dot{\lambda}_\mathrm{p}} + \frac{\partial s_\mathrm{p}}{\partial \varepsilon_\mathrm{p,f}^\mathrm{eq}} \frac{\mathrm{d}\varepsilon_\mathrm{p,f}^\mathrm{eq}}{\mathrm{d}\dot{\lambda}_\mathrm{p}} \tag{A.75}$$

$$\frac{\mathrm{d}s_\mathrm{p}}{\mathrm{d}\varepsilon_\mathrm{p}^\mathrm{eq}} = \frac{1}{\varepsilon_\mathrm{p,f}^\mathrm{eq} - \varepsilon_\mathrm{p,i}^\mathrm{eq}} \tag{A.76}$$

$$\frac{\mathrm{d}s_\mathrm{p}}{\mathrm{d}\varepsilon_\mathrm{p,i}^\mathrm{eq}} = \frac{\varepsilon_\mathrm{p}^\mathrm{eq} - \varepsilon_\mathrm{p,f}^\mathrm{eq}}{\left(\varepsilon_\mathrm{p,f}^\mathrm{eq} - \varepsilon_\mathrm{p,i}^\mathrm{eq}\right)^2} \tag{A.77}$$

$$\frac{\mathrm{d}s_\mathrm{p}}{\mathrm{d}\varepsilon_\mathrm{p,f}^\mathrm{eq}} = -\frac{\varepsilon_\mathrm{p}^\mathrm{eq} - \varepsilon_\mathrm{p,i}^\mathrm{eq}}{\left(\varepsilon_\mathrm{p,f}^\mathrm{eq} - \varepsilon_\mathrm{p,i}^\mathrm{eq}\right)^2} \tag{A.78}$$

$$\frac{\mathrm{d}\varepsilon_\mathrm{p,i}^\mathrm{eq}}{\mathrm{d}\dot{\lambda}_\mathrm{p}} = \frac{\partial \varepsilon_\mathrm{p,i}^\mathrm{eq}}{\partial \dot{\varepsilon}_\mathrm{p}^\mathrm{eq}} + \frac{\partial \varepsilon_\mathrm{p,i}^\mathrm{eq}}{\partial \eta} \frac{\mathrm{d}\eta}{\mathrm{d}\dot{\lambda}_\mathrm{p}} \tag{A.79}$$

$$\frac{\mathrm{d}\varepsilon_\mathrm{p,f}^\mathrm{eq}}{\mathrm{d}\dot{\lambda}_\mathrm{p}} = \frac{\partial \varepsilon_\mathrm{p,f}^\mathrm{eq}}{\partial \dot{\varepsilon}_\mathrm{p}^\mathrm{eq}} + \frac{\partial \varepsilon_\mathrm{p,f}^\mathrm{eq}}{\partial \eta} \frac{\mathrm{d}\eta}{\mathrm{d}\dot{\lambda}_\mathrm{p}} \tag{A.80}$$

$$\frac{\mathrm{d}\eta}{\mathrm{d}\dot{\lambda}_\mathrm{p}} = -\frac{\tau_\mathrm{eff}^\mathrm{m}}{\left[\tau_\mathrm{eff}^\mathrm{eq}\right]^2} \frac{\mathrm{d}\tau_\mathrm{eff}^\mathrm{eq}}{\mathrm{d}\dot{\lambda}_\mathrm{p}} = 3\, G_\mathrm{e}\, \Delta t\, \frac{\tau_\mathrm{eff}^\mathrm{m}}{\left[\tau_\mathrm{eff}^\mathrm{eq}\right]^2} \tag{A.81}$$

$$\frac{\mathrm{d}\varepsilon_\mathrm{p}^\mathrm{eq}}{\mathrm{d}\dot{\lambda}_\mathrm{p}} = \Delta t \tag{A.82}$$

Bibliography

[1] R. Abeyaratne and J. K. Knowles. A continuum model of a thermoelastic solid capable of undergoing phase transitions. *Journal of the Mechanics and Physics of Solids*, 41(3):541–571, 1993. doi:10.1016/0022-5096(93)90048-K.

[2] Y. Altintas, P. Kersting, D. Biermann, E. Budak, B. Denkena, and I. Lazoglu. Virtual process systems for part machining operations. *CIRP Annals*, 63(2):585–605, 2014. doi:10.1016/j.cirp.2014.05.007.

[3] M. Amirmaleki, J. Samei, D. E. Green, I. van Riemsdijk, and L. Stewart. 3D micromechanical modeling of dual phase steels using the representative volume element method. *Mechanics of Materials*, 101:27–39, 2016. doi:10.1016/j.mechmat.2016.07.011.

[4] C. E. Anderson Jr. An overview of the theory of hydrocodes. *International Journal of Impact Engineering*, 5(1-4):33–59, 1987. doi:10.1016/0734-743X(87)90029-7.

[5] B. Andersson, J. Ahlström, M. Ekh, and B. L. Josefson. Homogenization based macroscopic model of phase transformations and cyclic plasticity in pearlitic steel. *Journal of Thermal Stresses*, 45(6):470–492, 2022. doi:10.1080/01495739.2022.2056557.

[6] M. Asadi, F. Haji Aboutalebi, and M. Poursina. A comparative study of six fracture loci for DIN1623 St12 steel to predict strip tearing in a tandem cold rolling mill. *Archive of Applied Mechanics*, 91(4):1859–1878, 2021. doi:10.1007/s00419-020-01859-0.

[7] M. F. Ashby. The deformation of plastically non-homogeneous materials. *The Philosophical Magazine: A Journal of Theoretical Experimental and Applied Physics*, 21(170):399–424, 1970. doi:10.1080/14786437008238426.

[8] J. C. Aurich and B. Kirsch. Kinematic simulation of high-performance grinding for analysis of chip parameters of single grains. *CIRP Journal of Manufacturing Science and Technology*, 5(3):164–174, 2012. doi:10.1016/j.cirpj.2012.07.004.

[9] J. C. Aurich, D. Biermann, H. Blum, C. Brecher, C. Carstensen, B. Denkena, F. Klocke, M. Kröger, P. Steinmann, and K. Weinert. Modelling and simulation of process: Machine interaction in grinding. *Production Engineering*, 3(1):111–120, 2009. doi:10.1007/s11740-008-0137-x.

[10] M. Avrami. Kinetics of Phase Change. I General Theory. *The Journal of Chemical Physics*, 7(12):1103–1112, 1939. doi:10.1063/1.1750380.

[11] M. Avrami. Kinetics of Phase Change. II Transformation-Time Relations for Random Distribution of Nuclei. *The Journal of Chemical Physics*, 8(2):212–224, 1940. doi:10.1063/1.1750631.

[12] M. Avrami. Granulation, Phase Change, and Microstructure Kinetics of Phase Change. III. *The Journal of Chemical Physics*, 9(2):177–184, 1941. doi:10.1063/1.1750872.

[13] U. Ayachit. *The ParaView Guide: A Parallel Visualization Application*. Kitware, Clifton Park, NY, 2015.

[14] P. L. Baehmann, M. S. Shephard, R. A. Ashley, and A. Jay. Automated metal-forming modeling utilizing adaptive remeshing and evolving geometry. *Computers & Structures*, 30(1-2):319–325, 1988. doi:10.1016/0045-7949(88)90237-4.

[15] Y. Bao and T. Wierzbicki. On fracture locus in the equivalent strain and stress triaxiality space. *International Journal of Mechanical Sciences*, 46(1):81–98, 2004. doi:10.1016/j.ijmecsci.2004.02.006.

[16] D. Barbier, J.-D. Guérin, M. Dubar, T. Bénard, S. Bonneau, and E. S. P. Cabrera. Hot ductility and flow stress of AISI 4130 and 52100-type steels. *Materials Science and Engineering: A*, 690:37–43, 2017. doi:10.1016/j.msea.2017.02.053.

[17] K. Barmak. A Commentary on: "Reaction Kinetics in Processes of Nucleation and Growth". *Metallurgical and Materials Transactions B*, 49(6):3616–3680, 2018. doi:10.1007/s11663-010-9421-1.

[18] R. C. Batra and K.-I. Ko. An adaptive mesh refinement technique for the analysis of shear bands in plane strain compression of a thermoviscoplastic solid. *Computational Mechanics*, 10(6):369–379, 1992. doi:10.1007/BF00363993.

[19] T. Bergs, M. Hardt, and D. Schraknepper. Determination of Johnson-Cook material model parameters for AISI 1045 from orthogonal cutting tests using the Downhill-Simplex algorithm. *Procedia Manufacturing*, 48:541–552, 2020. doi:10.1016/j.promfg.2020.05.081.

[20] J. Beswick. Effect of Prior Cold Work on the Martensite Transformation in SAE 52100. *Metallurgical Transactions A*, 15(2):299–306, 1984. doi:10.1007/BF02645115.

[21] H. K. D. H. Bhadeshia. Steels for bearings. *Progress in Materials Science*, 57(2): 268–435, 2012. doi:10.1016/j.pmatsci.2011.06.002.

[22] A. Bhattacharyya and G. J. Weng. An energy criterion for the stress-induced martensitic transformation in a ductile system. *Journal of the Mechanics and Physics of Solids*, 42(11):1699–1724, 1994. doi:10.1016/0022-5096(94)90068-X.

[23] D. Biermann, R. Holtermann, A. Menzel, and S. Schumann. Modelling and simulation of thermal effects in internal traverse grinding of hardened bearing steel. *CIRP Annals*, 65(1):321–324, 2016. doi:10.1016/j.cirp.2016.04.005.

[24] A. D. Boccardo, P. M. Dardati, D. J. Celentano, and L. A. Godoy. Austempering heat treatment of ductile iron: Computational simulation and experimental validation. *Finite Elements in Analysis and Design*, 134:82–91, 2017. doi:10.1016/j.finel.2017.06.002.

[25] E. Brinksmeier, J. C. Aurich, E. Govekar, C. Heinzel, H.-W. Hoffmeister, F. Klocke, J. Peters, R. Rentsch, D. J. Stephenson, E. Uhlmann, K. Weinert, and M. Wittmann. Advances in Modeling and Simulation of Grinding Processes. *CIRP Annals*, 55(2):667–696, 2006. doi:10.1016/j.cirp.2006.10.003.

[26] F. G. Caballero. Carbide-free bainite in steels. In *Phase Transformations in Steels*, pages 436–467. Elsevier, 2012. doi:10.1533/9780857096104.3.436.

[27] G. T. Camacho and M. Ortiz. Adaptive Lagrangian modelling of ballistic penetration of metallic targets. *Computer Methods in Applied Mechanics and Engineering*, 142(3-4):269–301, 1997. doi:10.1016/S0045-7825(96)01134-6.

[28] H. Çetinel, M. Toparli, and L. Özsoyeller. A finite element based prediction of the microstructural evolution of steels subjected to the Tempcore process. *Mechanics of Materials*, 32(6):339–347, 2000. doi:10.1016/S0167-6636(00)00009-0.

[29] C. Cheng and R. Mahnken. A multi-mechanism model for cutting simulation: A Ginzburg-Landau type phase gradient and numerical implementations. *International Journal of Solids and Structures*, 160:1–17, 2019. doi:10.1016/j.ijsolstr.2018.10.007.

[30] C. Cheng and R. Mahnken. A modified Zerilli–Armstrong model as the asymmetric visco-plastic part of a multi-mechanism model for cutting simulations. *Archive of Applied Mechanics*, 91(9):3869–3888, 2021. doi:10.1007/s00419-021-01982-6.

[31] W. Cui, D. San-Martín, and P. E. J. Rivera-Díaz-del-Castillo. Towards efficient microstructural design and hardness prediction of bearing steels — An integrated experimental and numerical study. *Materials & Design*, 133:464–475, 2017. doi:10.1016/j.matdes.2017.08.013.

[32] A. M. Cuitino and M. Ortiz. Computational modelling of single crystals. *Modelling and Simulation in Materials Science and Engineering*, 1(3):225–263, 1993. doi:10.1088/0965-0393/1/3/001.

[33] Dassault Systèmes. Abaqus Documentation, version 2023, 2023. URL `https://www.3ds.com/`.

[34] E. S. Davenport and E. C. Bain. Transformation of austenite at constant subcritical temperatures. *Metallurgical Transactions*, 1(12):3503–3530, 1970. doi:10.1007/BF03037892.

[35] W. P. de Oliveira, M. A. Savi, P. M. C. L. Pacheco, and L. F. G. de Souza. Thermomechanical analysis of steel cylinders quenching using a constitutive model with diffusional and non-diffusional phase transformations. *Mechanics of Materials*, 42 (1):31–43, 2010. doi:10.1016/j.mechmat.2009.09.006.

[36] E. A. de Souza Neto, D. Perić, and D. Owens. *Computational Methods for Plasticity: Theory and Applications*. Wiley, Chichester, West Sussex, UK, 2008. doi:10.1002/9780470694626.

[37] M. Deichmueller, B. Denkena, K. M. de Payrebrune, M. Kröger, S. Wiedemann, A. Schroeder, and C. Carstensen. Determination of static and dynamic deflections in tool grinding using a dexel-based material removal simulation. In *CIRP 2nd International Conference Process Machine Interaction*, Vancouver, 2010.

[38] S. Denis, E. Gautier, A. Simon, and G. Beck. Stress–phase-transformation interactions – basic principles, modelling, and calculation of internal stresses. *Materials Science and Technology*, 1(10):805–814, 1985. doi:10.1179/mst.1985.1.10.805.

[39] S. Denis, S. Sjöström, and A. Simon. Coupled temperature, stress, phase transformation calculation Model Numerical Illustration of the Internal Stresses Evolution during Cooling of a Eutectoid Carbon Steel Cylinder. *Metallurgical Transactions A*, 18(7):1203–1212, 1987. doi:10.1007/BF02647190.

[40] B. Denkena, A. Krödel, and M. Wilckens. High performance peel grinding of steel shafts using coarse electroplated CBN grinding wheels. *Production Engineering*, 15(5):717–724, 2021. doi:10.1007/s11740-021-01047-1.

[41] Deutsches Institut für Normung e.V. Manufacturing processes chip removal - Part 0: General; Classification, subdivision, terms and definitions, 2003. URL `https://dx.doi.org/10.31030/9500664`.

[42] Deutsches Institut für Normung e.V. Heat-treated steels, alloy steels and free-cutting steels - Part 17: Ball and roller bearing steels, 2023. URL `https://dx.doi.org/10.31030/3415251`.

[43] P. Devloo, J. T. Oden, and T. Strouboulis. Implementation of an adaptive refinement technique for the SUPG algorithm. *Computer Methods in Applied Mechanics and Engineering*, 61(3):339–358, 1987. doi:10.1016/0045-7825(87)90099-5.

[44] A. R. Diaz, N. Kikuchi, and J. E. Taylor. A method of grid optimization for finite element methods. *Computer Methods in Applied Mechanics and Engineering*, 41 (1):29–45, 1983. doi:10.1016/0045-7825(83)90051-8.

[45] F. Ducobu, E. Rivière-Lorphèvre, and E. Filippi. Application of the Coupled Eulerian-Lagrangian (CEL) method to the modeling of orthogonal cutting. *European Journal of Mechanics - A/Solids*, 59:58–66, 2016. doi:10.1016/j.euromechsol.2016.03.008.

[46] F. Ducobu, P.-J. Arrazola, E. Rivière-Lorphèvre, G. O. de Zarate, A. Madariaga, and E. Filippi. The CEL Method as an Alternative to the Current Modelling Approaches for Ti6Al4V Orthogonal Cutting Simulation. *Procedia CIRP*, 58:245–250, 2017. doi:10.1016/j.procir.2017.03.188.

[47] F. Ducobu, E. Rivière-Lorphèvre, and E. Filippi. Finite element modelling of 3D orthogonal cutting experimental tests with the Coupled Eulerian-Lagrangian (CEL) formulation. *Finite Elements in Analysis and Design*, 134:27–40, 2017. doi:10.1016/j.finel.2017.05.010.

[48] G. Duvaut and J. L. Lions. *Inequalities in Mechanics and Physics*, volume 219 of *Grundlehren Der Mathematischen Wissenschaften*. Springer Berlin Heidelberg, Berlin, Heidelberg, 1976. doi:10.1007/978-3-642-66165-5.

[49] F. M. B. Fernandes, S. Denis, and A. Simon. Mathematical model coupling phase transformation and temperature evolution during quenching of steels. *Materials Science and Technology*, 1(10):838–844, 1985. doi:10.1179/mst.1985.1.10.838.

[50] P. Fernández-Pisón, A. R. Vishnu, G. Vadillo, and J. A. Rodríguez-Martínez. Modeling strain-induced martensitic transformation in austenitic stainless steels subjected to cryogenic temperatures using incremental mean-field homogenization schemes. *Mechanics of Materials*, 189:104891, 2024. doi:10.1016/j.mechmat.2023.104891.

[51] F. D. Fischer. A micromechanical model for transformation plasticity in steels. *Acta Metallurgica et Materialia*, 38(8):1535–1546, 1990. doi:10.1016/0956-7151(90)90121-V.

[52] F. D. Fischer, G. Reisner, E. Werner, K. Tanaka, G. Cailletaud, and T. Antretter. A new view on transformation induced plasticity (TRIP). *International Journal of Plasticity*, 16(7-8):723–748, 2000. doi:10.1016/S0749-6419(99)00078-9.

[53] T. Furlan, T. Tsagkir Dereli, N. Schmidt, D. Biermann, and A. Menzel. Application of the Coupled Eulerian Lagrangian method to the prediction of single-grain cutting forces in grinding. *Proceedings in Applied Mathematics and Mechanics*, 22 (1):e202200123, 2023. doi:10.1002/pamm.202200123.

[54] T. Furlan, M. Schewe, P. Scherm, P. Retzl, E. Kozeschnik, and A. Menzel. Modelling and finite element simulation of martensite and bainite phase transformations during quenching under consideration of carbon repartitioning. *Mechanics of Materials*, 204:105275, 2025. doi:10.1016/j.mechmat.2025.105275.

[55] T. Furlan, J. Stollberg, and A. Menzel. Paraqus: Exporting Finite Element Simulation Results from Abaqus to VTK. *Journal of Open Source Software*, 10(106): 5729, 2025. doi:10.21105/joss.05729.

[56] J. F. Ganghoffer and K. Simonsson. A micromechanical model of the martensitic transformation. *Mechanics of Materials*, 27(3):125–144, 1998. doi:10.1016/S0167-6636(97)00044-6.

[57] S. Gao, C. Yang, J. Xu, Y. Fu, H. Su, and W. Ding. Optimization for internal traverse grinding of valves based on wheel deflection. *The International Journal of Advanced Manufacturing Technology*, 92(1-4):1105–1112, 2017. doi:10.1007/s00170-017-0210-8.

[58] C. Geuzaine and J.-F. Remacle. Gmsh: A 3-D finite element mesh generator with built-in pre- and post-processing facilities. *International Journal for Numerical Methods in Engineering*, 79(11):1309–1331, 2009. doi:10.1002/nme.2579.

[59] G. Gottstein. *Materialwissenschaft und Werkstofftechnik: Physikalische Grundlagen.* Springer-Lehrbuch. Springer Berlin Heidelberg Imprint Springer Vieweg, Berlin, Heidelberg, 4., neu bearb. aufl. 2014 edition, 2014. doi:10.1007/978-3-642-36603-1.

[60] G. W. Greenwood and R. H. Johnson. The Deformation of Metals Under Small Stresses During Phase Transformations. *Proceedings of the Royal Society of London. Series A, Mathematical and Physical Sciences*, 283(1394):403–422, 1965. doi:10.1098/rspa.1965.0029.

[61] M. Grieves. Digital Twin: Manufacturing Excellence through Virtual Factory Replication. Technical report, 2015.

[62] Y. B. Guo and C. R. Liu. Mechanical Properties of Hardened AISI 52100 Steel in Hard Machining Processes. *Journal of Manufacturing Science and Engineering*, 124(1):1–9, 2002. doi:10.1115/1.1413775.

[63] C. H. Gür and C. Şimşir. Simulation of Quenching: A Review. *Materials Performance and Characterization*, 1(1):104479, 2012. doi:10.1520/MPC104479.

[64] C. H. Gür and A. E. Tekkaya. Numerical investigation of non-homogeneous plastic deformation in quenching process. *Materials Science and Engineering: A*, 319–321: 164–169, 2001. doi:10.1016/S0921-5093(01)01064-4.

[65] M. E. Gurtin. Two-phase deformations of elastic solids. *Archive for Rational Mechanics and Analysis*, 84(1):1–29, 1983. doi:10.1007/BF00251547.

[66] D. Güzel, T. Furlan, T. Kaiser, and A. Menzel. Neper-Mosaic: Seamless generation of periodic representative volume elements on unit domains. *SoftwareX*, 28:101912, 2024. doi:10.1016/j.softx.2024.101912.

[67] E. O. Hall. The Deformation and Ageing of Mild Steel: III Discussion of Results. *Proceedings of the Physical Society. Section B*, 64(9):747–753, 1951. doi:10.1088/0370-1301/64/9/303.

[68] F. Hashimoto, Y. B. Guo, and A. W. Warren. Surface Integrity Difference between Hard Turned and Ground Surfaces and Its Impact on Fatigue Life. *CIRP Annals*, 55(1):81–84, 2006. doi:10.1016/S0007-8506(07)60371-0.

[69] F. Hashimoto, H. Yamaguchi, P. Krajnik, K. Wegener, R. Chaudhari, H.-W. Hoffmeister, and F. Kuster. Abrasive fine-finishing technology. *CIRP Annals*, 65(2):597–620, 2016. doi:10.1016/j.cirp.2016.06.003.

[70] S. Hazar, B. Alfredsson, and J. Lai. Mechanical modeling of coupled plasticity and phase transformation effects in a martensitic high strength bearing steel. *Mechanics of Materials*, 117:41–57, 2018. doi:10.1016/j.mechmat.2017.10.001.

[71] O. M. Heeres, A. S. J. Suiker, and R. de Borst. A comparison between the Perzyna viscoplastic model and the Consistency viscoplastic model. *European Journal of Mechanics - A/Solids*, 21(1):1–12, 2002. doi:10.1016/S0997-7538(01)01188-3.

[72] S. Hellebrand, D. Brands, and J. Schröder. On the three-dimensional numerical analysis of residual stresses on two scales in hot bulk forming parts. *Proceedings in Applied Mathematics and Mechanics*, 23(3):e202300087, 2023. doi:10.1002/pamm.202300087.

[73] R. Hill. *The Mathematical Theory of Plasticity*. The Oxford Engineering Science Series. Clarendon Press, Oxford, 1950.

[74] R. Holtermann, S. Schumann, A. Zabel, D. Biermann, and A. Menzel. Numerical Determination of Process Values Influencing the Surface Integrity in Grinding. *Procedia CIRP*, 45:39–42, 2016. doi:10.1016/j.procir.2016.02.072.

[75] R. Holtermann, S. Schumann, A. Menzel, and D. Biermann. Modelling and Simulation of Internal Traverse Grinding—From Micro-thermo-mechanical Mechanisms to Process Models. In D. Biermann and F. Hollmann, editors, *Thermal Effects in Complex Machining Processes*, pages 369–403. Springer International Publishing, Cham, 2018. doi:10.1007/978-3-319-57120-1_16.

[76] R. Holtermann. *Computational Multiscale Modelling of Grinding Processes*. PhD thesis, TU Dortmund University, 2016. URL `https://www.doi.org/10.17877/DE290R-17735`.

[77] R. Holtermann, A. Menzel, S. Schumann, D. Biermann, T. Siebrecht, and P. Kersting. Modelling and simulation of Internal Traverse Grinding: Bridging meso- and macro-scale simulations. *Production Engineering*, 9(4):451–463, 2015. doi:10.1007/s11740-015-0613-z.

[78] A. Hor, F. Morel, J.-L. Lebrun, and G. Germain. An experimental investigation of the behaviour of steels over large temperature and strain rate ranges. *International Journal of Mechanical Sciences*, 67:108–122, 2013. doi:10.1016/j.ijmecsci.2013.01.003.

[79] C. Hortig. *Local and Non-Local Thermomechanical Modeling and Finite-Element Simulation of High-Speed Cutting*. PhD thesis, TU Dortmund University, 2010. URL `https://www.doi.org/10.17877/DE290R-15992`.

[80] C. Hortig and B. Svendsen. Simulation of chip formation during high-speed cutting. *Journal of Materials Processing Technology*, 186(1-3):66–76, 2007. doi:10.1016/j.jmatprotec.2006.12.018.

[81] A. Hosseinpour, F. Haji Aboutalebi, and M. S. Sadeghi Nezhad. Evaluation of Bao-Wierzbicki (BW) damage model in sheet metal forming processes. *Archive of Applied Mechanics*, 95(1):7, 2025. doi:10.1007/s00419-024-02717-z.

[82] M. Hunkel. Tempering effects of athermal martensite during quenching and reheating of a SAE 52100 bearing steel. *Materials Science and Engineering: A*, 790: 139601, 2020. doi:10.1016/j.msea.2020.139601.

[83] Y. Huo, T. He, S. Chen, and R. Wu. Mechanical Behavior and Microstructure Evolution of Bearing Steel 52100 During Warm Compression. *JOM*, 70(7):1112–1117, 2018. doi:10.1007/s11837-018-2914-0.

[84] F. Huyan, P. Hedström, and A. Borgenstam. Modelling of the Fraction of Martensite in Low-alloy Steels. *Materials Today: Proceedings*, 2:S561–S564, 2015. doi:10.1016/j.matpr.2015.07.347.

[85] J. Ingber and M. Kunert. Prediction of the Martensite Start Temperature in High-Carbon Steels. *steel research international*, 93(5):2100576, 2022. doi:10.1002/srin.202100576.

[86] R. D. James. Displacive phase transformations in solids. *Journal of the Mechanics and Physics of Solids*, 34(4):359–394, 1986. doi:10.1016/0022-5096(86)90008-6.

[87] S. Jentzsch, D. Stock, R. Häcker, B. Skrotzki, R. D. Kamachali, D. Klingbeil, and V. M. Kindrachuk. Shear Band Formation with Split Hopkinson Bar Experiments. *International Journal of Mechanical Sciences*, 284:109749, 2024. doi:10.1016/j.ijmecsci.2024.109749.

[88] T. Jia, M. Militzer, and Z. Y. Liu. General Method of Phase Transformation Modeling in Advanced High Strength Steels. *ISIJ International*, 50(4):583–590, 2010. doi:10.2355/isijinternational.50.583.

[89] G. R. Johnson and W. H. Cook. A Constitutive Model and Data for Metals Subjected to Large Strains, High Strain Rates and High Temperatures. In *Proceedings of the 7th International Symposium on Ballistics*, pages 541–547, The Hague, The Netherlands, 1983.

[90] G. R. Johnson and W. H. Cook. Fracture characteristics of three metals subjected to various strains, strain rates, temperatures and pressures. *Engineering Fracture Mechanics*, 21(1):31–48, 1985. doi:10.1016/0013-7944(85)90052-9.

[91] W. A. Johnson and R. F. Mehl. Reaction Kinetics in Processes of Nucleation and Growth. *Transactions of the American Institute of Mining and Metallurgical Engineers*, 135:416–442, 1939.

[92] P. Junker and K. Hackl. A thermo-mechanically coupled field model for shape memory alloys. *Continuum Mechanics and Thermodynamics*, 26(6):859–877, 2014. doi:10.1007/s00161-014-0345-x.

[93] Y. Kaymak. *Simulation of Metal Quenching Processes for the Minimization of Distortion and Stresses*. PhD thesis, Otto-von-Guericke-Universität Magdeburg, 2007. URL `https://www.doi.org/10.25673/4872`.

[94] D. Klein, K.-D. Thoben, and L. Nowag. Using Indicators to Describe Distortion Along a Process Chain. *Materialwissenschaft und Werkstofftechnik*, 37(1):19–22, 2006. doi:10.1002/mawe.200500956.

[95] F. Klocke, E. Brinksmeier, and K. Weinert. Capability Profile of Hard Cutting and Grinding Processes. *CIRP Annals*, 54(2):22–45, 2005. doi:10.1016/S0007-8506(07)60018-3.

[96] F. Klocke, B. Döbbeler, B. Peng, and T. Lakner. FE-simulation of the Cutting Process under Consideration of Cutting Fluid. *Procedia CIRP*, 58:341–346, 2017. doi:10.1016/j.procir.2017.03.235.

[97] F. Klocke. *Fertigungsverfahren 2: Zerspanung mit geometrisch unbestimmter Schneide*. VDI-Buch. Springer Berlin Heidelberg, Berlin, Heidelberg, 6th edition, 2018. doi:10.1007/978-3-662-58092-9.

[98] U. F. Kocks and H. Mecking. Physics and phenomenology of strain hardening: The FCC case. *Progress in Materials Science*, 48(3):171–273, 2003. doi:10.1016/S0079-6425(02)00003-8.

[99] D. P. Koistinen and R. E. Marburger. A general equation prescribing the extent of the austenite-martensite transformation in pure iron-carbon alloys and plain carbon steels. *Acta Metallurgica*, 7(1):59–60, 1959. doi:10.1016/0001-6160(59)90170-1.

[100] A. N. Kolmogorov. On the Statistical Theory of Crystallization of Metals [in Russian]. *Izv. Akad. Nauk SSSR, Ser. Mat.*, 3:355–359, 1937.

[101] A. N. Kolmogorov. On the statistical theory of metal crystallization [english translation]. In A. N. Shiryayev, editor, *Selected Works of A.N. Kolmogorov. Volume II, Probability Theory and Mathematical Statistics*, pages 188–192. Springer Netherlands, Dordrecht, 1992. URL `https://link.springer.com/book/10.1007/978-94-011-2260-3`.

[102] D. Lagoudas, D. Hartl, Y. Chemisky, L. Machado, and P. Popov. Constitutive model for the numerical analysis of phase transformation in polycrystalline shape memory alloys. *International Journal of Plasticity*, 32–33:155–183, 2012. doi:10.1016/j.ijplas.2011.10.009.

[103] J. B. Leblond and J. Devaux. A new kinetic model for anisothermal metallurgical transformations in steels including effect of austenite grain size. *Acta Metallurgica*, 32(1):137–146, 1984. doi:10.1016/0001-6160(84)90211-6.

[104] J.-B. Leblond, G. Mottet, J. Devaux, and J.-C. Devaux. Mathematical models of anisothermal phase transformations in steels, and predicted plastic behaviour. *Materials Science and Technology*, 1(10):815–822, 1985. doi:10.1179/mst.1985.1.10.815.

[105] J.-B. Leblond, G. Mottet, and J.-C. Devaux. A theoretical and numerical approach to the plastic behaviour of steels during phase transformations—I. Derivation of general relations. *Journal of the Mechanics and Physics of Solids*, 34(4):395–409, 1986. doi:10.1016/0022-5096(86)90009-8.

[106] D. Lee, W. W. Chen, L. Wang, Y.-C. Chan, and W. Chen. Data-Driven Design for Metamaterials and Multiscale Systems: A Review. *Advanced Materials*, 36(8): 2305254, 2024. doi:10.1002/adma.202305254.

[107] S.-J. Lee and C. J. Van Tyne. A Kinetics Model for Martensite Transformation in Plain Carbon and Low-Alloyed Steels. *Metallurgical and Materials Transactions A*, 43(2):422–427, 2012. doi:10.1007/s11661-011-0872-z.

[108] J. Lemaitre. A Continuous Damage Mechanics Model for Ductile Fracture. *Journal of Engineering Materials and Technology*, 107(1):83–89, 1985. doi:10.1115/1.3225775.

[109] J. Lemaitre. *A Course on Damage Mechanics*. Springer Berlin Heidelberg, Berlin, Heidelberg, 1992. doi:10.1007/978-3-662-02761-5.

[110] H. Li, K. Gai, L. He, C. Zhang, H. Cui, and M. Li. Non-isothermal phase-transformation kinetics model for evaluating the austenization of 55CrMo steel based on Johnson–Mehl–Avrami equation. *Materials & Design*, 92:731–741, 2016. doi:10.1016/j.matdes.2015.12.110.

[111] Y. Li, Z. Jiang, P. Wang, D. Li, and Y. Li. Effect of a modified quenching on impact toughness of 52100 bearing steels. *Journal of Materials Science & Technology*, 160: 96–108, 2023. doi:10.1016/j.jmst.2023.02.057.

[112] Y. Li, M. Xu, Y. Jin, and H. Lu. Finite-element Simulation of Low-alloy High Strength Steel Welding Incorporating Improved Martensite Transformation Kinetics and Recrystalization Annealing. *ISIJ International*, 55(7):1448–1453, 2015. doi:10.2355/isijinternational.55.1448.

[113] G. Liu, S. Shah, and T. Özel. Material Ductile Failure-Based Finite Element Simulations of Chip Serration in Orthogonal Cutting of Titanium Alloy Ti-6Al-4V. *Journal of Manufacturing Science and Engineering*, 141(4):041017, 2019. doi:10.1115/1.4042788.

[114] I.-S. Liu. *Continuum Mechanics*. Advanced Texts in Physics. Springer Berlin Heidelberg, Berlin, Heidelberg, 2002. doi:10.1007/978-3-662-05056-9.

[115] R. Löhner. Some useful data structures for the generation of unstructured grids. *Communications in Applied Numerical Methods*, 4(1):123–135, 1988. doi:10.1002/cnm.1630040116.

[116] C. Magee. *Transformation Kinetics, Microplasticity and Ageing of Martensite in Fe–31 Ni*. PhD thesis, Carnegie Institute of Technology, 1966.

[117] R. Mahnken, M. Johansson, and K. Runesson. Parameter estimation for a visco-plastic damage model using a gradient-based optimization algorithm. *Engineering Computations*, 15(7):925–955, 1998. doi:10.1108/02644409810236920.

[118] R. Mahnken, A. Schneidt, and T. Antretter. Macro modelling and homogenization for transformation induced plasticity of a low-alloy steel. *International Journal of Plasticity*, 25(2):183–204, 2009. doi:10.1016/j.ijplas.2008.03.005.

[119] C. Mareau. A thermodynamically consistent formulation of the Johnson–Cook model. *Mechanics of Materials*, 143:103340, 2020. doi:10.1016/j.mechmat.2020.103340.

[120] K. Marschalkowski. *Beitrag zur Prozessentwicklung für das Hochleistungsinnenrund-Schälschleifen mit galvanisch gebundenen CBN-Schleifscheiben*. PhD thesis, TU Dortmund University, Essen, 2011.

[121] K. Marschalkowski, D. Biermann, and K. Weinert. On the Characteristics of High-Performance Internal Peel Grinding Using Electroplated CBN Wheels. *Machining Science and Technology*, 16(4):580–600, 2012. doi:10.1080/10910344.2012.731950.

[122] T. D. Marusich and M. Ortiz. Modelling and simulation of high-speed machining. *International Journal for Numerical Methods in Engineering*, 38(21):3675–3694, 1995. doi:10.1002/nme.1620382108.

[123] A. Menzel and L. Sprave. Continuum Damage Mechanics—Computational Modelling. In J. Merodio and R. W. Ogden, editors, *Constitutive Modelling of Solid Continua*, volume 262, pages 265–297. Springer Nature Switzerland, Cham, 2025. doi:10.1007/978-3-031-89280-6_9.

[124] S. Mirhosseini, E. S. Perdahcıoğlu, E. H. Atzema, and A. H. van den Boogaard. Effect of temperature and heat generation on martensitic phase transformation in DH steels. *Results in Materials*, 14:100281, 2022. doi:10.1016/j.rinma.2022.100281.

[125] M. E. Miyambo, D. V. Von Kallon, T. Pandelani, and J. D. Reinecke. Review of the development of the split Hopkinson pressure bar. *Procedia CIRP*, 119:800–808, 2023. doi:10.1016/j.procir.2023.04.010.

[126] I. Müller. On the size of the hysteresis in pseudoelasticity. *Continuum Mechanics and Thermodynamics*, 1(2):125–142, 1989. doi:10.1007/BF01141998.

[127] O. Mustak, E. Evcil, and C. Şimşir. Simulation of through-hardening of SAE 52100 steel bearings – Part I: Determination of material properties. *Materialwissenschaft und Werkstofftechnik*, 47(8):735–745, 2016. doi:10.1002/mawe.201600607.

[128] K. Nadolny. Small-dimensional sandwich grinding wheels with a centrifugal coolant provision system for traverse internal cylindrical grinding of steel 100Cr6. *Journal of Cleaner Production*, 93:354–363, 2015. doi:10.1016/j.jclepro.2015.01.046.

[129] A. Needleman. Material rate dependence and mesh sensitivity in localization problems. *Computer Methods in Applied Mechanics and Engineering*, 67(1):69–85, 1988. doi:10.1016/0045-7825(88)90069-2.

[130] P. J. Noell, J. D. Carroll, and B. L. Boyce. The mechanisms of ductile rupture. *Acta Materialia*, 161:83–98, 2018. doi:10.1016/j.actamat.2018.09.006.

[131] I. Noll, T. Bartel, and A. Menzel. A thermodynamically consistent phase transformation model for multiphase alloys: Application to Ti6Al4V in laser powder bed fusion processes. *Computational Mechanics*, 74:1319–1338, 2024. doi:10.1007/s00466-024-02479-z.

[132] M. Oka, H. Okamoto, and K. Ishida. Transformation of lower bainite in hypereutectoid steels. *Metallurgical Transactions A*, 21(3):845–851, 1990. doi:10.1007/BF02656568.

[133] M. Ortiz and J. J. Quigley IV. Adaptive mesh refinement in strain localization problems. *Computer Methods in Applied Mechanics and Engineering*, 90(1-3): 781–804, 1991. doi:10.1016/0045-7825(91)90184-8.

[134] R. Ostwald, T. Bartel, and A. Menzel. Phase-transformations interacting with plasticity – A micro-sphere model applied to TRIP steel. *Computational Materials Science*, 64:12–16, 2012. doi:10.1016/j.commatsci.2012.05.015.

[135] R. Ostwald, T. Bartel, and A. Menzel. An energy-barrier-based computational micro-sphere model for phase-transformations interacting with plasticity. *Computer Methods in Applied Mechanics and Engineering*, 293:232–265, 2015. doi:10.1016/j.cma.2015.04.008.

[136] P. L. B. Oxley. Introducing strain-rate dependent work material properties into the analysis of orthogonal cutting. Technical report, College of Aeronautics, Cranfield University, 1964. URL `http://dspace.lib.cranfield.ac.uk/handle/1826/10812`.

[137] B. Peng, T. Bergs, F. Klocke, and B. Döbbeler. An advanced FE-modeling approach to improve the prediction in machining difficult-to-cut material. *The International Journal of Advanced Manufacturing Technology*, 103(5-8):2183–2196, 2019. doi:10.1007/s00170-019-03456-0.

[138] P. Perzyna. Fundamental Problems in Viscoplasticity. In *Advances in Applied Mechanics*, volume 9, pages 243–377. Elsevier, 1966. doi:10.1016/S0065-2156(08)70009-7.

[139] N. J. Petch. The Cleavage Strength of Polycrystals. *Journal of the Iron and Steel Institute*, 174:25–28, 1953.

[140] Y. Qin, D. Mayweg, P.-Y. Tung, R. Pippan, and M. Herbig. Mechanism of cementite decomposition in 100Cr6 bearing steels during high pressure torsion. *Acta Materialia*, 201:79–93, 2020. doi:10.1016/j.actamat.2020.09.069.

[141] R. Quey, P. R. Dawson, and F. Barbe. Large-scale 3D random polycrystals for the finite element method: Generation, meshing and remeshing. *Computer Methods in Applied Mechanics and Engineering*, 200(17-20):1729–1745, 2011. doi:10.1016/j.cma.2011.01.002.

[142] D. Raabe. The Materials Science behind Sustainable Metals and Alloys. *Chemical Reviews*, 123(5):2436–2608, 2023. doi:10.1021/acs.chemrev.2c00799.

[143] A. Ramesh, S. N. Melkote, L. F. Allard, L. Riester, and T. R. Watkins. Analysis of white layers formed in hard turning of AISI 52100 steel. *Materials Science and Engineering: A*, 390(1-2):88–97, 2005. doi:10.1016/j.msea.2004.08.052.

[144] A. Ramesh and S. N. Melkote. Modeling of white layer formation under thermally dominant conditions in orthogonal machining of hardened AISI 52100 steel. *International Journal of Machine Tools and Manufacture*, 48(3-4):402–414, 2008. doi:10.1016/j.ijmachtools.2007.09.007.

[145] A. Raßloff, P. Seibert, K. A. Kalina, and M. Kästner. Inverse design of spinodoid structures using Bayesian optimization. *Computational Mechanics*, 77:275–296, 2026. doi:10.1007/s00466-024-02587-w.

[146] S. Rausch and D. Biermann. High-performance Surface Peel Grinding on Conventional Surface Grinding Machines. *Procedia CIRP*, 1:669–670, 2012. doi:10.1016/j.procir.2012.05.020.

[147] S. Rausch, S. Odendahl, P. Kersting, D. Biermann, and A. Zabel. Simulation-Based Prediction of Process Forces for Grinding Free-Formed Surfaces on Machining Centers. *Procedia CIRP*, 4:161–165, 2012. doi:10.1016/j.procir.2012.10.029.

[148] S. Rausch. *Modellgestützte Endbearbeitung hartstoffbeschichteter Tiefziehwerkzeuge*. PhD thesis, TU Dortmund University, 2016. URL `https://www.doi.org/10.17877/DE290R-17163`.

[149] A. M. Ravi, J. Sietsma, and M. J. Santofimia. Exploring bainite formation kinetics distinguishing grain-boundary and autocatalytic nucleation in high and low-Si steels. *Acta Materialia*, 105:155–164, 2016. doi:10.1016/j.actamat.2015.11.044.

[150] A. M. Ravi, A. Navarro-López, J. Sietsma, and M. J. Santofimia. Influence of martensite/austenite interfaces on bainite formation in low-alloy steels below MS. *Acta Materialia*, 188:394–405, 2020. doi:10.1016/j.actamat.2020.02.003.

[151] T. Reti, Z. Fried, and I. Felde. Computer simulation of steel quenching process using a multi-phase transformation model. *Computational Materials Science*, 22 (3-4):261–278, 2001. doi:10.1016/S0927-0256(01)00240-3.

[152] P. Retzl, S. Zamberger, and E. Kozeschnik. Computational analysis of austenite film thickness and C-redistribution in carbide-free bainite. *Materials Research Express*, 8(7):076502, 2021. doi:10.1088/2053-1591/ac0d6f.

[153] J. Rezaei, M. H. Parsa, and H. Mirzadeh. Phase transformation kinetics of high-carbon steel during continuous heating. *Journal of Materials Research and Technology*, 27:2524–2537, 2023. doi:10.1016/j.jmrt.2023.10.089.

[154] J. R. Rice and D. M. Tracey. On the ductile enlargement of voids in triaxial stress fields. *Journal of the Mechanics and Physics of Solids*, 17(3):201–217, 1969. doi:10.1016/0022-5096(69)90033-7.

[155] A. Rohatgi. WebPlotDigitizer, 2024. URL `https://automeris.io/`.

[156] D. Said Schicchi, A. Caggiano, M. Hunkel, and E. A. B. Koenders. Thermodynamically consistent multiscale formulation of a thermo-mechanical problem with phase transformations. *Continuum Mechanics and Thermodynamics*, 31(1):273–299, 2019. doi:10.1007/s00161-018-0682-2.

[157] M. J. Santofimia, F. G. Caballero, C. Capdevila, C. García-Mateo, and C. G. De Andrés. Evaluation of Displacive Models for Bainite Transformation Kinetics in Steels. *Materials Transactions*, 47(6):1492–1500, 2006. doi:10.2320/matertrans.47.1492.

[158] E. Scheil. Anlaufzeit der Austenitumwandlung. *Archiv für das Eisenhüttenwesen*, 8(12):565–567, 1935. doi:10.1002/srin.193500186.

[159] N. Schmidt, T. Tsagkir Dereli, T. Furlan, R. Holtermann, D. Biermann, and A. Menzel. Towards the Prediction of Compliance Influences on Shape Deviations in Internal Traverse Grinding. In B.-A. Behrens, A. Brosius, W. Hintze, S. Ihlenfeldt, and J. P. Wulfsberg, editors, *Production at the Leading Edge of Technology*, pages 304–314. Springer Berlin Heidelberg, Berlin, Heidelberg, 2021. doi:10.1007/978-3-662-62138-7_31.

[160] N. Schmidt, T. Furlan, J. Peters, M. Kipp, S. Kaschnitz-Biegl, A. Menzel, F. Bleicher, and D. Biermann. Meso-scale geometric modeling of cutting edges on vitrified bonded aluminum oxide grinding wheels for the multi-scale simulation of internal plunge grinding processes. *Procedia CIRP*, 133:513–518, 2025. doi:10.1016/j.procir.2025.02.088.

[161] A. Schneidt and R. Mahnken. Macromodelling of Transformation Induced Plasticity combined with Viscoplasticity for Low-Alloy Steels. *steel research international*, 79(2):116–123, 2008. doi:10.1002/srin.200806326.

[162] S. Schumann, T. Siebrecht, P. Kersting, D. Biermann, R. Holtermann, and A. Menzel. Determination of the Thermal Load Distribution in Internal Traverse Grinding using a Geometric-Kinematic Simulation. *Procedia CIRP*, 31:322–327, 2015. doi:10.1016/j.procir.2015.03.020.

[163] S. Schumann. *Mehrskalige Modellierung und Simulation des Hochleistungs-Innenrundschälschleifens*. PhD thesis, TU Dortmund University, 2019. URL `https://www.doi.org/10.17877/DE290R-20295`.

[164] M. Shatla, C. Kerk, and T. Altan. Process modeling in machining. Part I: Determination of flow stress data. *International Journal of Machine Tools and Manufacture*, 41(10):1511–1534, 2001. doi:10.1016/s0890-6955(01)00016-5.

[165] T. Siebrecht, N. Potthoff, P. Wiederkehr, and D. Biermann. Modeling of process deflections in a point-based grinding simulation system. *Procedia Manufacturing*, 18:104–111, 2018. doi:10.1016/j.promfg.2018.11.014.

[166] T. Siebrecht. *Simulation von NC-Formschleifprozessen zur Vorhersage von Oberflächentopographien unter Berücksichtigung des Werkzeugverschleißes*. PhD thesis, TU Dortmund University, 2019.

[167] E. P. Silva, P. M. C. L. Pacheco, and M. A. Savi. On the thermo-mechanical coupling in austenite–martensite phase transformation related to the quenching process. *International Journal of Solids and Structures*, 41(3-4):1139–1155, 2004. doi:10.1016/j.ijsolstr.2003.09.049.

[168] J. C. Simo and T. J. R. Hughes. *Computational Inelasticity*, volume 7 of *Interdisciplinary Applied Mathematics*. Springer-Verlag, New York, 1998. doi:10.1007/b98904.

[169] C. Şimşir and C. H. Gür. Quenching: Simulation. In R. Colás and G. E. Totten, editors, *Encyclopedia of Iron, Steel, and Their Alloys*, pages 2892–2939. CRC Press, Boca Raton, 1st edition, 2016. doi:10.1081/E-EISA.

[170] L. J. Sluys and R. de Borst. Wave propagation and localization in a rate-dependent cracked medium—model formulation and one-dimensional examples. *International Journal of Solids and Structures*, 29(23):2945–2958, 1992. doi:10.1016/0020-7683(92)90151-I.

[171] S. Smith, S. N. Melkote, E. Lara-Curzio, T. R. Watkins, L. Allard, and L. Riester. Effect of surface integrity of hard turned AISI 52100 steel on fatigue performance. *Materials Science and Engineering: A*, 459(1-2):337–346, 2007. doi:10.1016/j.msea.2007.01.011.

[172] L. Sobisch, T. Kaiser, T. Furlan, and A. Menzel. A user material approach for the solution of multi-field problems in Abaqus: Theoretical foundations, gradient-enhanced damage mechanics and thermo-mechanical coupling. *Finite Elements in Analysis and Design*, 232:104105, 2024. doi:10.1016/j.finel.2023.104105.

[173] L. Sprave and A. Menzel. A large strain gradient-enhanced ductile damage model: Finite element formulation, experiment and parameter identification. *Acta Mechanica*, 231(12):5159–5192, 2020. doi:10.1007/s00707-020-02786-5.

[174] P. Sridhar, J. M. Rodríguez Prieto, and K. M. de Payrebrune. Discretization approaches to model orthogonal cutting with Lagrangian, Arbitrary Lagrangian Eulerian, Particle Finite Element method and Smooth Particle Hydrodynamics formulations. *Procedia CIRP*, 93:1496–1501, 2020. doi:10.1016/j.procir.2020.03.139.

[175] P. Suwanpinij, X. Li, U. Prahl, and W. Bleck. Modeling Bainite Transformation and Retained Austenite in Hot Rolled TRIP Steel by Instantaneous Carbon Enrichment. *steel research international*, 88(12):1700122, 2017. doi:10.1002/srin.201700122.

[176] H. W. Swift. Plastic instability under plane stress. *Journal of the Mechanics and Physics of Solids*, 1(1):1–18, 1952. doi:10.1016/0022-5096(52)90002-1.

[177] L. Taleb and S. Petit. New investigations on transformation induced plasticity and its interaction with classical plasticity. *International Journal of Plasticity*, 22(1): 110–130, 2006. doi:10.1016/j.ijplas.2005.03.012.

[178] L. Taleb. Transformation-Induced Plasticity (TRIP). In R. B. Hetnarski, editor, *Encyclopedia of Thermal Stresses*, pages 6153–6163. Springer Netherlands, Dordrecht, 2014. doi:10.1007/978-94-007-2739-7_858.

[179] T. Tawakoli, A. Rasifard, and M. Rabiey. High-efficiency internal cylindrical grinding with a new kinematic. *International Journal of Machine Tools and Manufacture*, 47(5):729–733, 2007. doi:10.1016/j.ijmachtools.2006.09.020.

[180] S. P. Timoshenko and J. N. Goodier. *Theory of Elasticity*. Engineering Societies Monographs. McGraw-Hill, Auckland, 3rd edition, 1970.

[181] D. D. Tjahjanto, S. Turteltaub, and A. S. J. Suiker. Crystallographically based model for transformation-induced plasticity in multiphase carbon steels. *Continuum Mechanics and Thermodynamics*, 19(7):399–422, 2008. doi:10.1007/s00161-007-0061-x.

[182] M. Toloui and M. Militzer. Phase field modeling of the simultaneous formation of bainite and ferrite in TRIP steel. *Acta Materialia*, 144:786–800, 2018. doi:10.1016/j.actamat.2017.11.047.

[183] M. Tomczyk and H. van der Valk. Digital Twin Paradigm Shift: The Journey of the Digital Twin Definition:. In *Proceedings of the 24th International Conference on Enterprise Information Systems*, volume 2, pages 90–97. SCITEPRESS - Science and Technology Publications, 2022. doi:10.5220/0010997600003179.

[184] T. Tsagkir Dereli, D. Biermann, A. Menzel, N. Schmidt, T. Furlan, and R. Holtermann. Prozessoptimierung für das Innenrundschälschleifen. *VDI-Z*, 162(03): 25–27, 2020.

[185] T. Tsagkir Dereli, N. Schmidt, T. Furlan, R. Holtermann, D. Biermann, and A. Menzel. Simulation Based Prediction of Compliance Induced Shape Deviations in Internal Traverse Grinding. *Journal of Manufacturing and Materials Processing*, 5(2):60, 2021. doi:10.3390/jmmp5020060.

[186] T. Tsagkir Dereli, T. Furlan, N. Schmidt, J. Liedel, A. Menzel, and D. Biermann. Standzeitverdopplung beim Hochgeschwindigkeits-Innenrundschälschleifen mit modifizierten galvanisch gebundenen CBN-Werkzeugen. *Diamond Business*, 2022(2), 2022.

[187] I. Tzitzelkov, H. P. Hougardy, and A. Rose. Mathematische Beschreibung des Zeit-Temperatur-Umwandlung-Schaubildes für isothermische Umwandlung und kontinuierliche Abkühlung. *Archiv für das Eisenhüttenwesen*, 45(8):525–532, 1974. doi:10.1002/srin.197403916.

[188] E. Uhlmann, R. Mahnken, I. M. Ivanov, and C. Cheng. Thermo-Mechanical Simulation of Hard Turning with Macroscopic Models. In D. Biermann and F. Hollmann, editors, *Thermal Effects in Complex Machining Processes*, Lecture Notes in Production Engineering, pages 95–132. Springer, Cham, 2018. doi:10.1007/978-3-319-57120-1_7.

[189] D. Umbrello, J. Hua, and R. Shivpuri. Hardness-based flow stress and fracture models for numerical simulation of hard machining AISI 52100 bearing steel. *Materials Science and Engineering: A*, 374(1-2):90–100, 2004. doi:10.1016/j.msea.2004.01.012.

[190] S. M. C. van Bohemen. Bainite and martensite start temperature calculated with exponential carbon dependence. *Materials Science and Technology*, 28(4):487–495, 2012. doi:10.1179/1743284711Y.0000000097.

[191] S. M. C. van Bohemen. Bainite growth retardation due to mechanical stabilisation of austenite. *Materialia*, 7:100384, 2019. doi:10.1016/j.mtla.2019.100384.

[192] S. M. C. van Bohemen and J. Sietsma. Martensite Formation in Partially and Fully Austenitic Plain Carbon Steels. *Metallurgical and Materials Transactions A*, 40(5):1059–1068, 2009. doi:10.1007/s11661-009-9796-2.

[193] E. Voce. The Relationship Between Stress and Strain For Homogeneous Deformations. *Journal of the Institute of Metals*, 74:537–562, 1948.

[194] R. von Mises. Mechanik der festen Körper im plastisch- deformablen Zustand. *Nachrichten von der Königlichen Gesellschaft der Wissenschaften zu Göttingen, Mathematisch-Physikalische Klasse*, 1913:582–592, 1913. URL `http://eudml.org/doc/58894`.

[195] A. Vovk, J. Sölter, and B. Karpuschewski. Finite element simulations of the material loads and residual stresses in milling utilizing the CEL method. *Procedia CIRP*, 87:539–544, 2020. doi:10.1016/j.procir.2020.03.005.

[196] W. M. Wang, L. J. Sluys, and R. de Borst. Viscoplasticity for instabilities due to strain softening and strain-rate softening. *International Journal for Numerical Methods in Engineering*, 40(20):3839–3864, 1997. doi:10.1002/(SICI)1097-0207(19971030)40:20<3839::AID-NME245>3.0.CO;2-6.

[197] P. R. Woodard, S. Chandrasekar, and H. T. Y. Yang. Analysis of temperature and microstructure in the quenching of steel cylinders. *Metallurgical and Materials Transactions B*, 30(4):815–822, 1999. doi:10.1007/s11663-999-0043-4.

[198] F. Wöste, T. Siebrecht, M. Fast, and P. Wiederkehr. Geometric Physically-Based and Numerical Simulation of NC-Grinding Processes for the Calculation of Process Forces. *Procedia CIRP*, 86:133–138, 2019. doi:10.1016/j.procir.2020.01.022.

[199] P. Wriggers. *Nonlinear Finite Element Methods*. Springer Berlin Heidelberg, Berlin, Heidelberg, 2008. doi:10.1007/978-3-540-71001-1.

[200] T. Wuest, D. Klein, and K.-D. Thoben. State of steel products in industrial production processes. *Procedia Engineering*, 10:2220–2225, 2011. doi:10.1016/j.proeng.2011.04.367.

[201] C. Yuksel. Sample Elimination for Generating Poisson Disk Sample Sets. *Computer Graphics Forum*, 34(2):25–32, 2015. doi:10.1111/cgf.12538.

[202] E. V. Zaretsky. Rolling Bearing Steels — A Technical and Historical Perspective. Technical Report NASA/TM—2012-217445, NASA Glenn Research Center, Cleveland, 2012.

[203] F. J. Zerilli and R. W. Armstrong. Dislocation-mechanics-based constitutive relations for material dynamics calculations. *Journal of Applied Physics*, 61(5): 1816–1825, 1987. doi:10.1063/1.338024.

[204] O. C. Zienkiewicz and J. Z. Zhu. A simple error estimator and adaptive procedure for practical engineering analysis. *International Journal for Numerical Methods in Engineering*, 24(2):337–357, 1987. doi:10.1002/nme.1620240206.

Publication series of the Institute of Mechanics

published to date:

2010/01 Palnau, V.: Implementierung eines netzfreien Diskretisierungsverfahrens und seine Anwendung auf die Scherbandanalyse.
ISBN 978-3-921823-51-4

2010/02 Klusemann, B.: Application of homogenization methods and crystal plasticity to the modeling of heterogeneous materials of technological interest.
ISBN 978-3-921823-53-8

2011/01 Hortig, C.: Local and non-local thermomechanical modeling and finite-element simulation of high-speed cutting.
ISBN 978-3-921823-54-5

2011/02 Parvizian, F.: Modeling of microstructure evolution in aluminum alloys during hot extrusion.
ISBN 978-3-921823-56-9

2011/03 Noman, M.: Characterization and model identification for the simulation of the forming behavior of ferritic steels.
ISBN 978-3-921823-55-2

2011/04 Kayser, T.: Characterization of microstructure in aluminum alloys based on electron backscatter diffraction.
ISBN 978-3-921823-57-6

2011/05 Bargmann, S.: Computational modeling of material behavior on different scales based on continuum mechanics.
ISBN 978-3-921823-58-3

2013/01 Waffenschmidt, T.: Modelling and simulation of adaptation and degradation in anisotropic biological tissues.
ISBN 978-3-921823-61-3

2015/01 Ostwald, R.: Modelling and simulation of phase-transformations in elastoplastic polycrystals.
ISBN 978-3-921823-66-8

2016/01 Subramanian, M.: Phenomenological modelling and simulation of ferroelectric ceramics.
ISBN 978-3-921823-74-3

2016/02 Clausmeyer, T.: Evolution of plastic anisotropy in metals.
ISBN 978-3-921823-76-7

2017/01 Holtermann, R.: Computational multiscale modelling of grinding processes.
ISBN 978-3-921823-86-6

2017/02 Bartels, A.: Modelling of evolving microstructures at different scales.
ISBN 978-3-921823-93-4

2017/03 Dusthakar Kumar Rao, D. K.: Computational modelling of single and polycrystalline ferroelectric materials.
ISBN 978-3-921823-94-1

2019/01 Buckmann, K.: Microstructure evolution in functional magnetic materials.
ISBN 978-3-947323-09-8

2019/02 Kaiser, T.: Computational modelling of non-simple and anisotropic materials.
ISBN 978-3-947323-14-2

2019/03 Heitbreder, T.: Modelling of material interfaces at different length scales.
ISBN 978-3-947323-18-0

2020/01 Berthelsen, R.: Computational homogenisation of thermomechanical problems.
ISBN 978-3-947323-19-7

2020/02 Sievers, C.: Describing the macroscopic behavior of surfaces based on atomistic models.
ISBN 978-3-947323-24-1

2022/01 Rose, L.: Optimisation based parameter identification using optical field measurements.
ISBN 978-3-947323-31-9

2023/01 Langenfeld, K.: Continuum modeling of brittle and ductile damage: theory and computational frameworks.
ISBN 978-3-947323-41-8

2023/02 Schulte, R.: Parameter identification approaches with application to different classes of materials.
ISBN 978-3-947323-45-6

2023/03 Kaiser, T.: Multiscale multiphysics material modelling.
ISBN 978-3-947323-46-3

2024/01 Noll, I.: Thermomechanical modelling and simulation of laser powder bed fusion processes.
ISBN 978-3-947323-49-4

2024/02 Witt, C.: Isogeometric analysis of anisotropic mechanical and electromechanical higher-gradient continua.
ISBN 978-3-947323-50-0

2025/01 Kurzeja, P.: Modeling, control and opportunities of mechanical interfaces across the scales.
ISBN 978-3-947323-51-7

2025/02 Lammen, H.: Modeling and simulation of general imperfect interfaces using phase-field-theory.
ISBN 978-3-947323-52-4

2025/03 Sprave, L.: Computational modelling and simulation of ductile damage in metals.
ISBN 978-3-947323-54-8

2025/04 Schewe, M.: Computational modelling of surface interactions – wear, material separation and deposition.
ISBN 978-3-947323-55-5

2025/05 Wiegold, T.: On the numerical modeling of interfaces in engineering applications.
ISBN 978-3-947323-53-1

2026/01 Güzel, D.: Multiscale modelling of thermo-electro-mechanically coupled material behaviour.
ISBN 978-3-947323-57-9

2026/02 Fohrmeister, V.: Efficient algorithmic formulations of finite-strain crystal-plasticity based on constrained non-linear optimization
ISBN 978-3-947323-58-6

2026/03 Furlan, T.: Computational modelling of quenching and grinding processes for bearing steels.
ISBN 978-3-947323-59-3